



# Kent Academic Repository

Hilton, Kira (2021) *Antimicrobial Handgels*. Master of Research (MRes) thesis, University of Kent,.

## Downloaded from

<https://kar.kent.ac.uk/89810/> The University of Kent's Academic Repository KAR

## The version of record is available from

<https://doi.org/10.22024/UniKent/01.02.89810>

## This document version

UNSPECIFIED

## DOI for this version

## Licence for this version

CC BY (Attribution)

## Additional information

## Versions of research works

### Versions of Record

If this version is the version of record, it is the same as the published version available on the publisher's web site. Cite as the published version.

### Author Accepted Manuscripts

If this document is identified as the Author Accepted Manuscript it is the version after peer review but before type setting, copy editing or publisher branding. Cite as Surname, Initial. (Year) 'Title of article'. To be published in *Title of Journal*, Volume and issue numbers [peer-reviewed accepted version]. Available at: DOI or URL (Accessed: date).

## Enquiries

If you have questions about this document contact [ResearchSupport@kent.ac.uk](mailto:ResearchSupport@kent.ac.uk). Please include the URL of the record in KAR. If you believe that your, or a third party's rights have been compromised through this document please see our [Take Down policy](https://www.kent.ac.uk/guides/kar-the-kent-academic-repository#policies) (available from <https://www.kent.ac.uk/guides/kar-the-kent-academic-repository#policies>).

University of Kent

Natural Sciences Division

School of Physical Sciences

# Antimicrobial Handgels

By

Kira Hilton

Thesis for the Masters of Sciences by Research

## Abstract

The fight against antimicrobial resistance needs new weapons. Bacteria resistant to all known antibiotics are anticipated to cause 10 million deaths by 2050. A series of novel Supramolecular Self-Associating Amphiphiles have been synthesised to add to the arsenal; either as unique antimicrobial agents or to act as drug delivery agents. The self-association properties of these compounds were studied in the gas phase, solid state and solution state using a range of physicochemical studies. These experiments included: electron spray ionisation mass spectrometry, single crystal X-ray diffraction, quantitative  $^1\text{H}$  NMR, diffusion ordered spectroscopy, tensiometry, dynamic light scattering and zeta potential. One of the novel compounds was observed to form hydrogels in aqueous salt solutions, and these gels were characterised using rheological methods.

# Contents

Abstract.....	2
Acknowledgements.....	5
Abbreviations.....	6
1. Introduction .....	9
1.1. Supramolecular chemistry.....	9
1.2. Non-covalent interactions.....	11
1.3. Non-covalent interactions in nature .....	15
1.4. Amphiphiles and Supra-amphiphiles.....	17
1.5. Incorporating host-guest chemistry into amphiphile design.....	20
1.6. Project aims and objectives.....	25
2. Self-association results and discussion.....	27
2.1. Self-association in the solid state .....	28
2.1.1. Single crystal XRD .....	29
2.2. Self-association in the gas phase.....	31
2.3. Self-association in the solution state.....	34
2.3.1. qNMR studies.....	35
2.3.2. <sup>1</sup> H NMR self-association studies .....	39
2.3.3. <sup>1</sup> H NMR DOSY studies.....	44
2.3.4. Tensiometry studies and Critical Micelle Concentration (CMC) determination ..	47
2.3.5. Dynamic Light Scattering Studies .....	49
2.3.6. Zeta Potential .....	52
2.4. Low level <i>in silico</i> modelling.....	53
3. Rheology .....	55
3.1. Introduction .....	55
3.2 Rheology results and discussion.....	57
3.2.1. Minimum gelation concentration.....	57
3.2.2. Amplitude sweep .....	58
3.2.3. The best way to conduct experiments .....	61
3.2.4. Frequency sweep .....	62
3.2.5. Test of oscillatory stress .....	64
3.2.6. Sonication test.....	66
3.2.7. Microscopy.....	67
4. Microbiological evaluation .....	70
4.1. Antimicrobial properties .....	70
4.2. Screening against <i>E. coli</i> and MRSA.....	70

4.3. MIC <sub>50</sub> calculation .....	72
4.4. Hydrogel antimicrobial efficacy experiments .....	72
5. Conclusion.....	74
6. Future works .....	75
7. Experimental techniques and synthesis .....	76
7.1. Experimental techniques.....	76
7.2. Chemical Synthesis.....	78
8. References .....	83
9. Appendix.....	95
9.1. Tables of data .....	95
9.2. NMR .....	96
9.2.1. Characterisation NMR .....	96
9.2.2. qNMR experiments .....	101
9.2.3. <sup>1</sup> H NMR Self-Association Studies .....	104
9.2.4. <sup>1</sup> H DOSY NMR experiments .....	110
9.3. Surface tension measurements and CMC determination.....	116
9.3.1. Overview .....	117
9.4. DLS data .....	118
9.4.1. Overview .....	125
9.5. Zeta potential data .....	127
9.5.1. Overview .....	129
9.6. Single Crystal X-ray Structures.....	130
9.7. Low Level <i>in silico</i> Modelling .....	133
9.7.1. Overview .....	134
9.8. Mass Spectrum Data .....	135
9.8.1. Overview .....	139
9.9. Rheology .....	140
9.9.1. Amplitude sweep .....	140
9.9.2. The best way to conduct experiments .....	142
9.9.3. Frequency sweep .....	143
9.9.4. Test of oscillatory stress .....	145
9.9.5. Sonication test.....	147
9.10. Microscopy.....	203
9.11. Biological experiments .....	210
9.11.1 Screening.....	210
9.11.2. MIC <sub>50</sub> data for <i>E. coli</i> .....	211
9.11.3. MIC <sub>50</sub> data for MRSA .....	214

Publications not related to this work:

"Controllable hydrogen bonded self-association for the formation of multifunctional antimicrobial materials" L. J. White, J. E. Boles, N. Allen, L. S. Alesbrook, M. J. Sutton, C. K. Hind, K. L. F. Hilton, L. R. Blackholly, R. J. Ellaby, G. T. Williams, D. P. Mulvihill and J. R. Hiscock, *J. Mater. Chem. B*, 2020, **8**, 4694–4700.

"Toward the application of supramolecular self-associating amphiphiles as next-generation delivery vehicles" L. J. White, J. E. Boles, K. L. F. Hilton, R. J. Ellaby and J. R. Hiscock, *Mol.* , 2020, 25.

## Acknowledgements

I would like to thank both Dr. Jennifer Hiscock for all her help throughout this year and also the whole of the Hiscock group for the sheer amount of proof reading, lunchtime chats and tea they have provided. Thank you to all my parental figures and smaller sisters, for all your support for ever. Finally, thank you to James who has been my rock throughout this.

## Abbreviations

Å	Ångstrom
<sup>13</sup> C	Carbon (NMR)
CDI	N,N'-Carbonyldiimidazole
CHCl <sub>3</sub>	Chloroform
CMC	Critical micelle concentration
CoEK	Co-operative equal K
d	doublet (NMR)
DCM	Dichloromethane
<i>d<sub>H</sub></i>	Hydrodynamic diameter
DLS	Dynamic light scattering
DMSO	Dimethylsulfoxide
DMSO- <i>d</i> <sub>6</sub>	Deuterated dimethylsulfoxide
DOSY	Diffusion-ordered spectroscopy
<i>E. coli</i>	<i>Escherichia coli</i>
EK	dimerization/equal K mathematical model
ESI	Electrospray ionisation
ESI-MS	Electron spray ionisation mass spectrometry
EtOAc	Ethyl acetate
EtOH	Ethanol
FTIR	Fourier transform infrared spectroscopy

g	Grams
HBA	Hydrogen bond acceptor
HBD	Hydrogen bond donator
HRMS	High resolution mass spectrometry
<i>J</i>	Coupling constant (NMR)
K	Kelvin
$K_a$	Association constant
$K_{dim}$	Dimerization constant
$K_e$	Equal constant
LVR	Linear viscoelastic region
LWM	Low weight molecular
m	multiplet (NMR)
MeOH	Methanol
MGC	Minimum gelation concetration
mol	Mole(s)
MS	Mass spectrometry
m/z	Mass to charge ratio
NaOBz	Sodium benzoate ( $C_6H_5COONa$ )
NMR	Nuclear magnetic resonance spectroscopy
PDI	Polydisperity index
q	quartet (NMR)

qNMR	quantitative <sup>1</sup> H NMR
s	singlet (NMR)
<i>S. aureus</i>	<i>Staphylococcus aureus</i>
SSA	Supramolecular self-associating amphiphiles
t	triplet (NMR)
TBA	Tetrabutylammonium
TFA	Trifluoroacetic acid
UV	Ultraviolet light
XRD	X-ray diffraction

# 1. Introduction

## 1.1. Supramolecular chemistry

The term “Supramolecular chemistry” was coined in 1969 by Jean-Marie Lehn, and defined as “*chemistry beyond the molecule*”.<sup>1,2</sup> Supramolecular chemistry is a branch of chemistry concerned with higher order complexes that occur as a result of non-covalent intermolecular forces between molecules.<sup>3</sup> Lehn, together with Charles Pederson and Donald Cram were awarded a Nobel Prize in chemistry in 1987 for this work.<sup>4</sup> Since this time, the field of supramolecular chemistry has continued to evolve, resulting in another Nobel Prize in chemistry in 2016. This prize was shared between Jean-Pierre Sauvage, Sir J. Fraser Stoddart and Bernard Feringa whose trail blazing work was in the field of molecular machines.<sup>5</sup> Stoddart’s work on rotaxanes,<sup>6</sup> building on work from Sauvage, showed that the supramolecular complexes could act as a motor, with a ring system able to move on an axle.<sup>7</sup> Further work utilising rotaxane-based motors led to the synthesis of synthetic muscles using the same principle; a ring system moving on an axle that can stretch and compress (Figure 1).<sup>8</sup>

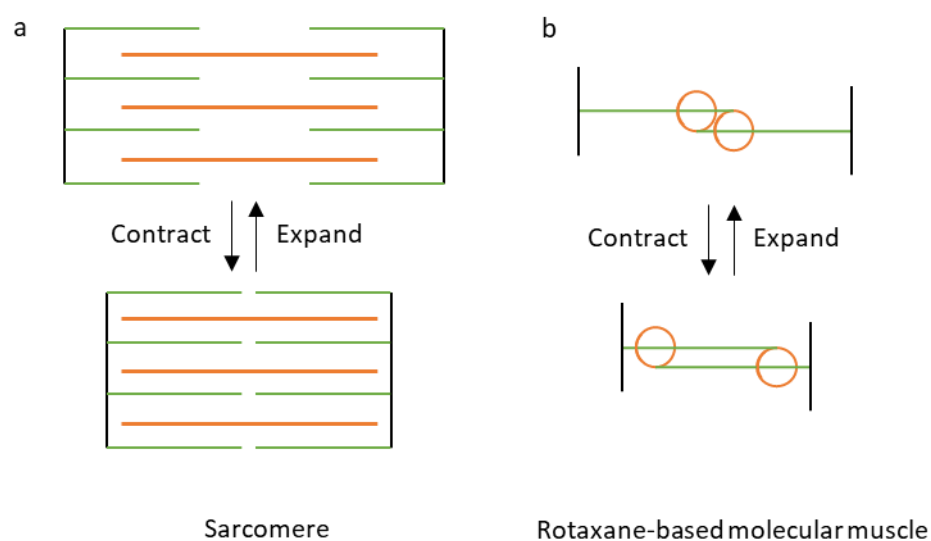
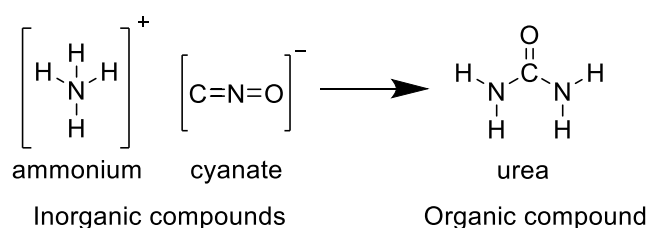


Figure 1 – Example of a) a sarcomere (human muscle) contracting and expanding, orange represents myosin, green represents actin and b) rotaxane-based molecular muscle system.

Although the field of supramolecular chemistry is a relatively young innovation, non-covalent interactions have been studied since Friedrich Wöhler first synthesised urea crystals from inorganic reactants (Scheme 1). This reaction could arguably be seen as the beginning of modern chemistry, occurring in the 17<sup>th</sup> century.<sup>9,10</sup> At the time, the formation of organic compounds from inorganic reactants was thought to be impossible and went against the laws of vitalism, a theory abandoned in modern times, as inorganic compounds do not contain the energy for life.<sup>11</sup>



Scheme 1 - Formation of an organic compound from inorganic compounds by Friedrich Wöhler.<sup>10</sup>

The formation of organic compounds caused the field of organic chemistry to grow and develop through the 19<sup>th</sup> century, with theories of how atoms were bonded heavily disputed. In 1913 Gilbert Lewis proposed the idea of the covalent bond, the currently accepted model of atomic bonding.<sup>12</sup> The covalent bond was described using the theory of “*valence*”, which uses dots and crosses to show lone and paired electrons and the bonds that form when these electrons are shared, as shown in Figure 2. The theory of valence described two different types of bonds: polar bonds which are formed through electron transfer; and non-polar, which are formed by the sharing of electrons.<sup>13,14</sup>

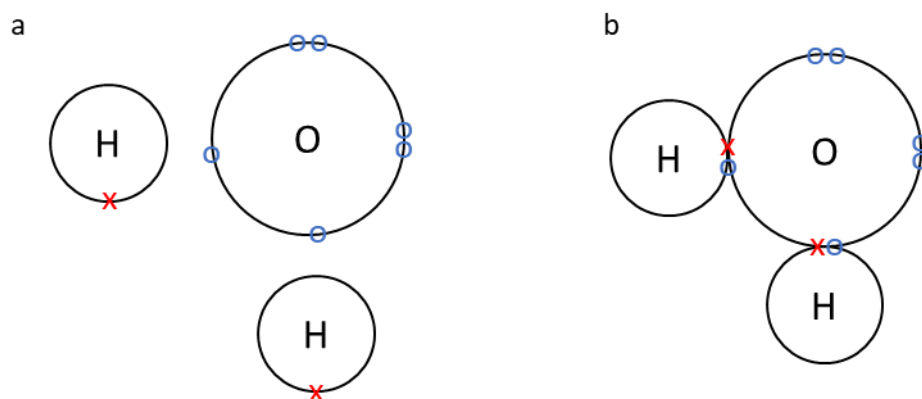


Figure 2 – Example of a Lewis dot and cross diagram: a) an oxygen atom and two hydrogen atoms; b) a water molecule, with electrons being shared between the oxygen and hydrogens.

## 1.2. Non-covalent interactions

Non-covalent interactions were theorised before the theory of the covalent bond was fully accepted. Johannes Diderik van der Waals theorised the existence of intermolecular non-covalent interactions in 1873, now known as van der Waals interactions.<sup>15–17</sup> In 1894 this theory led to Emil Fischer proposing that these non-covalent interactions were integral in the complex formed between an enzyme and substrate, known as the lock and key (or host-guest) concept.<sup>18</sup> The hypothesis was, a specific substrate (key/guest) possesses a complementary fit to the enzyme's active site (lock/host). Non-covalent interactions form between the host and guest, lowering the activation barrier and allowing the chemical reaction to occur. The three-dimensional shape of the enzyme's active site is held together by non-covalent interactions, which enable specific functions to be performed, allowing enzymes to act as catalysts. The lock and key principle led Tom Moore and Thomas Winmill to suggest the presence of the hydrogen bond.<sup>19</sup> Wendell Latimer and Worth Rodebush developed this theory to show that the hydrogen bond is different from dipoles.<sup>20</sup> A dipole is a bond or molecule whose ends have opposite charges. Hydrogen bonds only form between electronegative atoms and electropositive hydrogens, whereas dipoles form between any molecules with a net dipole.

Non-covalent interactions do not share electrons and arise through electrostatic interactions between the distributions of electrons. These non-covalent interactions can

have bond energies as small as  $< 4 \text{ kJ mol}^{-1}$  to  $200 \text{ kJ mol}^{-1}$  (comparable in strength to a covalent bond).<sup>20</sup> Non-covalent interactions include:

- i) van der Waals interactions which are comparatively weak electrostatic interactions between nuclei caused by the polarisation of electron clouds (Figure 3a). They typically have energies of  $< 4 \text{ kJ mol}^{-1}$  and, though individually, van der Waals forces are small, the sum of the interactions can be large.<sup>21,22</sup>
- ii) Dipole-dipole interactions are the next weakest non-covalent interactions with energies of  $5 - 50 \text{ kJ mol}^{-1}$  and are formed through the attraction of one dipole to another (Figure 3b).<sup>21,23</sup>
- iii)  $\pi$ - $\pi$  interactions occur between conjugated systems that have delocalised electrons due to multiple covalent bonds, and have energies between  $0 - 50 \text{ kJ mol}^{-1}$ . These can stack in three different ways: face to face; edge to face; or offset (Figure 3c).<sup>24</sup>
- iv) Hydrogen bonds have been extensively studied.<sup>25-27</sup> They have an energy range of  $4 - 165 \text{ kJ mol}^{-1}$  and can have both covalent and non-covalent character (Figure 3d). They occur between hydrogen bond donor (HBD) and hydrogen bond acceptor (HBA) groups.
- v) Ion-dipole interactions occur between dipoles and charged ions, for example  $\text{Na}^+$  and water ( $50 - 200 \text{ kJ mol}^{-1}$ ) (Figure 3e).<sup>28</sup>
- vi) Ion-ion interactions (Figure 3f) are the strongest type of non-covalent interaction with energies ranging from  $10 - 350 \text{ kJ mol}^{-1}$ , comparable to that of the covalent bond.<sup>29-31</sup>

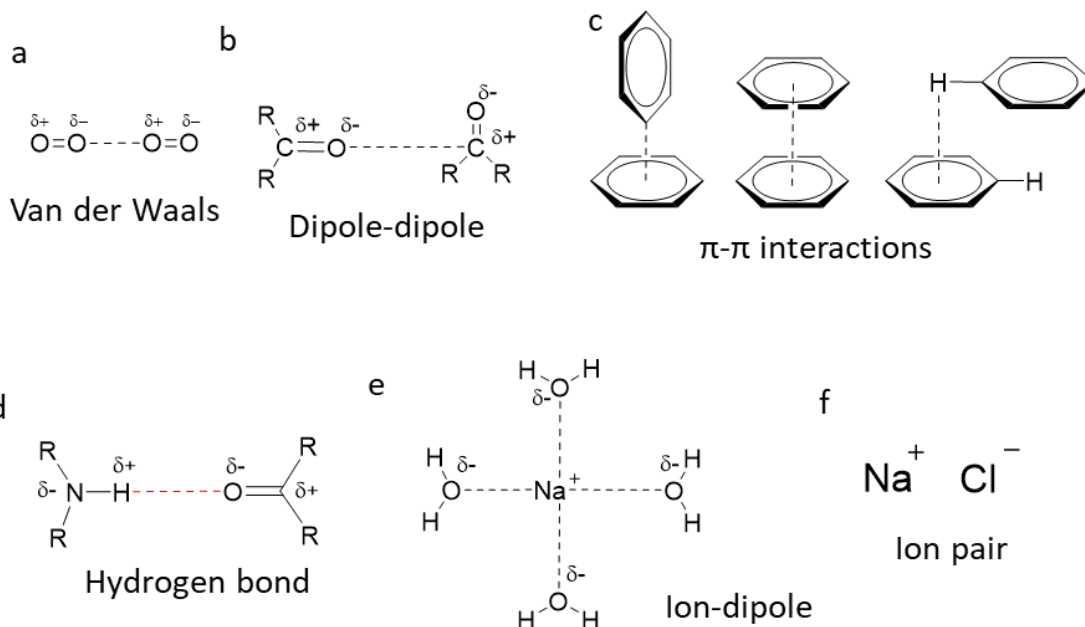


Figure 3 - Illustration of non-covalent interactions a) van der Waals; b) dipole-dipole; c)  $\pi$ - $\pi$  interactions (edge to face, face to face and off-set respectively); d) hydrogen bond; e) ion-dipole; e) ion-ion.

As stated previously, the hydrogen bond can have both covalent and non-covalent character, each with different energies.<sup>32-35</sup> An important thing about hydrogen bonds is that they are highly directional and optimise at 180°. To form the different geometries, there has to be a pay out of energy to move away from linearity. This energy pay out is often the “*additive effect*”, leading to the different geometries. The variety of different geometries are shown in Figure 4.<sup>36</sup> The length of hydrogen bonds (> 1.5 Å) is comparable to the length of the covalent bond (1.2 - 1.5 Å)<sup>33</sup> but the strength of the bond is dependent on the HBA/HBD pair that are involved. The HBA groups are electronegative atoms including oxygen and nitrogen, which interact with the HBD, electropositive acidic hydrogen atoms, such as those bonded to a nitrogen, sulphur or oxygen.

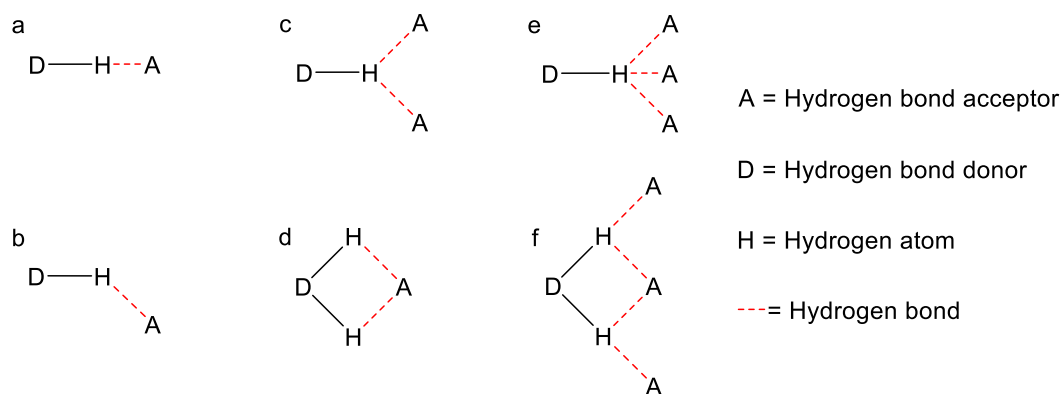


Figure 4 - Examples of hydrogen bond geometries a) preferred linear geometry, b) bent, c) accepting bifurcated, d) donating bifurcated, e) trifurcated, f) three-centred bifurcated. Dashed red lines represent a hydrogen bond.

Once these non-covalent interactions were beginning to be understood, a synthetic approach to host-guest supramolecular chemistry began. Pederson developed crown ethers (**1**),<sup>28</sup> Lehn developed cryptands (**2**) and Cram developed macrocyclic cylophanes (**3**) as seen in Figure 5.<sup>37</sup> These molecules are able to bind to metallic cations.

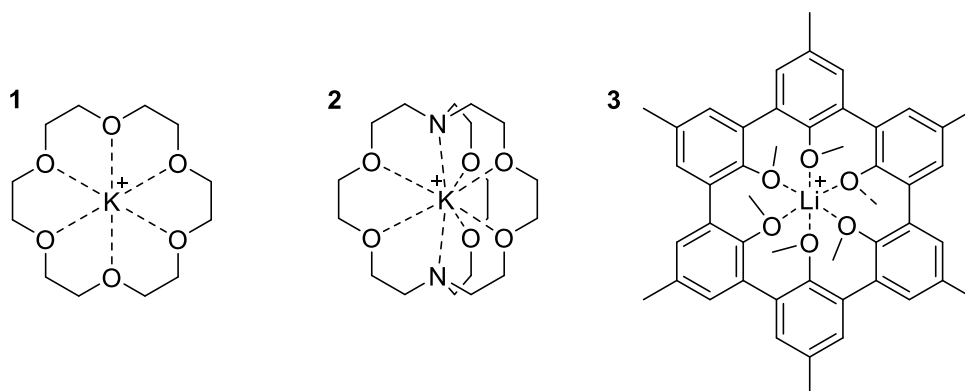


Figure 5 - Series of host-guest complexes examples: **1** crown ether; **2** cryptate; and **3** spherand.<sup>16</sup>

Supramolecular complexes are either preorganised, where they are designed with molecular rigidity to interact with a complementary molecule through non-covalent interactions, or can self-organise.<sup>38,39</sup> Self-organised complexes involve self-assembly events, resulting in both lower and higher ordered complex units through predominantly non-covalent intermolecular interactions.<sup>40,41</sup> A molecule that can form supramolecular complexes can be designed to both be preorganised and to self-organise.<sup>42</sup>

### 1.3. Non-covalent interactions in nature

Non-covalent interactions and resultant supramolecular complexation is abundant in nature. The characteristics of the hydrogen bonds that form in water allows many compounds to dissolve in high concentrations. At these high concentrations hydrogen bonds and/or dipole-dipole interactions can occur, which act as a stabilising force for macromolecules.<sup>43</sup> Examples of supramolecular complexes found in nature include: proteins, which represent fundamental building blocks for all living creatures;<sup>44</sup> DNA; and RNA.

Proteins are built from amino acids, a general unit with an R group that can change the property of the amino acid, and therefore the protein, as shown in Figure 6.

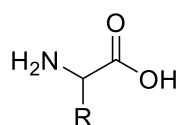
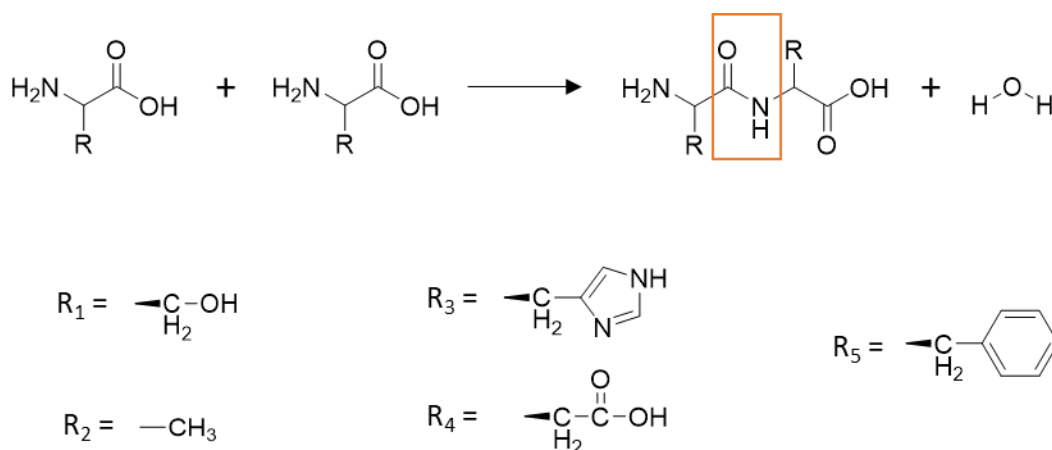


Figure 6 – General structure of an amino acid.

An R group can confer different chemical properties: polar; non-polar; acidic, basic; and aromatic.<sup>45</sup> Amino acids are joined together via peptide bonds (Scheme 2), and this chain of amino acids form the primary structure of the protein (Figure 7a), which then self-assembles into secondary structures dependent on the R groups of the amino acids.



Scheme 2 – A peptide bond formed via a condensation reaction (highlighted in orange). R<sub>1</sub> = serine (polar); R<sub>2</sub> = alanine (non-polar); R<sub>3</sub> = histidine (acidic); R<sub>4</sub> = aspartate (basic); R<sub>5</sub> = phenylalanine (aromatic).

These secondary structures include  $\beta$ -pleated sheets (Figure 7b),  $\alpha$ -helices (Figure 7c) and  $\beta$ -turns/coils and are formed depending on the sequence of amino acids in the

primary structure. The secondary structures are stabilised by hydrogen bonds between the peptide bonds.<sup>43,46,47</sup> The higher structure of the protein brings amino acids which are not covalently joined, close together in space enabling the formation of non-covalent interactions and covalent disulfide bridges between R groups.<sup>48,49</sup> The final three-dimensional conformation of an individual protein or peptide is the tertiary structure (Figure 7d). If a protein requires multiple peptide chains or co-factors these can come together to form a quaternary structure (Figure 7d). Quaternary structure formation can be driven by the hydrophobic effect, and is stabilised by a range of non-covalent interactions and covalent bonds.<sup>46</sup> Hydrogen bonds, van der Waals interactions, electrostatic interactions, hydrophobic interactions and disulfide bridges all help stabilise protein structures.<sup>43,50-52</sup>

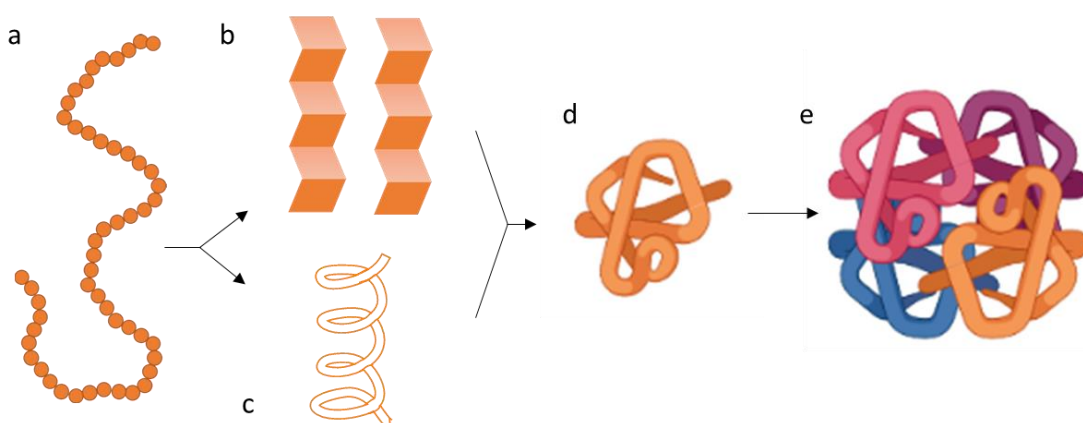


Figure 7 – Different levels of structure of proteins: a) primary, the sequence of amino acids; b) beta sheets; c) alpha helix, which are both secondary structures; d) tertiary structure, the final structure of a peptide; e) quaternary structure, the final conformation of the protein.

As previously discussed, in Fischer's lock and key hypothesis, non-covalent interactions stabilise the enzyme and substrate complex. Another notable biological molecule that relies on non-covalent interactions is deoxyribonucleic acid (DNA). The structure of DNA was discovered by James Watson and Francis Crick, with Rosalind Franklin in 1953. Two antiparallel repeating strands of nucleotides interact to form a double helix (Figure 8).<sup>53</sup> The number of hydrogen bonds that form between the nucleobases depends on the bases present; adenosine (A) and thymine (T) form two hydrogen bonds and cytosine (C) and guanine (G) form three. This difference in the number of hydrogen bonds can have a profound effect on the stability of the DNA. The strength of hydrogen bonds are additive,

therefore, DNA with higher GC content has higher stability.<sup>54</sup> As well as hydrogen bonds between the bases, DNA utilises multiple non-covalent interactions, from the  $\pi$ - $\pi$  interactions between bases on the same strand, van der Waals forces throughout the whole structure, to the hydrophilic interactions between the cytoplasm of the cell and the phosphate backbone. This molecule highlights the importance of non-covalent interactions, both in nature and within supramolecular chemistry.

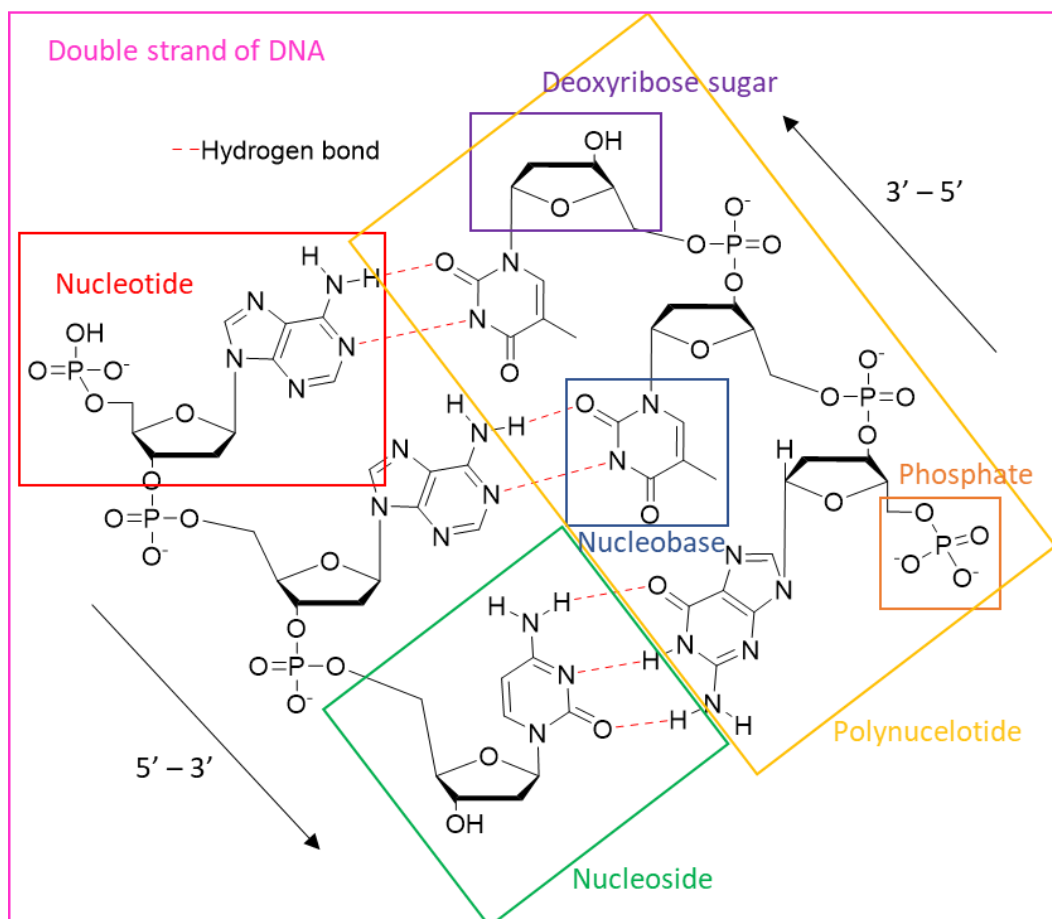


Figure 8 - Deoxyribonucleic acid (DNA) formed of nitrogenous bases (blue), deoxyribose sugar (purple) and phosphate (orange). Deoxyribose + base = nucleoside (green), nucleoside + phosphate = nucleotide (red). Multiple nucleotides = polynucleotide (yellow). Two antiparallel strands of polynucleotides = double stranded DNA (pink).

#### 1.4. Amphiphiles and Supra-amphiphiles

An amphiphile has hydrophobic and hydrophilic components that are covalently bound.<sup>55</sup> There are multiple ways of categorising amphiphiles. One depends on the nature of the hydrophilic group: zwitterionic; anionic; cationic; or nonionic (Figure 9).<sup>56</sup> Zwitterionic amphiphiles (Figure 9, **4**, POPC) carry both a positive and negative charge in the head group.<sup>57</sup>

Cationic amphiphiles (Figure 9, 5, SDS) carry a positively charged head group with a non-amphiphilic counter anion.<sup>58</sup> Anionic amphiphiles (Figure 9, 6, CTA) carry a negatively charged head group, often sulfonate, sulfate, phosphate or carboxylate with a non-amphiphilic counter cation.<sup>59</sup> Nonionic amphiphiles (Figure 9, 7) carry no charge, their solubility depends on the functional group of the amphiphile and its acidity. The hydrophobic component of the amphiphile is typically a hydrocarbon chain, but aromatic rings and trifluoromethyl groups are also sufficiently hydrophobic.<sup>60,61</sup>

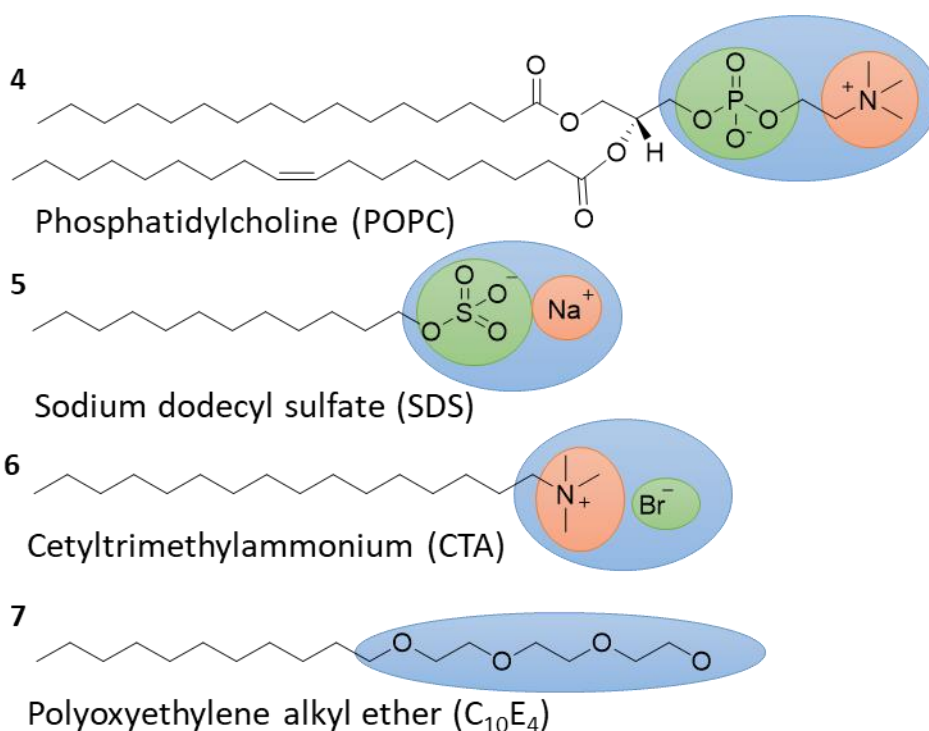


Figure 9 - Examples of amphiphiles: zwitterionic (4); anionic (5); cationic (6); and nonionic (7). The hydrophilic area of the compound is highlighted in blue and is the head of the amphiphile, the anionic area is highlighted in green and the cationic in orange. The hydrophobic tail of the amphiphile is the hydrocarbon chain.

Compound 4 can be found in the eukaryotic cell membrane, and makes up about half of all membrane lipids.<sup>62</sup> The cell membrane is a very important supramolecular complex found in nature and predominantly consist of phospholipid bilayers, which themselves are amphiphiles.<sup>62</sup> The self-associating nature of amphiphiles is used as a tool by supramolecular chemists.

One main feature of an amphiphile is its ability to aggregate to form multiple macromolecular structures dependent on the solvent system. Amphiphiles self-associate by

minimising non-preferential interactions and maximising preferential interactions within the solution state. This self-association allows the formation of many different structures, including reverse micelles (Figure 10a), micelles (Figure 10b), vesicles (Figure 10c), and lipid bilayers (Figure 10d).<sup>63,64</sup> Reverse micelles (Figure 10a) are formed in non-polar solvents, where the tails interact with the non-polar solvent and the heads are encapsulated. Micelles (Figure 10b) form in aqueous solvents, as the hydrophilic head group interacts with the water molecules whilst the hydrophobic tails are enclosed away from the aqueous solvent. The structure of the amphiphile also influences which structures are formed, for example, amphiphiles with single hydrophobic hydrocarbon chains will predominantly form micelles or reverse micelles. However, amphiphiles with multiple hydrocarbon chains form vesicles (Figure 10c) due to the fact that the chains are too large to fit inside the micelle. Phospholipids form the bilayer (Figure 10d) in the membranes found in cells.<sup>63,64</sup>

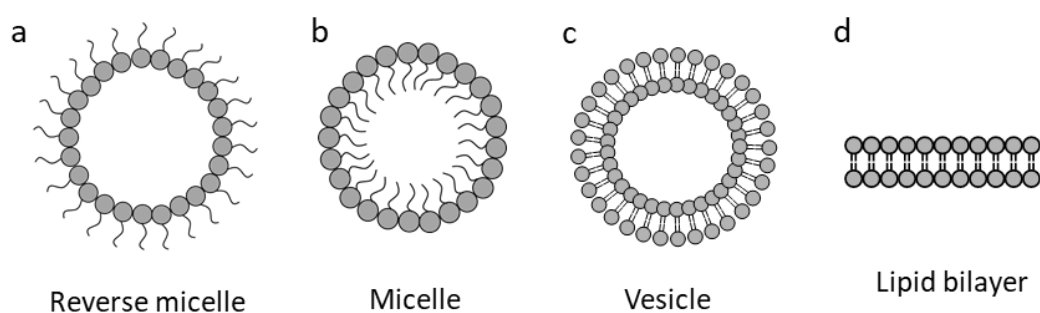


Figure 10 – a) Reverse micelle, b) micelle, c) vesicle, d) lipid bilayer.

In 2009 Wang *et al.* published an extensive review on self-assembly using amphiphilicity.<sup>65</sup> Whilst the focus of this review was on irreversible binding, the concept of self-assembly through non-covalent interactions was also explored. Supramolecular chemists have taken inspiration from nature and developed amphiphilic molecules that are capable of forming supramolecular complexes. These so called “*supra-amphiphile*” complexes utilise non-covalent interactions to self-assemble.<sup>56,66</sup> These supra-amphiphiles are amphiphiles that are built on the principle of non-covalent interactions and dynamic covalent bonds.<sup>66,67</sup> A supra-amphiphile can also be formed by modifying the amphiphile with non-covalent interactions, thereby changing the physical properties (amphiphilicity).<sup>68–70</sup>

Supra-amphiphile complexes are also formed using other non-covalent interactions. Zhang *et al.* synthesised supra-amphiphiles using wedge shaped amphiphiles that self-assembled into spherical aggregates using  $\pi$ - $\pi$  interactions (**8**, Figure 11).<sup>71</sup> Kabanov *et al.* used electrostatic attraction between single-tail cation surfactants and an ionic head group which, when combined together, formed micelle-like aggregations (**9**, Figure 11).<sup>72</sup> Metal-ligand coordination can also be used as a driving force of assembly of supra-amphiphiles. Gohy *et al.* synthesized block co-polymers that self-assemble with ruthenium ions to form micelles in water (**10** Figure 11).<sup>73</sup> These examples of supra-amphiphile complexes use only one form of non-covalent bond, but in most cases, multiple different non-covalent interactions contribute to the driving force of self-assembly.<sup>66</sup>

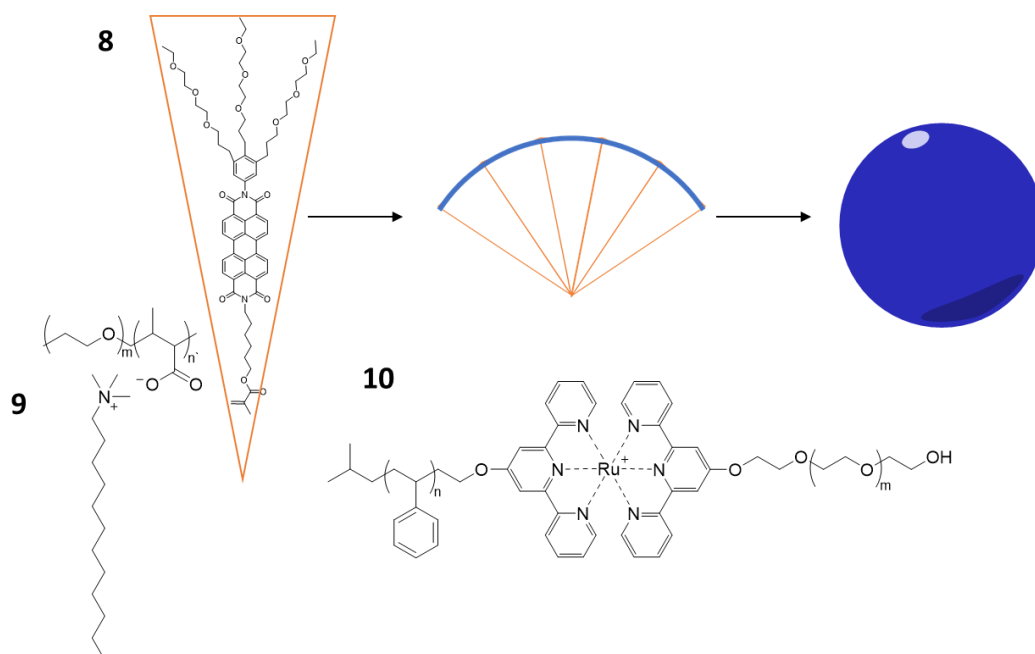


Figure 11 – Examples of supra-amphiphile complexes using different non-covalent interactions.<sup>71–73</sup>

### 1.5. Incorporating host-guest chemistry into amphiphile design

Host-guest chemistry is an area of chemistry involved in the complexation of two or more molecules/ions that are held together in a unique conformation. Non-covalent bonding is crucial in holding these resultant complexes. Hydrogen bonds are one of the most commonly found bonds in host-guest chemistry interactions. The urea motif (**11**, Figure 12) acts as a potent H-bond donor, enabling the entrapment of anions such as sulfonates,



Drawing on the work of Faustino *et al.*, Hiscock *et al.* incorporated the use of the urea functionality into their family of “*Supramolecular Self-associating Amphiphiles*” (SSAs). The general structure of the SSA can be seen in Figure 15: an anionic HBA group; a urea group; and a hydrophobic region. The hydrophobic region contains R groups which change the acidity of the amines, an idea first seen in **15** – **18**.<sup>81,82</sup>

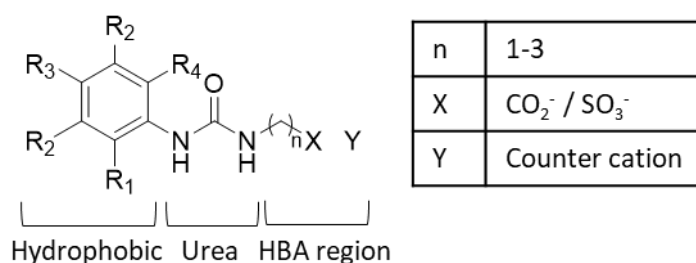


Figure 15 – General structure of frustrated amphiphile system, reported by Hiscock *et al.*.<sup>83</sup>

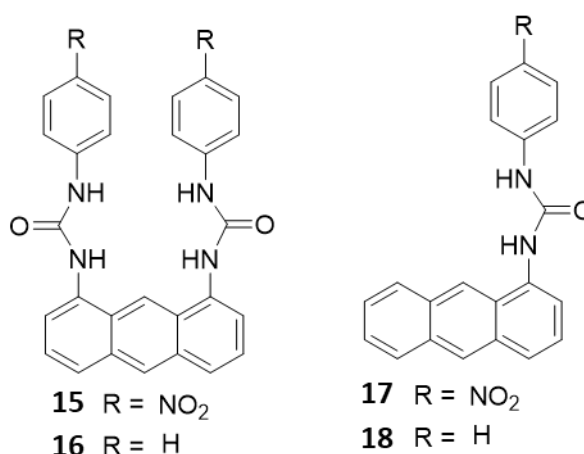


Figure 16 - Urea functionalities used in conjunction to  $\pi$ - $\pi$  interactions.<sup>81,82</sup>

The SSA can adopt four different binding modes leading to a “*frustrated*” system. The different binding modes include tapes (Figure 17a) and dimers (Figure 17b) whilst binding through urea-anion, or stacking modes, both *syn*- (Figure 17c) and *anti*- (Figure 17d) through urea-urea binding.<sup>83,84</sup> The frustrated system is due to there being only one HBD group (the NHs in the urea functionality) and two different HBA groups (the O in the urea functionality and the X anion). The binding modes of the system are dependent on the solvent system, the physical state, the counter cation and the chemical composition of the compound. The solvent system also defines the larger aggregates that these amphiphiles self-associate into.<sup>83</sup>

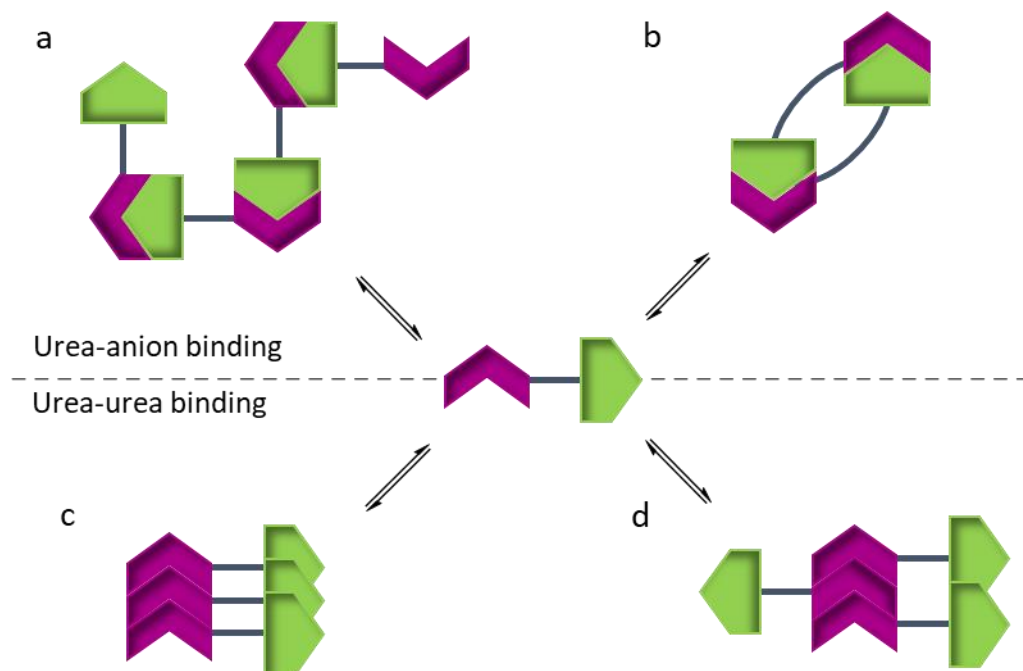


Figure 17 – Possible modes of self-association of the amphiphiles. a) tape, b) dimer, c) *syn*-stacking, d) *anti*-stacking.

To define the structure-activity relationship of self-association, Hiscock *et al.* expanded the family of SSAs, whilst keeping the general structure of the amphiphile the same (Figure 15).<sup>85</sup> The R groups on the aromatic ring were modified, adding both electron withdrawing and donating groups. Analogues were synthesised, replacing urea for thiourea, sulfonate for carboxylate, and different cations that co-ordinated with different strengths. Further to this, the self-association properties of these compounds were studied in the solid state, gas phase, solution state and *in silico*.<sup>86</sup>

Hiscock *et al.* used electron spray ionisation mass spectrometry (ESI-MS) of the anionic component and found that a proportion of the compounds self-associated in the gas phase to form dimers.<sup>86</sup> Using single crystal X-ray diffraction (XRD), they were able to visualise different stacking modes within the solid state: dimers with different interior angles of self-association; hydrogen bonded tapes; and larger extended structures, such as pseudo water channels.<sup>83–85</sup> In the solution state, the self-association depends on the solvent. In dimethyl sulfoxide (DMSO), the compounds predominantly form dimers, whereas in EtOH:H<sub>2</sub>O 1:19 primarily spherical aggregates are formed with a range of sizes (91 - 460 nm).<sup>85</sup> They used a variety of NMR experiments and other solution state studies to study the association events.

These experiments include: quantitative  $^1\text{H}$  NMR; dilution studies; diffusion ordered spectroscopy (DOSY); dynamic light scattering (DLS); zeta potential; and CMC (all further explained in Section 2). To allow visualisation of the structures using fluorescence microscopy, an intrinsically fluorescent group (benzothiazole or anthracene) was added to the SSA.<sup>86</sup> Hiscock *et al.* have also synthesised DNA inspired molecules to investigate the formation of extended structures of the SSAs due to the complementarity of the inspired compounds.<sup>87,88</sup> The SSAs have also been shown to have antimicrobial activity against clinically relevant gram-negative and gram-positive bacteria.<sup>89,90</sup>

Most recently, Hiscock *et al.* found that **19** (Figure 18) formed hydrogels in 15 different salt solutions.<sup>90</sup> The researchers found that when the SSAs were dissolved in  $\text{H}_2\text{O}$ , stable spherical aggregates were formed and, although the zeta potential for these aggregates was  $-71$  mV (stable)<sup>91,92</sup> when additional salts were added, a hydrogel was formed. It was concluded that the added salt was responsible for the higher order structures that produced the gel fibres. The properties of the hydrogel in the different salt solutions were characterised, including the minimum gelation concentration, pH and melting point. Hiscock *et al.* used rheology to find the comparative storage ( $G'$ ) and loss ( $G''$ ) modulus, which are used to find the energy needed to untangle the gel fibres.<sup>90,93</sup> The researchers found the SSAs had an increased efficacy to MRSA over *E. coli* which they hypothesised was due to differences in phospholipid composition and the presence of the single phospholipid bilayer.<sup>90</sup> Hiscock *et al.* also found that the SSA hydrogelator (**19**) could be added to an ampicillin NaCl salt, which greatly increased the zone of inhibition, adding to the usability of the hydrogels as potential drug transportation.<sup>90</sup>

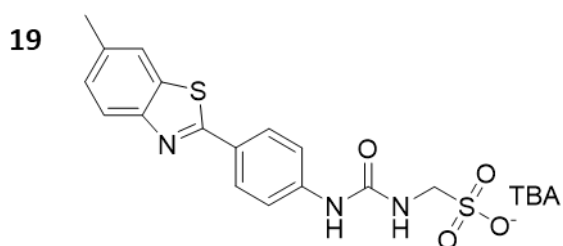


Figure 18 – Original SSA gelator.<sup>90</sup>

The next steps are to determine the structure activity relationship of gelation. This project will focus on stepwise modifications of the general SSA structure to produce next generation SSAs, to further aid understanding of the structure-activity relationship of gelation.

## 1.6. Project aims and objectives

### 1.6.1. Project aim

To produce new molecular weapons in the fight against antimicrobial resistance.

### 1.6.2. Objectives

1. To synthesise and characterise the next generation SSAs **20 – 24** (Figure 19) and explore their self-association properties in the gas phase using mass spectrometry (ESI-MS), the solution state using <sup>1</sup>H NMR spectroscopy, tensiometry, zeta potential and rheometry, the solid state using single crystal XRD and *in silico* using low level computational modelling methods.<sup>45,94</sup>
2. To establish whether **20 – 24** (Figure 19) could also act as supramolecular hydrogels.
3. To explore the possibility that **20 – 24** (Figure 19) could act as antimicrobial agents either in the solution state as self-associated aggregates or as supramolecular materials.

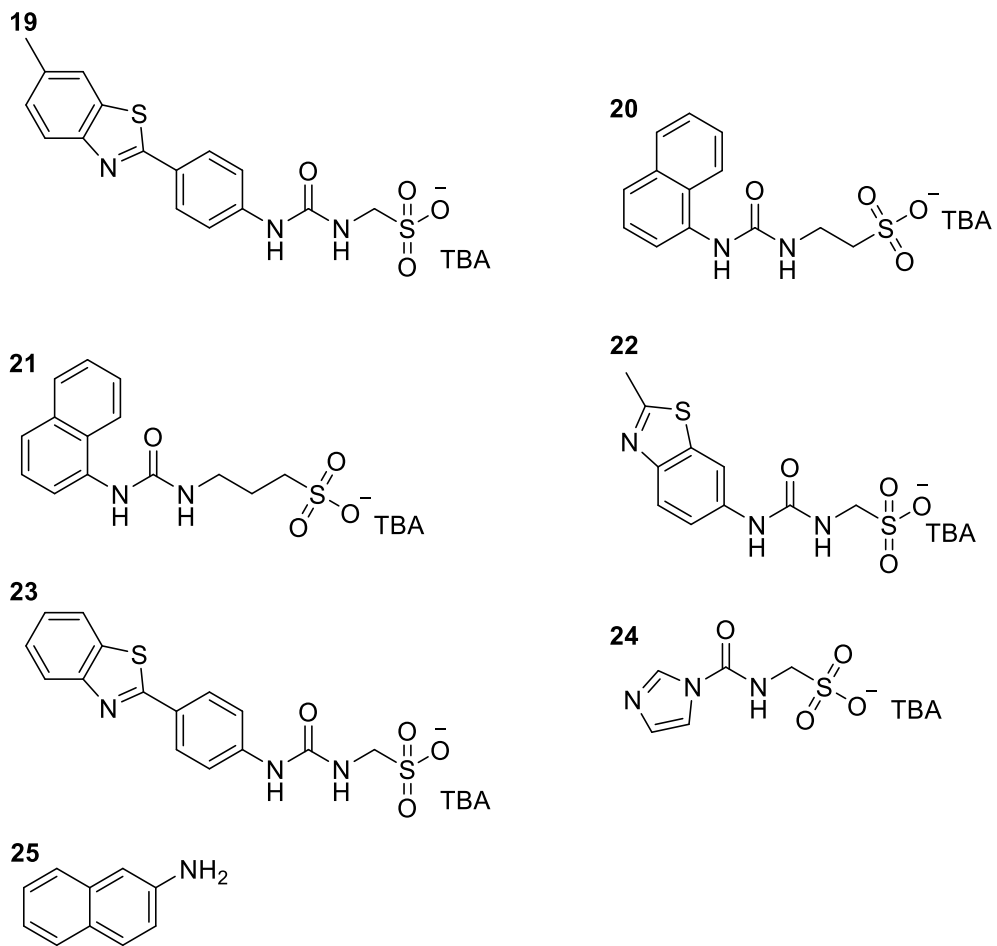


Figure 19 – Chemical structures of SSAs **19** – **24**, and compound **25**.

## 2. Self-association results and discussion

The self-association process of SSAs is complex and can be observed in the solid state, solution state and gas phase. Due to the complexity of the associations, a range of methods is needed to characterise these compounds. The process is presented as a flow chart as shown in Figure 20.

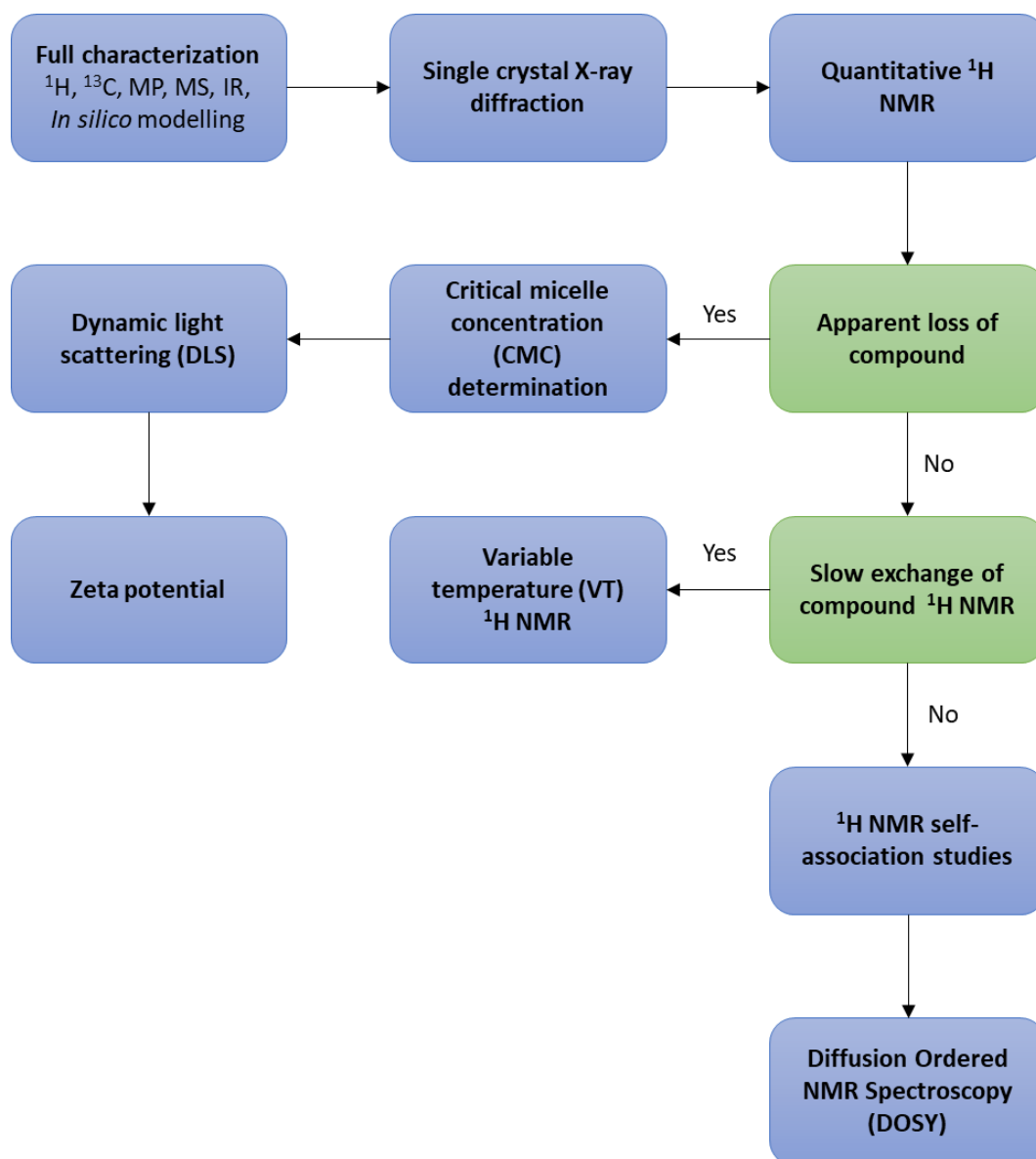


Figure 20 – The techniques used in SSA characterisation. Blue squares represent an action, green squares represent a decision.

In the solid state, single crystal X-ray diffraction is used to detect self-association (see section 2.1.). In the gas phase, dimerization of SSAs using ESI-MS has been observed, however this technique is used primarily as a characterisation technique (see section 2.1.2.).<sup>83</sup> A range

of different experiments are used in the solution state to detect the different association events. qNMR is used to detect the presence of larger self-associated aggregates that cannot be observed by NMR, this is calculated as a percentage “loss”. This percentage “loss” is an apparent loss, as the compound cannot disappear, but becomes NMR silent as the individual molecular units self-associate, causing the resultant structure to adopt solid-like properties which can no longer be observed using standard solution state  $^1\text{H}$  NMR spectroscopy. The proportion of “loss” of a molecular component can be determined (see section 2.3.1.).

If there is no “loss” of compound,  $^1\text{H}$  NMR self-association studies are used to calculate association constants and DOSY is used to calculate the size of the aggregates. If the aggregates are too large to be observed using solution state NMR (there is a “loss” of compound), then DLS is used to calculate the size of these aggregates, zeta potential to determine the stability, and tensiometry to ascertain the CMC and surfactant properties of the aggregates.

## 2.1. Self-association in the solid state

Single crystal XRD was first developed by Max von Laue in 1912, and further developed by Paul Knipping and Walter Friedrich.<sup>95</sup> This led to these researchers receiving the Nobel Prize in Physics in 1914.<sup>96</sup> Single crystal XRD is used regularly as an analytical technique within supramolecular chemistry and is a non-destructive technique used to obtain a three-dimensional structure of the repeating molecular unit within the single crystal.<sup>97</sup> A single crystal is a material in which the crystal lattice structure is completely continuous, thus can act as a grating for the diffraction of X-rays.<sup>95</sup> Single crystals of **22** and **23** were obtained through slow evaporation of an EtOH:H<sub>2</sub>O 1:19 solution. Single crystals of **24** were obtained through slow evaporation of EtOAc. Crystallography data was obtained and refined by Dr Jennifer Hiscock.

### 2.1.1. Single crystal XRD

Dimerization between the urea and anion groups has previously been observed for many SSAs.<sup>83–90</sup> Interestingly, only two hydrogen bonds formed between dimers of **22** (Figure 21) with H<sub>2</sub>O molecules binding instead, compared to other SSAs, which form four.<sup>88</sup> The crystal structure for **23** was also found to dimerize in the solid state, forming four hydrogen bonds between the urea and the sulfonate anion, but also binding to water (Figure 22). The single crystal X-ray structure of **24** has also been elucidated and shows two hydrogen bonds between the dimers (Figure 23).

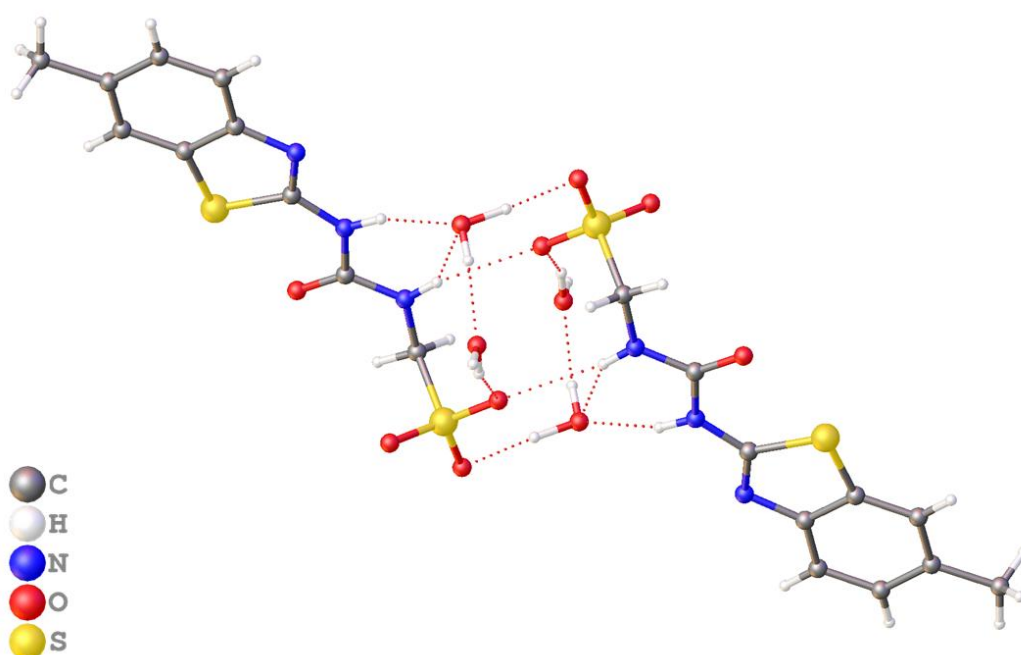


Figure 21 - Single crystal X-ray structure of **22**, exhibiting a hydrogen bonded dimer, TBA counter cation omitted for clarity.

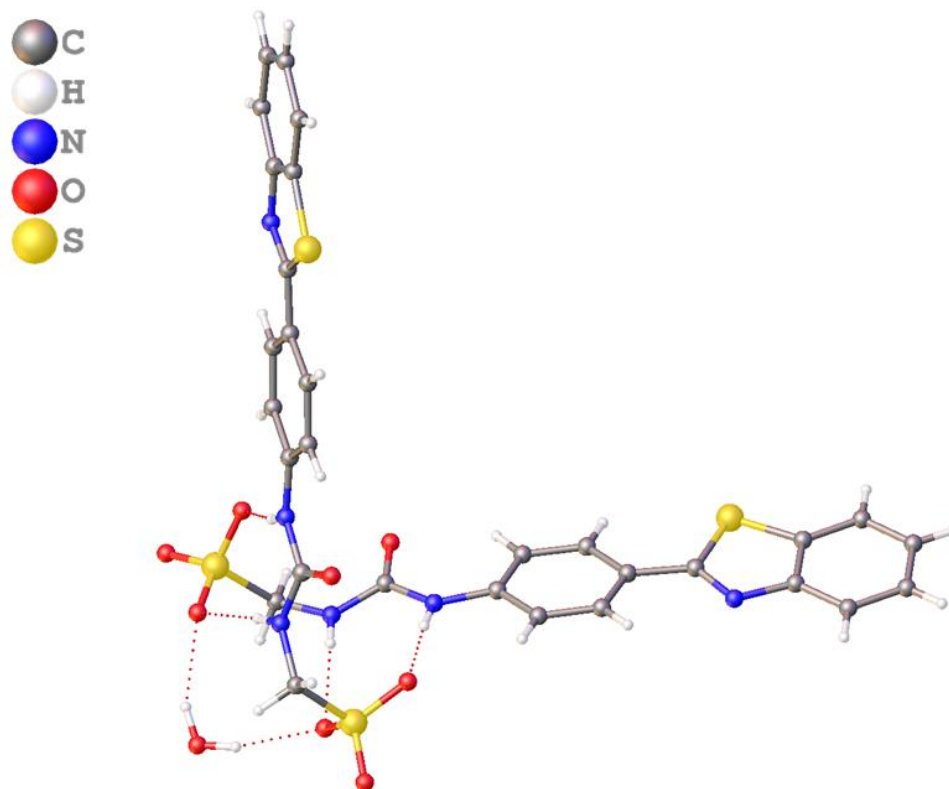


Figure 22 – Single crystal X-ray structure of **23**, exhibiting a hydrogen bonded dimer. TBA counter cation omitted for clarity.

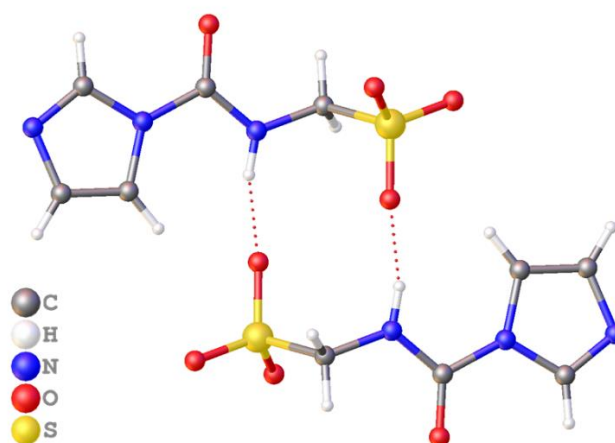


Figure 23 – Single crystal X-ray structure of **24**, TBA counter cation omitted for clarity.

The difference in hydrogen bond number in similar molecules has been previously seen in **26** compared to **19**. Compound **19** forms four hydrogen bonds and can form hydrogels in 0.505 M salt solutions (as discussed in Section 3.), but **26** only forms two hydrogen bonds and cannot form hydrogels due to the formation of a competing intramolecular hydrogen bond.<sup>90</sup> This hydrogen bond forms between the benzothiazole nitrogen and the urea NH,

which means that there is only one free NH free to take part in any molecular self-association events.<sup>90</sup>

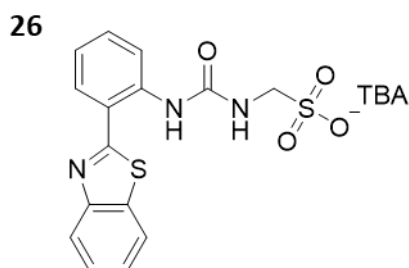


Figure 24 – Compound **26**, previously reported by White et al. that shows only two hydrogen bonds as a dimer in the solid state.<sup>85</sup>

## 2.2. Self-association in the gas phase

Mass spectrometry (MS) is an analytical technique used to separate compounds/molecules by their mass and electrical charge, plotted as  $m/z$  ratio.<sup>98</sup> MS can be used to identify unknown compounds by calculating the molecular weight, quantify known compounds with the use of an internal or external standard, and can also be used to identify the structure and chemical properties of molecules.<sup>99</sup> MS requires the components to have an electrical charge, therefore, ionisation must occur.<sup>100</sup> ESI is an ionisation technique often used to analyse fragile polar molecules as this method is a “softer” ionisation technique.<sup>100–102</sup> The compounds/molecules in solution are sprayed into a strong electric field which causes the sample solution to disperse into charged droplets. The droplets start to evaporate, increasing the charge density on the surface of the droplet. Finally, the droplets either become so charged that ions are repelled, or the droplet explodes, releasing the ions into the vacuum chamber.<sup>103</sup> Other ionisation methods bombard the gaseous samples with an electron beam to knock off electrons from the sample to form positive ions, but this often leads to multiple charges within the sample and causes significant fragmentation.<sup>103</sup> In this project, ESI-MS is not only used to fully characterise the compounds, but also shows the presence of dimers of the anionic component.<sup>83,85–90</sup> It was shown in 1994 that non-covalent interactions, including hydrogen bonds, can be observed in the gas phase, allowing further characterisation of larger complexes.<sup>104</sup>

Molecular self-association in the gas phase has been previously reported for the anionic component of SSAs.<sup>83–90</sup> Self-association and binding to other compounds has also been reported in perylene diimide ligands by Carolyn Mazzitelli *et al.* (**27**, Figure 25) where different perylene diimide ligands are used to bind to single stranded guanine-rich (G-quadruplex) regions of DNA that fold into stable four stranded structures.<sup>105,106</sup> The group used ESI-MS as a tool to distinguish between non-selective and selective binding, to characterise binding stoichiometry and to determine the binding modes between the ligands and the G-quadruplex DNA.<sup>105</sup> Similar to Zhang *et al.*, the researchers discovered that the self-association and binding modes are facilitated through  $\pi$ - $\pi$  stacking around the G-quadruplex DNA.<sup>71,105</sup>

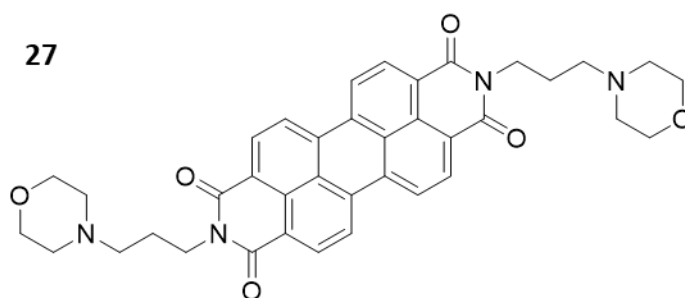


Figure 25 – Perylene diimide synthesised by Mazzitelli *et al.* that shows binding to DNA in ESI-MS.<sup>105</sup>

The anionic component [M] of compounds **20** - **24** were analysed using ESI-MS to determine if self-association is present in the gas phase. Each compound was run at a concentration of  $\sim 1 \times 10^{-6}$  mol in MeOH. ESI-MS data was obtained and refined by Rebecca Ellaby. Compounds were found to be no exception to the general observation that the anionic component of SSAs **20** – **24** exists in both the monomeric [M] and dimeric [M + M + H] species (Table 1).

Table 1 – High resolution ESI<sup>-</sup> mass spectrometry. Theoretical and experimentally derived values.

Compound	m/z [M]		m/z [M + M + H <sup>+</sup> ]	
	Theoretical	Actual	Theoretical	Actual
<b>20</b>	293.0602	293.0612	587.1274	587.1278
<b>21</b>	307.0758	307.0769	615.1586	615.1585
<b>22</b>	300.0118	300.0133	601.0306	601.0319
<b>23</b>	390.0853	390.2425 $\alpha$	723.0550	723.3008
<b>24</b>	200.0084	204.0132	409.0238	409.0301

$\alpha$  – [M+C<sub>2</sub>H<sub>4</sub>] **23** contaminated with ethylene (28.0532).

Using **20** as an example, the theoretical [M] m/z value was calculated to be 293.0602 for the SSA anion, and a signal for this anion was observed at 293.0612 (Figure 26). The protonated dimeric species [M + M + H<sup>+</sup>] m/z was calculated to be 587.1274 (293.0602 x 2 + 1.0072), and giving an actual value of 587.1278 (Figure 27). Dimeric species was also observed for the anionic component of **21**, **22** and **23**. Due to ethylene impurities being present within the spectrometer, the monomeric unit of **23** [M] was not found, it was instead observed as [M + C<sub>2</sub>H<sub>4</sub>].<sup>107</sup>

As self-association occurs in the gas phase, it indicates that the non-covalent interactions that are formed between the dimers are relatively strong. The actual strength of these interactions cannot be determined in the gas phase, but these properties are explored in the solution state. All ESI-MS spectra for **20** – **24** can be found in the appendix (Figure S68 – S77).

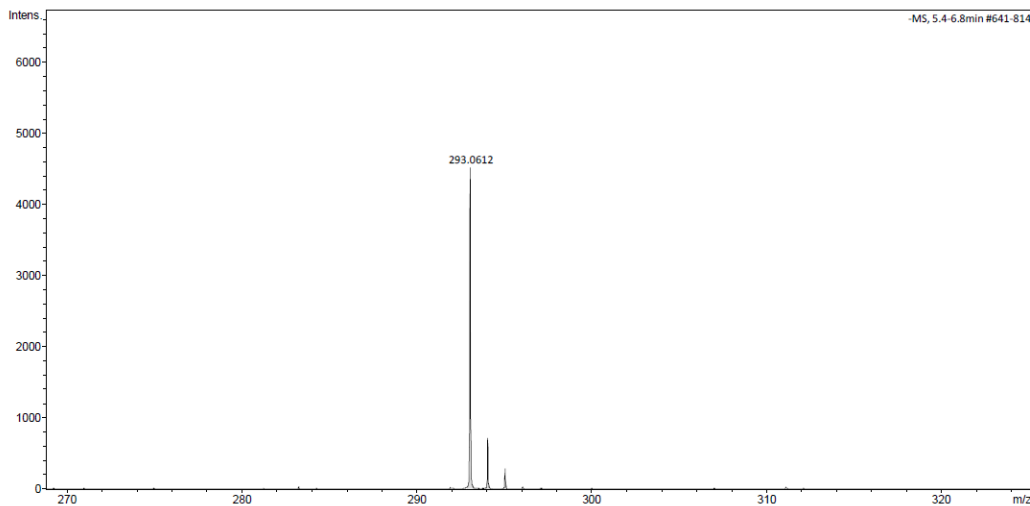


Figure 26 – ESI-MS spectrum of **20** showing the monomeric species [M].

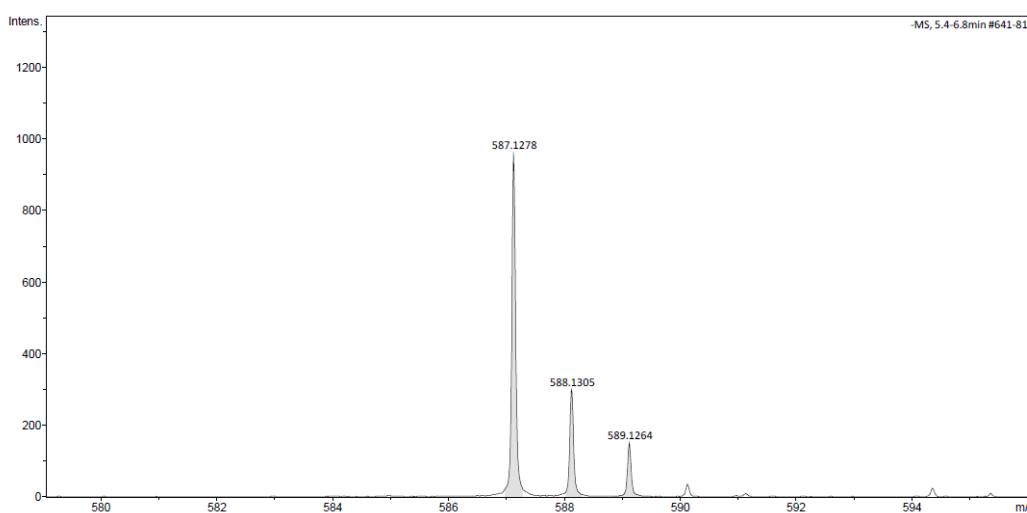


Figure 27 – ESI-MS spectrum of **20** showing the dimeric species [M + M + H<sup>+</sup>].

### 2.3. Self-association in the solution state

The solid state and gas phase allow for the study of self-association without solvent. In the solution state however, solvent interactions must be considered. The binding modes of the SSAs depend on which solvent they are in, for example, in DMSO the SSAs predominantly form dimers, in EtOH:H<sub>2</sub>O 1:19 they form spherical aggregates and for some SSAs, in 0.505 M salt solutions they have been shown to form hydrogels,<sup>83–90</sup> which is explained further in Section 3.1. The self-association patterns of the SSAs in different solvents are partially due to the hydrogen bonding nature of the solvents, but also the hydrophobic and hydrophilic affects driven by the solvent systems. DMSO and water interact with the SSAs due to their HBD and HBA groups, but as they have different numbers of HBA/HBDs, the

solvents interact with the SSAs in various ways.<sup>108,109</sup> A range of different studies have been used to characterise the self-association of the SSAs.

### 2.3.1. qNMR studies

The application of qNMR to quantify the concentration of different molecular components that are visible to solution state NMR against an internal standard has been developed by the Hiscock group.<sup>86,110</sup> This experiment exploits one of the properties of NMR: the integration of the peak is proportional to the number of nuclei responsible for the signal.<sup>111</sup> For this experiment, the  $T_1$ , the relaxation time, or the spin-lattice relaxation time, is increased to 60 seconds to ensure that the entire signal for all nuclei are collected, maintaining the accuracy of the experiment as different environmental conditions change the relaxation time. The limitations of 400 MHz NMR spectroscopy are to do with abundance of specific isotopes. NMR is less sensitive than MS, the natural abundance of the isotope needed must be considered, for example using  $C^{13}$  NMR, the relative abundance of  $C^{13}$  is low, so the sample must be more concentrated. Using solution NMR, all samples must be dissolved in deuterated solvent.<sup>112</sup>

Hiscock *et al.* use qNMR to determine if the SSAs form aggregates that have solid like properties, which therefore cannot be observed using solution state NMR. Two solvent systems were incorporated within the scope of this study, DMSO doped with 1 % DCM and  $D_2O$  doped with 5 % EtOH. DCM and EtOH are used as internal standards as these solvents are miscible within the bulk solvent of choice and the doped peaks appear away from the compound signals. The signal of the doped solvent is then comparatively integrated against the signal of both the anionic and cationic component of the SSA.

To work out percentage “loss” of the anionic component, using **23** in  $DMSO-d_6$  as an example (Figure 28), the ratio of DCM to **23** is calculated (Equation 1). Therefore, the DCM peak at 5.75 ppm integrates for 2.88. The  $CH_2$  peak at 4 ppm should integrate for 2, but it integrates for 1.55 (Figure 28). To work out the percentage “loss” of signal, the actual value

is taken away from the expected ( $2 - 1.55 = 0.45$ ), and then this value is divided by the expected ( $0.45/2 = 0.23$ ), therefore, percentage loss ( $0.23 \times 100 = 23\%$ ) shows a 23% “loss” of signal. This same calculation, but with EtOH as the dopant is carried out in D<sub>2</sub>O (Figure 29).

Equation 1 – In DMSO-*d*<sub>6</sub>, millimoles of **20** calculated (0.0556 mM), the ratio of DCM (0.08 mM) to **20** (0.0556 mM in 0.5 mL) is 1.44 per proton, but as DCM has two protons, the peak at 5.75 ppm integrates for 2.88.

$$\frac{33.61 \text{ mg}}{604.86 \text{ g mol}^{-1}} = 0.0556 \text{ mmol} \qquad \frac{0.08 \text{ mmol}}{0.0556 \text{ mmol}} = 1.44 \times 2 = 2.88$$

In DMSO-*d*<sub>6</sub> there is no apparent percentage “loss” of signal for the anionic or cationic components of compounds **20** – **22** which indicates no large aggregates are formed that become invisible via conventional solution state NMR techniques, as shown in Table 2. Compound **23**, unusually, shows a 22% “loss” of signal of the anionic component, and 20% “loss” of the cationic component in DMSO-*d*<sub>6</sub>, which has only occasionally been observed within this class of compound.<sup>87</sup> This “loss” in DMSO-*d*<sub>6</sub> could be due to the increased hydrophobicity of **23** due to the additional benzene ring. Rabah Khalil and Fadya Saadon looked at the effect of adding benzene rings to the surfactant molecule sodium dodecyl sulfate (SDS) to form sodium dodecylbenzenesulfonate (SDBS).<sup>113</sup> The researchers discovered that the added benzene ring caused the surfactants to form one-dimensional aggregations, whereas SDS formed wormlike micelles when added to varying concentrations of cetyltrimethylammonium bromide in the same aqueous conditions.<sup>113</sup> The one-dimensional aggregates would enable π-π stacking between the anionic components of **23**, potentially causing the formation of the larger aggregates which become NMR silent. Although **19** has a similar structure, it did not show a percentage “loss” in DMSO-*d*<sub>6</sub>, which could be due to the presence of the methyl group which provides steric hinderance, preventing effective stacking.

In D<sub>2</sub>O, all the SSAs showed a “loss” of both anionic and cationic component signal, **20** showing 31 and a 32% “loss”, **21** 44 and 39%, **22** 62 and 0.1% (although this data must be treated with caution as the TBA signal integrated under the EtOH signal), and **23** showing

55 and 51 % of the anionic and cationic components respectively, as shown in Table 2. Due to the “loss” of signal of the compound, the extended structures of the SSAs cannot be observed or studied further using this solvent with solution state NMR spectroscopy.

The “loss” of signal of the SSA is attributed to the larger aggregates having solid-like characteristics, meaning in solution they become NMR silent. As **20** – **22** did not show a “loss” of signal in DMSO- $d_6$ , all of the compound can be observed using solution state NMR, allowing determination of self-association constants and the sizes of the aggregates found. As **23** showed a “loss” of signal in DMSO- $d_6$ , these experiments cannot be carried out. In  $D_2O$ , as all the compounds showed a “loss” of signal, different studies must be carried out to determine the size and stability of these aggregates. All qNMR spectra can be found in the appendix (Figure S16 – S23).

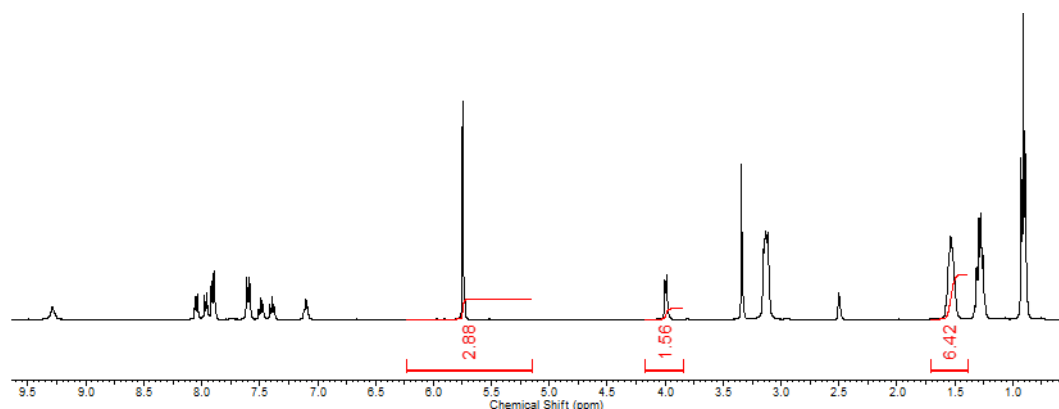


Figure 28 -  $^1H$  NMR spectrum ( $d_1 = 60$  s) of compound **23** (112 mM) in DMSO- $d_6$ /1.0 % DCM. Comparative integration indicates 22 % of the anionic component and 20 % of the cationic component of **23** has become NMR silent.

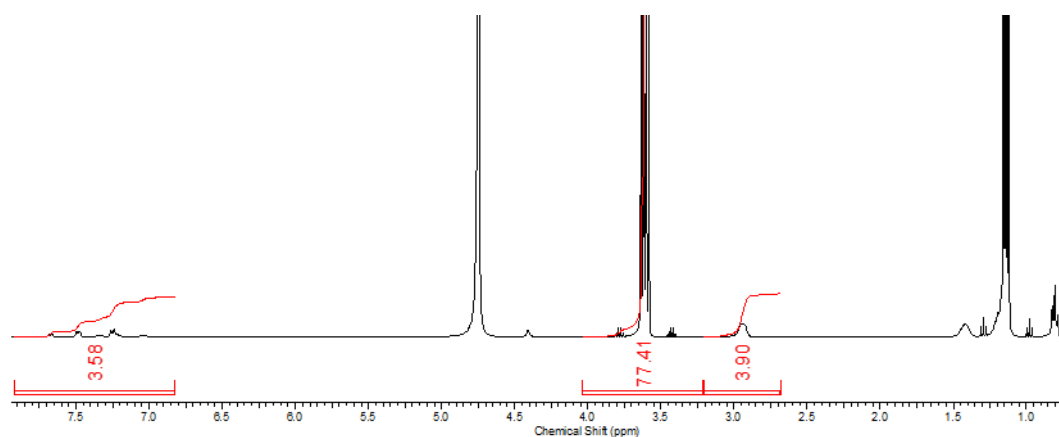


Figure 29 -  $^1H$  NMR spectrum ( $d_1 = 60$  s) of compound **23** (5.56 mM) in  $D_2O$ /5.0 % EtOH. Comparative integration indicates 55 % of the anionic component and 51 % of the cationic component of **23** has become NMR silent.

Table 2 – Overview of results of qNMR studies. Values given in % represent the observed proportion of the anionic component of the compound that has become NMR silent. SSAs were at concentrations of 111.12 mM in DMSO-*d*<sub>6</sub>, and 5.56 mM in D<sub>2</sub>O for all compounds except **22** which was carried out at 0.56 mM due to solubility issues.

Compound	DMSO- <i>d</i> <sub>6</sub> 1% DCM (%)		D <sub>2</sub> O 5 % EtOH (%)	
	Anionic component	Cationic component	Anionic component	Cationic component
<b>20</b>	0	0	31	32
<b>21</b>	0	0	44	39
<b>22</b>	0	0	62	0.1 $\alpha$
<b>23</b>	22	20	55	51

$\alpha$  -Signal integrated under the EtOH signal so data must be treated with caution.

Interestingly, **22** shows a high “loss” of signal in D<sub>2</sub>O, 62 %. This high “loss” of signal of compound could be due to the benzothiazole unit. Alma García-Ortiz *et al.* looked into the nature of the self-assembly of benzothiazole derivatives and found that non-covalent bonds were forming between oxygen and sulfur (**28**, Figure 30).<sup>114</sup> This interaction between S-O could potentially occur between dimers of **22**, between the urea and the free sulfur on the benzothiazole unit. García-Ortiz *et al.* also discussed the planarity of the benzothiazole unit and how it enables  $\pi$ - $\pi$  stacking.<sup>114</sup> Although **23** also contains the benzothiazole unit, it is attached to a benzene ring, making the sulfur much less accessible to interact with the other molecules of **23**. The added benzene ring also adds rotational movement into the structure, reducing its planarity. Peizhi Guo and Minghua Liu also looked at the self-association properties of the benzothiazole unit.<sup>115</sup> The researchers swapped a benzimidazole unit (**29**, Figure 30) for a benzothiazole unit (**30**, Figure 30) and discovered that the two compounds had different stacking patterns in water.<sup>115</sup>

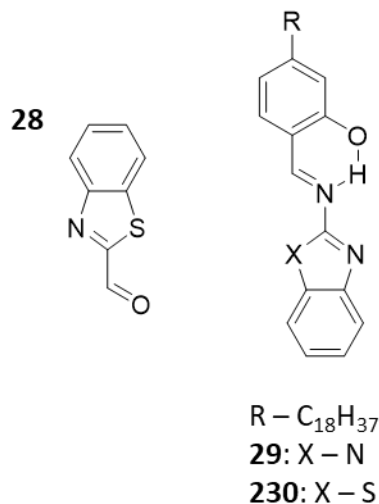


Figure 30 – Garcia -Ortiz *et al.* used **28** to analyse the weak interactions resulting in self-assembly.<sup>114</sup> Guo and Liu used **29** and **30** to illustrate the importance of steric hindrance in self-assembly.<sup>115</sup>

### 2.3.2. <sup>1</sup>H NMR self-association studies

As shown in Figure 20, if there is no observable “loss” of signal in qNMR, the next step is to determine self-association constants. NMR has the ability to monitor weak and non-covalent interactions,<sup>116</sup> for example, hydrogen bonds can be observed as the shift in ppm of <sup>1</sup>H signals (up to 5 ppm)<sup>117–119</sup> and  $\pi$ - $\pi$  interactions through <sup>1</sup>H chemical shifts of CHs in quinacridone derivatives.<sup>120</sup>

To directly monitor the hydrogen bonds that form between the HBD urea NHs and the HBA’s on the SSAs, a series of <sup>1</sup>H NMR dilution studies were performed. Binding constants were also calculated by fitting data to binding isotherms using Bindfit.<sup>121</sup> The isotherms used in this study, the Equal K (EK) and Co-operative equal K (CoEK) have limitations: both assume one component, one-dimensional homogenous aggregates.<sup>122</sup> The CoEK model assumes the first association event has different energy than that of subsequent events and the EK model assumes all association events are constant.<sup>123</sup>

Compounds **20** and **21** were synthesised to determine the importance of alkyl chain length in self-association (Figure 31a and b). Hiscock *et al.* observed that the ethyl linker causes the SSA to cyclise and form an intermolecular bond to form a six membered ring in the crystal structure,<sup>85</sup> and it is hypothesised that **20** forms a similar ring structure (Figure

31a). The propyl linker (**21**) instead forms dimers (Figure 31b) which has previously been reported.<sup>86</sup>

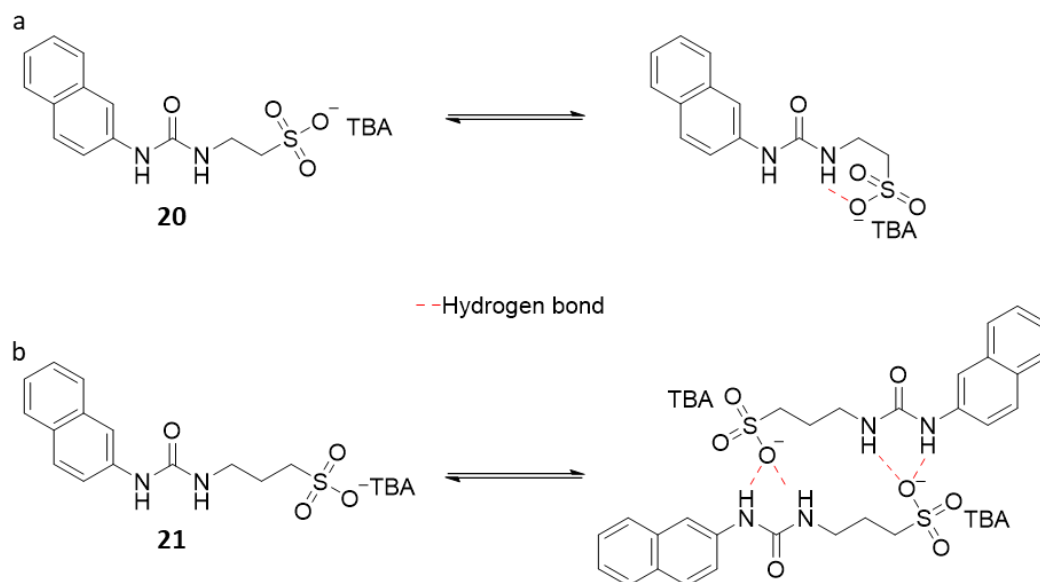


Figure 31 – The hypothesised self-association observed in **20** and **21**. a) Compound **20** forms an intermolecular bond to form a six membered stable ring, b) compound **21** dimerizes which is characteristic of SSAs.<sup>83–90</sup>

To quantify the strength of the hydrogen bonds that form in SSA self-association events, a series of <sup>1</sup>H NMR dilution studies were performed. These studies were undertaken in a DMSO-*d*<sub>6</sub> 0.5 % H<sub>2</sub>O solution. Due to the hygroscopic nature of DMSO-*d*<sub>6</sub>, an aliquot of H<sub>2</sub>O was added to minimise changes in H<sub>2</sub>O concentration to ensure that the samples of the study were comparable.

The results these of dilution studies show that as the concentration of the SSA increases, the NHs protons shift downfield. The change of chemical shift is due to the formation of the hydrogen bond. Kumar *et al.* proposed that the bigger the chemical shift, the greater the strength of the bond.<sup>118</sup> For **20**, there is a very small change in the chemical shift of the urea NHs. This is shown in Figure 32 as an illustrative representation, and Figure 33 graphically.

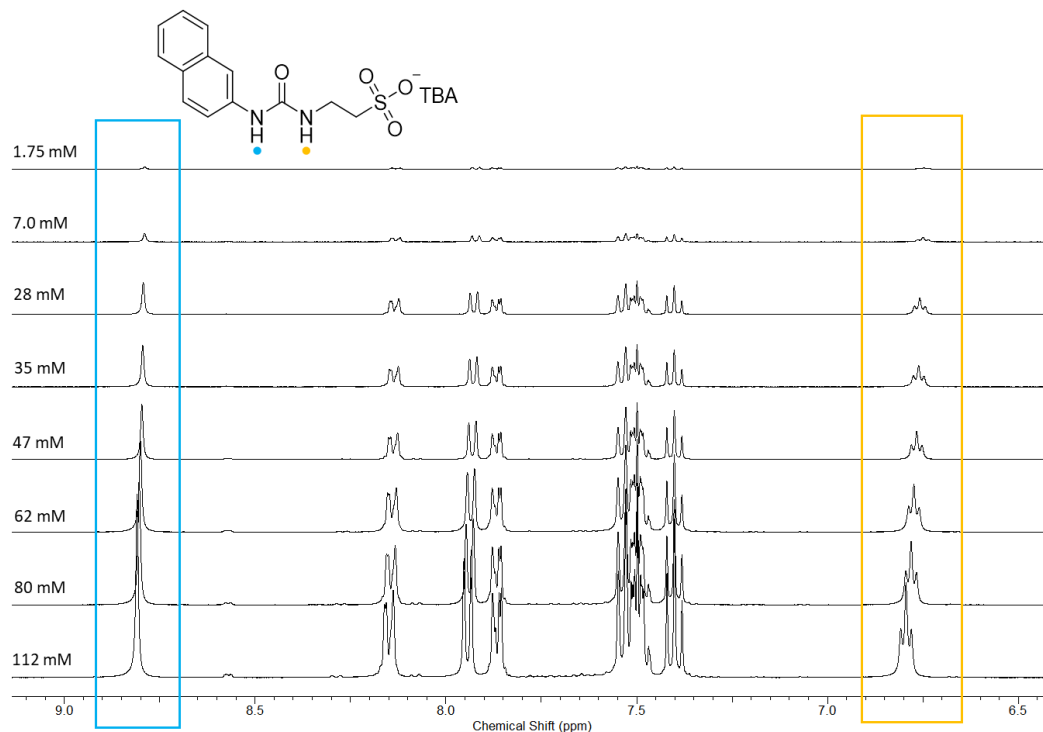


Figure 32 – Enlarged  $^1\text{H}$  NMR stack plot of compound **20** in a  $\text{DMSO-}d_6$  0.5 %  $\text{H}_2\text{O}$  solution. Samples were prepared in series with an aliquot of the most concentrated solution undergoing serial dilution.

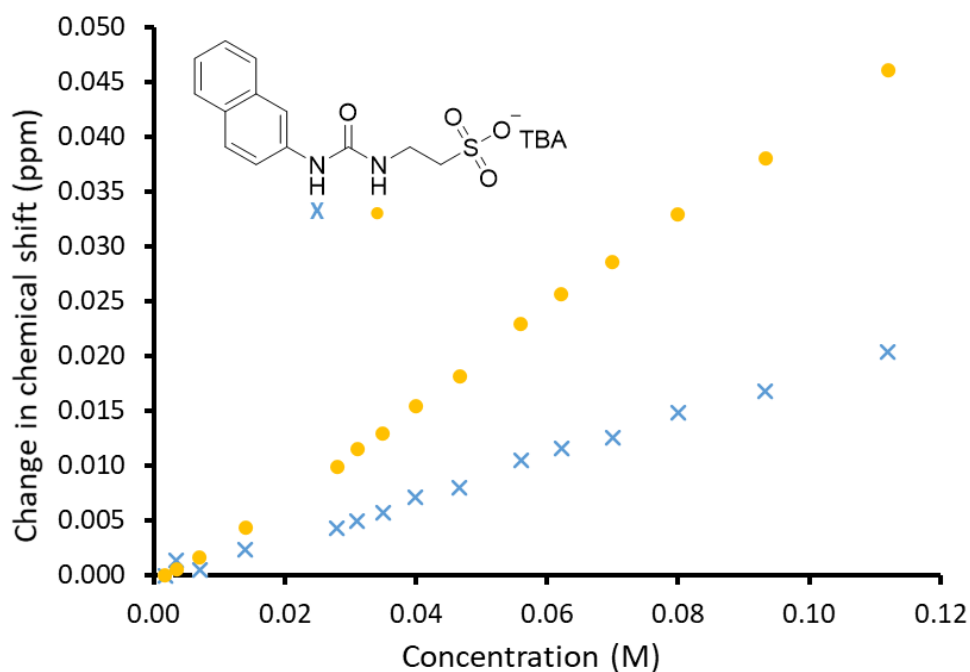


Figure 33 - Graph illustrating the  $^1\text{H}$  NMR down-field change in chemical shift of urea NH resonances with increasing concentrations of compound **20** in  $\text{DMSO-}d_6$  0.5 %  $\text{H}_2\text{O}$  solution (298 K).

Due to both the small change in chemical shift (0.047 ppm for **20** compared to 0.170 ppm for **21**) and the linearity of the trend line points to the fact that there is no real self-association between the anionic components of the SSA, adding to the hypothesis that **20** forms an intermolecular hydrogen bond to form a cyclic structure (Figure 31). The six

membered ring is more kinetically stable than a dimer, so increasing the concentration of **20** has a smaller effect on dimer formation, as the cyclic structure is already formed. Comparing the change in chemical shift of **20** to **21**, which has an almost identical structure, the change in ppm is almost four times greater (Figure 34).

To quantify the strength of the hydrogen bonds that formed during the self-association events, the changes in chemical shift were fitted to two binding isotherms; the dimerization EK and the CoEK (Table 3). The majority of SSAs form dimers in DMSO,<sup>83-90</sup> but, as **20** has a negative  $K_e$  and  $K_{dim}$  value it shows that the data does not fit the isotherm. The data does not fit as there are technically two self-association events occurring; i) the cyclisation event with the intermolecular hydrogen bond, and ii) the dimerization event that usually occurs between the anionic component of the SSAs. As two self-association events are being fitted, technically the CoEK model fits better, as the  $K_{dim}$  values are higher than the EK values (CoEK –  $K_{dim} = 3.66 \text{ M}^{-1}$ , EK –  $K_{dim} = -4.13 \times 10^{-2} \text{ M}^{-1}$ ). Although the errors are lower, the solution does not fit the one compound one directional binding event so the data cannot be fitted to either isotherm as there are more complex equilibria that are involved. Compound **21** shows a relatively small EK  $K_{dim}$  value of  $1.21 \text{ M}^{-1}$ , but due to the high errors for the CoEK isotherm, ( $K_{dim} = \pm 1.9 \%$ ,  $\rho = \pm 11.2 \%$ ), it can be inferred that **21** forms dimers in DMSO- $d_6$ , which is supported by the DOSY data as shown in Section 2.3.3.

Compound **22** also shows a relatively small change in ppm and little to no curvature of the graph (Figure 35), leading to negligible association constants ( $K_{dim} = 0.09 \text{ M}^{-1}$ ). As seen in the solid state (Section 2.1.1), the anionic component of **22** only forms two hydrogen bonds compared to the usual four observed in anionic components of SSAs, similarly to **26**. Interestingly, **26** also shows very small EK dimerization constants ( $K_{dim} = 0.6 \text{ M}^{-1}$ ) compared to **19** ( $K_e = 2.7 \text{ M}^{-1}$ ) which forms four hydrogen bonded dimers between the anionic component in solid state.<sup>85</sup> It could therefore be inferred that, due to the hydrogen bonding seen in the solid state in both the anionic components of **22** and **26**, the hydrogen

bonds that form in the solution state are weak also, as observed in the low association constants compared to **19** that forms both four hydrogen bonds and has a high association constant ( $K_e = 2.7 \text{ M}^{-1}$ ). Due to peak overlap, the position of the NHs could not be determined for 0.093 M and 0.080 M. All  $^1\text{H}$  NMR spectra and Bindfit links can be found in the appendix (Figure S24 – S32).

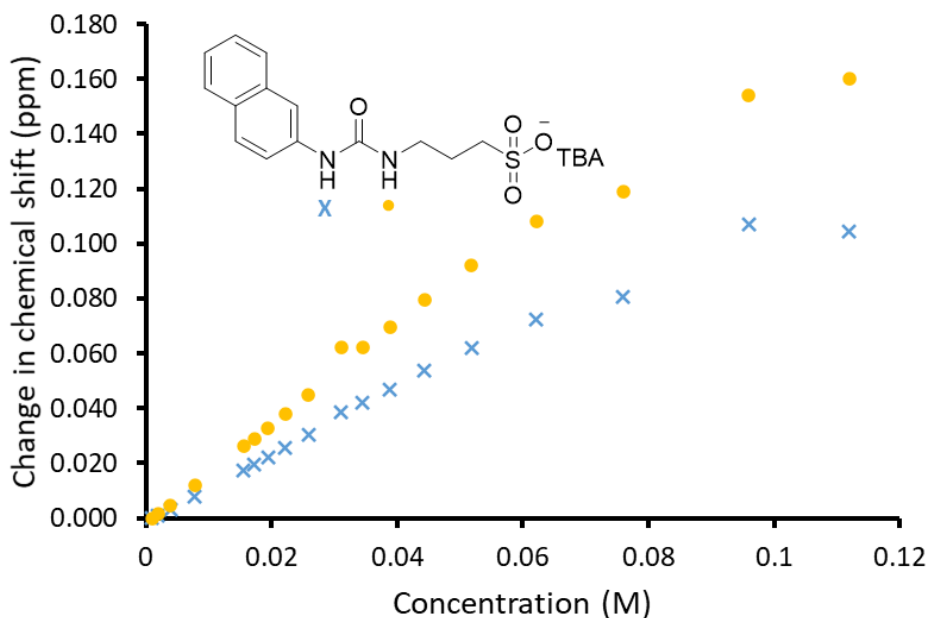


Figure 34 - Graph illustrating the  $^1\text{H}$  NMR down-field change in chemical shift of urea NH resonances with increasing concentrations of compound **21** in  $\text{DMSO-}d_6$  0.5 %  $\text{H}_2\text{O}$  solution (298 K).

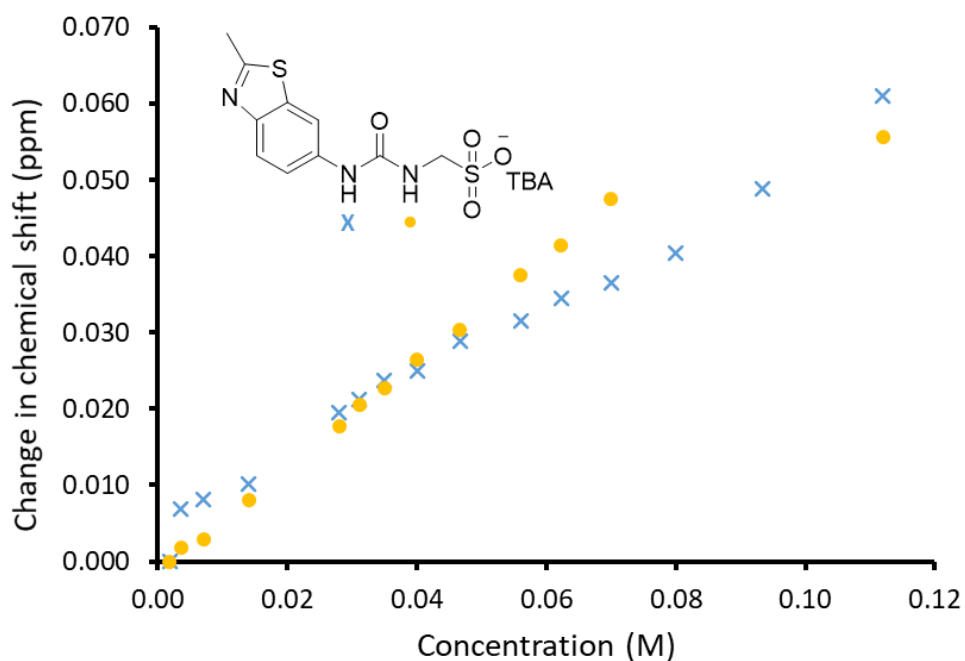


Figure 35 - Graph illustrating the  $^1\text{H}$  NMR down-field change in chemical shift of urea NH resonances with increasing concentrations of compound **22** in  $\text{DMSO-}d_6$  0.5 %  $\text{H}_2\text{O}$  solution (298 K).

Table 3 – Self-association constants ( $M^{-1}$ ) calculated for **20** – **22** in DMSO- $d_6$  0.5% H<sub>2</sub>O solution at 298 K. Constants obtained for EK and CoEK isotherms by fitting <sup>1</sup>H NMR dilution data to Bindfit v0.5.<sup>121</sup>

Compound	EK model ( $M^{-1}$ )		CoEK model ( $M^{-1}$ )		
	$K_e$	$K_{dim}$	$K_e$	$K_{dim}$	$\rho$
<b>20</b>	-0.08 ( $\pm 0.9\%$ )	$-4.13 \times 10^{-2}$ ( $\pm 0.4\%$ )	7.32 ( $\pm 2.6\%$ )	3.66 ( $\pm 1.3\%$ )	0.26 ( $\pm 6.2\%$ )
<b>21</b>	2.43 ( $\pm 2.0\%$ )	1.21 ( $\pm 1.0\%$ )	13.2 ( $\pm 3.9\%$ )	6.60 ( $\pm 1.9\%$ )	0.32 ( $\pm 11.2\%$ )
<b>22</b>	0.18 ( $\pm 3.8\%$ )	0.09 ( $\pm 1.9\%$ )	-0.68 ( $\pm 17.3\%$ )	-0.34 ( $\pm 8.6\%$ )	-212.19 ( $\pm 14.9\%$ )
<b>23</b>	<i>a</i>	<i>a</i>	<i>a</i>	<i>a</i>	<i>a</i>

*a* – Data could not be fitted as a “loss” of the anionic component of the compound was observed in DMSO- $d_6$ .

### 2.3.3. <sup>1</sup>H NMR DOSY studies

NMR DOSY is a technique that separates NMR signals according to the diffusion coefficient of each molecule and allows mixtures of compounds to be analysed, and is the next step shown in Figure 20.<sup>124,125</sup> The diffusion coefficient can be converted into the hydrodynamic diameter using the Stokes-Einstein equation (Equation 2).<sup>126</sup>

Equation 2 – The Stokes-Einstein equation which is used to calculate the hydrodynamic diameter using the diffusion coefficient.

$$d_H = \frac{k_B T}{3\pi\eta D}$$

$d_H$  = Hydrodynamic diameter (m)  
 $k_B$  = Boltzmann constant  
 $T$  = Temperature (K)  
 $\eta$  = Solvent viscosity ( $kgm^{-1}s^{-1}$ )  
 $D$  = Diffusion coefficient ( $m^2s^{-1}$ )

The major limitation of DOSY is the Stokes-Einstein equation which assumes the molecule is spherical, when often this is not true (Figure 36). Due to this limitation, the hydrodynamic diameters of molecules determined with this technique must be considered estimations.

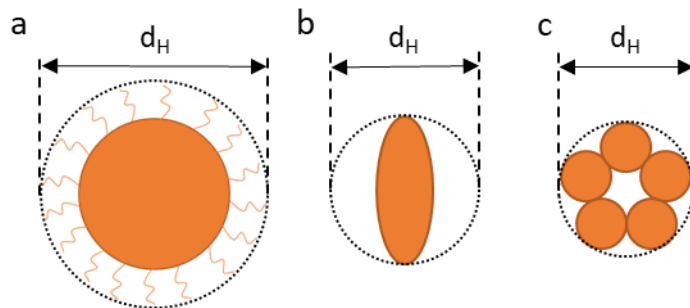


Figure 36 – Limitations of using the Stokes-Einstein equation: a) large molecule with tails, but the  $d_H$  includes the tails of, b) non-spherical molecule, but the  $d_H$  assumes it is spherical, c) multiple molecules, but the  $d_H$  is assumed to be the collective size.

To calculate the hydrodynamic diameter of the anionic and cationic components, using the cationic component of **20** as an example (Figure 37), the diffusion constant ( $D$ ) is averaged ( $1.71 \times 10^{-10} \text{ m}^2/\text{s}$ ) and then substituted into the Stokes-Einstein equation (Equation 3), to get a value of 1.28 nm as shown in Table 4.

Equation 3 – Calculation of  $d_H$  using the cationic component of **20** as an example.

$$d_H = \frac{1.38 \times 10^{-23} \times 298 \text{ K}}{3 \times \pi \times 0.00199 \times 1.71 \times 10^{-10}}$$

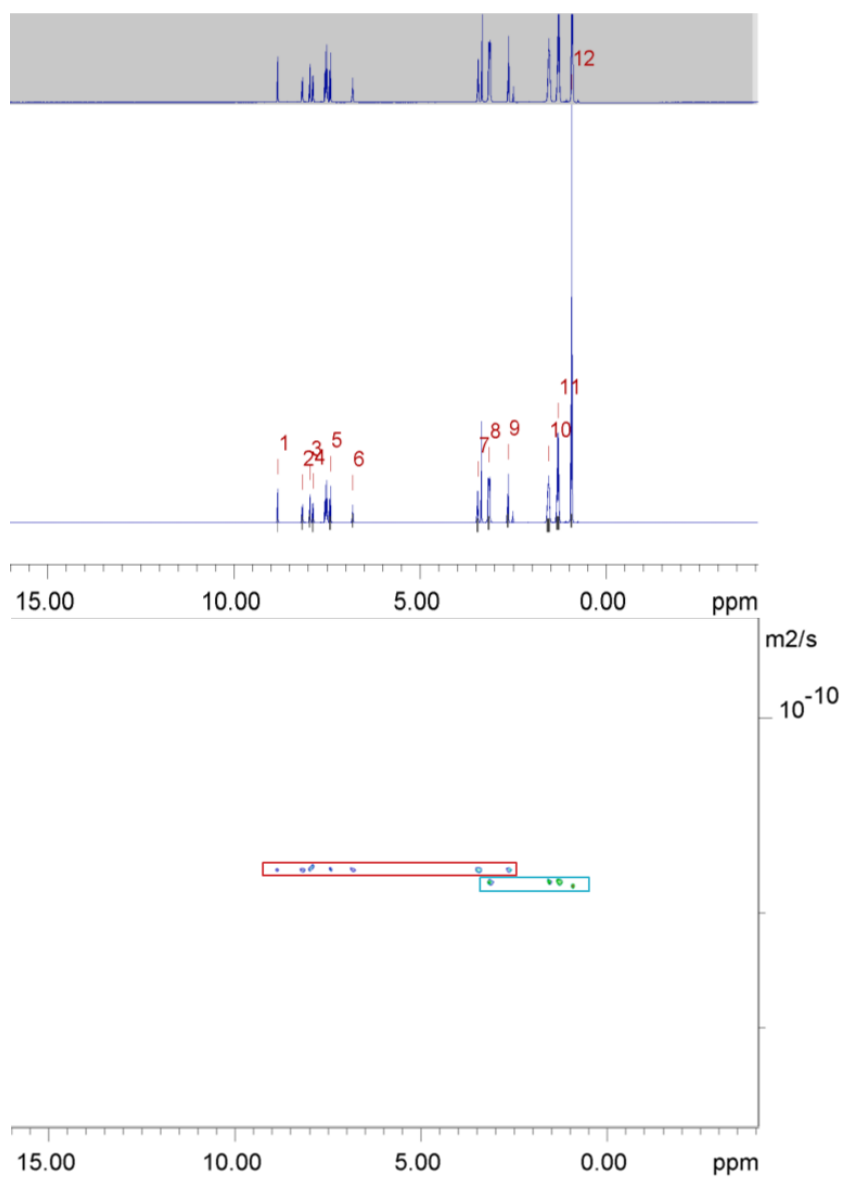
Table 4 – Overview of hydrodynamic diameters (nm) for **20** – **21** in DMSO- $d_6$  at 298 K.

Compound	Hydrodynamic diameter (nm)	
	Anion	Cation
<b>20</b>	1.28	1.22
<b>21</b>	1.37	1.22
<b>22</b>	1.29	1.20
<b>23</b>	<i>a</i>	<i>a</i>

*a* – Study not completed due to signal “loss” in DMSO- $d_6$ .

The  $^1\text{H}$  NMR DOSY of **20** - **22** in DMSO- $d_6$  showed that the anionic and cationic components of the compounds diffuse at different rates, so therefore have different hydrodynamic diameters, as shown in Table 4. As the anion and cation have different diffusion constants, it shows that TBA does not co-ordinate strongly with the anionic SSA component in DMSO- $d_6$ . The anionic component of **20** – **22** have hydrodynamic diameters of 1.28, 1.37 and 1.20 nm respectively, which represent low order complex formation, such as monomers, dimers or trimers. The cation for **20** – **22** is TBA, and, as the measured

hydrodynamic diameter in each compound is within  $\pm 0.02\%$  (1.20 nm – 1.22 nm) it indicates the validity of these data. All  $^1\text{H}$  NMR DOSY spectra can be viewed in the appendix (Figure S33 – S38).



Peak name	F2 [ppm]	lo	error	D [m <sup>2</sup> /s]	error
1	8.824	1.08e+09	3.794e+04	1.71e-10	1.301e-14
2	8.165	1.23e+09	4.875e+04	1.70e-10	1.466e-14
3	7.958	1.28e+09	4.542e+04	1.70e-10	1.316e-14
4	7.877	1.45e+09	5.186e+04	1.70e-10	1.324e-14
5	7.411	1.39e+09	5.910e+04	1.72e-10	1.590e-14
6	6.814	9.69e+08	4.878e+04	1.71e-10	1.867e-14
7	3.457	2.55e+09	6.287e+04	1.71e-10	9.169e-15
8	3.152	6.88e+09	6.522e+04	1.80e-10	3.687e-15
9	2.640	2.52e+09	5.482e+04	1.71e-10	8.062e-15
10	1.555	9.04e+09	8.638e+04	1.80e-10	3.720e-15
11	1.300	1.13e+10	8.638e+04	1.80e-10	2.969e-15
12	0.929	1.77e+10	6.120e+04	1.80e-10	1.345e-15

Figure 37 - <sup>1</sup>H DOSY NMR spectrum of the compound **20** (55.56 mM) in DMSO-*d*<sub>6</sub> at 298 K. The anionic component is highlighted in red and the cationic component in blue. A table showing diffusion constants for each peak used to calculate the hydrodynamic diameter. Anionic component of **20** ( $d_H = 1.28$  nm). Peaks 1 - 7 and 9 correspond to the anionic component of **20** while peaks 8, 10 - 12 correspond to the cationic component of **20**.

#### 2.3.4. Tensiometry studies and Critical Micelle Concentration (CMC)

determination

The CMC is the concentration at which surface tension does not continue to decrease with increasing concentration of a compound with surfactant properties.<sup>127</sup> The CMC is determined to be the concentration above which any extra addition of compound will form larger self-associated structures within the bulk of the solution (micelles, reverse micelles, vesicles, aggregations) as shown in Figure 38.<sup>128,129</sup> Figure 38 illustrates CMC determination, but, although this process is shown as micelles/spherical aggregates, there are hypothesised to be many types of structures present. One of the limitations of CMC determination is that aggregates may be present before CMC is reached as the larger structures are in dynamic equilibrium with the surface structures as the surface is not yet saturated.<sup>130</sup> Another limitation of this experiment is that not only micelles are formed. It is hypothesised that the aggregates SSAs form are multilamellar. The CMC for **21** and **23** were determined using a pendant drop method in EtOH:H<sub>2</sub>O 1:19.

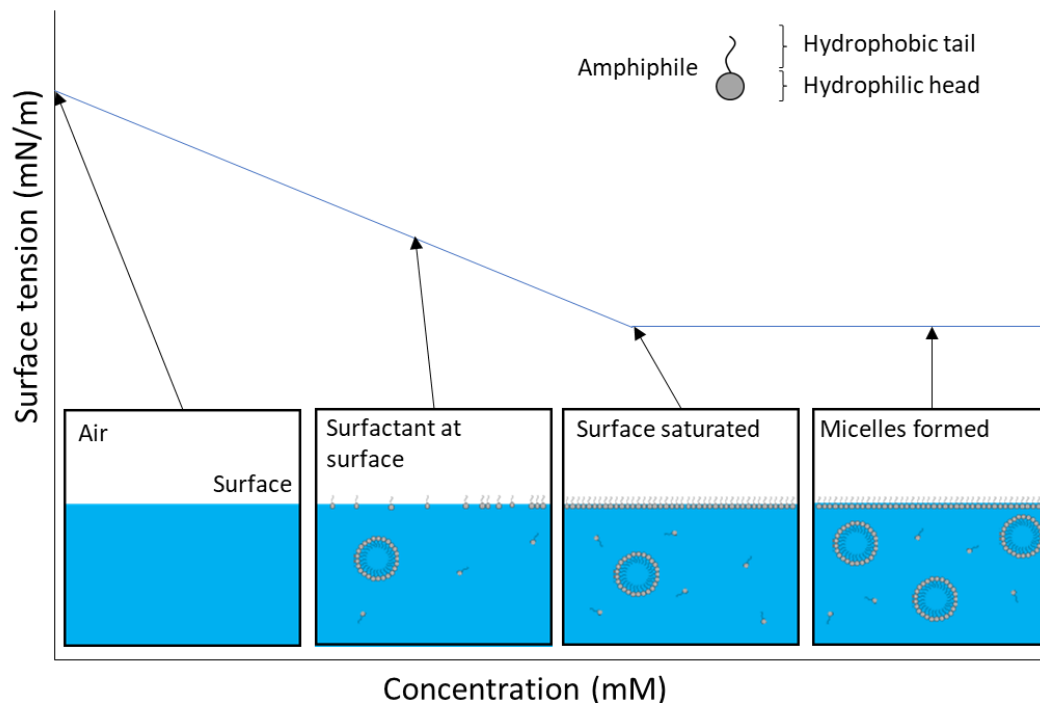


Figure 38 – The initial determination of CMC by Williams *et al.*<sup>129</sup>

The CMC and the surface tension at the CMC for **21** (Figure 39) and **23** were calculated (Table 5). The CMC is determined by using simultaneous equations of the lines to find the point where they intercept.

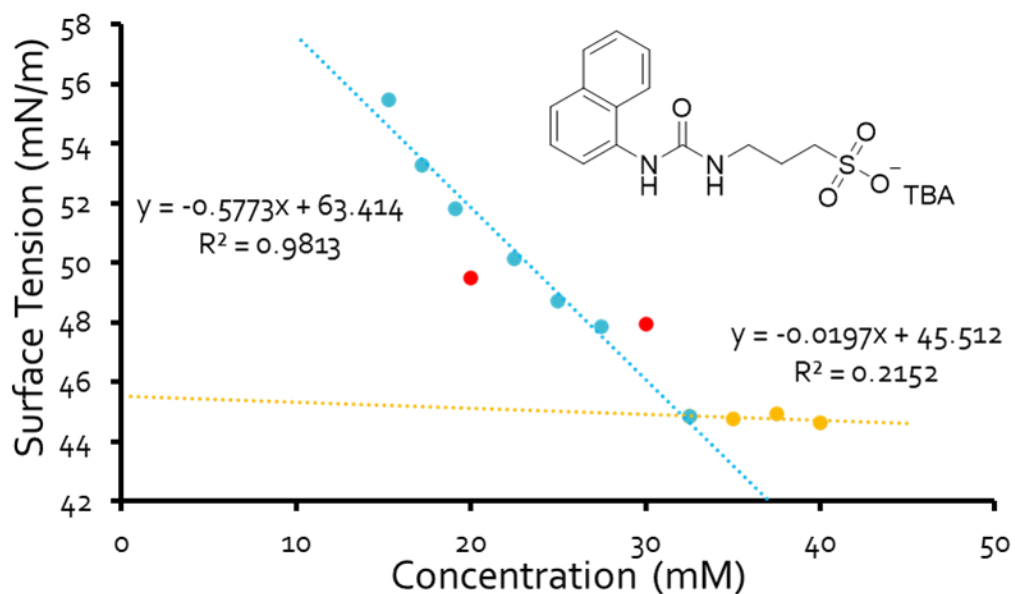


Figure 39 - Calculation of CMC (32.12 mM) for compound **21** in an EtOH:H<sub>2</sub>O 1:19 mixture using surface tension measurements. Outliers are coloured in red, the two lines are coloured blue and yellow.

Table 5 –Summary of CMC and surface tension at CMC. Data obtained in an EtOH:H<sub>2</sub>O 1:19 solution.

Compound	CMC (mM)	Surface tension at CMC (mN/M)
<b>20</b>	<i>a</i>	<i>a</i>
<b>21</b>	32.12	44.88
<b>22</b>	<i>a</i>	<i>a</i>
<b>23</b>	5.16	66.97

*a* – Could not be calculated due to compound solubility.

The difference in CMC between **21** (32.12 mM) and **23** (5.16 mM) is over 6 times. The difference in CMC is most likely due to the difference in hydrophobicity of the compound: **23** is more hydrophobic as the anionic component has a larger conjugated ring system. Anoune *et al.* completed a study of 49 surfactants and discovered that increasing the hydrophobicity of the compound causes a decrease in CMC, as seen with compounds **21** and **23**.<sup>131</sup> The lower the CMC, the greater the surfactant properties of the compound, increasing the ability of the compounds to lower the surface tension of the water. Therefore, **23** is a more effective surfactant than **21** as less compound is needed to saturate the interface. All CMC graphs can be found in the appendix (Figure S39 – S40).

### 2.3.5. Dynamic Light Scattering Studies

As shown in Figure 20, if there is a “loss” of compound in the qNMR experiment, the larger aggregates must be studied outside of NMR spectroscopy as they are outside the scope of the machine. DLS is a non-destructive method often used for characterisation of nanoparticles.<sup>132,133</sup> This method uses the scattering of light and the Brownian motion of the particles to calculate the size of the particles in solution.<sup>133</sup> The size of the particle changes the intensity of the scattered light (Figure 40) and, using the Stokes-Einstein equation (Equation 2), the hydrodynamic diameter can be calculated.<sup>134</sup> The limits of the size calculation is 1 – 1000 nm,<sup>132</sup> therefore, low ordered complexation will be visible, but the sizes cannot be calculated. As the Stokes-Einstein equation is used, there is an assumption that everything is spherical (Figure 36). The graphs that are produced are intensity

distributions, weighted by size, so the graphs cannot be treated as a comparative number of that size in the solution. As the refractive indexes of the compounds are unknown, the polydispersity (PDI) must be considered. A higher PDI (%) means the molecules/aggregates have a larger range of sizes.

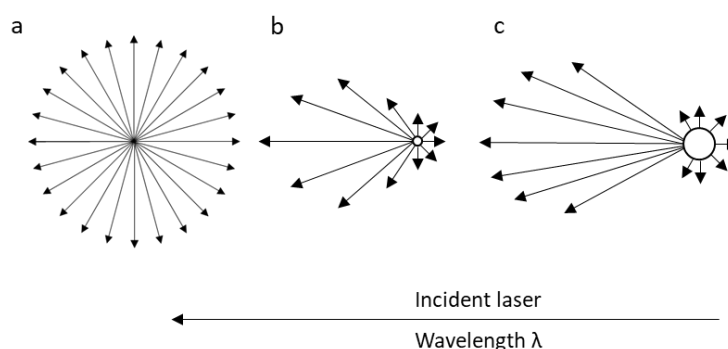


Figure 40 – The difference between Rayleigh and Mie scattering. a) Rayleigh scattering, not angle-dependent, b) Mie scattering, angle dependent, c) Mie scattering, angle-dependence increases with particle size.

Large aggregates that are invisible to the solution state  $^1\text{H}$  NMR were found for compounds **20** - **22** in EtOH:H<sub>2</sub>O 1:19, evidence of these first obtained through qNMR studies (Section 2.3.1.). The compounds exhibit a range of different sizes as shown in Table 6 and PDI of 16 – 36 %. The lower PDI shows that the aggregates are of a similar size, therefore have a higher uniformity.

All the compounds have a PDI of ~25 – 30 % at both 0.56 mM and 5.56 mM, except **23**. Compound **23** has a PDI of only 16 % at 0.56, and 27 % at 5.56 mM. It is proposed that as the DLS was carried out below the CMC for **23**, less larger aggregations form as the interface is not yet saturated. This hypothesis is corroborated by the difference in peak maxima of **23**: 255 nm at 5.56 mM and 155 nm at 0.56 mM. Additionally, there is a 40 % decrease in peak maxima for **23**, whereas the biggest difference in peak maxima observed in the compounds other than **23** is observed in **20**, where a 20 % decrease in peak maxima is observed (200 nm at 5.56 mM and 156 nm at 0.56 mM).

As there was a “loss” of signal in the qNMR of **23** in DMSO-*d*<sub>6</sub>, the extended aggregates were characterised by DLS in DMSO. Compound **23** shows an increased

polydispersity, 36 % compared to 15 – 25 %, thus there are hypothesised to be lots of different macrostructures present.<sup>84</sup> Due to the many macrostructures, indicated by the increased polydispersity, there is a much higher error on the peak maxima. The peak maxima for **23** in DMSO also is much higher, at 1381 nm, compared to the other compounds in EtOH:H<sub>2</sub>O 1:19, 156 – 255 nm, an order of magnitude in difference, as within solutions of **23** in DMSO, many different structures are present, so these structures “clump” together to form even larger aggregates.<sup>83–90</sup> All DSL data can be found in the appendix (Figure S41 **Error! Reference source not found.** – S56).

Table 6 – Average intensity particle size distribution for **20** - **23**, calculated from 10 DLS runs in EtOH:H<sub>2</sub>O 1:19. Samples were prepared in series, with an aliquot of the most concentrated solution undergoing serial dilution and measured after heating to 40 °C and cooling to 25 °C. Error = standard error of the mean and given to 1 dp.

Compound	Concentration (mM)	Peak maxima (nm)	Polydispersity (%)
<b>20</b>	5.56	199.94 (± 3.1 %)	26.05 (± 0.3 %)
	0.56	156.33 (± 1.8 %)	24.74 (± 0.5 %)
<b>21</b>	5.56	153.86 (± 1.1 %)	24.67 (± 0.1 %)
	0.56	142.49 (± 1.8 %)	24.81 (± 0.2 %)
<b>22</b>	0.56	180.95 (± 2.5 %)	25.93 (± 0.2 %)
<b>23</b>	5.56	255.42 (± 7.1 %)	27.37 (± 0.2 %)
	0.56	155.46 (± 2.4 %)	15.96 (± 0.3 %)

Table 7 - Average intensity particle size distribution for **20** - **23**, calculated from 10 DLS runs in DMSO. Samples were prepared in series, with an aliquot of the most concentrated solution undergoing serial dilution and measured after heating to 40 °C and cooling to 25 °C. Error = standard error of the mean and given to 1 dp.

Compound	Concentration (mM)	Peak maxima (nm)	PDI (%)
<b>20</b>	<i>a</i>	<i>a</i>	<i>a</i>
<b>21</b>	<i>a</i>	<i>a</i>	<i>a</i>
<b>22</b>	<i>a</i>	<i>a</i>	<i>a</i>
<b>23</b>	111.12	1380.55 (± 23.17)	35.74 (± 1.4 %)

a – Study not completed due to no signal “loss” in DMSO-*d*<sub>6</sub>.

### 2.3.6. Zeta Potential

Zeta potential, or “*electrokinetic potential*”, defines the potential of a colloid particle moving through an electrical field.<sup>134,135</sup> Zeta potential is often used to define the stability of a colloid particle or aggregation. Values of  $\pm 0 - 10$  mV are unstable,  $\pm 10 - 20$  mV are moderately stable and  $\pm 20 - 30$  mV are stable.<sup>91,136</sup> In reality, it is much more complicated. In the cell, liposomes, which are stable vesicles made from phospholipids, have a zeta potential of  $-10 - -40$  mV.<sup>92</sup> This data implies that zeta potential can act as a “*ball park*” figure of stability of aggregates, but context is important. For example, the solvent used must be taken into account, also whether the sample is *in vivo*, or *ex vivo*. The zeta potentials for **20** - **23** were found in EtOH:H<sub>2</sub>O 1:19.

Table 8 contains the zeta potential values for **20**, **21** and **23**, at 5.56 mM and for **22** at 0.56 mM due to solubility issues. The zeta potentials for **20** and **21** are  $\pm 20 - 10$  mV, implying moderately stable aggregates. Although the aggregates are only considered to be “*moderately stable*” the DLS studies (Table 6) suggest that they are stable enough to be characterised. The zeta potentials for **22** and **23** are both  $\pm 30$  mV, so are “*stable*” aggregates. Both **22** and **23** contain the benzothiazole unit, which is thought to contribute towards the stability of the aggregates, previously suggested by García-Ortiz *et al.* (Figure 30).<sup>114</sup>

Table 8 - Summary of zeta potential at 5.56 mM for **20**, **21** and **23** and 0.56 mM for **22** due to solubility issues.

Compound	Zeta potential (mV)
<b>20</b>	-13.77
<b>21</b>	-24.03
<b>22</b>	-42.71
<b>23</b>	-67.13

This increased stability of **22** could also explain the higher percentage “loss” of signal in the qNMR (Table 2). All zeta potential graphs can be found in the appendix (Figure S57 - S60).

## 2.4. Low level *in silico* modelling

Computational modelling is used to model then predict the properties and 3D conformation of compounds and are able to predict hydrogen-bonding and the geometry of the bonds that are formed. One of the ways computational chemistry can support organic chemistry by predicting electrostatic potential maps. These potential maps visualize the electropositive and electronegative areas of a compound to see whether molecular interactions will form.<sup>137</sup> Electrostatic potential maps for the anionic component of **20** - **23** were calculated using Spartan 16<sup>''</sup> with energy minimised, semi-empirical PM6 modelling methods to derive comparative  $E_{\max}$  and  $E_{\min}$  surface values.<sup>138</sup> The *in silico* data was obtained and refined by Rebecca Ellaby.

The  $E_{\max}$  is the most negative point on the surface of the molecule, and the  $E_{\min}$  the most positive. Log $P$  value is used as a comparative measure of lipophobicity, the higher the log $P$  value, the more hydrophobic the compound. The  $E_{\max}$ ,  $E_{\min}$ , and Log $P$  values for **20** – **23** can be found in Table 9. The  $E_{\min}$  of the compound is expected to be at the sulfonate and/or the urea oxygen of the compound, the most likely HBA groups. The  $E_{\max}$  of the compound is, for **20** and **21**, the naphthalene as this part of the compound is most electron rich due to the  $\pi$  electrons that delocalise over the aromatic rings. Due to the missing alkyl group between the sulfonate and urea in **20**, it has a much lower  $E_{\min}$  value of  $-88 \text{ kJ mol}^{-1}$  (Figure 41), compared to **20**,  $12 \text{ kJ mol}^{-1}$ **Error! Reference source not found.** All *in silico* data can be found in the appendix (Figure S64 – S67).

Table 9 –  $E_{\max}$ ,  $E_{\min}$ , and Log $P$  values for **20** - **23**.

Compound	$E_{\max}$ (kJ mol <sup>-1</sup> )	$E_{\min}$ (kJ mol <sup>-1</sup> )	Log $P$
<b>20</b>	-721.417	-88.0876	1.05
<b>21</b>	-768.478	12.0290	1.51
<b>22</b>	-717.433	-48.5147	0.86
<b>23</b>	-706.202	-38.2374	1.86

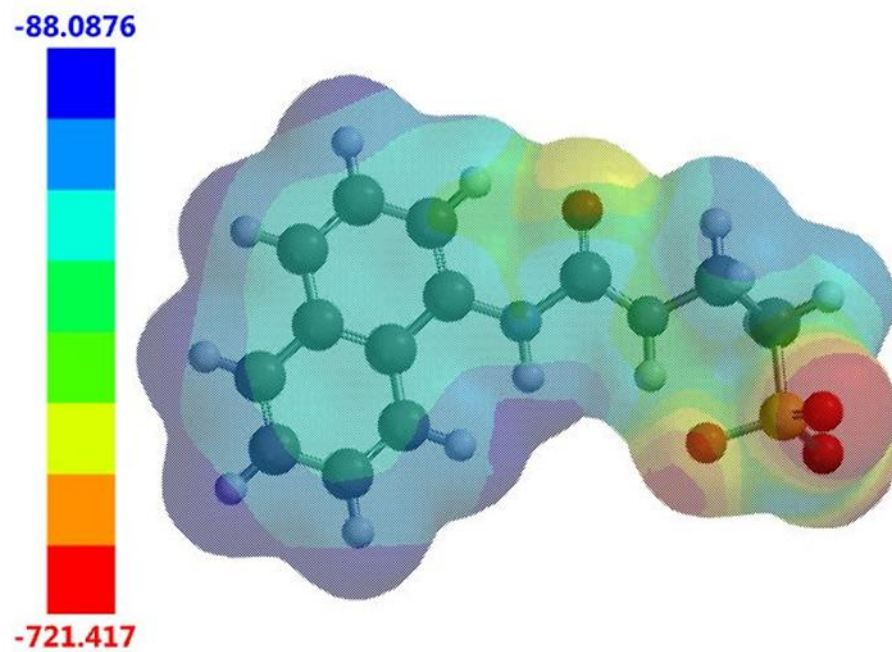


Figure 41 - Electrostatic potential map calculated for **20**.  $E_{\max}$  and  $E_{\min}$  values depicted in the figure legends are given in kJ mol<sup>-1</sup>.

### 3. Rheology

#### 3.1. Introduction

A gel is composed of a liquid (solvent) which is encapsulated by the second component, the gelator. According to Estroff *et al.* the liquid component takes up ~99 % of the gel by weight, with the gelator only accountable for 1 %.<sup>139</sup> The classification of gels can be broken down, as shown in Figure 42, as the general term “gel” is quite broad – gels are solid-like and have viscolastic properties.<sup>140</sup> A “gel” can be classified by the origin of the material, the constituents that make up the gel, the type of crosslinking, and also the media they encapsulate.<sup>141</sup>

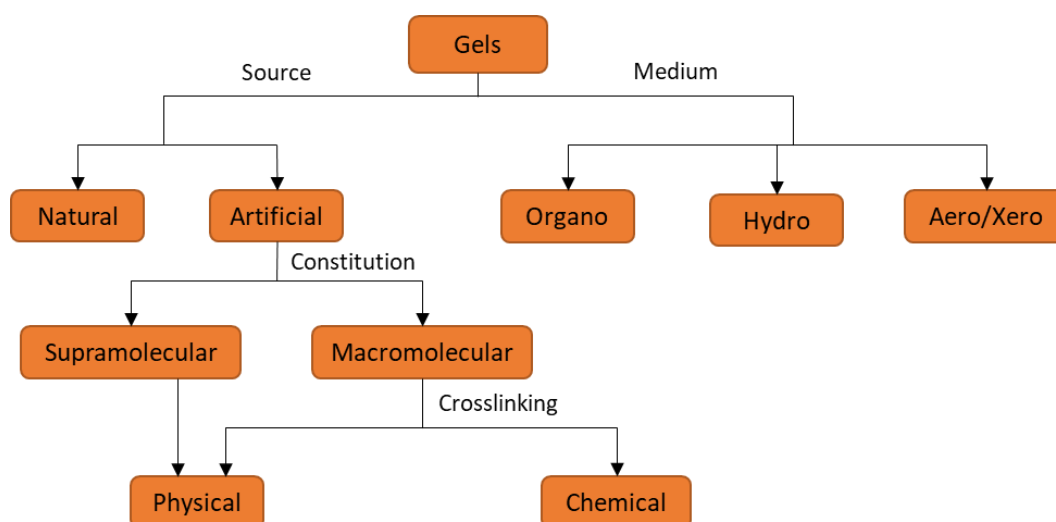


Figure 42 – Flow chart of the classification of different gel systems.

Brezingler discovered the first low molecular weight (LMW) hydrogelator, **30** (Figure 43) in 1892.<sup>142</sup> However, the properties of the gel were not studied until 1921, by Gortner and Hoffman.<sup>143</sup> Gortner and Hoffman discovered that the gel could withstand an inversion test in ~5 % EtOH ~95 % H<sub>2</sub>O, at 0.1 % concentration by weight.<sup>143</sup> The characteristics of the gel were studied in 1978 by Menger *et al.* using NMR studies and X-ray crystallography.<sup>144</sup> These researchers went on to modify the structure of **30**, decreasing the minimum gelation concentration (MGC) to 0.01 % by weight by increasing the electron-withdrawing properties through the addition of aromatic ring systems (**31**, Figure 43).<sup>145</sup>

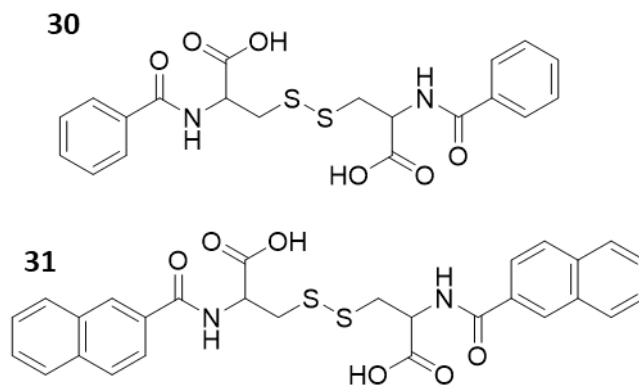
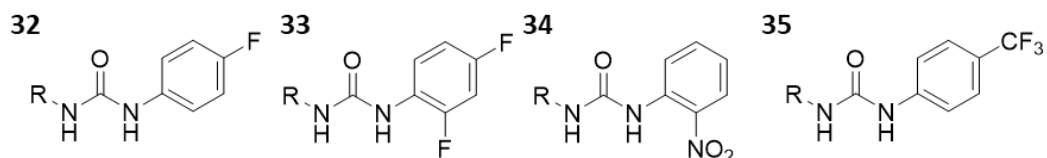


Figure 43 – The first reported LMW gelator, **30**<sup>142</sup> and the modifications made by Menger *et al.*, **31**.<sup>145</sup>

Supramolecular gels form through self-assembly via non-covalent interactions, unlike polymeric gels which are based on covalently cross-linked networks of polymers.<sup>146,147</sup> These non-covalent interactions occur between monomeric units of LMW gelators.<sup>148</sup> These gels are broadly classified into two categories based on the solvent that has been immobilised within the 3D gel matrix; organogels, which trap organic solvent,<sup>140,149,150</sup> and hydrogels, which trap water.<sup>38,139,146,151–153</sup> Another difference between the two classes of gels is how the gelation is driven, initially discovered by Miravet *et al.*; organogels are enthalpy driven and hydrogels are entropy driven.<sup>154–158</sup> The chemical driving force of gelation can range from weak intermolecular interactions to chemical covalent bonds.<sup>159</sup> Any and all non-covalent interactions play a part in acting as the driving force of gelation, from van der Waals interactions, to hydrogen bonds,  $\pi$ - $\pi$  interactions to ionic bonds, but solvent interactions, including the solvophobic effect are incredibly important.<sup>160</sup> The solvophobic effect is the tendency of dissolved molecules to cluster as the interactions between the solvent particles and the molecules increase.<sup>161</sup>

Hydrogen bonding is one of the most used non-covalent interactions in the construction of supramolecular gels.<sup>159</sup> As explained in Section 1.4, the urea motif is often used to facilitate hydrogen bonding. Pyridyl based ureas have been extensively studied by Steed *et al.*<sup>162,163</sup> These researchers have also explored the ability of these compounds to form supramolecular gels.<sup>164</sup> Pandurangan *et al.* used the urea functional group to synthesise a family of compounds that form supramolecular gels in various solvents (THF:H<sub>2</sub>O with or

without the addition of  $\text{AgNO}_3$ ).<sup>165</sup> The general structure of these hydrogelators are shown in Figure 44, **32** - **35**.<sup>165</sup> The researchers deduced that, in the solid state (single crystal XRD) hydrogen bonded dimers and the effect of face-to-face and edge-to-face  $\pi$ - $\pi$  stacking helped give rise to the supramolecular network.<sup>165</sup> As these interactions were discovered in the solid state, it can be hypothesised that similar structures could be present within the solid state gel fibres.



$\text{R}$  = Pyridyl at ortho, meta and para positions

Figure 44 - Chemical structure of pyridyl ureas.<sup>165</sup>

Hiscock *et al.* discovered that **19** formed a hydrogel in 15 different 0.505 M salt solutions.<sup>90</sup> The properties of these hydrogels were initially characterised using rheology, and then further analysed these gels using a plate reader.<sup>166</sup> As the main aim of this project was to produce potential topical antimicrobial hand gels, the pH of the gel must be between 4 and 7, the range of human skin.<sup>167</sup>  $\text{NaCl}$ ,  $\text{KCl}$ ,  $\text{NaNO}_3$ ,  $\text{NaH}_2\text{PO}_4$ ,  $\text{NaOBz}$  and  $\text{Na}_2\text{SO}_4$  salts and gels all fell within this range, and enabled observation of how the geometries of the salts effected the gelation of the novel compound **23**. In this set of salts the changes include: the cation ( $\text{Na}^+$  to  $\text{K}^+$ ); the effect of different geometries of the anion; trigonal ( $\text{NaNO}_3$ ); tetrahedral ( $\text{NaH}_2\text{PO}_4$ ); the effect of increasing the hydrophobicity of the salt ( $\text{NaOBz}$ ); and the number of cations and thus the basicity of the salt ( $\text{Na}_2\text{SO}_4$ ).

## 3.2 Rheology results and discussion

### 3.2.1. Minimum gelation concentration

The MGC of a compound is the minimum amount of gelator (mass) required to gelate a standard volume of liquid, in this case 1 mL of an aqueous salt solution. To find the MGC of **23** in the different salt solutions the vial inversion test was conducted at a temperature of 25

°C. Table 10 gives an overview of the MGCs of the hydrogels produced from the six salt solutions explored in this project. The samples were heated to ~ 50 °C and left to cool on the benchtop.

Table 10 – Minimum gelation concentrations for **19** and **23**.<sup>90</sup>

Salt solution	Concentration (mg/mL)	
	<b>23</b>	<b>19</b> <sup>90</sup>
NaCl	1.5	1.5
KCl	<i>a</i>	2.5
NaNO <sub>3</sub>	1	1.5
NaH <sub>2</sub> PO <sub>4</sub>	<i>b</i>	1.5
NaOBz	2	1.5
Na <sub>2</sub> SO <sub>4</sub>	<i>b</i>	3.5

*a* – Partial gel formed at 5 mg/mL.

*b* – Precipitation occurred at 5 mg/mL.

The structures of **19** and **23** are almost identical, differing only by the presence of a methyl group on the benzothiazole found in **19**. It is hypothesised that the reduction in hydrophobicity and steric effects caused by the removal of the methyl group has resulted in changes in the physical properties of the gels of **23** compared to **19**.<sup>90</sup>

### 3.2.2. Amplitude sweep

Rheological methods can be used to characterise the viscoelastic behaviour and properties of gels.<sup>159,168</sup> Gels can be characterised by the way that the materials react to oscillatory stress, based on the behaviour of flow and deformation.<sup>146</sup> In the graphs produced, storage modulus ( $G'$ ) refers to the elastic component and the materials ability to store energy, and loss modulus ( $G''$ ) refers to the materials ability to dissipate energy, which relates to the liquid component. The viscoelastic properties of hydrogels formed of 5 mg/mL of **23** in various salt solutions were studied. At 5 mg/mL gel fibres can form (as discussed in Section 3.2.7), allowing the formation of the gel network. Salt solutions where 5 mg/mL of

**23** did not pass the inversion test ( $\text{NaH}_2\text{PO}_4$  and  $\text{Na}_2\text{SO}_4$ ) so cannot be considered gels and were not therefore characterised using rheology.

An amplitude sweep is used to determine how robust the material is and also determines the samples linear viscoelastic region (LVR), the area where deformation of the sample is non-destructive. Amplitude sweeps for **23** (5 mg/mL) in NaCl (Figure 45),  $\text{NaNO}_3$  (Figure 46) and NaOBz (Figure 47) were carried out.

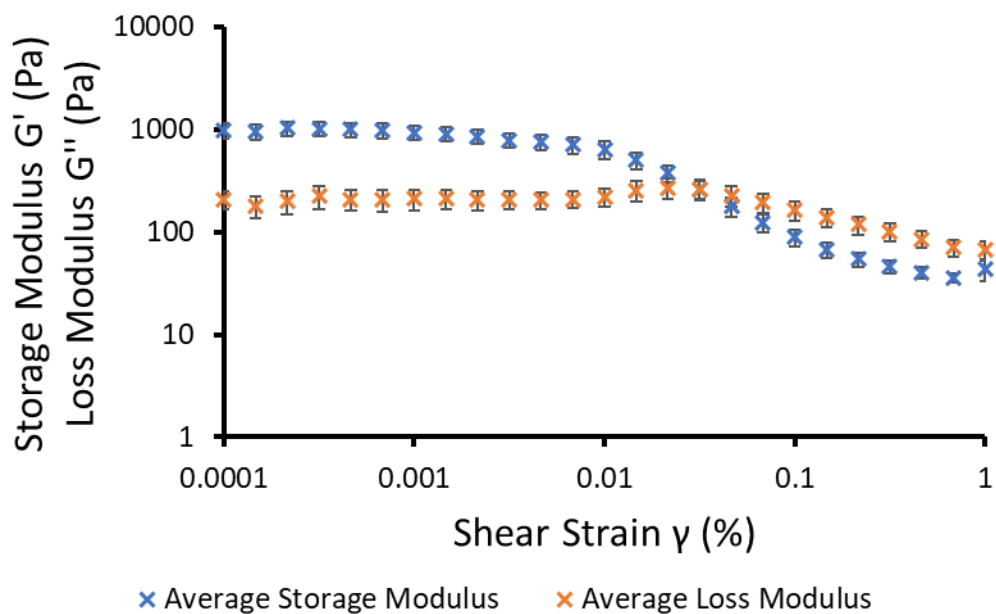


Figure 45 - Graph showing average results ( $n=3$ ) from amplitude sweep experiments used to define the linear viscoelastic region of the sample at 298 K. Compound **23** (5 mg) in 1 mL of aqueous NaCl solution (0.505 M) ( $1 = 100\%$ ).

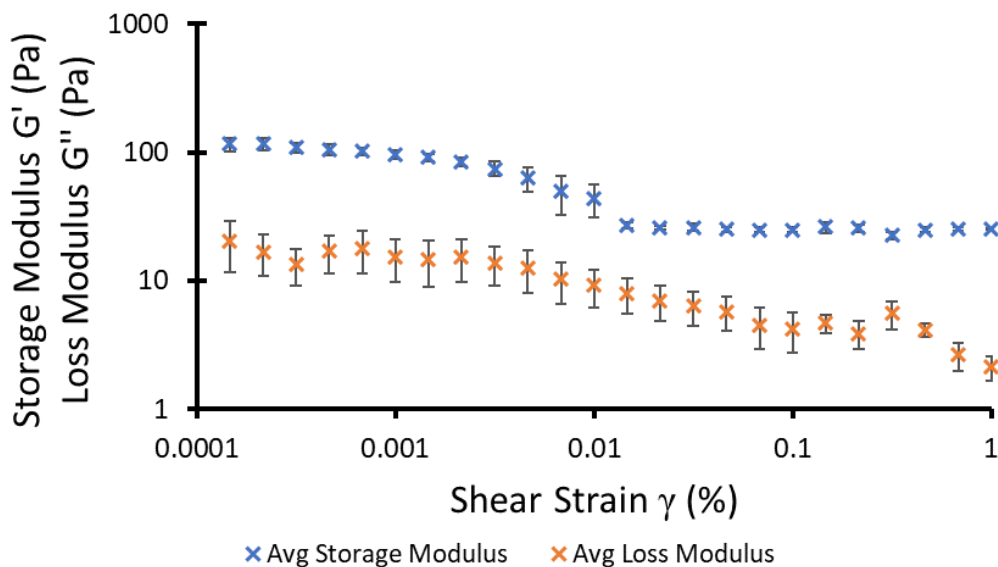


Figure 46 - Graph showing average results ( $n=3$ ) from amplitude sweep experiments used to define the linear viscoelastic region of the sample at 298 K. Compound **23** (5 mg) in 1 mL of aqueous  $\text{NaNO}_3$  solution (0.505 M) (1 = 100 %).

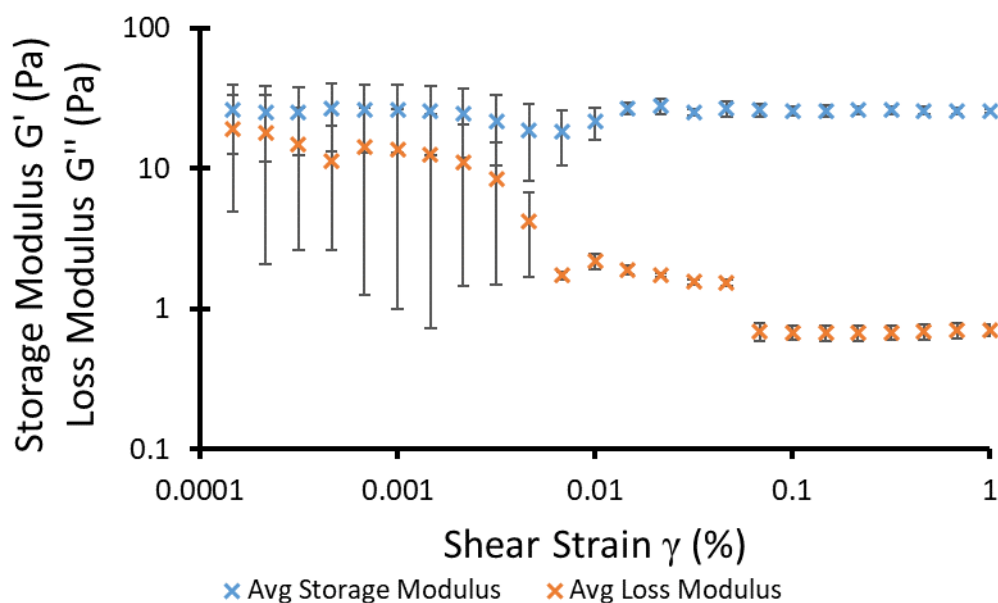


Figure 47 - Graph showing average results ( $n=3$ ) from amplitude sweep experiments used to define the linear viscoelastic region of the sample at 298 K. Compound **23** (5 mg) in 1 mL of aqueous  $\text{NaOBz}$  solution (0.505 M) (1 = 100 %).

Interestingly, hydrogels of **23** in  $\text{NaNO}_3$  and  $\text{NaOBz}$  do not exhibit a cross over point.

The lack of crossover point could be due to these gels having stress responsive behaviour as the  $G'$  does not decrease, implying that the elastic behaviour of these gels is maintained at high oscillatory stress. Hydrogels of compound **19** in the same salts did not exhibit this behaviour.<sup>90</sup>

### 3.2.3. The best way to conduct experiments

To ensure the whole of the sample was studied in its entirety, a solution of **19** was heated and allowed to set with the spindle geometry (in this case a Krebs spindle, a rotating paddle that sits inside a vial) submerged, allowing the hydrogel to form around the vanes.<sup>90</sup> Submerging the geometry prior to gel formation reduces the likelihood of disruption to the gel.<sup>90</sup> For **23**, whilst conducting frequency sweeps across the range of salts, it became apparent that for the hydrogels that contained  $\text{NaNO}_3$  and  $\text{NaOBz}$ , occasionally a gel would not form. Instead, **23** would precipitate out of solution. An experiment was devised using the  $\text{NaCl}$  hydrogel, where the heated solution was allowed to gel around the geometry and the frequency sweep conducted. A separate experiment where the geometry was plunged into the already formed hydrogel then the frequency sweep was also performed. It is hypothesised that the geometry of the rheometer disturbs the gel fibres that form, disrupting the gel network. Figure 48 shows the frequency sweep from the gel forming around the geometry whilst Figure 49 shows the frequency sweep of the gel formed before inserting the geometry.

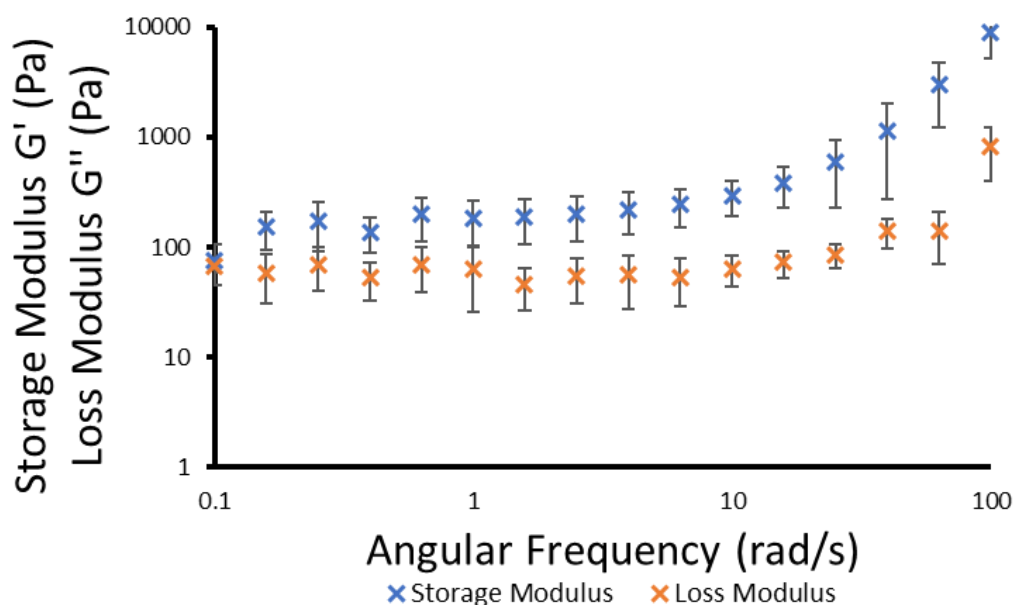


Figure 48 - Graph showing average results ( $n=3$ ) from frequency sweep experiments obtained from the linear viscoelastic region under a constant shear strain ( $\gamma$ ) of 0.0277 % (298 K). Solution heated and gel formed around geometry. Compound **23** (5 mg) in 1 mL of aqueous  $\text{NaCl}$  solution (0.505 M) (1 = 100 %).

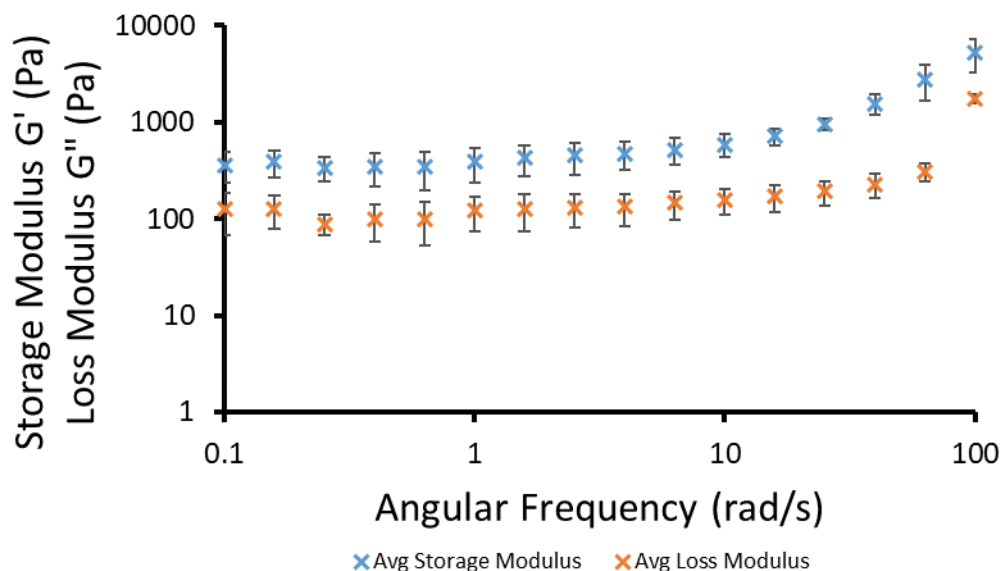


Figure 49 - Graph showing average results (n=3) from frequency sweep experiments obtained from the linear viscoelastic region under a constant shear strain ( $\gamma$ ) of 0.0277 % (298 K). Solution heated and gel formed before inserting geometry. Compound **23** (5 mg) in 1 mL of aqueous NaCl solution (0.505 M) (1 = 100 %).

The results of this experiment showed that the frequency sweep of the pre-formed gel (Figure 49) had smaller errors than when the gel formed around the geometry (Figure 48). This data shows that the geometry can be inserted in either the hot solution or a pre-formed gel and the results are comparable.

#### 3.2.4. Frequency sweep

Previously, for **19**, the frequency sweep was carried out at a standard % strain across all the salt solutions that were tested.<sup>90</sup> However, as **23** formed substantially different gels in each of the different salts, one LVR could not be found for all hydrogels. Instead, the LVR was calculated for each gel individually. Figure 50 shows the angular frequency sweep of **23** (5 mg/mL) in 1 mL of aqueous NaCl (0.505 M) solution and was found to exhibit similar behaviour to **19** in the same conditions: the  $G'$  is stable, then increases.<sup>90</sup> The two other salts tested, NaNO<sub>3</sub> (Figure 51) and NaOBz (Figure 52) show very different behaviour to **19** in the same conditions.  $G'$  varies to a higher degree in the hydrogel of NaNO<sub>3</sub> (10 - >100 Pa for **23** compared to **19** with variation of 80 – 100 Pa).<sup>90</sup> For the frequency sweep carried out for

NaOBz (Figure 52), the errors are both very large and also cross over, indicating that this gel falls on the boundary of what is a 'gel'.

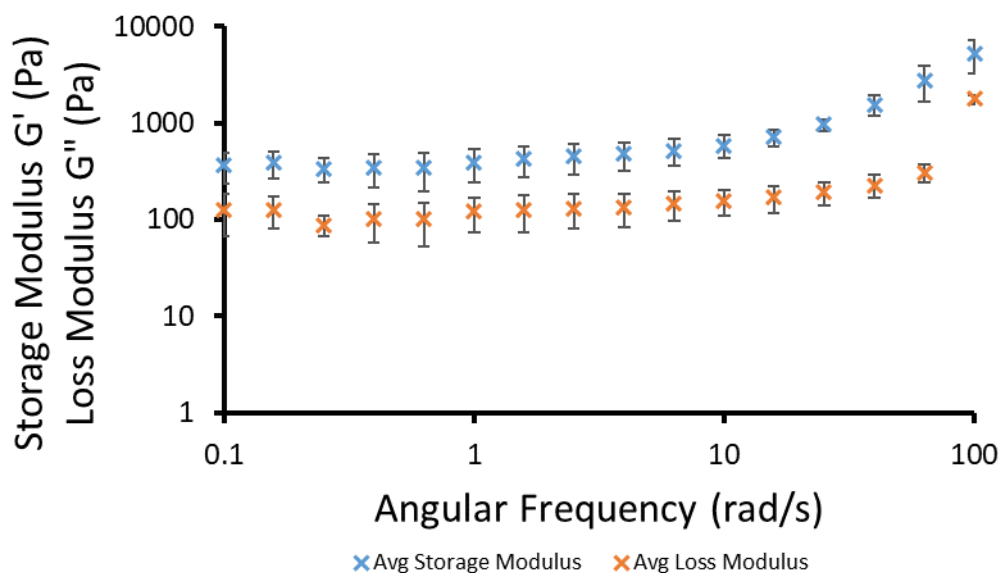


Figure 50 - Graph showing average results (n=3) from frequency sweep experiments obtained from the linear viscoelastic region under a constant shear strain ( $\gamma$ ) of 0.0277 % (298 K). Compound **23** (5 mg) in 1 mL of aqueous NaCl solution (0.505 M).

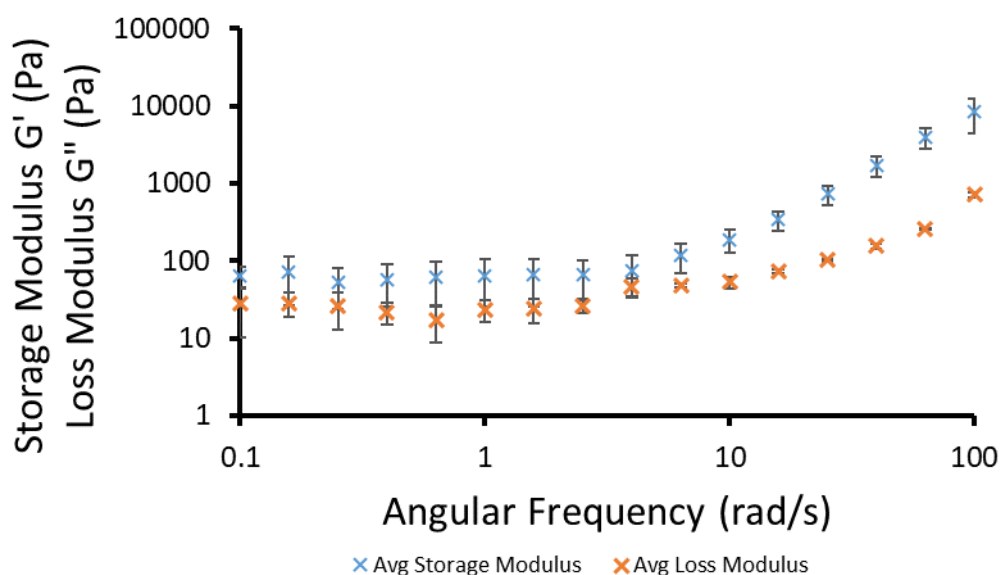


Figure 51 - Graph showing average results (n=3) from frequency sweep experiments obtained from the linear viscoelastic region under a constant shear strain ( $\gamma$ ) of 0.0195 % (298 K). Compound **23** (5 mg) in 1 mL of aqueous NaNO<sub>3</sub> solution (0.505 M).

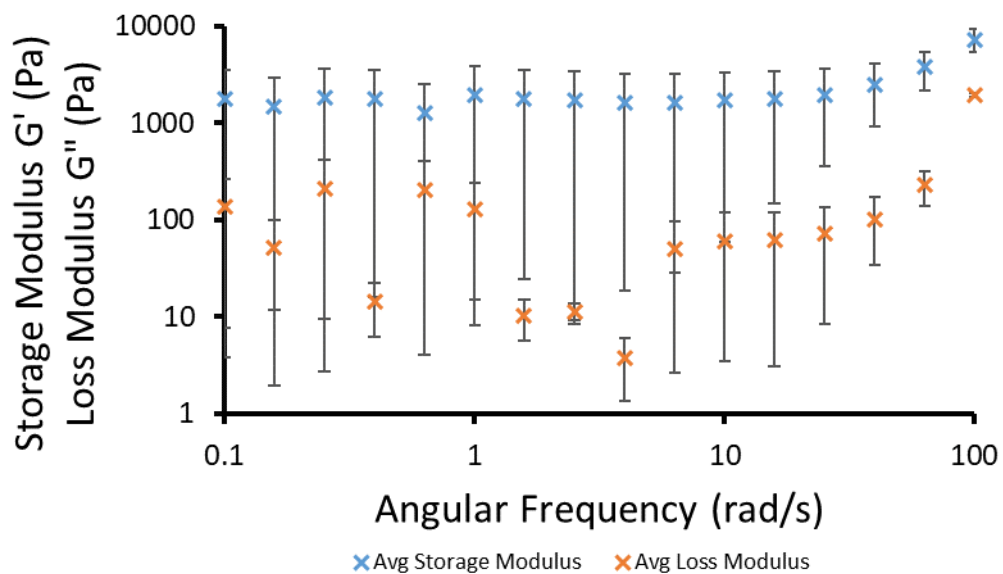


Figure 52 - Graph showing average results (n=3) from frequency sweep experiments obtained from the linear viscoelastic region under a constant shear strain ( $\gamma$ ) of 0.0720 % (298 K). Compound **23** (5 mg) in 1 mL of aqueous NaOBz solution (0.505 M).

### 3.2.5. Test of oscillatory stress

Due to the lack of cross over point observed in the NaNO<sub>3</sub> (Figure 46) and NaOBz (Figure 47) hydrogels, it was hypothesised that these gels could be strengthened by oscillatory stress. To test this hypothesis, an amplitude sweep was run on a sample, the LVR determined, and the frequency sweep carried out on the same sample. The amplitude sweeps of NaNO<sub>3</sub> and NaOBz can be found in the appendix (**Error! Reference source not found.** and S88). The subsequent frequency sweep of NaNO<sub>3</sub> (Figure 53) is very different to that of the frequency sweep on a complete hydrogel (Figure 51). Interestingly in Figure 53, the elastic component of the hydrogel,  $G'$ , changes only a small amount, implying that this stays constant, but the liquid component of the gel,  $G''$ , has higher errors and also varies to a higher degree compared to the frequency sweep on the complete hydrogel. This would need to be explored further in future work to understand the complete connotations of this experiment.

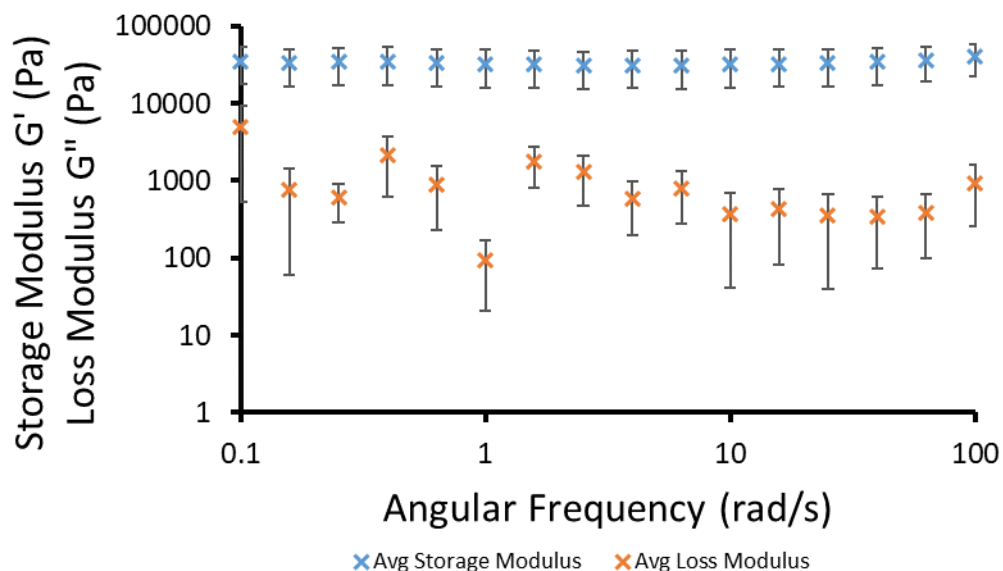


Figure 53 - Graph showing average results ( $n=3$ ) from frequency sweep experiments obtained from the linear viscoelastic region under a constant shear strain ( $\gamma$ ) of 0.0209 % (298 K), after running an amplitude sweep on the same sample. Compound **23** (5 mg) in 1 mL in aqueous  $\text{NaNO}_3$  solution (0.505 M).

The hydrogel of NaOBz (Figure 54) exhibits a similar trend, after an amplitude sweep the  $G'$  stays relatively constant, although the error bars for both  $G'$  and  $G''$  are much larger, often crossing over. Large error bars can also be seen in the frequency sweep of NaOBz on a complete gel (Figure 52), so this could potentially be due to the limit of the gel rather than the experiment.

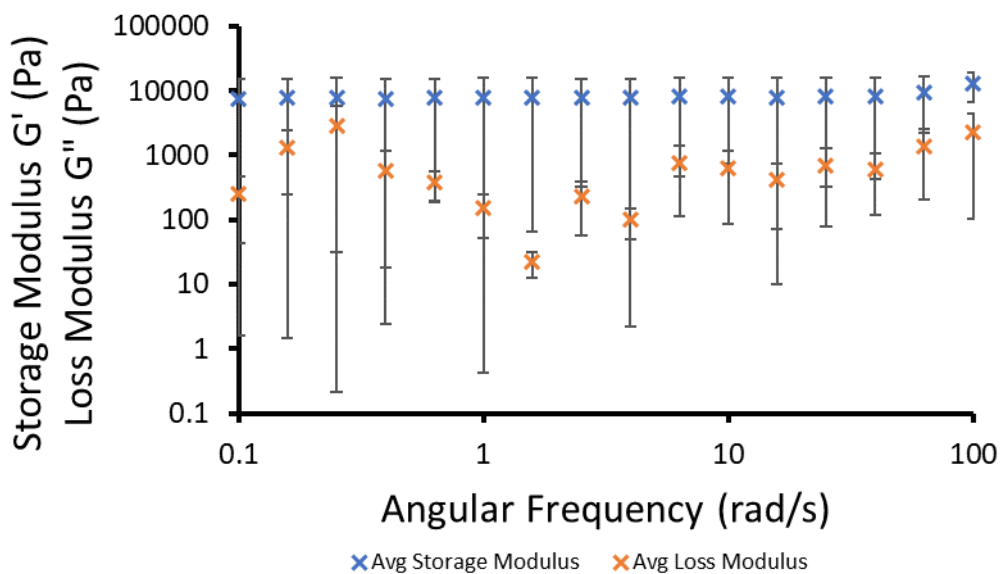


Figure 54 - Graph showing average results (n=3) from frequency sweep experiments obtained from the linear viscoelastic region under a constant shear strain ( $\gamma$ ) of 0.0174 % (298 K), after running an amplitude sweep on the same sample. Compound **23** (5 mg) in 1 mL of aqueous NaOBz solution (0.505 M).

### 3.2.6. Sonication test

For NaNO<sub>3</sub> and NaOBz it was hypothesised that the gels were being strengthened by stress, so this was investigated by sonicating a salt solution containing **23**, taking images every 5 minute up to 30 minutes, and every 10 minutes up to an hour to see if gelation occurred. This test was to prove whether shear strain in the form of sonication would cause gelation, following observations from the amplitude sweep of NaNO<sub>3</sub> and NaOBz to a certain extent (Figure 46 and Figure 47). This experiment was repeated n=3, but gelation did not occur after one hour of sonication. Although in the second test, the NaNO<sub>3</sub> gel formed a gel-like structure (held up under the inversion test but not homologous, Figure 55) that only broke down at 30 minutes (Figure 56). The data from this sonication experiment shows that heat is required to break down the self-associated structures formed initially (spherical aggregations as shown in Section 2.3.5). Pictures of gels can be found in the appendix (Figure S90 – S209).

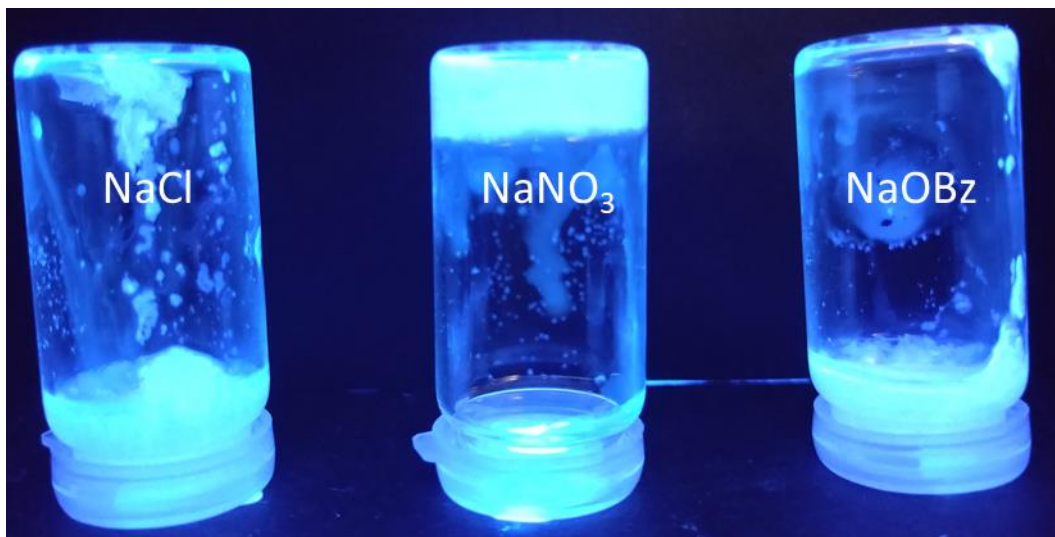


Figure 55 - Sonication test at 0 minutes. Compound **23** (5 mg, 1 mL) in NaCl, NaNO<sub>3</sub> and NaOBz inverted imaged under UV irradiation (test no. 2).

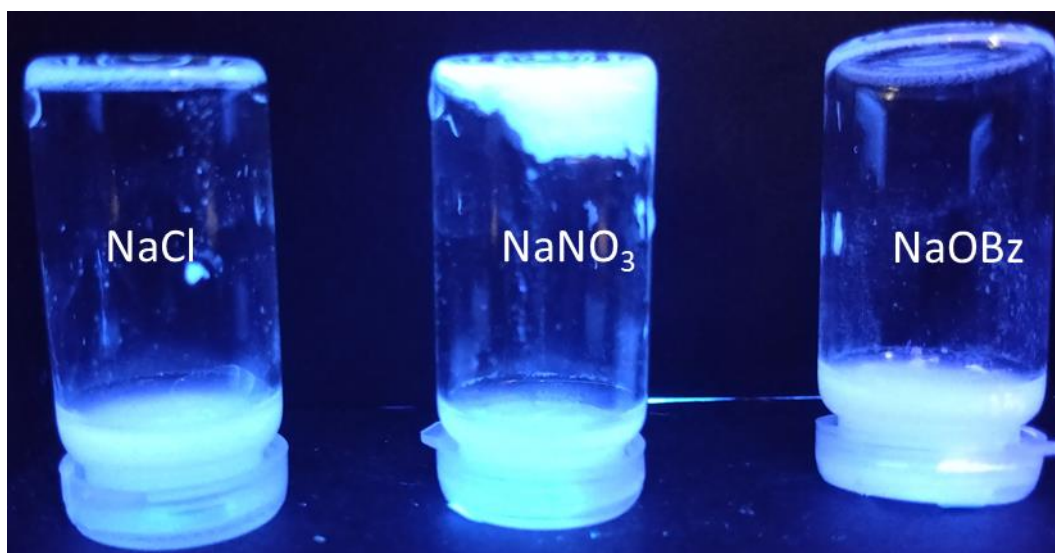


Figure 56 - Sonication test at 25 minutes. Compound **23** (5 mg, 1 mL) in NaCl, NaNO<sub>3</sub> and NaOBz inverted imaged under UV irradiation (test no. 2).

### 3.2.7. Microscopy

Due to the intrinsic fluorescent nature of both **22** and **23**, fluorescence microscopy was used to help understand the nature of gel formation. Although **22** does not form gels, a sample in a NaCl (0.505 M) solution was imaged to potentially explain why this compound does not form hydrogels. The hydrogels of **23** in the various salt solutions were also viewed under the fluorescence microscope to observe the gel fibres. All microscopy data was obtained and refined by Nyasha Allen.

Figure 57 is a transmitted LED image of **22** (5 mg/mL) in a 0.505 M NaCl solution. In Figure 57 only small circular aggregates can be observed, circled in orange, characteristic of SSAs, as explained in Section 2.3.5.

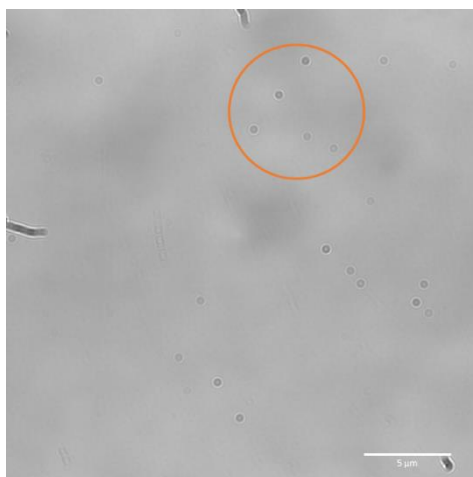


Figure 57 - Transmitted LED microscopy image of compound **22** (5 mg/mL) in NaCl (0.505 M).

The microscopy of **23** however, shows the gel fibres that form when the sample has been heated and then cooled. Figure 58a is a DAPI LED microscopy image of **23** (5 mg/mL) in 0.505 M of aqueous NaCl, and the gel fibres can easily be seen as the long white lines running through the image. Interestingly, the way the fibres that form are salt dependent. The gel fibres in Figure 58a (NaCl) are relatively long and thin, with the bright spots hypothesised to be large aggregations of **23**. Figure 58b (KCl), where the cation of the salt solution is the only difference, show a more conjugated network, where the fibres seem to curl around each other. The hydrogel using NaNO<sub>3</sub> as the salt solution (Figure 58c) shows a very fibrous and circular network.

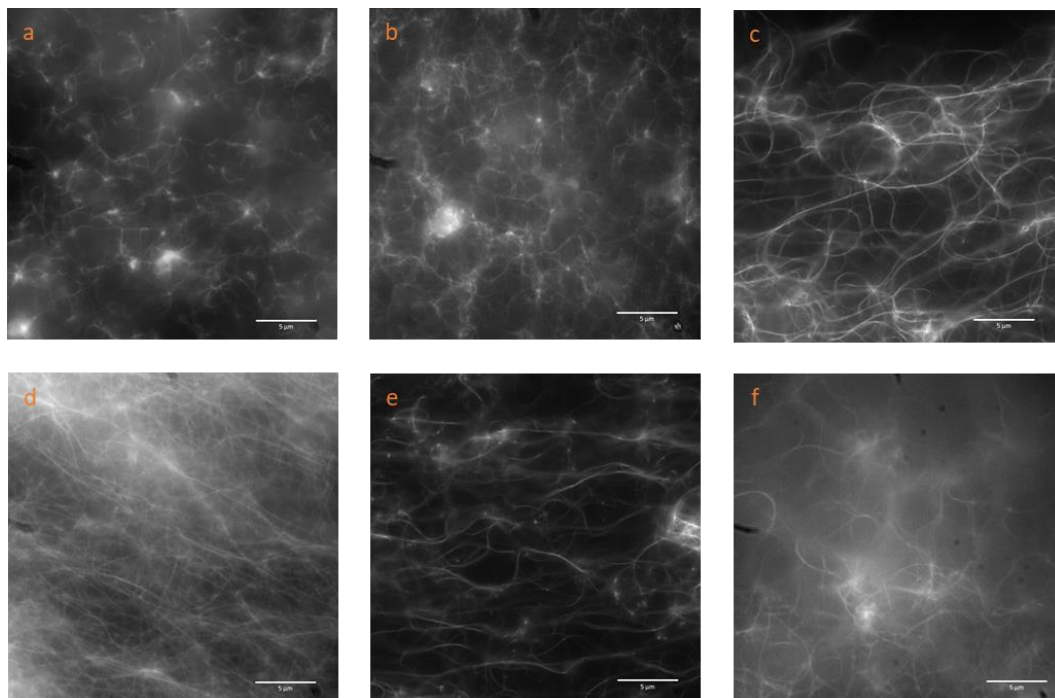


Figure 58 - DAPI LED fluorescent microscopy image of **23** (5 mg/mL) in a) NaCl, b) KCl, c) NaNO<sub>3</sub>, d) NaH<sub>2</sub>PO<sub>4</sub>, e) NaOBz, f) Na<sub>2</sub>SO<sub>4</sub> at 0.505 M. Scale bar illustrates 5 μm.

The gel fibres observed in Figure 58d (NaH<sub>2</sub>PO<sub>4</sub>) are much straighter compared to the hydrogels observed in NaCl and KCl (Figure 58a and b). Again, the only difference between the hydrogels is the salt solution. This difference in the gel fibres could explain why the hydrogel of NaH<sub>2</sub>PO<sub>4</sub> could not be characterised using rheology as the material that formed could not withstand the inversion test at 5 mg/mL. The hydrogel containing NaOBz as a salt solution Figure 58e has gel fibres that create pockets of the salt solution, potentially aiding in the gelating process. Finally, the hydrogel of a Na<sub>2</sub>SO<sub>4</sub> solution (Figure 58f) shows a relatively disperse and much more branched network. Again, this disperse network could explain why this gel was not stable enough to enable rheology experiments to be undertaken. All microscopy data can be found in the appendix (Figure S210 – S222).

## 4. Microbiological evaluation

### 4.1. Antimicrobial properties

By the year 2050, antimicrobial resistance is predicted to become the greatest threat to global health, directly responsible for 10 million deaths per year, overtaking the number of deaths caused by cancer in 2014.<sup>169</sup> There has been a significant dip in the production and invention of new antimicrobial materials and agents mainly due to the high failure rate of 95 % due to the poor market returns and lack of financial gains for big pharmaceutical companies.<sup>170</sup> To date, antimicrobial resistant bacteria have been found that are resistant to all current marketed antimicrobial agents.<sup>171</sup> This resistance is due to the overuse and misuse of antibiotics and antimicrobials, leading to bacteria forming resistance mechanisms.<sup>172</sup> New antimicrobial agents are needed, ones that bypass these resistance mechanisms.

There are two main types of bacteria, gram positive and gram negative, distinguished by the gram stain test. Gram positive bacteria have a singular cell membrane and a thick cell wall made from peptidoglycan that retains the stain, whereas gram negative bacteria have two cell membranes with a thin cell wall between them that does not retain the stain, and instead are counterstained. Methicillin-resistant *Staphylococcus aureus* (MRSA) (gram positive) and *Escherichia coli* (*E. coli*) (gram negative) are clinically relevant bacteria that **20** – **23** were first screened against at 3.33 mM using a micro broth dilution method.<sup>173</sup> If the compound inhibited more than 10 % of growth, it was taken forward to calculate MIC<sub>50</sub>. For the compounds that formed hydrogels, a gel plate assay was completed where 5 mg/mL in a 0.505 M NaCl salt solution was tested against MRSA and *E. coli* to determine the antimicrobial activity of the hydrogels. All antimicrobial studies were completed by Nyasha Allen.

### 4.2. Screening against *E. coli* and MRSA

All compounds were screened at 3.33 mM against *E. coli* (Figure 59) and MRSA (Figure 60). Compounds **20**, **21** and **23** passed screening as they killed or inhibited 10 % of

the bacterial growth after 700 minutes, or once the stationary phase has been reached. These compounds were then taken forward to calculate the minimum concentration of compound needed to kill or inhibit 50 % of bacteria growth ( $MIC_{50}$ ) values. Compound **22** did not pass screening and it is hypothesised that this is due to the lack of the benzene ring present in the structure.

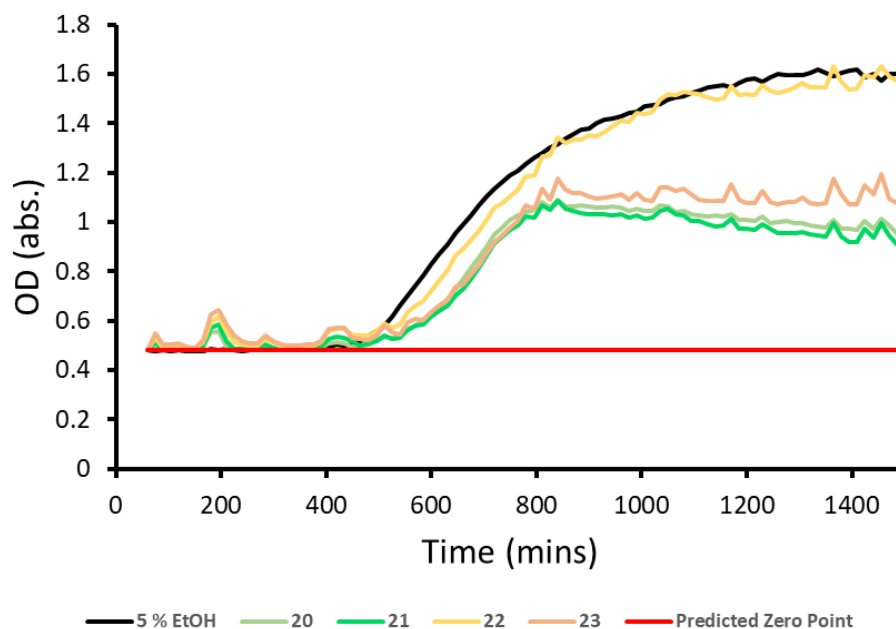


Figure 59 - Averaged growth curves created from absorbance readings of *E. coli* in the presence of different compounds. The 5 % EtOH acts as the control.

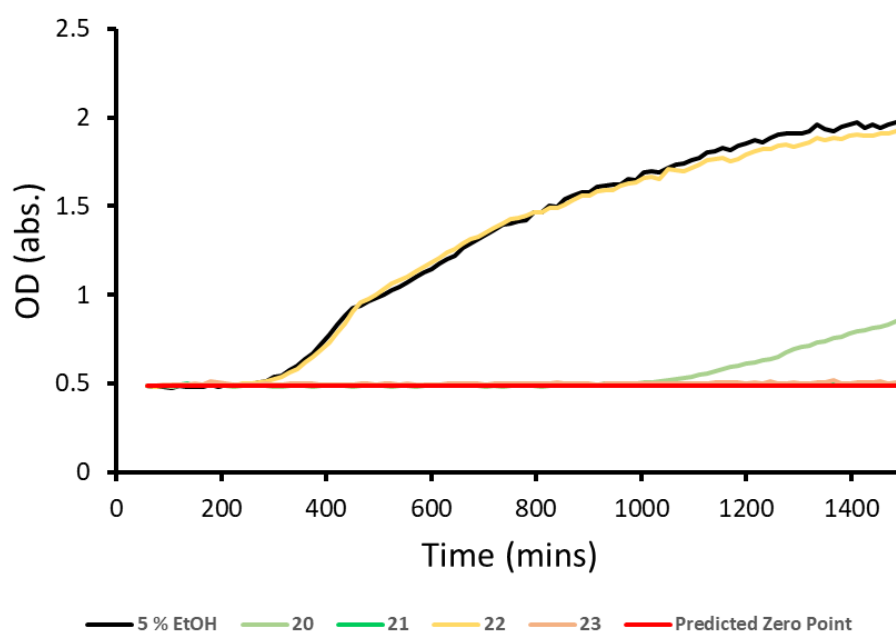


Figure 60 - Averaged growth curves created from absorbance readings of *S. aureus* in the presence of different compounds. The 5 % EtOH acts as the control.

### 4.3. MIC<sub>50</sub> calculation

After the initial screening of the compounds, MIC<sub>50</sub> was calculated. As only one biological repeat was completed, the data must be treated with caution. An overview of the MIC<sub>50</sub> data is shown in Table 11.

Table 11 – Calculated MIC<sub>50</sub> of **20**, **21** and **23**.

	<i>E. coli</i> (mM)	MRSA (mM)	Ratio ( <i>E. coli</i> :MRSA)
<b>20</b>	1.68	1.07	1:1.57
<b>21</b>	1.83	<i>a</i>	<i>a</i>
<b>23</b>	2.54	1.14	1:2.23

*a* – Data could not be calculated.

The results from the MIC<sub>50</sub> experiments show that **20** exhibits the greatest antimicrobial activity against both *E. coli* and MRSA. The ratio between *E. coli*:MRSA indicates if the compound could be used as a broad spectrum antimicrobial agent. Therefore, as **20** has a very low ratio between *E. coli*:MRSA, this compound may be a good candidate. This ratio is also interesting as gram positive is often easier to kill or inhibit than gram negative, so as **20** has a low ratio, this model of SSA: ethyl linker with a naphthalene/aromatic unit would be a good route to explore further. All graphs can be found in the appendix (Figure S225 – S236).

### 4.4. Hydrogel antimicrobial efficacy experiments

To test the antimicrobial efficacy of the hydrogels, a series of antimicrobial surface disc diffusion assays were performed against *E. coli* and MRSA. An aliquot of ~ 50 mg of the hydrogel was transferred to the surface of an agar plate inoculated with either *E. coli* or MRSA and incubated at 37 °C overnight.

If the hydrogels conferred antimicrobial activity, then a “ring” of dead bacteria (the zone of inhibition) would be observed. The results of the disc diffusion assay show no zone of inhibition on either the *E. coli* (Figure 61) or MRSA (Figure 62) plates. Although these compounds have shown to have antimicrobial properties, the concentration of SSA within

this sample of hydrogel is at a concentration below the calculated MIC<sub>50</sub>. As well as the hydrogel being below the MIC<sub>50</sub>, White *et al.* discussed that as the SSA forms the gel network, it is unable to diffuse through the agar, stopping any interactions between the SSA and bacteria.<sup>90</sup> Instead, the researchers formed a hydrogel of **19** and ampicillin salt which was tested against both bacteria. The zone of inhibition increased by 78 % and 30 % for *E. coli* and MRSA respectively compared to the NaCl salt solution hydrogel (15 mm to 59 mm for *E. coli* and 16 mm to 23 mm for MRSA).<sup>90</sup> All plates can be found in the appendix (Figure S237 – S240).

This data implies that these hydrogels may be better suited for drug delivery rather than topical use antimicrobial materials themselves.

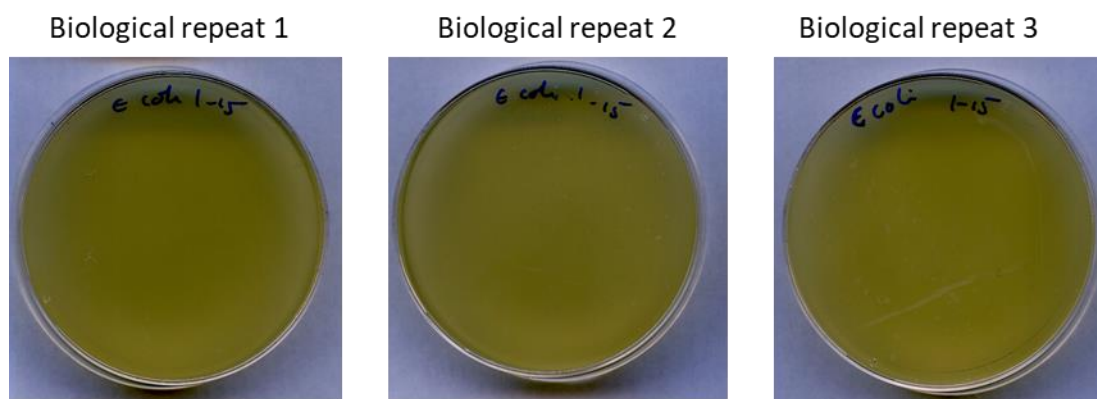


Figure 61 - Disc diffusion assays showing no zone of inhibition of growth of *E. coli* DH5B due to the presence of  $\approx$  50 mg SSA hydrogel gel of **1-15** formed in NaCl solution (0.505 M) on the surface of the plate.

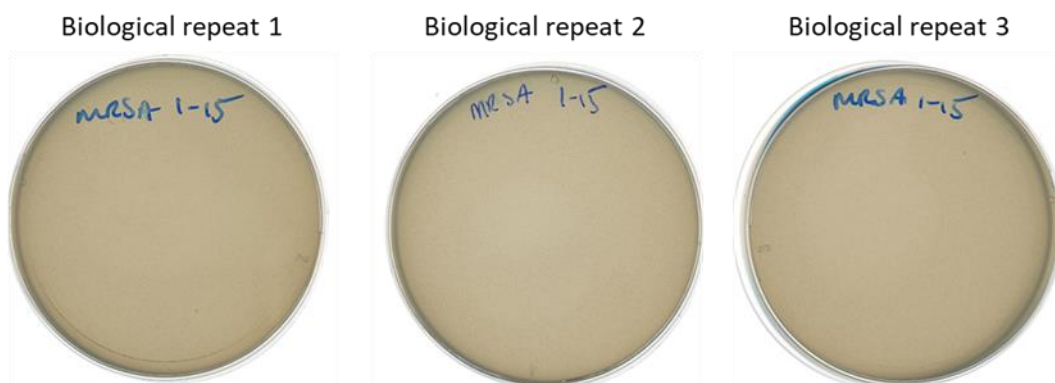


Figure 62-- Disc diffusion assays showing no zone of inhibition of growth of MRSA USA300 due to the presence of  $\approx$  50 mg SSA hydrogel gel of **1-15** formed in NaCl solution (0.505 M) on the surface of the plate.

## 5. Conclusion

In conclusion, five novel next generation SSAs were synthesised and the self-associated structures studied in the gas phase, solution state and solid state using a range of different methods. The length of the alkyl chain was determined to be an important factor in self-association. Increasing the alkyl chain length between the amide and sulfonate by a single methylene group to become an ethyl linker (CH<sub>2</sub>) causes intermolecular hydrogen bonding, forming a six-membered cyclic structure that competes with dimer formation. This cyclisation is evident in the self-association <sup>1</sup>H NMR studies, subsequent fitting to the binding isotherms EK and CoEK and was also observed in the *in silico* data.

Compound **23** was the only compound that formed hydrogel in salt solutions of 0.505 M. In comparison to **19**, an SSA that has been previously rheologically characterised,<sup>90</sup> it was hypothesised that the difference in gelation is due to the steric effects and change in hydrophobicity due to the removal of the methyl group on the benzothiazole unit.

When the antimicrobial properties of **20** – **23** were tested, **22** failed the screening process: it did not kill or inhibit 10 % of either *E. coli* or MRSA after 700 minutes. The other compounds were moved forward to determine MIC<sub>50</sub> although only one biological repeat was performed, so the data must be treated with caution. Compound **20** was determined to have the lowest MIC<sub>50</sub> for both bacteria with the lowest ratio between *E.coli*:MRSA, although **23** showed 6 % difference against MRSA (**20** – 1.07 mM, **23** – 1.14 mM). Further repeats would need to be performed to increase the validity of this data.

A NaCl hydrogel of **23** was also screened for antimicrobial efficacy, but no zone of inhibition was observed. It was hypothesised that there was no zone of inhibition as the concentration of the hydrogel was below the MIC<sub>50</sub> of the compound. It was also discussed that as the gel network is formed from the monomers of **23**, it cannot diffuse through the agar and effectively kill or inhibit the bacteria. The same observation was also seen in hydrogels of **19**.<sup>90</sup>

## 6. Future works

1. Two more biological repeats will be performed to calculate valid MIC<sub>50S</sub> for **20**, **21** and **23**.
2. Compound **20** showed a relatively low ratio between *E. coli*:MRSA. This model of SSA will be explored further by increasing the alkyl chain length, which could increase antimicrobial efficacy against both gram positive and gram negative bacteria.
3. As **19** has been characterised using the novel technique using a plate reader, this same strategy will be used for the hydrogels of **23** to help determine why this compound forms such different hydrogels in the salt solutions compared to **19**.
4. Previously, swapping the sulfonate to carboxylate has shown to increase the antimicrobial efficacy of the SSA,<sup>89</sup> but the effect on gelation has not been discovered yet. A carboxylate version of **19** and **23** will be synthesised to observe the effect on gelation and if these compounds or hydrogels have an increased efficacy against *E. coli* and MRSA.

## 7. Experimental techniques and synthesis

### 7.1. Experimental techniques

**General remarks:** A positive pressure of nitrogen and oven dried glassware were used for all reactions. All solvents and starting materials were purchased from known chemical suppliers or available stores and used without further purification. All NMR spectra were obtained using a Bruker AV2 400 MHz or AVNEO 400 MHz spectrometer. The data was processed using ACD labs or Topspin software. NMR Chemical shift values are reported in parts per million (ppm) and calibrated to the centre of the residual solvent peak set (s = singlet, br = broad, d = doublet, t = triplet, q = quartet, m = multiplet). Tensiometry measurements were undertaken using the Biolin Scientific Theta Attension optical tensiometer. The data was processed using Biolin OneAttension software. A Hamilton (309) syringe was used for these measurements. The melting point for each compound was measured using Stuart SMP10 melting point apparatus. High resolution mass spectrometry was performed using a Bruker microTOF-Q mass spectrometer and spectra recorded and processed using Bruker's Compass Data Analysis software. Infrared spectra were obtained using Shimadzu IR-Affinity-1 model Infrared spectrometer. The data was analysed in wavenumbers ( $\text{cm}^{-1}$ ) using IRsolution software. DLS and Zeta Potential studies were carried out using an Anton Paar Litesizer<sup>TM</sup> 500 and processed using Kalliope TM professional. Rheological measurements were recorded on an Anton Parr modular compact rheometer (MCR302) using a cylinder probe ST10-4V-8.8/97.5. The pH was determined a Fisherbrand hydrous 300 pH detector and calibrated using stock buffer solution.

**Self-association constant calculation:** Self-association constants were determined using Bindfit v0.5 (<http://app.supramolecular.org/bindfit/>).<sup>121</sup> All data can be accessed online using the hyperlinks provided.

**Tensiometry Studies:** All samples were prepared in an EtOH:H<sub>2</sub>O (1:19) solution. All samples underwent an annealing process in which the various solutions were heated to

approximately 313 K before being allowed to cool to room temperature, allowing each sample to reach a thermodynamic minimum. All samples were prepared through serial dilution of the most concentrated sample. Three surface tension measurements were obtained for each sample at a given concentration, using the pendant drop method. The average of the three values were plotted to calculate the critical micelle concentration (CMC).

**Mass spectrometry:** Approximately 1 mg of each compound was dissolved in 1 mL of methanol. This solution was further diluted 100-fold before undergoing analysis where 10  $\mu$ L of each sample was injected directly into a flow of 10 mM ammonium acetate in 95 % water (flow rate = 0.02 mL/min).

**DLS studies:** All vials used for preparing the samples were clean and dry. All solvents used were filtered to remove any particulates that may interfere with the results obtained. Samples of differing concentrations were obtained through serial dilution of a concentrated solution. All samples underwent an annealing process, in which they were heated to 313 K before being allowed to cool to 298 K to allow each sample to reach a thermodynamic minimum. A series of 10 runs were recorded at 298 K.

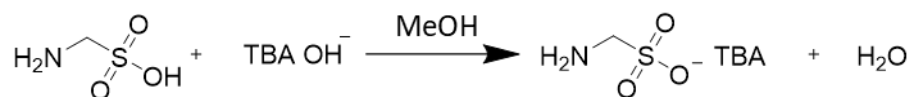
**Zeta potential studies:** All vials used for preparing the samples were clean and dry. All solvents used were filtered to remove any particulates that may interfere with the results obtained. All samples underwent an annealing process, in which they were heated to 313 K before being allowed to cool to room temperature, allowing each sample to reach a thermodynamic minimum. The final zeta potential value given is an average of the number of experiments conducted at 298 K.

**Rheometer hydrogel preparation and experimental:** Each experiment was run in triplicate. The appropriate aqueous salt solution (1 mL, 0.505 M) was added to 5 mg of the compound in a glass vial with an internal diameter of 1 cm and heated to approximately 333 K, until dissolved. The sample was positioned on the rheometer and set with a relaxation time of 60

minutes. Oscillatory amplitude experiments maintained a frequency of  $10 \text{ rad s}^{-1}$  and were performed with the amplitude of oscillation from 0.01 % up to 100 % at 298 K. Oscillatory frequency sweep experiments maintained a constant shear strain ( $\gamma$ ) with an increasing frequency from 0.01-100  $\text{rad s}^{-1}$  at 298 K.

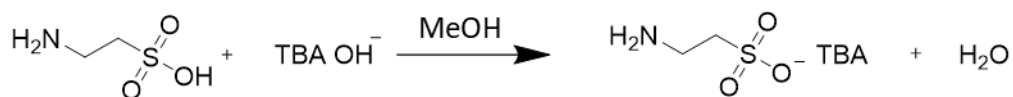
**Hydrogel preparation:** The appropriate aqueous salt solution (1 mL, 0.505 M) was added to the specified quantity of the compound in a glass vial and heated to approximately 333 K until dissolved and then left at room temperature to allow gelation to occur. Gel formation was achieved through an annealing process in which the pre-gel mixture was sonicated and heated until the gelator (**23**) had dissolved. At this point, the samples were sealed and allowed to cool to room temperature, before undergoing an inversion test for the formation of a hydrogel, this was then confirmed through rheological measurements.

## 7.2. Chemical Synthesis



Scheme 3 – The synthesis of TBA aminomethansulfonate.

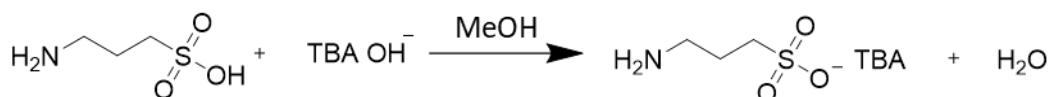
**TBA aminomethansulfonate** (Scheme 3): 1-Aminomethan-2-sulfonic acid (0.33 g, 3.00 mM) was dissolved in TBA hydroxide (1 M) in methanol (3.00 mL), excess methanol was then added (5 mL) before the mixture was taken to complete dryness under reduced pressure. Assume yield 100 %.<sup>a</sup> This compound was not characterised but used directly in the synthesis of compound **19**, **22**, **23** and **24**.



Scheme 4 - The synthesis of TBA aminoethansulfonate.

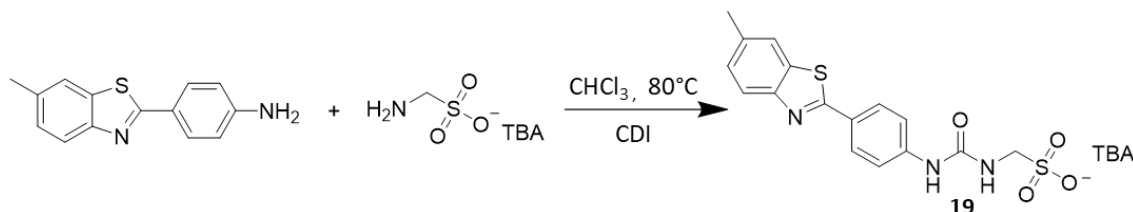
<sup>a</sup> We assume it is 100 % as there is nothing else that can happen, the slightly basic conditions deprotonates the sulfonate, the released  $\text{H}^+$  then reacts with the  $\text{OH}^-$  from the TBA, forming water and the salt. The water is then driven off on the high vac, pushing over the equilibrium.

**TBA aminoethansulfonate** (Scheme 4): 1-aminoethane-2-sulfonic acid (0.13 g, 2.00 mM) was dissolved in TBA hydroxide (1 M) in methanol (2.00 mL) excess methanol was then added (5 mL) before the mixture was taken to complete dryness under reduced pressure. Assume yield 100 %.<sup>b</sup> This compound was not characterised but used directly in the synthesis of compound **20**.



Scheme 5 - The synthesis of TBA aminopropansulfonate.

**TBA aminomethansulfonate** (Scheme 5): 3-aminopropane-1-sulfonic acid (0.28 g, 2.00 mM) was dissolved in TBA hydroxide (1 M) in methanol (2.00 mL) excess methanol was then added (5 mL) before the mixture was taken to complete dryness under reduced pressure. Assume yield 100 %.<sup>c</sup> This compound was not characterised but used directly in the synthesis of compound **21**.

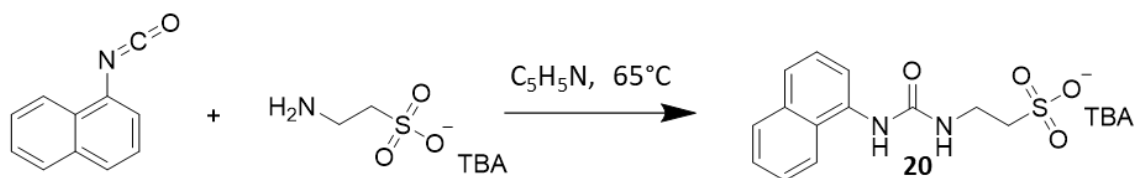


Scheme 6 – The synthesis of compound **19**.

**Compound 19** (Scheme 6): This compound was synthesized in line with previously published methods.<sup>86</sup> <sup>1</sup>H NMR (400 MHz, 298 K, DMSO-*d*<sub>6</sub>): δ: 0.93 (t, *J* = 7.44 Hz, 12H), 1.30 (m, 8H), 1.56 (m, 8H), 2.44 (s, 3H), 3.17 (m, 8H), 3.90 (d, *J* = 5.76 Hz, 2H), 6.62 (s, 1H), 7.32 (m, 1H), 7.56 (d, *J* = 8.87 Hz, 2H), 7.90 (m, 4H), 9.15 (s, 1H). This NMR spectrum was found to match previously published values.<sup>86</sup>

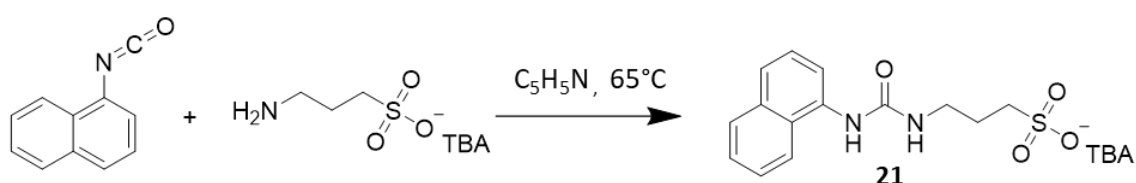
<sup>b</sup> See footnote a.

<sup>c</sup> See footnote a.



Scheme 7 - The synthesis of compound **20**.

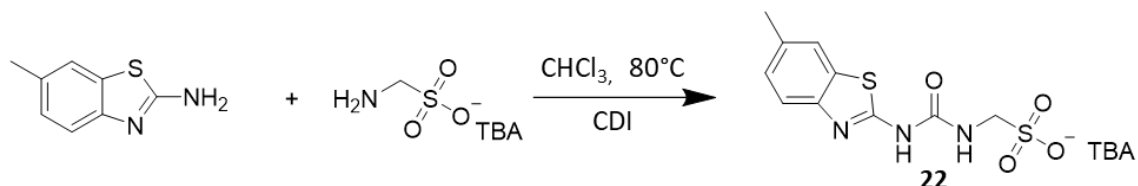
**Compound 20** (Scheme 7): TBA 1-aminomethan-2-sulfonate (0.44 g, 1.20 mM) and 1-isocyanatonaftalene (0.17 mL, 1.20 mM) were mixed in anhydrous pyridine and the reaction was left overnight at 338 K. The resulting solution was taken to dryness and re-dissolved in ethyl acetate, producing the pure product as a cream powder with a yield of 82 % (0.53 g, 0.99 mM). Melting point: 454 K;  $^1\text{H}$  NMR (400 MHz, 298 K,  $\text{DMSO-}d_6$ ):  $\delta$ : 0.93 (t,  $J = 7.24$  Hz, 12H), 1.29 (m, 8H), 1.56 (m, 8H), 2.59 (t,  $J = 6.44$  Hz, 2H), 3.15 (m, 8H), 3.42 (q,  $J = 6.6$  Hz, 2H), 6.77 (t,  $J = 5.48$  Hz, 1H), 7.40 (t,  $J = 7.92$  Hz, 1H), 7.45 (m, 3H), 7.90 (m, 2H), 8.14 (m, 1H), 8.82 (s, 1H);  $^{13}\text{C}\{^1\text{H}\}$  NMR (100 MHz, 298 K,  $\text{DMSO-}d_6$ ):  $\delta$ : 13.5 ( $\text{CH}_3$ ), 19.2 ( $\text{CH}_2$ ), 23.1 ( $\text{CH}_2$ ), 36.3, ( $\text{CH}_2$ ), 51.2 ( $\text{CH}_2$ ), 57.5 ( $\text{CH}_2$ ), 116.9 (ArCH), 121.9, (ArCH), 122.0 (ArCH), 125.2 (ArCH), 125.7 (ArCH), 125.9 (ArCH), 128.2 (ArC), 133.7 (ArC), 135.5 (ArC), 155.6 (C=O); IR (film):  $\nu$  ( $\text{cm}^{-1}$ ) = 3282 (NH stretch), 1685 (C=O stretch), 1029 (CN stretch); HRMS for the sulfonate-urea ion ( $\text{C}_{13}\text{H}_{13}\text{N}_2\text{O}_4\text{S}^-$ ) (ESI):  $m/z$ : act: 293.0612,  $[\text{M}]^-$  cal: 293.0602  $[\text{M}]^-$ .



Scheme 8 - The synthesis of compound **21**.

**Compound 21** (Scheme 8): TBA 3-aminopropane-1-sulfonate (0.46 g, 1.20 mM) and 1-isocyanatonaftalene (0.17 mL, 1.20 mM) were added to in anhydrous pyridine and left overnight at 338 K in a sealed vessel. The resulting solution was taken to dryness and re-dissolved in ethyl acetate, producing the pure product as a pale pink powder with a yield of 78 % (0.51 g, 0.93 mM). Melting point: 428 K;  $^1\text{H}$  NMR (400 MHz, 298 K,  $\text{DMSO-}d_6$ ):  $\delta$ : 0.93 (t,  $J = 7.44$  Hz, 12H), 1.30 (m, 8H), 1.56 (m, 8H), 1.75 (m, 2H), 3.18 (m, 10H), 6.64 (t,  $J = 5.6$  Hz, 1H), 7.40 (t,  $J = 7.96$  Hz, 1H), 7.52 (m, 3H), 7.88 (m, 1H), 8.00 (d,  $J = 7.16$  Hz, 1H), 8.09 (d,

$J = 8.28$  Hz, 1H), 8.53 (br s, H);  $^{13}\text{C}\{^1\text{H}\}$  NMR (100 MHz, 298 K, DMSO- $d_6$ ):  $\delta$ : 13.5 (CH<sub>3</sub>), 19.2 (CH<sub>2</sub>), 23.1 (CH<sub>2</sub>), 26.1 (CH<sub>2</sub>), 38.4 (CH<sub>2</sub>), 49.0 (CH<sub>2</sub>), 57.5 (CH<sub>2</sub>), 121.5 (ArCH), 121.7 (ArCH), 125.3 (ArCH), 125.4 (ArC), 125.7 (ArCH), 125.9 (ArCH), 128.3 (ArCH), 133.7 (ArC), 135.4 (ArC), 155.6 (C=O); IR (film):  $\nu$  (cm<sup>-1</sup>) = 1690 (C=O stretch), 1032 (CN stretch); HRMS for the sulfonate-urea ion (C<sub>14</sub>H<sub>15</sub>N<sub>2</sub>O<sub>4</sub>S<sup>-</sup>) (ESI<sup>-</sup>):  $m/z$ : act: 307.0769, [M]<sup>-</sup> cal: 307.0758 [M]<sup>-</sup>.



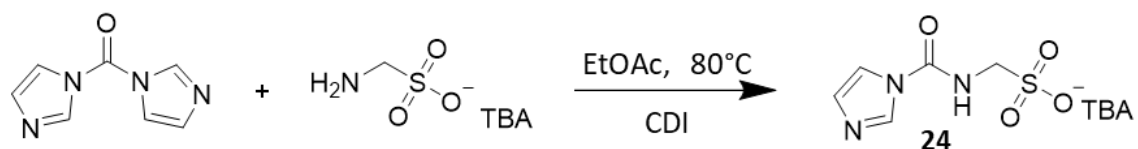
Scheme 9 - The synthesis of compound **22**.

**Compound 22** (Scheme 9): A mixture of 2-Aminobenzothiazole (0.23 g, 1.40 mM) and CDI (0.27 g, 1.68 mM) were heated at reflux for 4 hours in chloroform (10.00 mL). TBA aminomethanesulfonate (0.49 g, 1.40 mM) was dissolved in chloroform and added to the original reaction mixture which was then heated at reflux overnight. The precipitate was removed, the filtrate taken to dryness and then dissolved in methanol (30.00 mL). The precipitate was removed and the filtrate taken to dryness and dissolved in ethyl acetate producing the pure product as a white solid with a yield of 73% (0.45 g, 0.68 mM). Melting point: > 473 K;  $^1\text{H}$  NMR (400 MHz, 298 K, DMSO- $d_6$ ):  $\delta$ : 0.92 (t,  $J = 7.28$  Hz, 12H), 1.30 (m, 8H), 1.55 (m, 8H), 2.37 (s, 3H), 3.15 (m, 8H), 3.93 (d,  $J = 5.88$  Hz, 2H), 7.16 (m, 1H), 7.50 (d,  $J = 8.16$  Hz, 1H), 7.66 (s, 1H), 10.54 (br s, H);  $^{13}\text{C}\{^1\text{H}\}$  NMR (100 MHz, 298K, DMSO- $d_6$ ):  $\delta$ : 13.5 (CH<sub>3</sub>), 19.2 (CH<sub>2</sub>), 20.9 (CH<sub>3</sub>), 23.1 (CH<sub>2</sub>), 55.9 (CH<sub>2</sub>), 57.5 (CH<sub>2</sub>), 119.4 (ArCH), 121.1 (ArCH), 127.0 (ArCH), 131.7 (ArC), 132.0 (ArC), 147.1 (ArC), 153.3 (ArC), 158.7 (C=O); IR (film):  $\nu$  (cm<sup>-1</sup>) = 3345 (NH stretch), 1697 (C=O stretch), 1038 (CN stretch); HRMS for the sulfonate-urea ion (C<sub>10</sub>H<sub>10</sub>N<sub>3</sub>O<sub>4</sub>S<sub>2</sub><sup>-</sup>) (ESI<sup>-</sup>):  $m/z$ : act: 300.0133, [M]<sup>-</sup> cal: 300.0118 [M]<sup>-</sup>.



Scheme 10 - The synthesis of compound **23**.

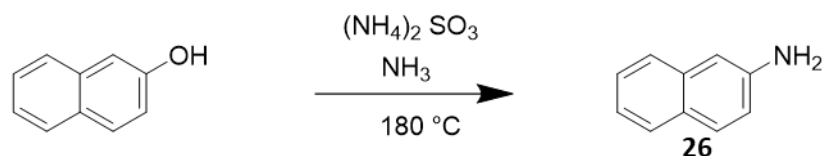
**Compound 23** (Scheme 10): A mixture of 4-(benzothiazol-2-yl)aniline (0.20 g, 0.84 mM) and CDI (0.17 g, 1.06 mM) was heated at reflux for 4 hours in chloroform (10.00 mL). TBA aminomethanesulfonate (0.30 g, 0.84 mM) was dissolved in pyridine (2.00 mL) and added to the original reaction mixture which was then heated at reflux overnight. The crude was taken to dryness, dissolved in chloroform (10.00 mL) and washed with water (10.00 mL x 3). The precipitate was removed, the filtrate was taken to dryness and then dissolved in ethyl acetate. The resulting white precipitate product with a yield of 63 % (0.34 g, 0.56 mM); Melting point: 468 K;  $^1\text{H}$  NMR (400 MHz, 298 K, DMSO- $d_6$ ):  $\delta$ : 0.93 (t,  $J$  = 7.28 Hz, 12H), 1.30 (m, 8H), 1.56 (m, 8H), 3.16 (m, 8H), 3.90 (d,  $J$  = 5.84 Hz, 2H), 6.63 (br s, 1H), 7.49 (m, 4H), 7.98 (m, 3H), 8.09 (d,  $J$  = 7.80 Hz, 1H), 9.17 (br s, 1H);  $^{13}\text{C}\{^1\text{H}\}$  NMR (100 MHz, 298K, DMSO- $d_6$ ):  $\delta$ : 13.5 (CH<sub>3</sub>), 19.2 (CH<sub>2</sub>), 23.1 (CH<sub>2</sub>), 56.0 (CH<sub>2</sub>), 57.5 (CH<sub>2</sub>), 117.6 (ArCH), 122.2 (ArCH), 122.4 (ArCH), 25.0 (ArCH), 125.4 (ArC), 126.5 (ArCH), 128.0 (ArCH), 134.1 (ArC), 143.7 (ArC), 153.7 (ArC), 154.2 (ArC), 167.3 (C=O); IR (film):  $\nu$  (cm<sup>-1</sup>) = 3267 (NH stretch), 1697 (C=O stretch), 1327 (S=O stretch), 1038 (CN stretch); HRMS for the sulfonate-urea ion (C<sub>15</sub>H<sub>12</sub>N<sub>3</sub>O<sub>4</sub>S<sub>2</sub>)<sup>-</sup> (ESI):  $m/z$ : act: 390.2425, [M + C<sub>2</sub>H<sub>4</sub>]<sup>-</sup> cal: 362.0275 [M]<sup>-</sup>.



Scheme 11 - The synthesis of compound **24**.

**Compound 24** (Scheme 11): CDI (0.30 g, 1.82 mM) was in dissolved ethyl acetate (10.00 mL) and left to reflux for 1.5 hours, then TBA aminomethanesulfonate (0.64 g, 1.82 mM) in ethyl acetate was added to the mixture and heated at reflux overnight. The resulting precipitate was the product with a yield of 71 % (0.58 g, 1.20 mM); Melting point: 388 K  $^1\text{H}$  NMR (400

MHz, 298 K, DMSO- $d_6$ ):  $\delta$ : 0.93 (t,  $J$  = 7.36 Hz, 12H), 1.31 (m, 8H), 1.56 (m, 8H), 3.16 (m, 8H), 4.02 (d,  $J$  = 6.32 Hz, 2H), 7.01 (s, 1H), 7.78 (m, 1H), 8.31 (m, 1H), 8.97 (t,  $J$  = 6.08, H);  $^{13}\text{C}\{^1\text{H}\}$  NMR (100 MHz, 298 K, DMSO- $d_6$ ):  $\delta$ : 13.5 (CH<sub>3</sub>), 19.2 (CH<sub>2</sub>), 23.1 (CH<sub>2</sub>), 56.2 (CH<sub>2</sub>), 57.5 (CH<sub>2</sub>), 116.7 (ArCH), 129.5 (ArCH), 136.1 (ArCH), 148.3 (C=O); IR (film):  $\nu$  (cm<sup>-1</sup>) = 3229 (NH stretch), 1717 (C=O stretch), 1364 (S=O stretch), 1042 (CN stretch); HRMS for the sulfonate-urea ion (C<sub>5</sub>H<sub>6</sub>N<sub>3</sub>O<sub>4</sub>S<sup>-</sup>) (ESI<sup>-</sup>):  $m/z$ : act: 204.0132, [M]<sup>-</sup> cal: 204.0084 [M]<sup>-</sup>.



Scheme 12 - The synthesis of compound **26**.

**Compound 26** (Scheme 12): This compound was synthesized in line with previously published methods.<sup>174</sup> Yield of 84.9 % (0.845 g, 5.86 mM);  $^1\text{H}$  NMR (298K, 400 MHz, DMSO- $d_6$ ):  $\delta$ : 5.39 (br s, 2H), 6.82 (d,  $J$  = 2.20 Hz, 1H), 6.94 (dd,  $J$  = 8.68, 2.20 Hz, 1H), 7.08 (t,  $J$  = 7.48 Hz, 1H), 7.27 (t,  $J$  = 7.44 Hz, 1H), 7.49 (d,  $J$  = 8.22 Hz, 1H), 7.60 (m, 2H);  $^{13}\text{C}\{^1\text{H}\}$  NMR (100 MHz, 298 K, DMSO- $d_6$ ):  $\delta$ : 105.8 (ArCH), 118.4 (ArCH), 120.9 (ArCH), 125.1 (ArCH), 125.9 (ArCH), 126.3 (ArC), 127.5 (ArCH), 128.5 (ArCH), 135.0 (ArC), 146.7 (ArC).

## 8. References

- 1 J.-M. Lehn, *Angew. Chemie Int. Ed. English*, 1990, **29**, 1304–1319.
- 2 B. Dietrich, J. M. Lehn and J. P. Sauvage, *Tetrahedron Lett.*, 1969, **10**, 2885–2888.
- 3 J. M. Lehn, *Acc. Chem. Res.*, 1978, **11**, 49–57.
- 4 J.-M. Lehn, *Angew. Chemie Int. Ed. English*, 1988, **27**, 89–112.
- 5 V. Richards, *Nat. Chem.*, 2016, **8**, 1090.
- 6 S. A. Nepogodiev and J. F. Stoddart, *Chem. Rev.*, 1998, **98**, 1959–1976.
- 7 V. Richards, *Nat. Chem.*, 2016, **8**, 1090.

- 8 C. J. Bruns and J. F. Stoddart, *Acc. Chem. Res.*, 2014, **47**, 2186–2199.
- 9 P. S. Cohen and S. M. Cohen, *J. Chem. Educ.*, 1996, **73**, 883.
- 10 F. Wöhler, *Ann. Phys.*, 1828, **88**, 253–256.
- 11 M. Kirschner, J. Gerhart and T. Mitchison, *Cell*, 2000, **100**, 79–88.
- 12 B. Olenyuk, A. Fechtenkötter and P. J. Stang, *J. Chem. Soc. Dalton Trans.*, 1998, 1707–1728.
- 13 J. J. Thomson, *London, Edinburgh, Dublin Philos. Mag. J. Sci.*, 1914, **27**, 757–789.
- 14 G. N. Lewis, *J. Am. Chem. Soc.*, 1913, **35**, 1448–1455.
- 15 H. Margenau, *Rev. Mod. Phys.*, 1939, **11**, 1.
- 16 J. D. van der Waals, *Nature*, 1874, **10**, 477.
- 17 J. S. Rowlinson, *JD van der Waals: On the Continuity of the Gaseous and Liquid States*, North-Holland, 1988.
- 18 E. Fischer, *Berichte der Dtsch. Chem. Gesellschaft*, 1894, **27**, 3479–3483.
- 19 T. S. Moore and T. F. Winmill, *J. Chem. Soc. Trans.*, 1912, **101**, 1635–1676.
- 20 W. M. Latimer and W. H. Rodebush, *J. Am. Chem. Soc.*, 1920, **42**, 1419–1433.
- 21 J. W. Steed and J. L. Atwood, *Supramolecular chemistry*, John Wiley & Sons, 2013.
- 22 P. D. Beer, P. A. Gale and D. K. Smith, *Supramolecular chemistry*, Oxford University Press, 1999.
- 23 X. Lin and M. W. Grinstaff, *Isr. J. Chem.*, 2013, **53**, 498–510.
- 24 M. L. Waters, *Curr. Opin. Chem. Biol.*, 2002, **6**, 736–741.
- 25 P. Dapporto, P. Paoli and S. Roelens, *J. Org. Chem.*, 2001, **66**, 4930–4933.
- 26 M. M. Conn and J. Rebek, *Chem. Rev.*, 1997, **97**, 1647–1668.

- 27 G. Ono, A. Izuoka, T. Sugawara and Y. Sugawara, *J. Mater. Chem.*, 1998, **8**, 1703–1709.
- 28 C. J. Pedersen, *Angew. Chemie Int. Ed. English*, 1988, **27**, 1021–1027.
- 29 B. Davarcioglu, *Int J Mod Eng Res*, 2011, **1**, 443–454.
- 30 D. A. Dougherty, *Acc. Chem. Res.*, 2013, **46**, 885–893.
- 31 B. L. Schottel, H. T. Chifotides and K. R. Dunbar, *Chem. Soc. Rev.*, 2008, **37**, 68–83.
- 32 J. W. Larson and T. B. McMahon, *Inorg. Chem.*, 1984, **23**, 2029–2033.
- 33 J. Emsley, *Chem. Soc. Rev.*, 1980, **9**, 91–124.
- 34 J. J. Dannenberg, L. Haskamp and A. Masunov, *J. Phys. Chem. A*, 1999, **103**, 7083–7086.
- 35 A. Bonnet, J. Chisholm, W. D. S. Motherwell and W. Jones, *Cryst. Eng. Comm*, 2005, **7**, 71–75.
- 36 T. Steiner, *Angew. Chemie Int. Ed.*, 2002, **41**, 48–76.
- 37 D. J. Cram and R. H. Bauer, *J. Am. Chem. Soc.*, 1959, **81**, 5971–5977.
- 38 J. . W. and L. Isaacs, *Supramolecular Chemistry*, John Wiley & Sons, Ltd, Chichester, 2012.
- 39 J.-M. Lehn, *Chem. Soc. Rev.*, 2007, **36**, 151–160.
- 40 G. M. Whitesides and M. Boncheva, *Proc. Natl. Acad. Sci.*, 2002, **99**, 4769 LP – 4774.
- 41 M. Lal Saha and M. Schmittel, *Org. Biomol. Chem.*, 2012, **10**, 4651–4684.
- 42 A. F. Herbort and K. Schuhen, *Environ. Sci. Pollut. Res.*, 2017, **24**, 11061–11065.
- 43 H. Lodish, A. Berk, S. L. Zupursky, D. B. Matsudaira and J. Darnell, *Molecular Cell Biology*, New York, 4th Editio., 2000.

- 44 A. Breda, N. F. Valadares, O. N. de Souza and R. Charles, *Natl. Cent. Biotechnol. Inf.*
- 45 C. A. Hunter, *Angew. Chemie Int. Ed.*, 2004, **43**, 5310–5324.
- 46 J. M. Berg, J. L. Tymoczko and L. Stryer, *Biochemistry*, 2002, **262**, 159–173.
- 47 M. SELA, F. H. J. WHITE and C. B. ANFINSEN, *Science*, 1957, **125**, 691–692.
- 48 S. Tayyab and A. N. Boyce, *A Journey from Amino Acids to Proteins*, University of Malaya Press, 2006.
- 49 S. E. Phillips, *J. Mol. Biol.*, 1980, **142**, 531–554.
- 50 B. A. Shirley, *Protein stability and folding: Theory and practice*, Springer, 1995, vol. 21.
- 51 N. Darby and T. E. Creighton, in *Protein Stability and Folding*, Springer, 1995, pp. 219–252.
- 52 K. P. Murphy, in *Protein Stability and Folding*, Springer, 1995, pp. 1–34.
- 53 J. D. Watson and F. H. C. Crick, *Nature*, 1953, **171**, 737–738.
- 54 P. Yakovchuk, E. Protozanova and M. D. Frank-Kamenetskii, *Nucleic Acids Res.*, 2006, **34**, 564–574.
- 55 P. A. Hassan, G. Verma and R. Ganguly, *Funct. Mater. SB Tyagi, Ed. London Elsevier*, 2012, 1–59.
- 56 D. Lombardo, M. A. Kiselev, S. Magazù and P. Calandra, *Adv. Condens. Matter Phys.*
- 57 A. Wu, Y. Gao and L. Zheng, *Green Chem.*, 2019, **21**, 4290–4312.
- 58 V. S. Kulkarni and C. Shaw, *Essential chemistry for formulators of semisolid and liquid dosages*, Academic Press, 2015.
- 59 R. Azarmi and A. Ashjarian, *J. Chem. Pharm. Res*, 2015, **7**, 632–640.

- 60 G. Graziano, *Biophys. Chem.*, 1999, **82**, 69–79.
- 61 R. Godawat, S. N. Jamadagni and S. Garde, *Proc. Natl. Acad. Sci.*, 2009, **106**, 15119–15124.
- 62 M. Aktas, M. Wessel, S. Hacker, S. Klüsener, J. Gleichenhagen and F. Narberhaus, *Eur. J. Cell Biol.*, 2010, **89**, 888–894.
- 63 D. Bradburn and T. Bittinger, *Micelles: Structural Biochemistry, Formation and Functions & Usage*, Nova Science Publishers, Incorporated, 2013.
- 64 B. Alberts, A. Johnson, J. Lewis, M. Raff, K. Roberts and P. Walter, *There is no Corresp. Rec. this Ref. Sch.*
- 65 Y. Wang, H. Xu and X. Zhang, *Adv. Mater.*, 2009, **21**, 2849–2864.
- 66 X. Zhang and C. Wang, *Chem. Soc. Rev.*, 2011, **40**, 94–101.
- 67 C. Wang, Z. Wang and X. Zhang, *Small*, 2011, **7**, 1379–1383.
- 68 W.-R. Zhuang, Y. Wang, P.-F. Cui, L. Xing, J. Lee, D. Kim, H.-L. Jiang and Y.-K. Oh, *J. Control. release*, 2019, **294**, 311–326.
- 69 Y. Kang, K. Liu and X. Zhang, *Langmuir*, 2014, **30**, 5989–6001.
- 70 C. Wang, Z. Wang and X. Zhang, *Acc. Chem. Res.*, 2012, **45**, 608–618.
- 71 X. Zhang, Z. Chen and F. Würthner, *J. Am. Chem. Soc.*, 2007, **129**, 4886–4887.
- 72 A. V Kabanov, T. K. Bronich, V. A. Kabanov, K. Yu and A. Eisenberg, *J. Am. Chem. Soc.*, 1998, **120**, 9941–9942.
- 73 J.-F. Gohy, B. G. G. Lohmeijer and U. S. Schubert, *Macromolecules*, 2002, **35**, 4560–4563.
- 74 S. Shinde, A. Incel, M. Mansour, G. Olsson, I. Nicholls, C. Esen, J. Urraca and B. Sellergren, *J. Am. Chem. Soc.*, , DOI:10.1021/jacs.0c00707.

- 75 C. Pérez-Casas and A. K. Yatsimirsky, *J. Org. Chem.*, 2008, **73**, 2275–2284.
- 76 N. Kimizuka, T. Kawasaki and T. Kunitake, *J. Am. Chem. Soc.*, 1993, **115**, 4387–4388.
- 77 N. Kimizuka, T. Kawasaki, K. Hirata and T. Kunitake, *J. Am. Chem. Soc.*, 1998, **120**, 4094–4104.
- 78 C. M. C. Faustino, A. R. T. Calado and L. Garcia-Rio, *J. Phys. Chem. B*, 2009, **113**, 977–982.
- 79 C. M. C. Faustino, A. R. T. Calado and L. Garcia-Rio, *J. Colloid Interface Sci.*, 2010, **351**, 472–477.
- 80 C. M. C. Faustino, A. R. T. Calado and L. Garcia-Rio, *J. Colloid Interface Sci.*, 2011, **359**, 493–498.
- 81 M. Boiocchi, L. Del Boca, D. E. Gómez, L. Fabbrizzi, M. Licchelli and E. Monzani, *J. Am. Chem. Soc.*, 2004, **126**, 16507–16514.
- 82 J. Y. Kwon, Y. J. Jang, S. K. Kim, K.-H. Lee, J. S. Kim and J. Yoon, *J. Org. Chem.*, 2004, **69**, 5155–5157.
- 83 J. R. Hiscock, G. P. Bustone, B. Wilson, K. E. Belsey and L. R. Blackholly, *Soft Matter*, 2016, **12**, 4221–4228.
- 84 L. R. Blackholly, H. J. Shepherd and J. R. Hiscock, *CrystEngComm*, 2016, **18**, 7021–7028.
- 85 L. J. White, S. N. Tyuleva, B. Wilson, H. J. Shepherd, K. K. L. Ng, S. J. Holder, E. R. Clark and J. R. Hiscock, *Chem. – A Eur. J.*, 2018, **24**, 7761–7773.
- 86 L. J. White, N. J. Wells, L. R. Blackholly, H. J. Shepherd, B. Wilson, G. P. Bustone, T. J. Runacres and J. R. Hiscock, *Chem. Sci.*, 2017, **8**, 7620–7630.
- 87 K. K. L. Ng, M. Dimitrovski, J. E. Boles, R. J. Ellaby, L. J. White and J. R. Hiscock, *Supramol. Chem.*, 2020, 1–11.

- 88 T. L. Gumbs, L. J. White, N. J. Wells, H. J. Shepherd and J. R. Hiscock, *Supramol. Chem.*, 2018, **30**, 286–295.
- 89 S. N. Tyuleva, N. Allen, L. J. White, A. Pepes, H. J. Shepherd, P. J. Saines, R. J. Ellaby, D. P. Mulvihill and J. R. Hiscock, *Chem. Commun.*, 2018, **55**, 95–98.
- 90 L. J. White, J. E. Boles, N. Allen, L. S. Alesbrook, M. J. Sutton, C. K. Hind, K. L. F. Hilton, L. R. Blackholly, R. J. Ellaby, G. T. Williams, D. P. Mulvihill and J. R. Hiscock, *J. Mater. Chem. B*, 2020, **8**, 4694–4700.
- 91 J. D. Clogston and A. K. Patri, in *Characterization of nanoparticles intended for drug delivery*, Springer, 2011, pp. 63–70.
- 92 R. Vogel, A. K. Pal, S. Jambhrunkar, P. Patel, S. S. Thakur, E. Reategui, H. S. Parekh, P. Saa, A. Stassinopoulos and M. F. Broom, *Sci. Rep.*, 2017, **7**, 17479.
- 93 A. Franck and T. A. I. Germany, *TA Instruments, New Castle, DE, USA AN004*.
- 94 H. A. Kurtz, J. J. P. Stewart and K. M. Dieter, *J. Comput. Chem.*, 1990, **11**, 82–87.
- 95 M. Eckert, *Ann. Phys.*, 2012, **524**, A83–A85.
- 96 N. Lectures, Nobel Prize in Physics 1914,  
<https://www.nobelprize.org/prizes/physics/1914/press-release/>, (accessed 28 May 2020).
- 97 J.-P. Zhang, P.-Q. Liao, H.-L. Zhou, R.-B. Lin and X.-M. Chen, *Chem. Soc. Rev.*, 2014, **43**, 5789–5814.
- 98 P. L. Urban, *Philos. Trans. R. Soc. A Math. Phys. Eng. Sci.*, 2016, 374.
- 99 F. A. Mellon, ed. B. B. T.-E. of F. S. and N. (Second E. Caballero, Academic Press, Oxford, 2003, pp. 3739–3749.
- 100 C. S. Ho, C. W. K. Lam, M. H. M. Chan, R. C. K. Cheung, L. K. Law, L. C. W. Lit, K. F. Ng, M. W. M. Suen and H. L. Tai, *Clin. Biochem. Rev.*, 2003, **24**, 3.

- 101 J. B. Fenn, M. Mann, C. K. Meng, S. F. Wong and C. M. Whitehouse, *Science (80-. )*, 1989, **246**, 64 LP – 71.
- 102 T. D. Veenstra, *Biophys. Chem.*, 1999, **79**, 63–79.
- 103 G. Siuzdak, *JALA J. Assoc. Lab. Autom.*, 2004, **9**, 50–63.
- 104 C.-C. Liou, H.-F. Wu and J. S. Brodbelt, *J. Am. Soc. Mass Spectrom.*, 1994, **5**, 260–273.
- 105 C. L. Mazzitelli, J. S. Brodbelt, J. T. Kern, M. Rodriguez and S. M. Kerwin, *J. Am. Soc. Mass Spectrom.*, 2006, **17**, 593–604.
- 106 R. Hänsel-Hertsch, M. Di Antonio and S. Balasubramanian, *Nat. Rev. Mol. Cell Biol.*, 2017, **18**, 279–284.
- 107 UWPR, ESI common background ions: Repeating common units, [http://www.proteomicsresource.washington.edu/protocols05/esi\\_background\\_ions\\_repeat\\_units.php](http://www.proteomicsresource.washington.edu/protocols05/esi_background_ions_repeat_units.php), (accessed 4 August 2020).
- 108 J. Kiefer, K. Noack and B. Kirchner, *Curr. Phys. Chem.*, 2011, **1**, 340–351.
- 109 V. M. Wallace, N. R. Dhumal, F. M. Zehentbauer, H. J. Kim and J. Kiefer, *J. Phys. Chem. B*, 2015, **119**, 14780–14789.
- 110 S. Bharti and R. Roy, *TrAC Trends Anal. Chem.*, 2012, **35**, 5–26.
- 111 R. F. Evilia, *Anal. Lett.*, 2001, **34**, 2227–2236.
- 112 M. V. Silva Elipe, *Anal. Chim. Acta*, 2003, **497**, 1–25.
- 113 R. A. Khalil and F. A. Saadoon, *J. Saudi Chem. Soc.*, 2015, **19**, 423–428.
- 114 A. L. García-Ortiz, R. Domínguez-González, M. Romero-Ávila, B. Flores-Pérez, L. Guillén, M. Castro and N. Barba-Behrens, *Inorganica Chim. Acta*, 2018, **471**, 550–560.
- 115 P. Guo and M. Liu, *Langmuir*, 2005, **21**, 3410–3412.

- 116 M. A. Nanny, J. M. Bortiatynski and P. G. Hatcher, *Environ. Sci. Technol.*, 1997, **31**, 530–534.
- 117 M. H. Abraham, R. J. Abraham, J. Byrne and L. Griffiths, *J. Org. Chem.*, 2006, **71**, 3389–3394.
- 118 G. A. Kumar and M. A. McAllister, *J. Org. Chem.*, 1998, **63**, 6968–6972.
- 119 J. E. Del Bene, S. A. Perera and R. J. Bartlett, *J. Phys. Chem. A*, 1999, **103**, 8121–8124.
- 120 H. Sun, Y. Zhao, Z. Huang, Y. Wang and F. Li, *J. Phys. Chem. A*, 2008, **112**, 11382–11390.
- 121 P. Thordarson, *Chem. Soc. Rev.*, 2011, **40**, 1305–1323.
- 122 L. K. S. von Krbek, C. A. Schalley and P. Thordarson, *Chem. Soc. Rev.*, 2017, **46**, 2622–2637.
- 123 R. B. Martin, *Chem. Rev.*, 1996, **96**, 3043–3064.
- 124 N. S. Morris, D. J. Stickler and R. J. McLean, *World J. Urol.*, 1999, **17**, 345–350.
- 125 Y. Shrot and L. Frydman, *J. Magn. Reson.*, 2008, **195**, 226–231.
- 126 J. T. Edward, *J. Chem. Educ.*, 1970, **47**, 261.
- 127 Y. H. A. Hussein and M. Youssry, *Materials (Basel)*, 2018, **11**, 688.
- 128 T. Tadros, *Encyclopedia of Colloid and Interface Science.*, Springer, 2013.
- 129 R. J. Williams, J. N. Phillips and K. J. Mysels, *Trans. Faraday Soc.*, 1955, **51**, 728–737.
- 130 D. E. Kile and C. T. Chiou, *Environ. Sci. Technol.*, 1989, **23**, 832–838.
- 131 N. Anoune, M. Nouiri, Y. Berrah, J. Gauvrit and P. Lanteri, *J. Surfactants Deterg.*, 2002, **5**, 45–53.
- 132 E. Tomaszewska, K. Soliwoda, K. Kadziola, B. Tkacz-Szczesna, G. Celichowski, M.

- Cichomski, W. Szmaja and J. Grobelny, *J. Nanomater.*, 2013, **2013**, 313081.
- 133 W. I. Goldberg, *Am. J. Phys.*, 1999, **67**, 1152–1160.
- 134 S. Bhattacharjee, *J. Control. Release*, 2016.
- 135 M. Kaszuba, J. Corbett, F. M. Watson and A. Jones, *Philos. Trans. R. Soc. A Math. Phys. Eng. Sci.*, 2010, **368**, 4439–4451.
- 136 V. R. Patel and Y. K. Agrawal, *J. Adv. Pharm. Technol. Res.*, 2011, **2**, 81.
- 137 M. Schaefer and C. Froemmel, *J. Mol. Biol.*, 1990, **216**, 1045–1066.
- 138 P. S. Stewart and J. W. Costerton, *Lancet*, 2001.
- 139 L. A. Estroff and A. D. Hamilton, *Chem. Rev.*, 2004, **104**, 1201–1218.
- 140 N. M. Sangeetha and U. Maitra, *Chem. Soc. Rev.*, 2005, **34**, 821–836.
- 141 Y. Osada, K. Kajiwara and H. Ishida, *Gels handbook*, Elsevier, 2001.
- 142 Z. Brezinger, *Physiol. Chem.*, 1892, **16**, 537.
- 143 R. A. Gortner and W. F. Hoffman, *J. Am. Chem. Soc.*, 1921, **43**, 2199–2202.
- 144 F. M. Menger and K. S. Venkatasubban, *J. Org. Chem.*, 1978, **43**, 3413–3414.
- 145 F. M. Menger, Y. Yamasaki, K. K. Catlin and T. Nishimi, *Angew. Chemie Int. Ed. English*, 1995, **34**, 585–586.
- 146 X. Du, J. Zhou, J. Shi and B. Xu, *Chem. Rev.*, 2015, **115**, 13165–13307.
- 147 Z. Yang and B. Xu, *Adv. Mater.*, 2006, **18**, 3043–3046.
- 148 J. W. Steed, *Chem. Commun.*, 2011, **47**, 1379–1383.
- 149 A. Vintiloiu and J.-C. Leroux, *J. Control. release*, 2008, **125**, 179–192.
- 150 P. Terech and R. G. Weiss, *Chem. Rev.*, 1997, **97**, 3133–3160.

- 151 E. M. Ahmed, *J. Adv. Res.*, 2015, **6**, 105–121.
- 152 L. E. Buerkle and S. J. Rowan, *Chem. Soc. Rev.*, 2012, **41**, 6089–6102.
- 153 C. D. Jones and J. W. Steed, *Chem. Soc. Rev.*, 2016, **45**, 6546–6596.
- 154 J. F. Miravet and B. Escuder, *Chem. Commun.*, 2005, 5796–5798.
- 155 V. J. Nebot, J. Armengol, J. Smets, S. F. Prieto, B. Escuder and J. F. Miravet, *Chem. Eur. J.*, 2012, **18**, 4063–4072.
- 156 E. K. Johnson, D. J. Adams and P. J. Cameron, *J. Mater. Chem.*, 2011, **21**, 2024–2027.
- 157 A. Ghosh and J. Dey, *Langmuir*, 2009, **25**, 8466–8472.
- 158 M. De Loos, B. L. Feringa and J. H. van Esch, *European J. Org. Chem.*, 2005, **2005**, 3615–3631.
- 159 J. Zhang, Y. Hu and Y. Li, *Gel Chemistry: Interactions, Structures and Properties*, Springer, 2018, vol. 96.
- 160 M. C. Hacker and A. G. Mikos, *Princ. Regen. Med. 2nd ed.; Atala, A., Lanza, R., Thomson, J., Nerem, RM, Eds*, 2011, 587–622.
- 161 D. Ronis, E. Martina and J. M. Deutch, *Chem. Phys. Lett.*, 1977, **46**, 53–55.
- 162 G. O. Lloyd and J. W. Steed, *Nat. Chem.*, 2009, **1**, 437–442.
- 163 J. W. Steed, *Chem. Soc. Rev.*, 2010, **39**, 3686.
- 164 L. Meazza, J. A. Foster, K. Fucke, P. Metrangolo, G. Resnati and J. W. Steed, *Nat. Chem.*, 2013, **5**, 42–47.
- 165 K. Pandurangan, J. A. Kitchen, S. Blasco, F. Paradisi and T. Gunnlaugsson, *Chem. Commun.*, 2014, **50**, 10819–10822.
- 166 L. J. White, C. Wark, L. Croucher, E. R. Draper and J. R. Hiscock, *Chem. Commun.*, 2020, **56**, 9557–9560.

- 167 H. Lambers, S. Piessens, A. Bloem, H. Pronk and P. Finkel, *Int. J. Cosmet. Sci.*, 2006, **28**, 359–370.
- 168 L. S. Birchall, S. Roy, V. Jayawarna, M. Hughes, E. Irvine, G. T. Okorogheye, N. Saudi, E. De Santis, T. Tuttle, A. A. Edwards and R. V. Ulijn, *Chem. Sci.*, 2011, **2**, 1349.
- 169 *Antimicrobial Resistance: Tackling a Crisis for the Health and Wealth of Nations: December 2014*, Review on Antimicrobial Resistance, 2014.
- 170 D. J. Payne, M. N. Gwynn, D. J. Holmes and D. L. Pompliano, *Nat. Rev. Drug Discov.*, 2007, **6**, 29–40.
- 171 E. D. Brown and G. D. Wright, *Nature*, 2016, **529**, 336–343.
- 172 C. L. Ventola, *Pharm. Ther.*, 2015, **40**, 277.
- 173 I. Wiegand, K. Hilpert and R. E. W. Hancock, *Nat. Protoc.*, 2008, **3**, 163.
- 174 I. T. Alt, C. Guttroff and B. Plietker, *Angew. Chemie Int. Ed.*, 2017, **56**, 10582–10586.

## 9. Appendix

### 9.1. Tables of data

Table S1 – Overview of gaseous and solution state studies observed for compounds **19** – **24**.

Compound	Gas Phase Dimer	$K_{dim}$ ( $M^{-1}$ )	Size (nm) (5.56 mM)	Zeta potential (mV)	CMC (mM)	Surface tension ( $mN m^{-1}$ )
<b>19</b> <sup>86</sup>	Y	2.70	122	-101	0.50	46.05
<b>20</b>	Y	$-4.13 \times 10^{-2}$	174	-13.77	<i>c</i>	<i>c</i>
<b>21</b>	Y	1.21	127	-24.03	<i>c</i>	<i>c</i>
<b>22</b>	Y	0.09	127	-42.71	32.12	44.88
<b>23</b>	Y	<i>a</i>	215	-67.13	5.16	66.97
<b>24</b>	Y	<i>b</i>	<i>b</i>	<i>b</i>	<i>b</i>	<i>b</i>

*a* – Multiple association events prevent data fitting.

*b* – No self-association occurs.

*c* – Could not be calculated due to compound solubility.

Table S2 – Overview of the results from quantitative <sup>1</sup>H NMR studies. Values given in % represent the observed proportion of compound that became NMR silent.

Compound	DMSO- <i>d</i> <sub>6</sub> 1% DCM (%)		D <sub>2</sub> O 5 % EtOH (%)	
	Anionic component	Cationic component	Anionic component	Cationic component
<b>20</b>	0	0	31	32
<b>21</b>	0	0	44	39
<b>22</b>	0	0	62	<i>a</i>
<b>23</b>	22	20	55	51

*a* – Could not be calculated due to overlapping peaks.

Table S3 – Overview of the calculated  $E_{max}$ ,  $E_{min}$  and  $\log P$ , values using semi empirical PMS modelling methods of the anionic components of compounds **20** – **23**.

Compound	$E_{max}$ ( $kJ mol^{-1}$ )	$E_{min}$ ( $kJ mol^{-1}$ )	$\log P$
<b>20</b>	-721.417	-88.0876	1.05
<b>21</b>	-768.478	12.0290	1.51
<b>22</b>	-717.433	-48.5147	0.86
<b>23</b>	-706.202	-38.2374	1.86

## 9.2. NMR

### 9.2.1. Characterisation NMR

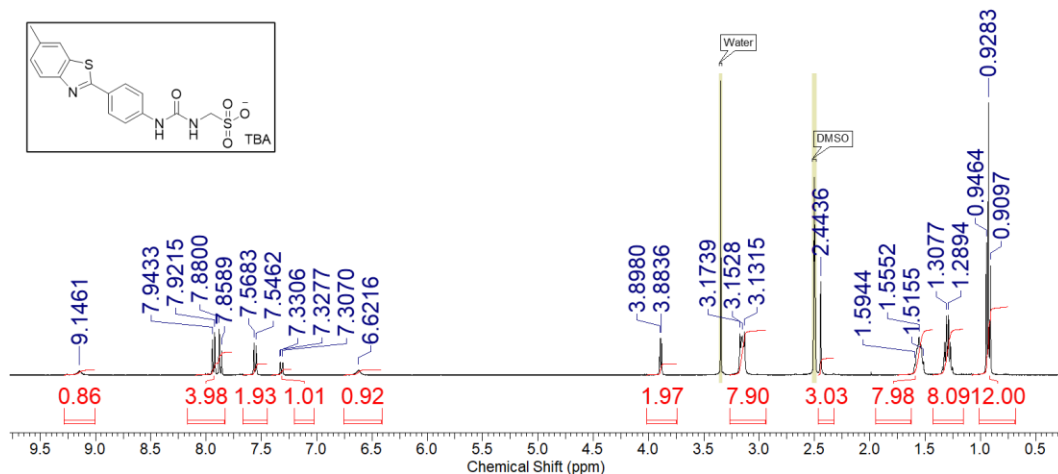


Figure S1 - <sup>1</sup>H NMR of compound **19** in DMSO-*d*<sub>6</sub> conducted at 298 K.

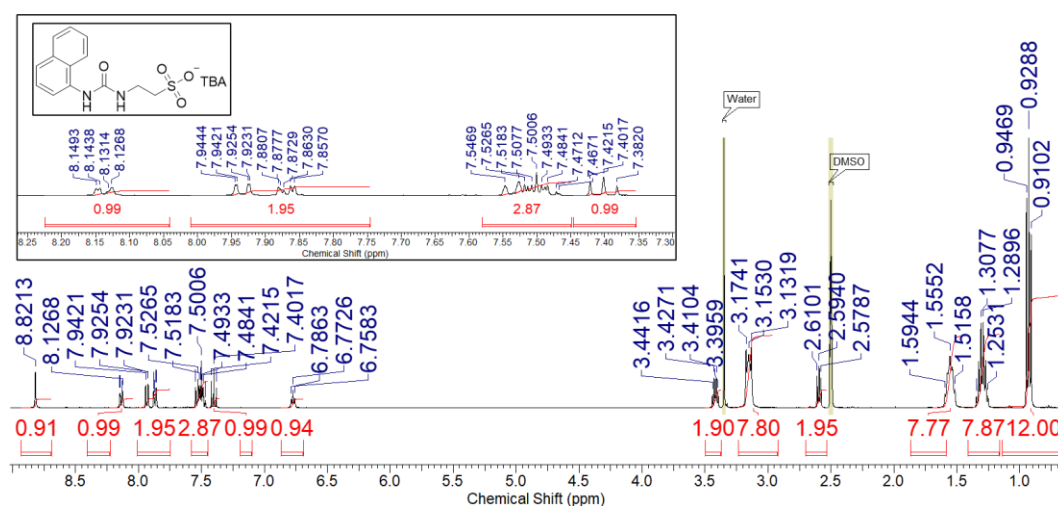


Figure S2 - <sup>1</sup>H NMR of compound **20** in DMSO-*d*<sub>6</sub> conducted at 298 K.

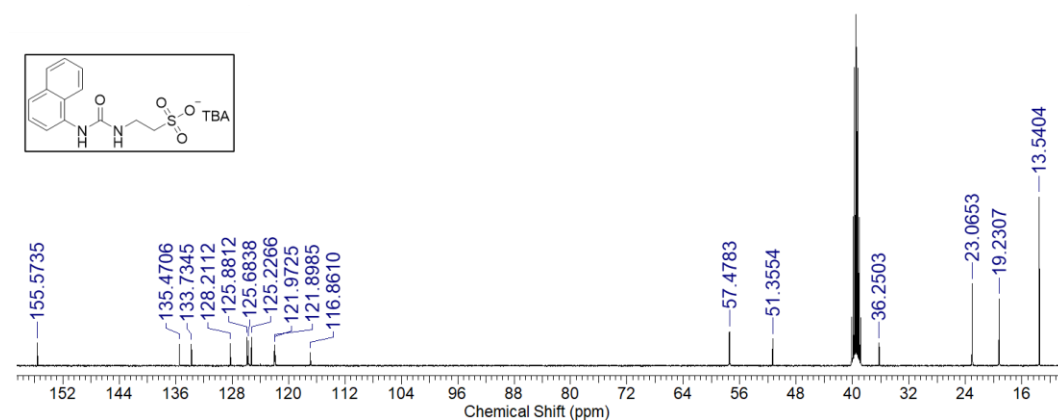


Figure S3 - <sup>13</sup>C NMR of compound **20** in DMSO-*d*<sub>6</sub> conducted at 298 K.

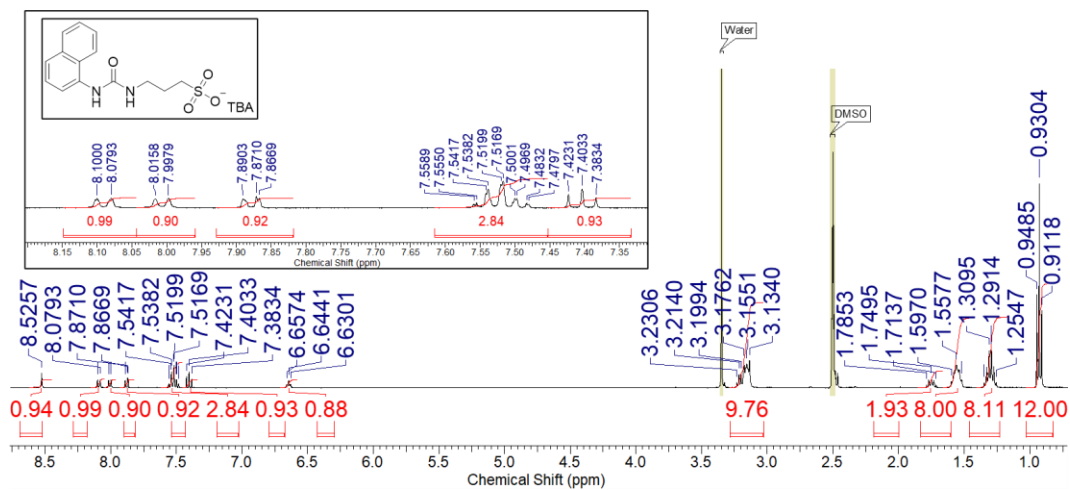


Figure S4 -  $^1\text{H}$  NMR of compound **21** in  $\text{DMSO-}d_6$  conducted at 298 K.

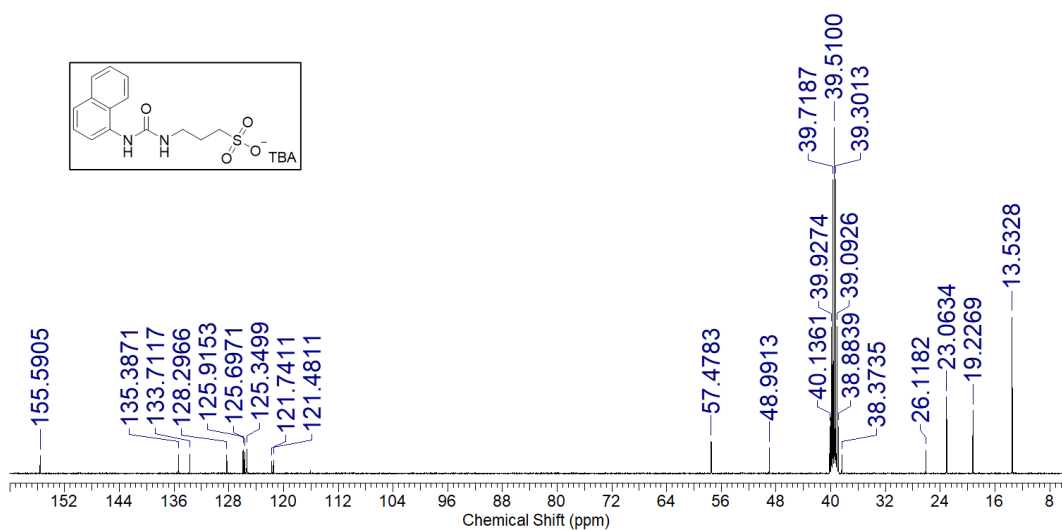


Figure S5 -  $^{13}\text{C}$  NMR of compound **21** in  $\text{DMSO-}d_6$  conducted at 298 K.

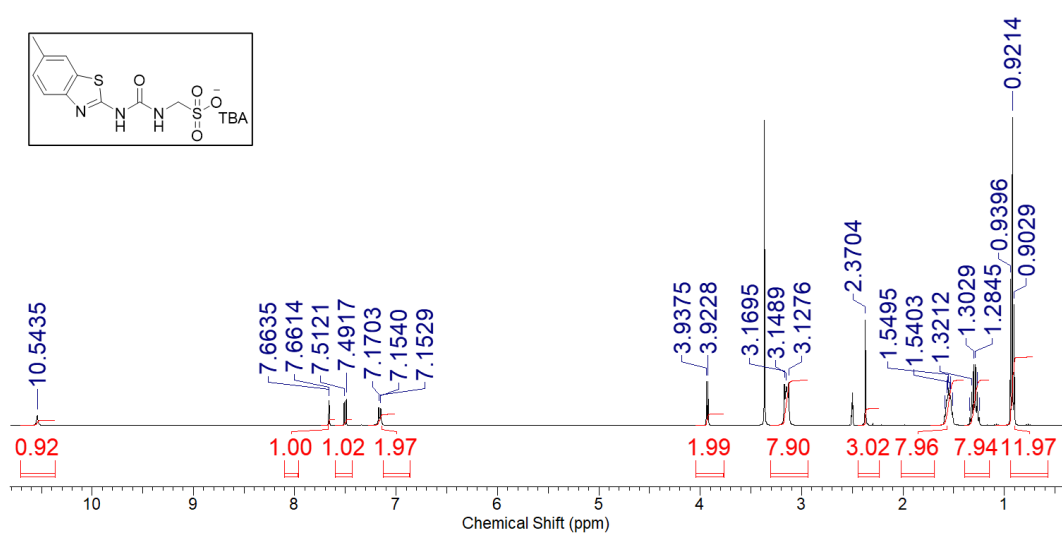


Figure S6 -  $^1\text{H}$  NMR of compound **22** in  $\text{DMSO-}d_6$  conducted at 298 K.

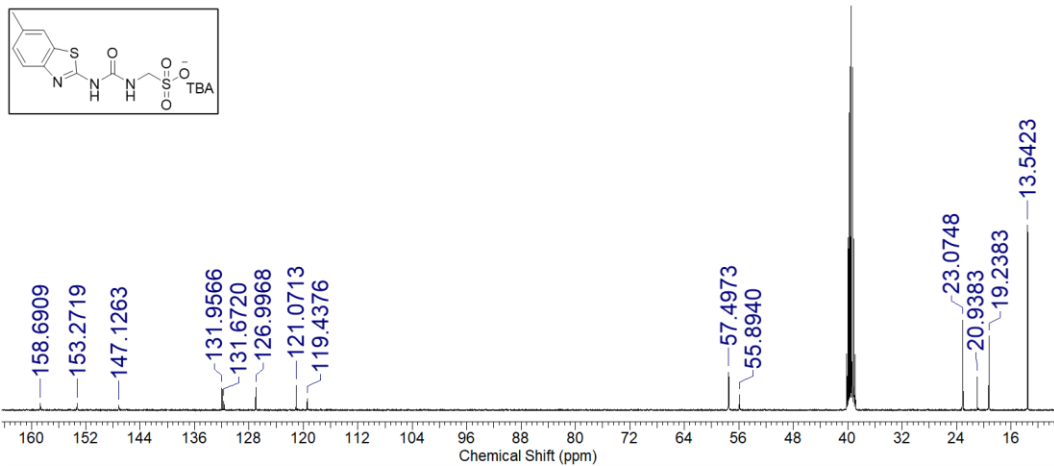


Figure S7 - <sup>13</sup>C NMR of compound **22** in DMSO-*d*<sub>6</sub> conducted at 298 K.

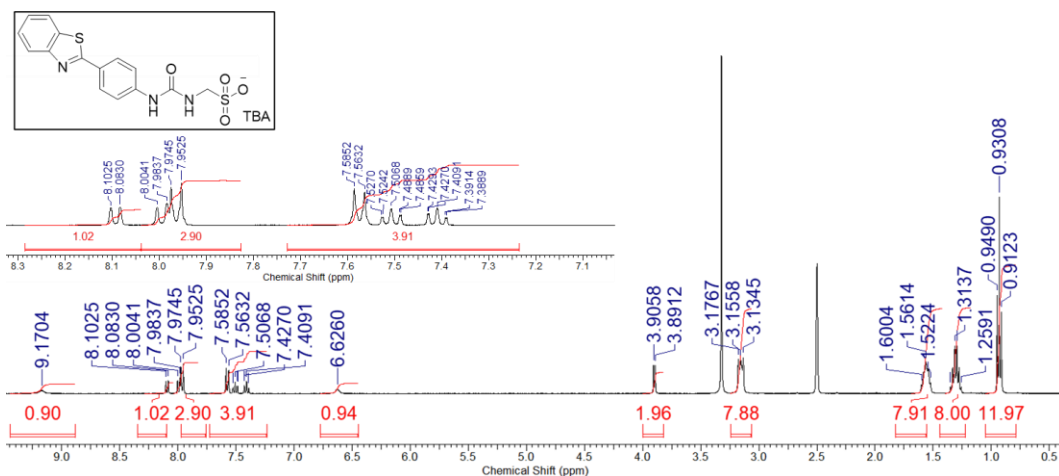


Figure S8 - <sup>1</sup>H NMR of compound **23** in DMSO-*d*<sub>6</sub> conducted at 298 K.

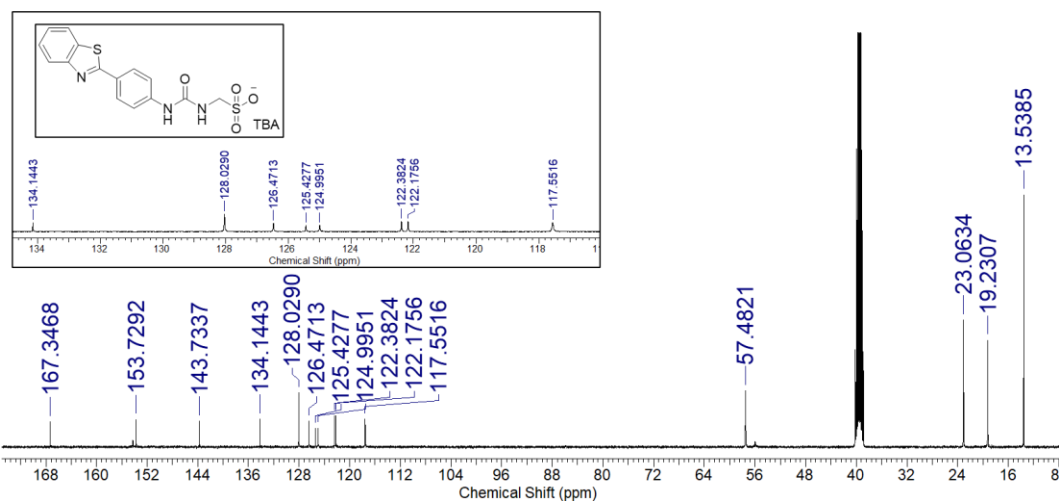


Figure S9 - <sup>13</sup>C NMR of compound **23** in DMSO-*d*<sub>6</sub> conducted at 298 K.

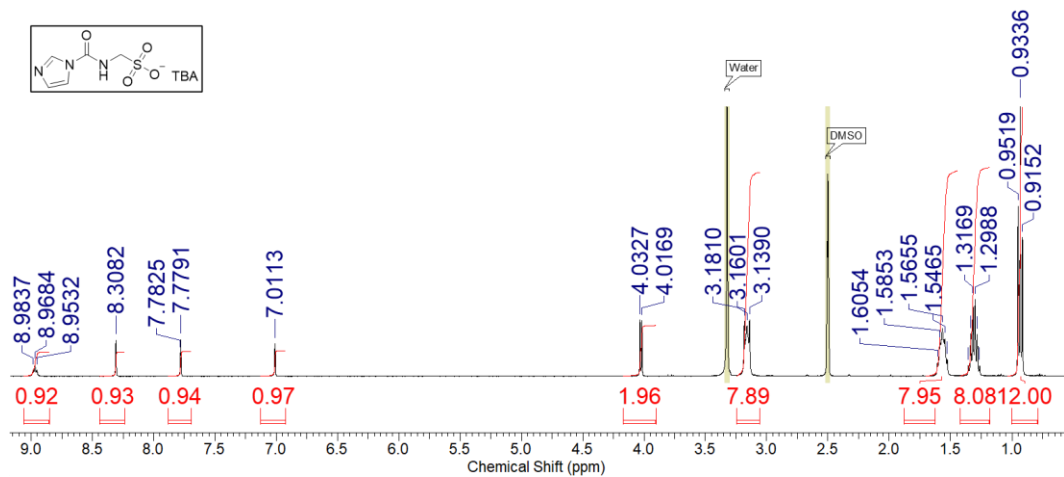


Figure S10 - <sup>1</sup>H NMR of compound **24** in DMSO-*d*<sub>6</sub> conducted at 298 K.

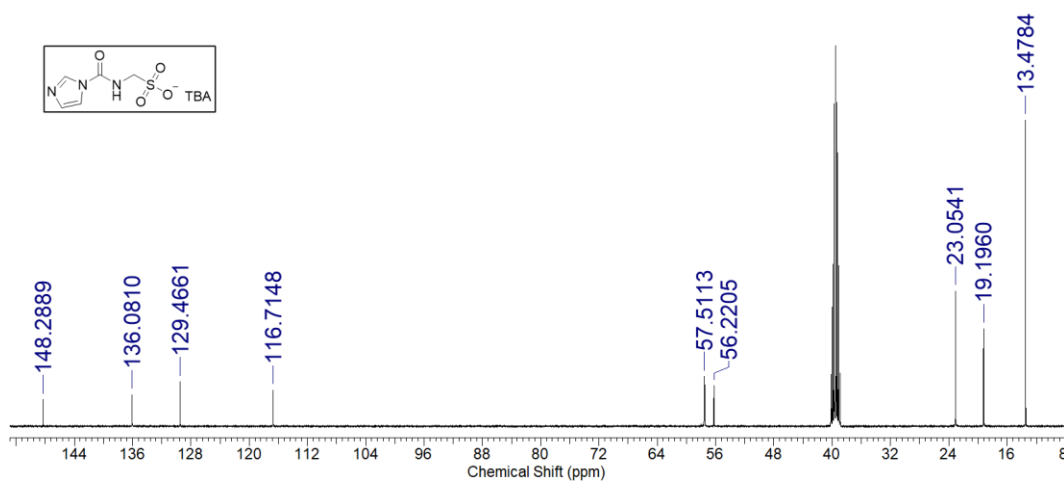


Figure S11 - <sup>13</sup>C NMR of compound **24** in DMSO-*d*<sub>6</sub> conducted at 298 K.

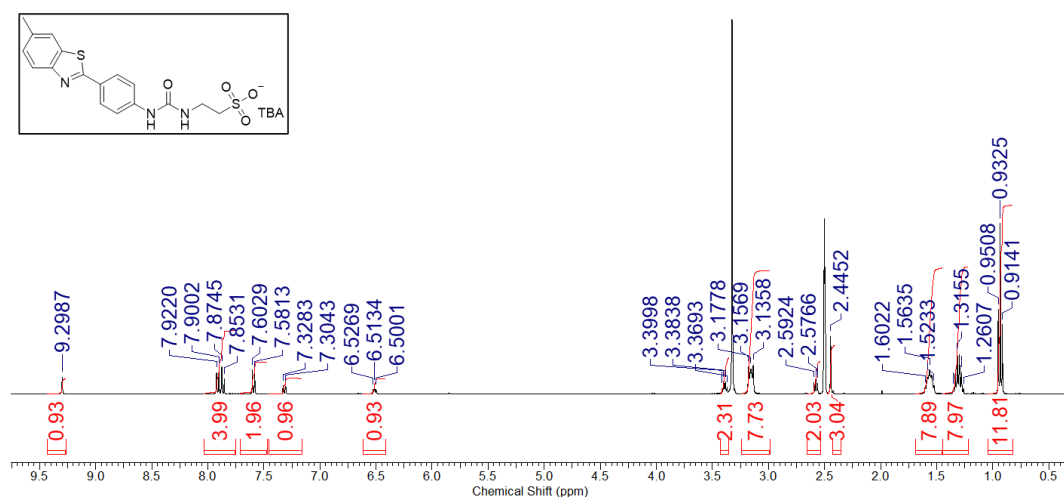


Figure S12 - <sup>1</sup>H NMR of compound **25** in DMSO-*d*<sub>6</sub> conducted at 298 K.

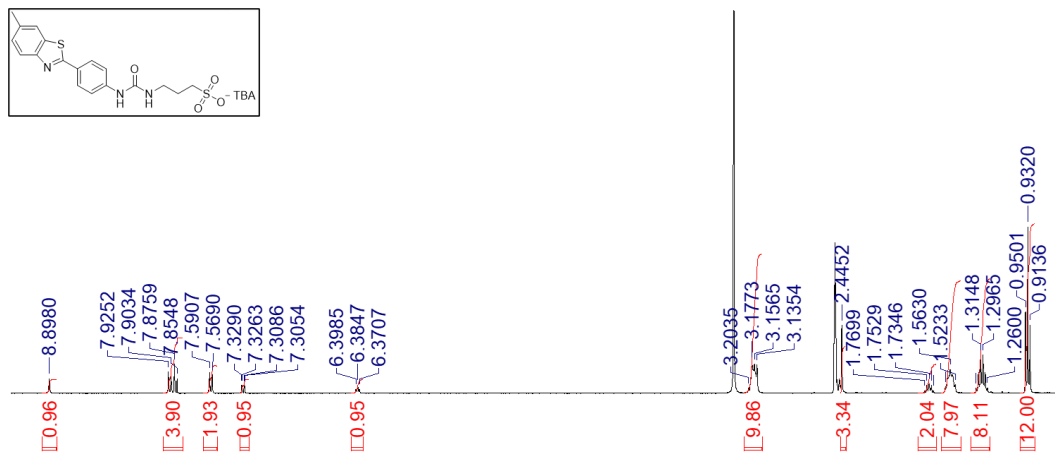


Figure S13 -  $^1\text{H}$  NMR of compound **26** in  $\text{DMSO}-d_6$  conducted at 298 K.

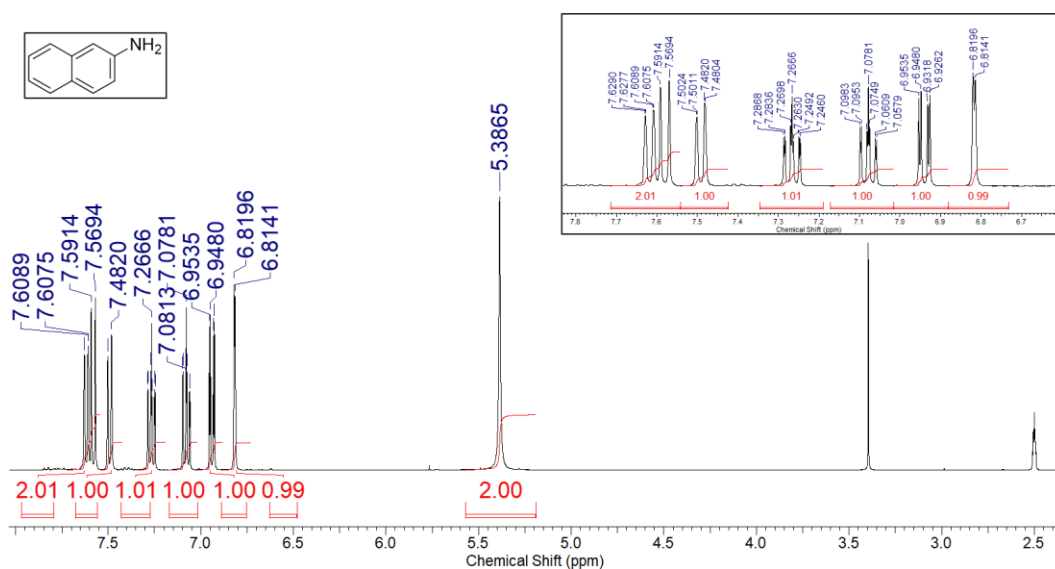


Figure S14 -  $^1\text{H}$  NMR of compound **27** in  $\text{DMSO}-d_6$  conducted at 298 K.

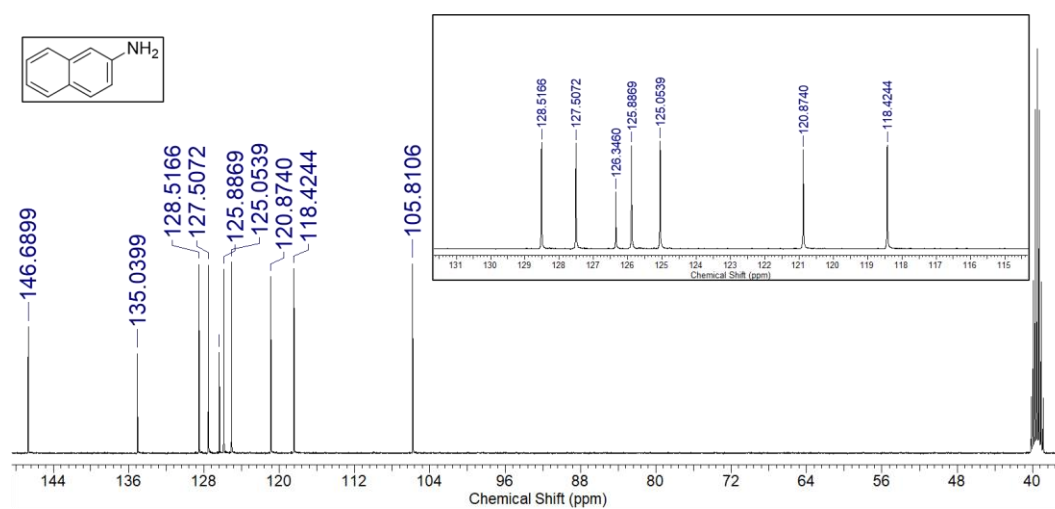


Figure S15 -  $^{13}\text{C}$  NMR of compound **27** in  $\text{DMSO}-d_6$  conducted at 298 K.

## 9.2.2. qNMR experiments

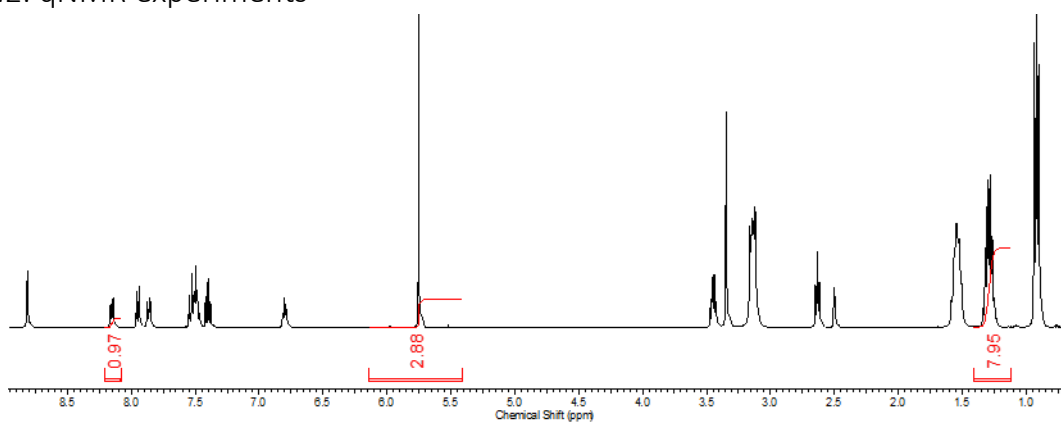


Figure S16 - <sup>1</sup>H NMR spectrum ( $d_1 = 60$  s) of compound **20** (112 mM) in DMSO- $d_6$ /1.0 % DCM. Comparative integration indicates 0 % of the anionic component of **20** has become NMR silent.

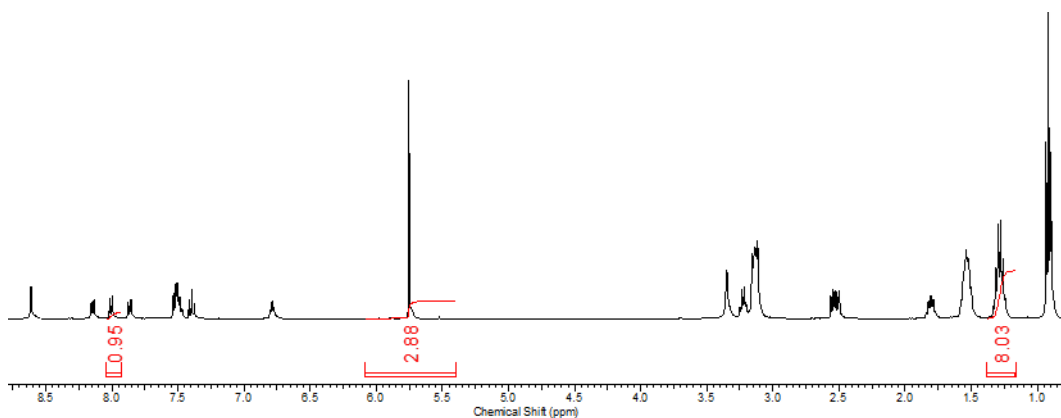


Figure S17 - <sup>1</sup>H NMR spectrum ( $d_1 = 60$  s) of compound **21** (112 mM) in DMSO- $d_6$ /1.0 % DCM. Comparative integration indicates 0 % of the anionic and cationic component of **21** has become NMR silent.

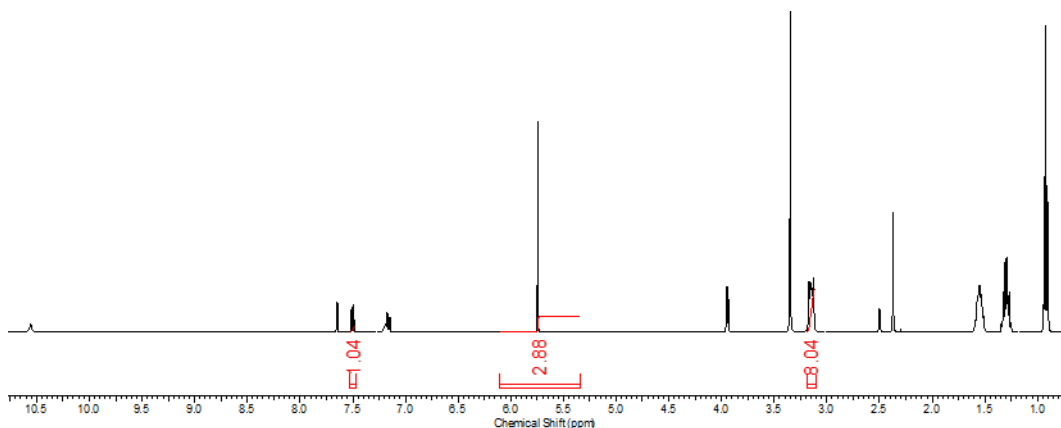


Figure S18 - <sup>1</sup>H NMR spectrum ( $d_1 = 60$  s) of compound **22** (112 mM) in DMSO- $d_6$ /1.0 % DCM. Comparative integration indicates 0 % of the anionic and cationic component of **22** has become NMR silent.

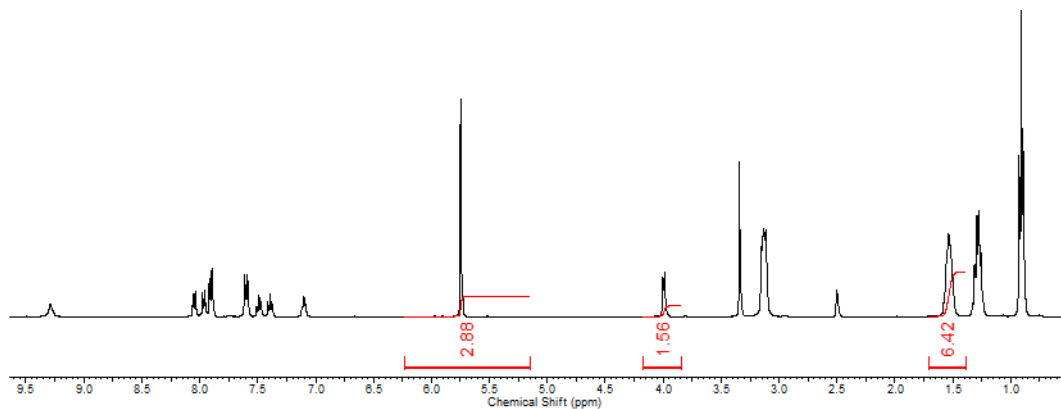


Figure S19 -  $^1\text{H}$  NMR spectrum ( $d_1 = 60$  s) of compound **23** (112 mM) in  $\text{DMSO-}d_6/1.0\%$  DCM. Comparative integration indicates 23 % of the anionic component of **23** has become NMR silent.

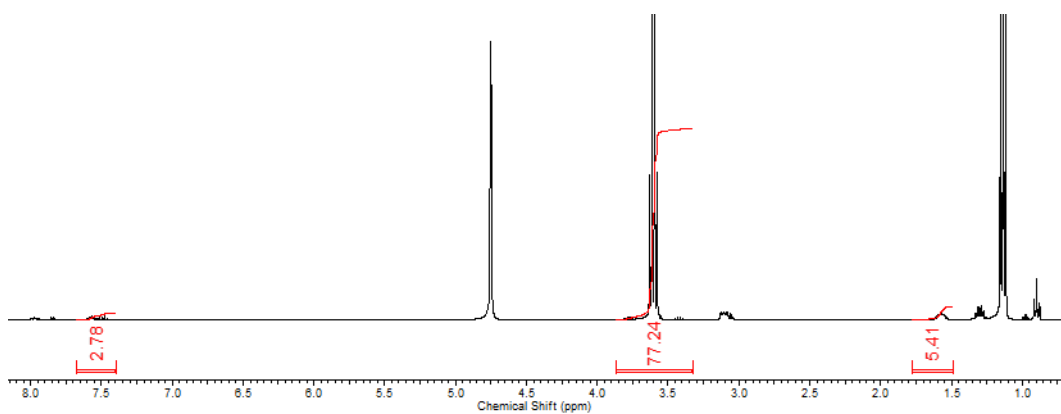


Figure S20 -  $^1\text{H}$  NMR spectrum ( $d_1 = 60$  s) of compound **20** (5.56 mM) in  $\text{D}_2\text{O}/5.0\%$  EtOH. Comparative integration indicates 23 % of the anionic component of **20** has become NMR silent.

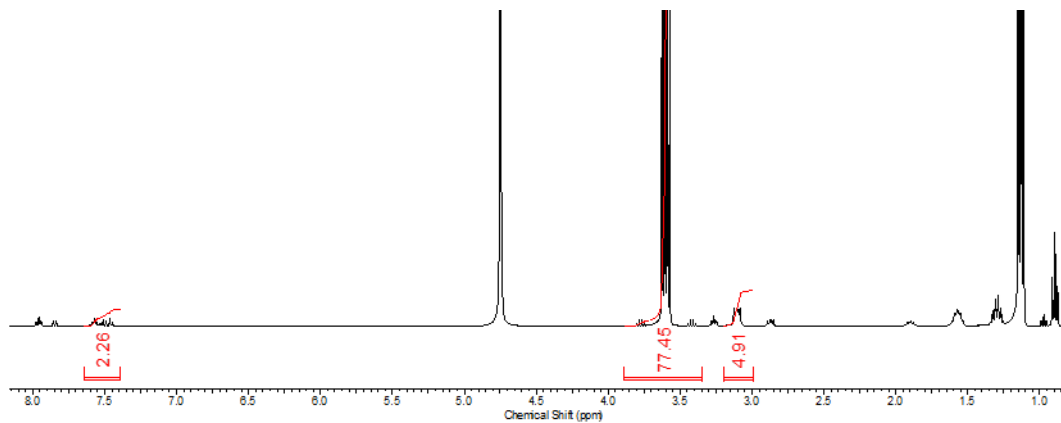


Figure S21 –  $^1\text{H}$  NMR spectrum ( $d_1 = 60$  s) of compound **21** (5.56 mM) in  $\text{D}_2\text{O}/5.0\%$  EtOH. Comparative integration indicates 44 % of the anionic component and 39 % of the cationic component of **21** has become NMR silent.

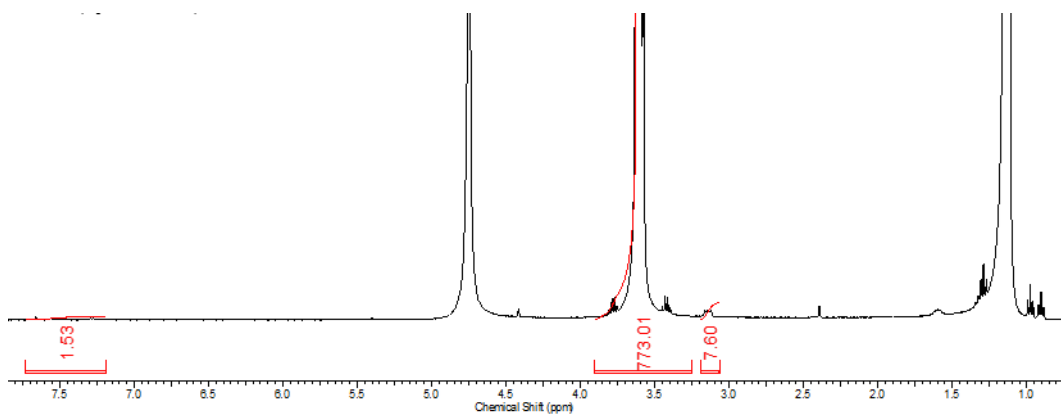


Figure S22 -  $^1\text{H}$  NMR spectrum ( $d_1 = 60$  s) of compound **22** (0.56 mM) in  $\text{D}_2\text{O}/5.0\%$  EtOH. Comparative integration indicates 62 % of the anionic component and 0.1 % of the cationic component of **22** has become NMR silent.

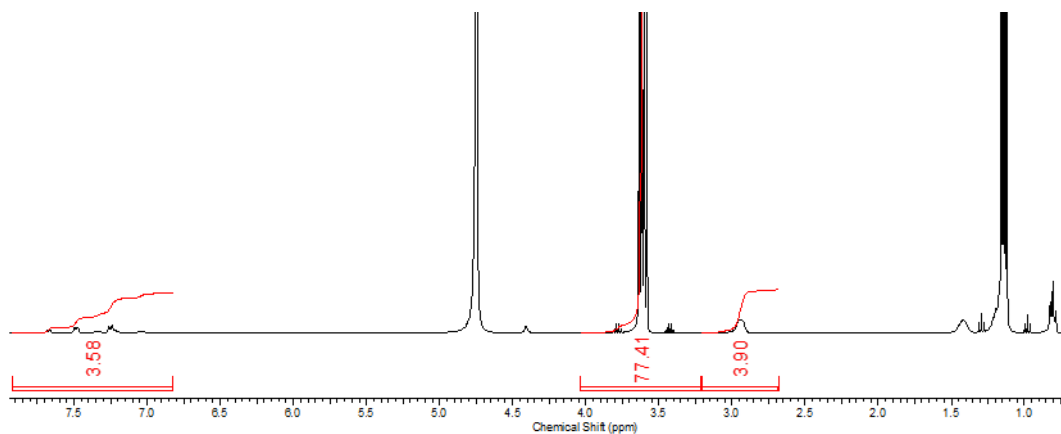


Figure S23 -  $^1\text{H}$  NMR spectrum ( $d_1 = 60$  s) of compound **23** (5.56 mM) in  $\text{D}_2\text{O}/5.0\%$  EtOH. Comparative integration indicates 55 % of the anionic component and 51 % of the cationic component of **23** has become NMR silent.

### 9.2.3. $^1\text{H}$ NMR Self-Association Studies

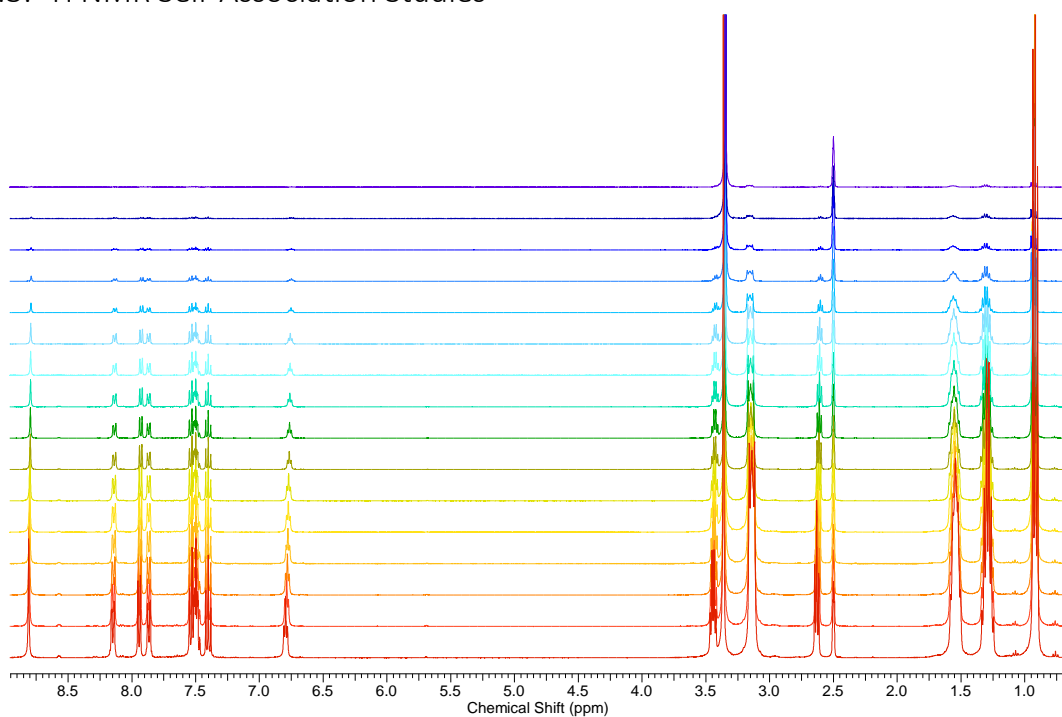


Figure S24 -  $^1\text{H}$  NMR stack plot of compound **20** in a  $\text{DMSO-}d_6$  0.5 %  $\text{H}_2\text{O}$  solution. Samples were prepared in series with an aliquot of the most concentrated solution undergoing serial dilution.

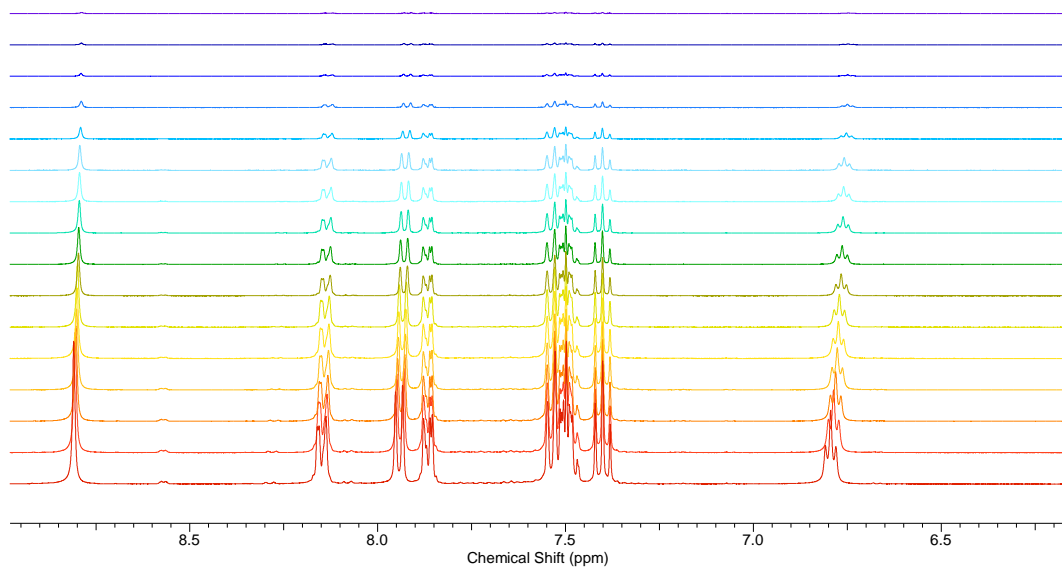


Figure S25 - Enlarged  $^1\text{H}$  NMR stack plot of compound **20** in a  $\text{DMSO-}d_6$  0.5 %  $\text{H}_2\text{O}$  solution. Samples were prepared in series with an aliquot of the most concentrated solution undergoing serial dilution.

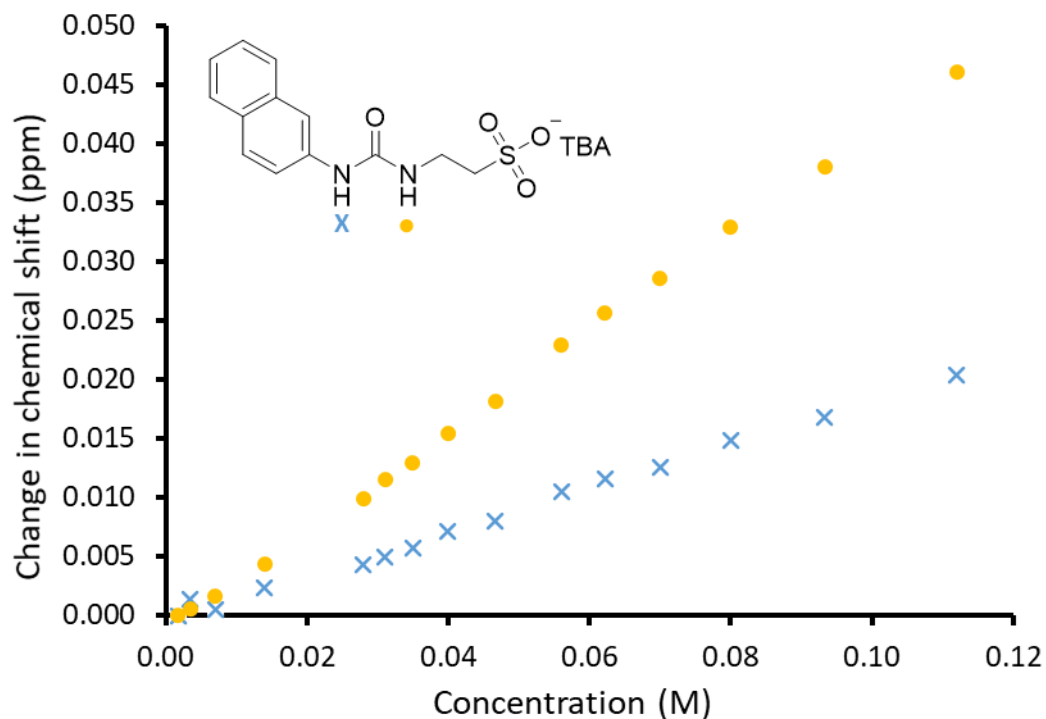


Figure S26 – Graph illustrating the  $^1\text{H}$  NMR down-field change in chemical shift of urea NH resonances with increasing concentrations of compound **20** in  $\text{DMSO-}d_6$  0.5 %  $\text{H}_2\text{O}$  solution (298 K).

#### Self-association constant calculation

Compound **20** – Dilution study in  $\text{DMSO-}d_6$  0.5 %  $\text{H}_2\text{O}$ . Values calculated from data gathered from both NH 1 and 2.

*Equal K/Dimerisation model*

$$K_e = -0.08\text{M}^{-1} \pm -0.8800 \%$$

$$K_{\text{dim}} = -4.13 \times 10^{-2} \pm -0.4400 \%$$

<http://app.supramolecular.org/bindfit/view/67f89666-60a4-42c5-a43f-2eb9329f40be>

*CoEK model*

$$K_e = 7.32 \text{ M}^{-1} \pm 2.5630 \%$$

$$K_{\text{dim}} = 3.66 \text{ M}^{-1} \pm 1.2815 \%$$

$$\rho = 0.26 \pm 6.2493 \%$$

<http://app.supramolecular.org/bindfit/view/86c2fbb3-67b5-478e-87c7-3c1112dc5f22>

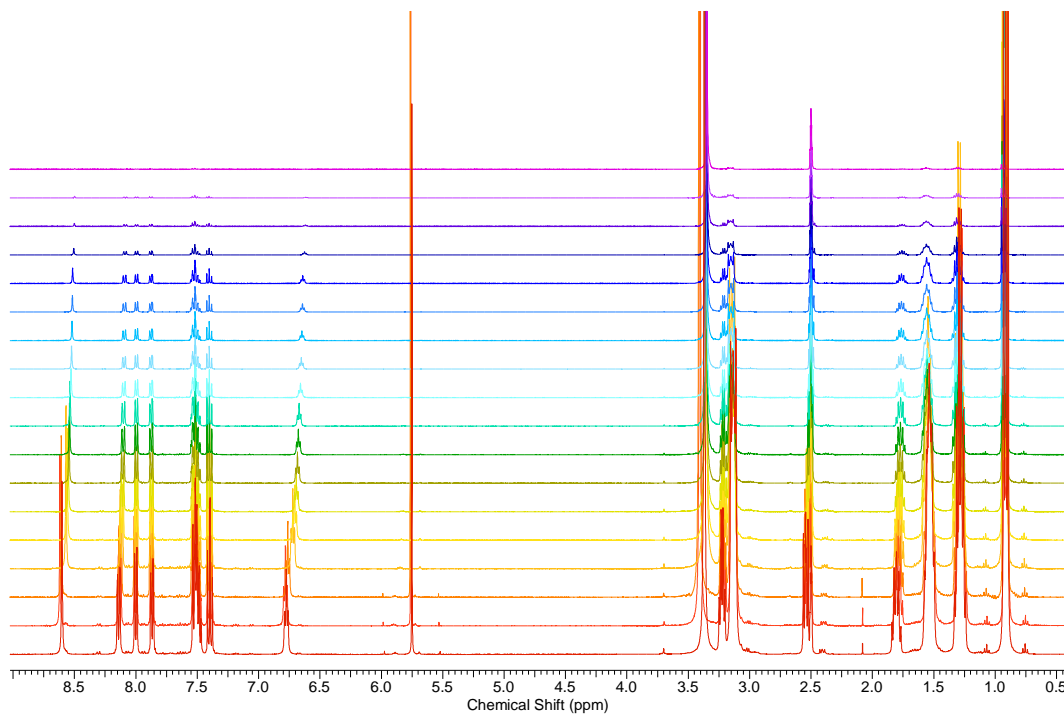


Figure S27 -  $^1\text{H}$  NMR stack plot of compound **21** in a  $\text{DMSO-}d_6$  0.5 %  $\text{H}_2\text{O}$  solution. Samples were prepared in series with an aliquot of the most concentrated solution undergoing serial dilution.

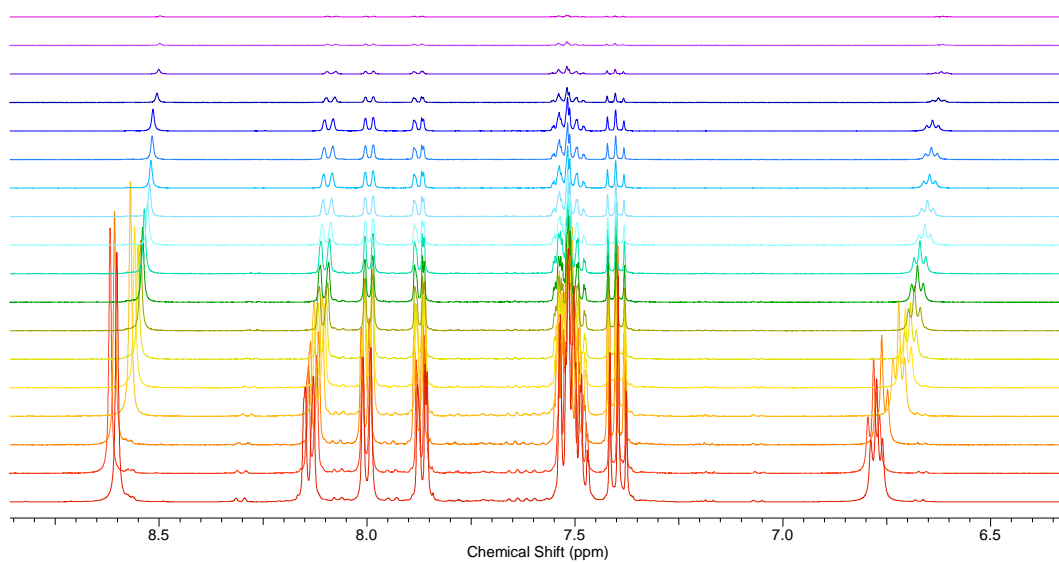


Figure S28 - Enlarged  $^1\text{H}$  NMR stack plot of compound **21** in a  $\text{DMSO-}d_6$  0.5 %  $\text{H}_2\text{O}$  solution. Samples were prepared in series with an aliquot of the most concentrated solution undergoing serial dilution.

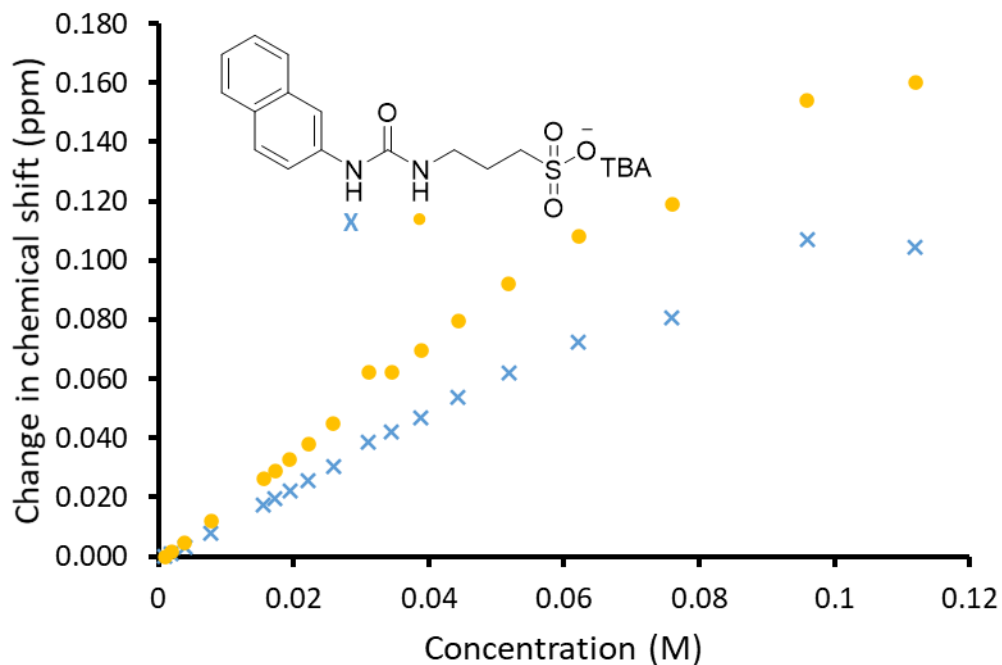


Figure S29 - Graph illustrating the  $^1\text{H}$  NMR down-field change in chemical shift of urea NH resonances with increasing concentrations of compound **21** in  $\text{DMSO-}d_6$  0.5 %  $\text{H}_2\text{O}$  solution (298 K).

#### Self-association constant calculation

Compound **21** – Dilution study in  $\text{DMSO-}d_6$  0.5 %  $\text{H}_2\text{O}$ . Values calculated from data gathered from both NH 1 and 2.

*Equal K/Dimerisation mode*

$$K_e = 2.43 \text{ M}^{-1} \pm 2.0432 \%$$

$$K_{\text{dim}} = 1.21 \text{ M}^{-1} \pm 1.0216 \%$$

<http://app.supramolecular.org/bindfit/view/5a70f25f-8a90-483e-96a2-47f3b012057a>

*CoEK model*

$$K_e = 13.2 \text{ M}^{-1} \pm 3.8595 \%$$

$$K_{\text{dim}} = 6.60 \text{ M}^{-1} \pm 1.9297 \%$$

$$\rho = 0.32 \pm 11.2191 \%$$

<http://app.supramolecular.org/bindfit/view/9529e72c-bdfa-4195-b09b-74c4153dac19>

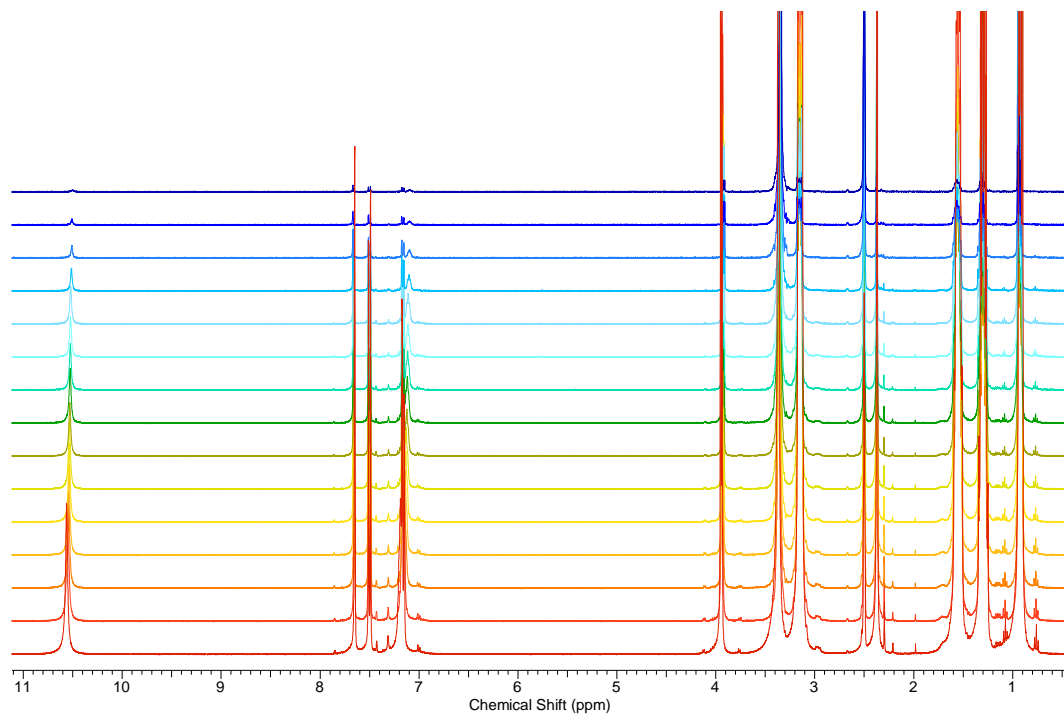


Figure S30 -  $^1\text{H}$  NMR stack plot of compound **22** in a  $\text{DMSO-}d_6$  0.5 %  $\text{H}_2\text{O}$  solution. Samples were prepared in series with an aliquot of the most concentrated solution undergoing serial dilution.

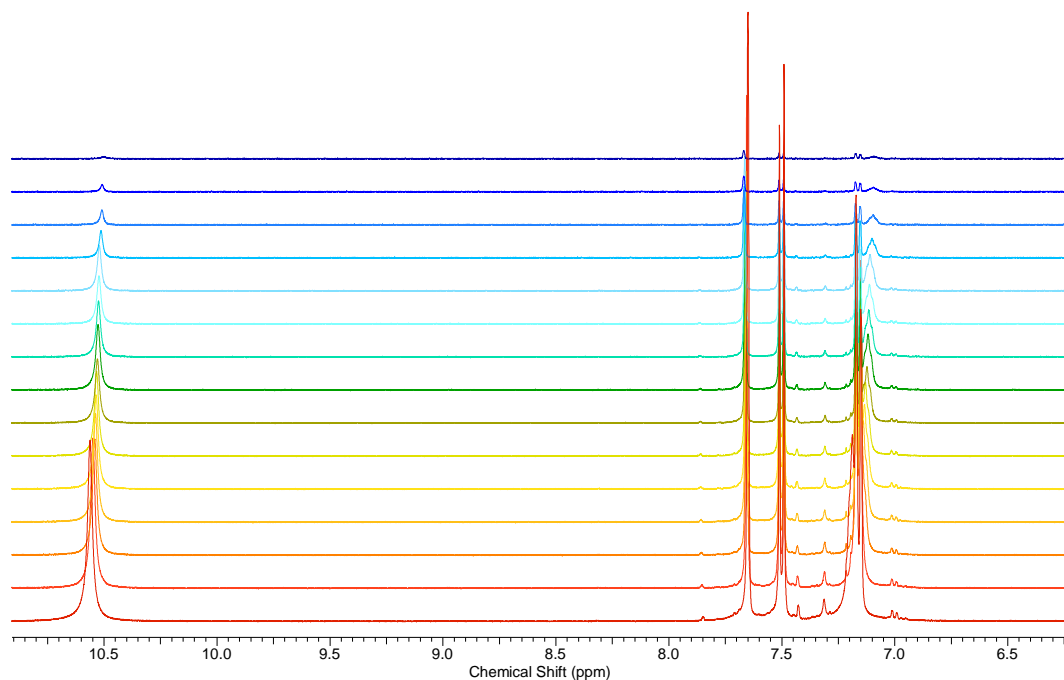


Figure S31 – Enlarged  $^1\text{H}$  NMR stack plot of compound **22** in a  $\text{DMSO-}d_6$  0.5 %  $\text{H}_2\text{O}$  solution. Samples were prepared in series with an aliquot of the most concentrated solution undergoing serial dilution.

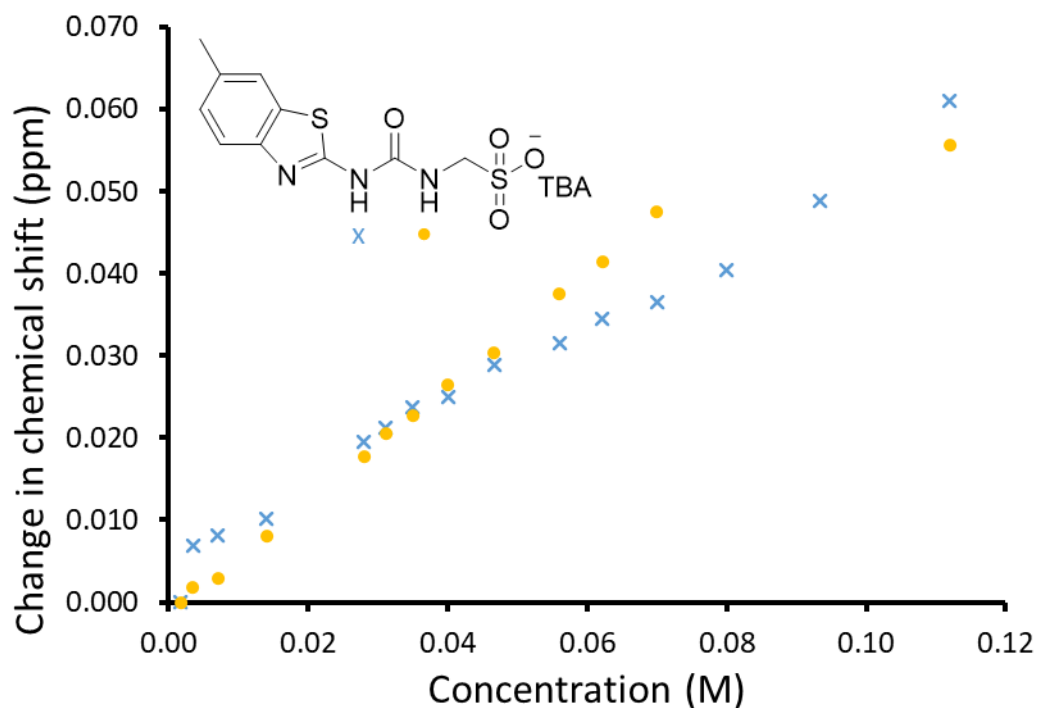


Figure S32 - Graph illustrating the  $^1\text{H}$  NMR down-field change in chemical shift of urea NH resonances with increasing concentrations of compound **22** in  $\text{DMSO-}d_6$  0.5 %  $\text{H}_2\text{O}$  solution (298K).

#### Self-association constant calculation

Compound **22** – Dilution study in  $\text{DMSO-}d_6$  0.5 %  $\text{H}_2\text{O}$ . Values calculated from data gathered from both NH 1 and 2.

*Equal K/Dimerisation mode*

$$K_e = 0.18 \text{ M}^{-1} \pm 3.7764 \%$$

$$K_{\text{dim}} = 0.09 \text{ M}^{-1} \pm 1.8882 \%$$

<http://app.supramolecular.org/bindfit/view/6a664418-0fe3-40cb-8e35-ab26dbb81505>

*CoEK model*

$$K_e = -0.68 \text{ M}^{-1} \pm -17.2912 \%$$

$$K_{\text{dim}} = -0.34 \text{ M}^{-1} \pm -8.6456 \%$$

$$\rho = -212.19 \pm -14.8621 \%$$

<http://app.supramolecular.org/bindfit/view/493a2d8b-c6a2-4320-b45d-e4c75330c974>

#### 9.2.4. $^1\text{H}$ DOSY NMR experiments

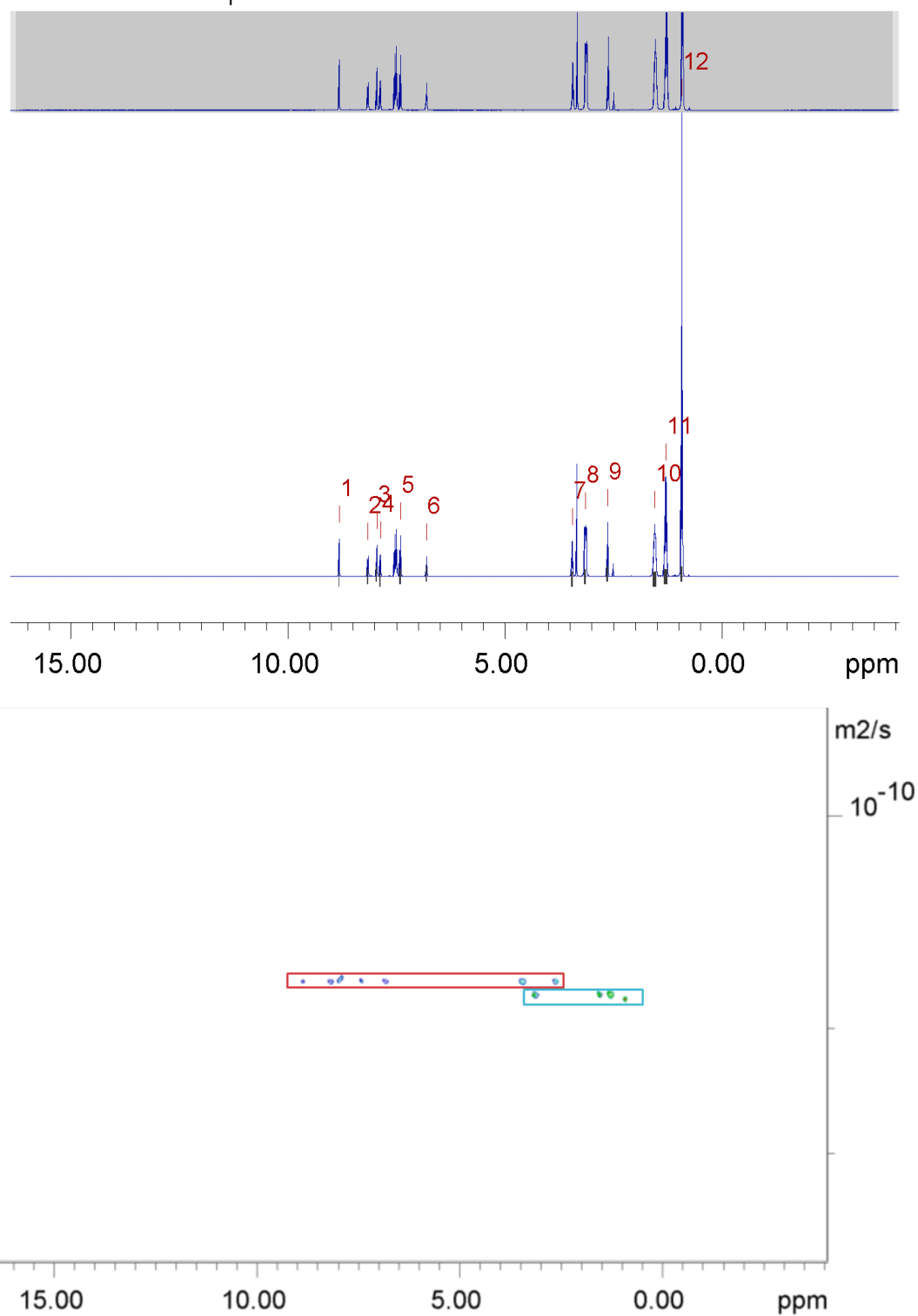


Figure S33 -  $^1\text{H}$  DOSY NMR of compound **20** (55.56 mM) in  $\text{DMSO}-d_6$  conducted at 298 K. Anionic component highlighted in red, TBA counter cation highlighted in blue.

Peak name	F2 [ppm]	lo	error	D [m <sup>2</sup> /s]	error
1	8.824	1.08e+09	3.794e+04	1.71e-10	1.301e-14
2	8.165	1.23e+09	4.875e+04	1.70e-10	1.466e-14
3	7.958	1.28e+09	4.542e+04	1.70e-10	1.316e-14
4	7.877	1.45e+09	5.186e+04	1.70e-10	1.324e-14
5	7.411	1.39e+09	5.910e+04	1.72e-10	1.590e-14
6	6.814	9.69e+08	4.878e+04	1.71e-10	1.867e-14
7	3.457	2.55e+09	6.287e+04	1.71e-10	9.169e-15
8	3.152	6.88e+09	6.522e+04	1.80e-10	3.687e-15
9	2.640	2.52e+09	5.482e+04	1.71e-10	8.062e-15
10	1.555	9.04e+09	8.638e+04	1.80e-10	3.720e-15
11	1.300	1.13e+10	8.638e+04	1.80e-10	2.969e-15
12	0.929	1.77e+10	6.120e+04	1.80e-10	1.345e-15

Figure S34 - <sup>1</sup>H DOSY NMR spectrum of the compound **20** (55.56 mM) in DMSO-*d*<sub>6</sub> at 298 K and a table reporting the diffusion constants calculated for each peak used to determine the solvation sphere diameter of the anionic component of **20** ( $d_H = 1.28$  nm). Peaks 1 - 7 and 9 correspond to the anionic component of **20** while peaks 8, 10 - 12 correspond to the cationic component of **20**.

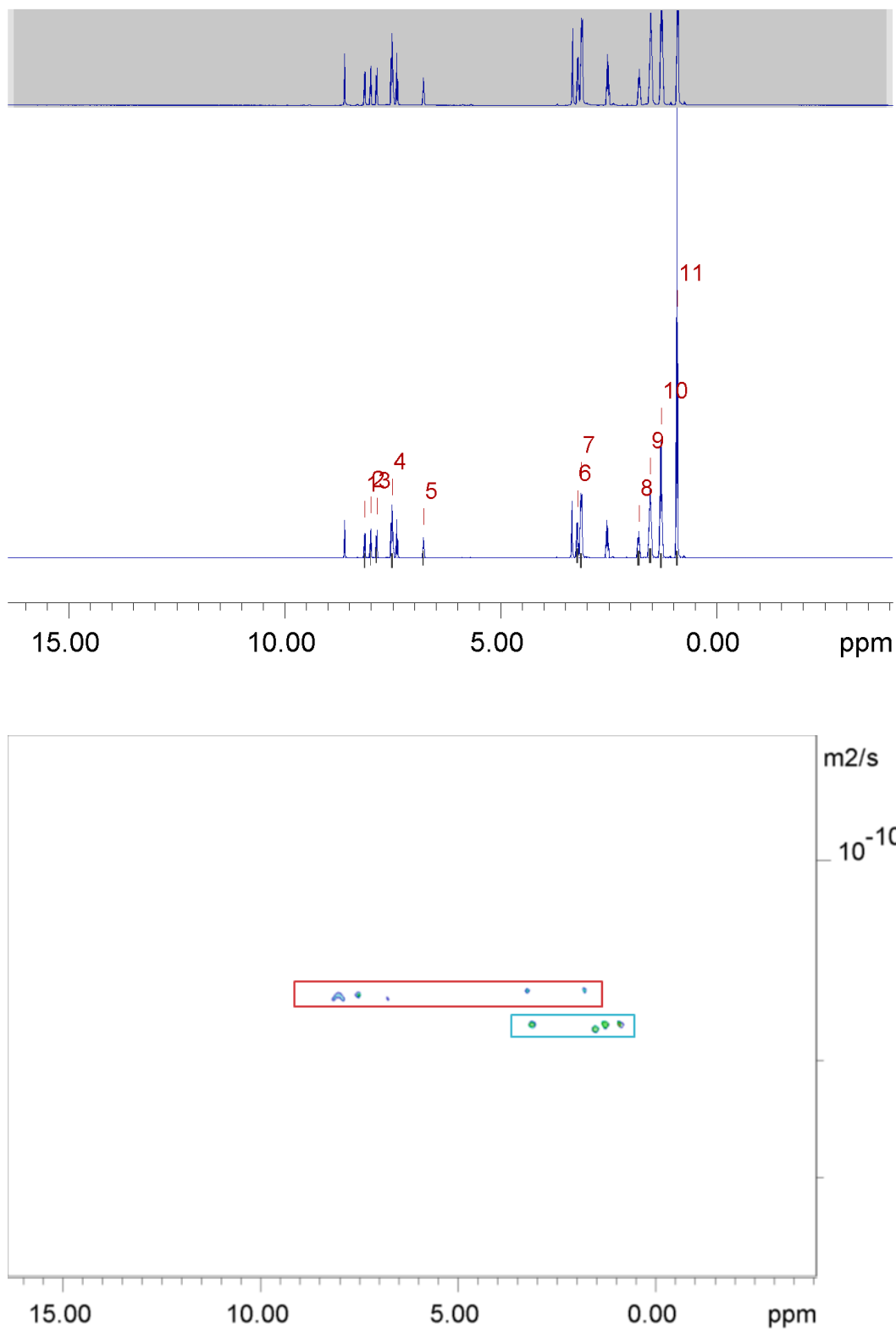


Figure S35 -  $^1\text{H}$  DOSY NMR of compound **21** (55.56 mM) in  $\text{DMSO-}d_6$  conducted at 298 K. Anionic component highlighted in red, TBA counter cation highlighted in blue.

Peak name	F2 [ppm]	lo	error	D [m <sup>2</sup> /s]	error
1	8.151	1.03e+09	5.066e+04	1.61e-10	1.613e-14
2	8.013	1.11e+09	5.052e+04	1.59e-10	1.478e-14
3	7.874	1.24e+09	5.287e+04	1.62e-10	1.403e-14
4	7.514	3.93e+09	7.267e+04	1.59e-10	6.000e-15
5	6.792	8.15e+08	5.066e+04	1.61e-10	2.040e-14
6	3.231	2.33e+09	6.658e+04	1.58e-10	9.245e-15
7	3.139	5.68e+09	6.539e+04	1.78e-10	4.130e-15
8	1.809	2.26e+09	7.403e+04	1.58e-10	1.055e-14
9	1.542	6.84e+09	7.384e+04	1.78e-10	3.890e-15
10	1.290	8.58e+09	7.197e+04	1.76e-10	2.987e-15
11	0.917	1.43e+10	6.195e+04	1.77e-10	1.545e-15

Figure S36 - <sup>1</sup>H DOSY NMR spectrum of the compound **21** (55.56 mM) in DMSO-*d*<sub>6</sub> at 298 K and a table reporting the diffusion constants calculated for each peak used to determine the solvation sphere diameter of the anionic component of **21** (*d*<sub>H</sub> = 1.37 nm). Peaks 1- 6 and 8 correspond to the anionic component of **21** while peaks 7, 9 - 11 correspond to the cationic component of **21**.

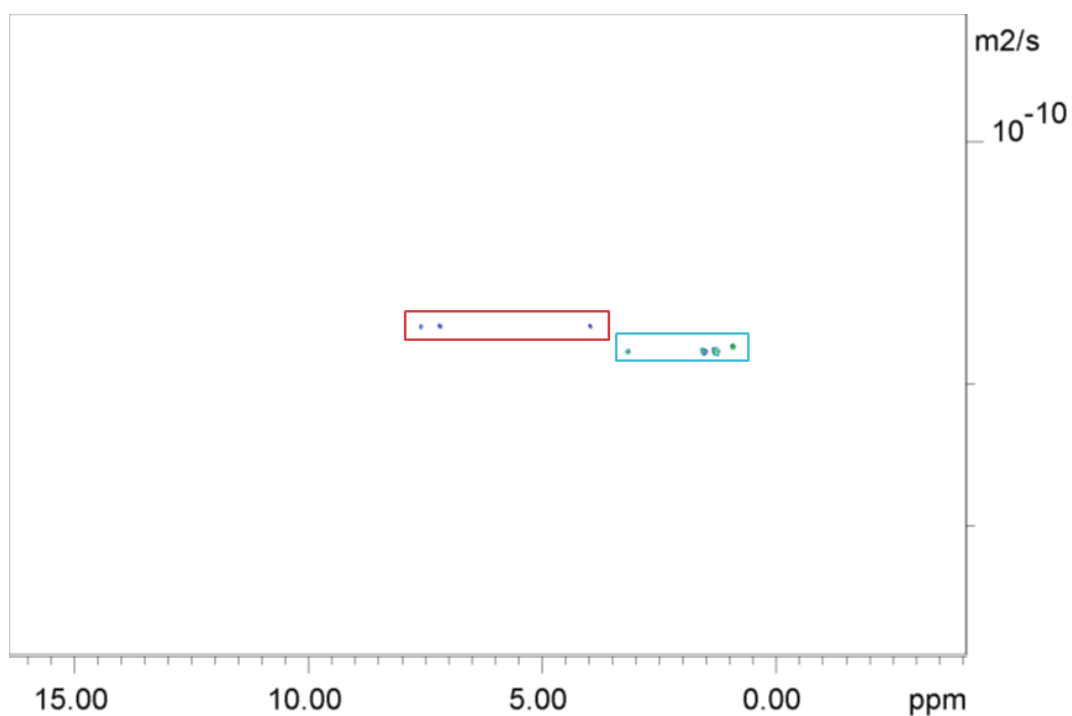
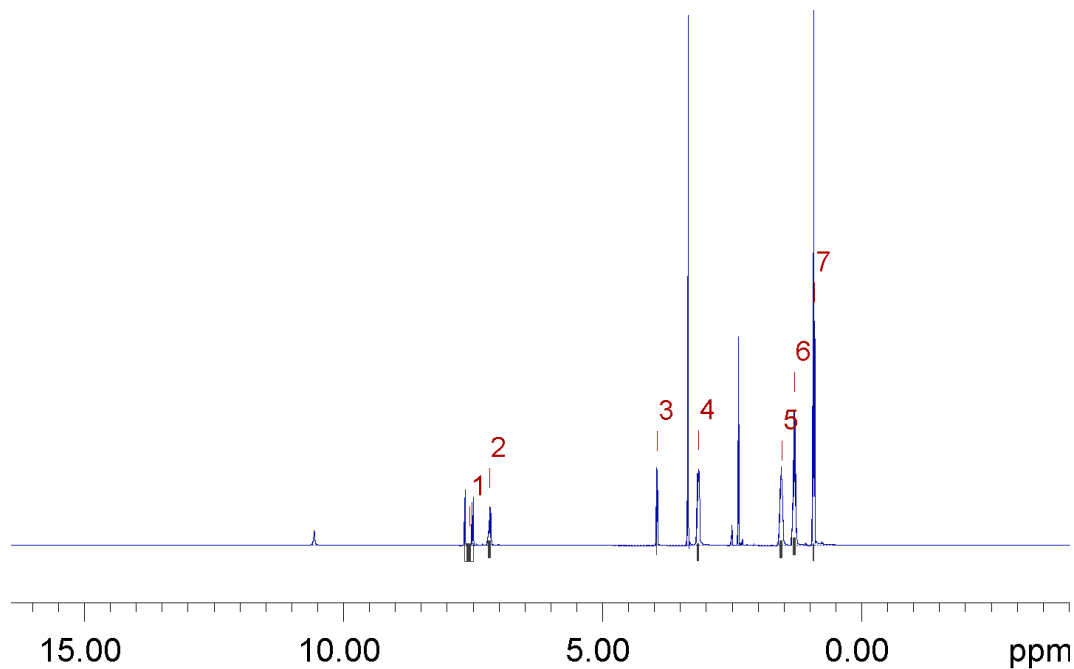


Figure S37 -  $^1\text{H}$  DOSY NMR of compound **22** (55.56 mM) in  $\text{DMSO-}d_6$  conducted at 298 K. Anionic component highlighted in red, TBA counter cation highlighted in blue.

Peak name	F2 [ppm]	lo	error	D [m <sup>2</sup> /s]	error
1	7.577	2.27e+09	1.184e+05	1.69e-10	1.877e-14
2	7.183	2.08e+09	7.218e+04	1.70e-10	1.261e-14
3	3.949	1.51e+09	3.684e+04	1.71e-10	8.860e-15
4	3.155	5.50e+09	6.090e+04	1.83e-10	4.290e-15
5	1.552	7.28e+09	7.607e+04	1.82e-10	4.016e-15
6	1.301	8.53e+09	7.062e+04	1.82e-10	3.182e-15
7	0.925	1.31e+10	5.645e+04	1.81e-10	1.651e-15

Figure S38 - <sup>1</sup>H DOSY NMR spectrum of the compound **22** (55.56 mM) in DMSO-*d*<sub>6</sub> at 298 K and a table reporting the diffusion constants calculated for each peak used to determine the solvation sphere diameter of the anionic component of **22** (*d*<sub>H</sub> = 1.29 nm). Peaks 1 - 3 correspond to the anionic component of **22** while peaks 4 - 7 correspond to the cationic component of **22**.

#### 8.2.4.1. Overview

Table S2 - Overview of diffusion coefficients (m<sup>2</sup>s<sup>-1</sup>) for compounds **20** – **23**, and **25c** in DMSO-*d*<sub>6</sub> at 298 K. Errors for diffusion constants are no greater than ± 1 x 10<sup>-13</sup> m<sup>2</sup>s<sup>-1</sup>.

Compound	Diffusion Coefficient (m <sup>2</sup> s <sup>-1</sup> )	
	Anion	TBA
<b>20</b>	1.71 x 10 <sup>-10</sup>	1.8 x 10 <sup>-10</sup>
<b>21</b>	1.60 x 10 <sup>-10</sup>	1.8 x 10 <sup>-10</sup>
<b>22</b>	1.70 x 10 <sup>-10</sup>	1.82 x 10 <sup>-10</sup>
<b>23</b>	<i>a</i>	<i>a</i>

*a* – Compound showed loss in DMSO-*d*<sub>6</sub>.

Table S3 – Overview of hydrodynamic diameters (nm) for compounds **20** – **23**, and **25c** in DMSO-*d*<sub>6</sub> at 298 K.

Compound	Hydrodynamic diameter (nm)	
	Anion	TBA
<b>20</b>	1.28	1.22
<b>21</b>	1.37	1.22
<b>22</b>	1.29	1.20
<b>23</b>	<i>a</i>	<i>a</i>

*a* – Compound showed loss in DMSO-*d*<sub>6</sub>.

### 9.3. Surface tension measurements and CMC determination

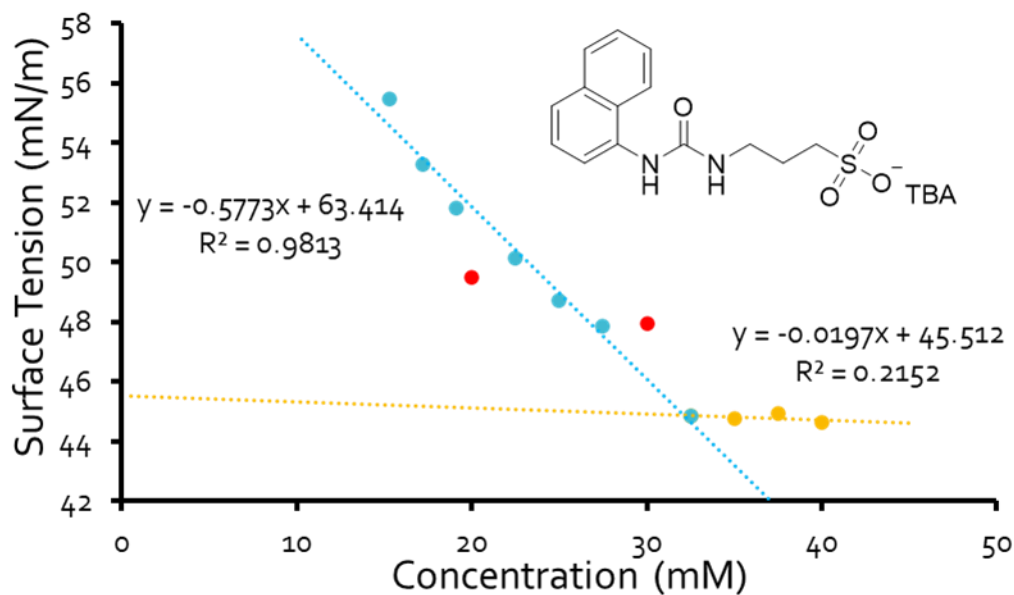


Figure S39 - Calculation of CMC (32.12 mM) for compound **21** in an EtOH:H<sub>2</sub>O 1:19 mixture using surface tension measurements.

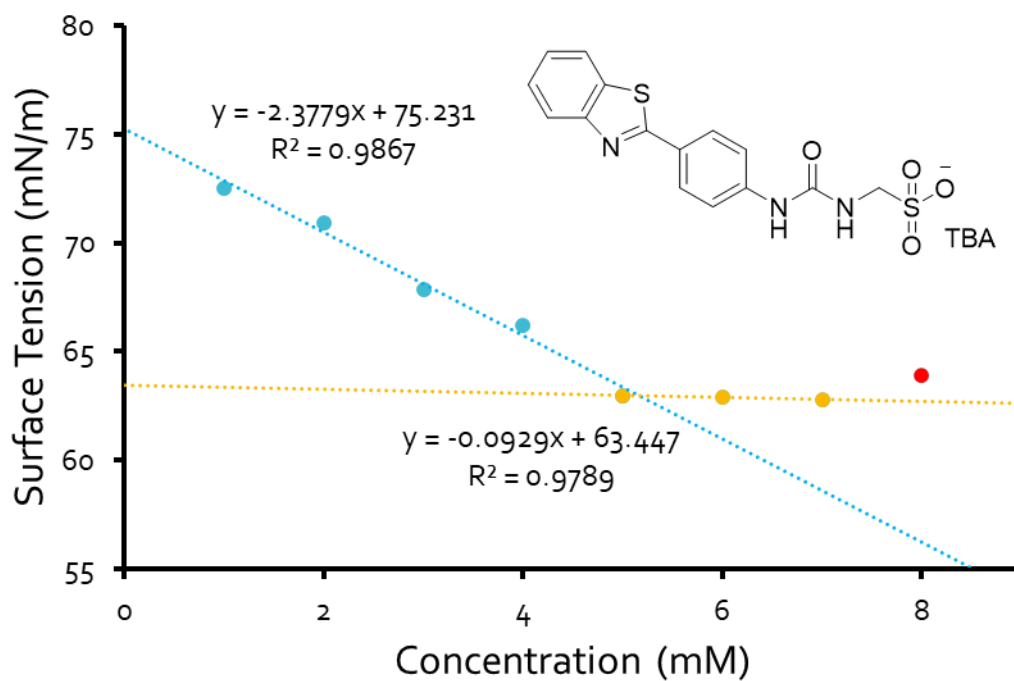


Figure S40 - Calculation of CMC (5.16 mM) for compound **23** in an EtOH:H<sub>2</sub>O 1:19 mixture using surface tension measurements.

### 9.3.1. Overview

Table S4 - Summary CMC and surface tension at CMC. Data obtained in an EtOH:H<sub>2</sub>O (1:19) solution.

<b>Compound</b>	<b>Zeta potential (mV)</b>	<b>CMC (mM)</b>	<b>Surface tension at CMC (mN/M)</b>
<b>20</b>	-13.77	<i>a</i>	<i>a</i>
<b>21</b>	-24.03	32.12	44.88
<b>22</b>	-42.71	<i>a</i>	<i>a</i>
<b>23</b>	-67.13	5.16	66.97

*a* – Could not be calculated due to compound solubility.

#### 9.4. DLS data

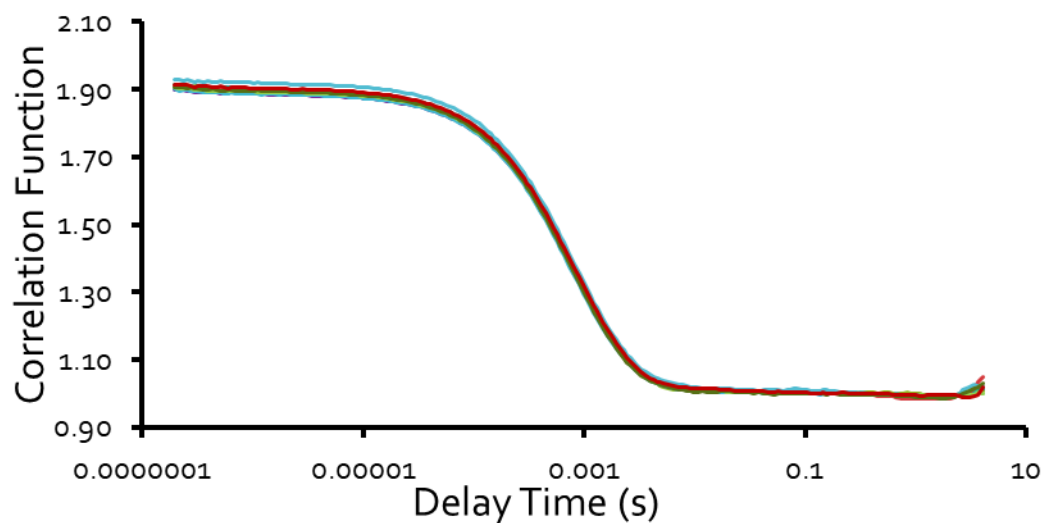


Figure S41 – Correlation function data for 10 DLS runs of compound **20** (5.56 mM) in an EtOH:H<sub>2</sub>O (1:19) solution at 298 K.

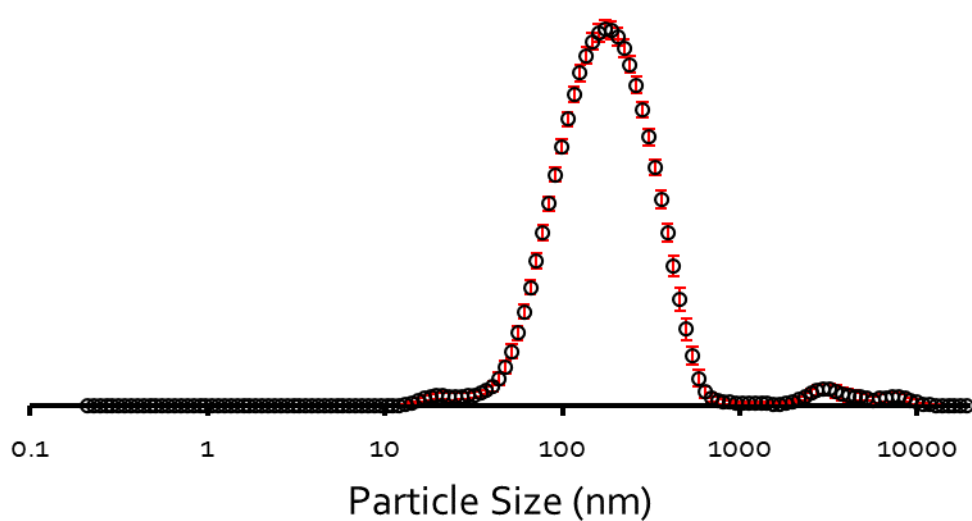


Figure S42 – The average intensity particle size distribution calculated (174 nm) using 10 DLS runs for compound **20** (5.56 mM) in an EtOH:H<sub>2</sub>O (1:19) solution at 298 K.

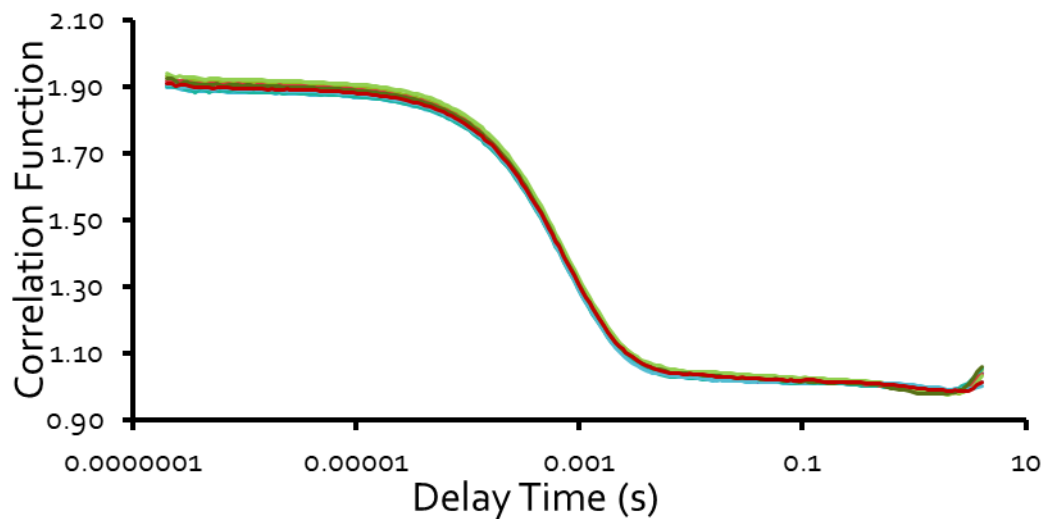


Figure S43 – Correlation function data for 10 DLS runs of compound **20** (0.56 mM) in an EtOH:H<sub>2</sub>O (1:19) solution at 298 K.

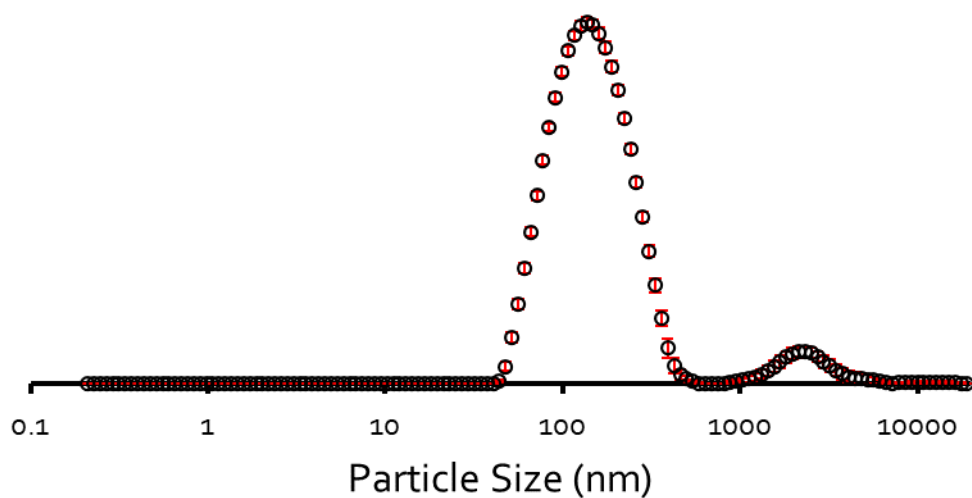


Figure S44 – The average intensity particle size distribution calculated (160 nm) using 10 DLS runs for compound **20** (0.56 mM) in an EtOH:H<sub>2</sub>O (1:19) solution at 298 K.

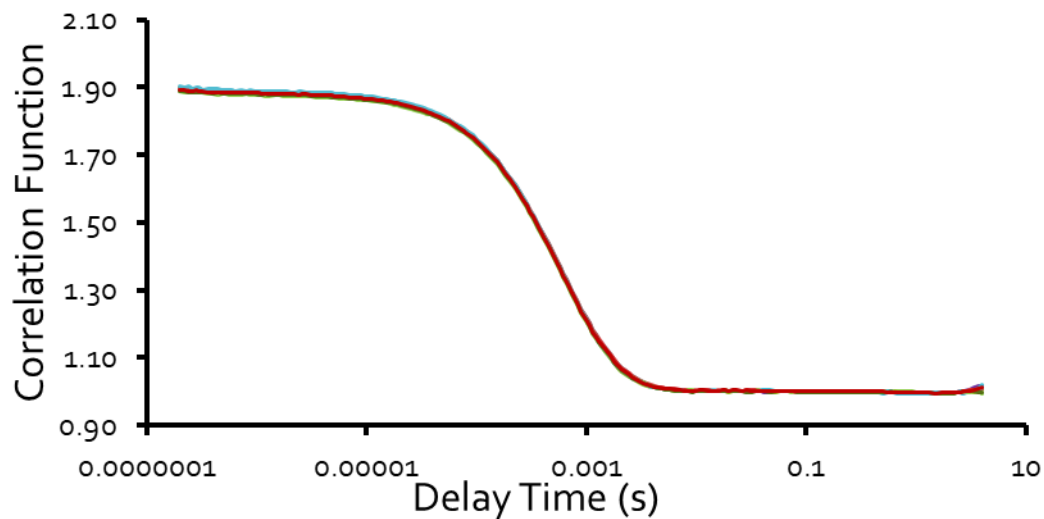


Figure S45 – Correlation function data for 9 DLS runs of compound **21** (5.56 mM) in an EtOH: H<sub>2</sub>O (1:19) solution at 298 K.

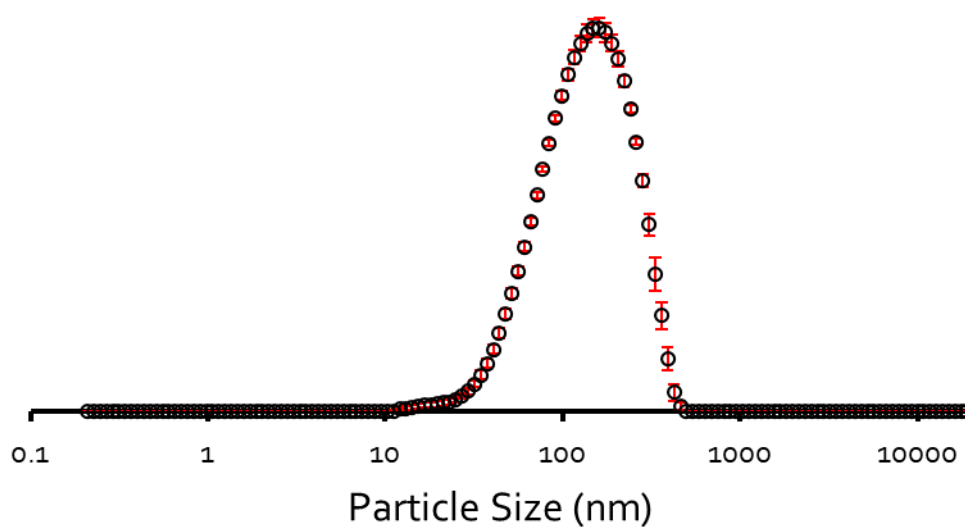


Figure S46 – The average intensity particle size distribution calculated (127 nm) using 9 DLS runs for compound **21** (5.56 mM) in an EtOH:H<sub>2</sub>O (1:19) solution at 298 K.

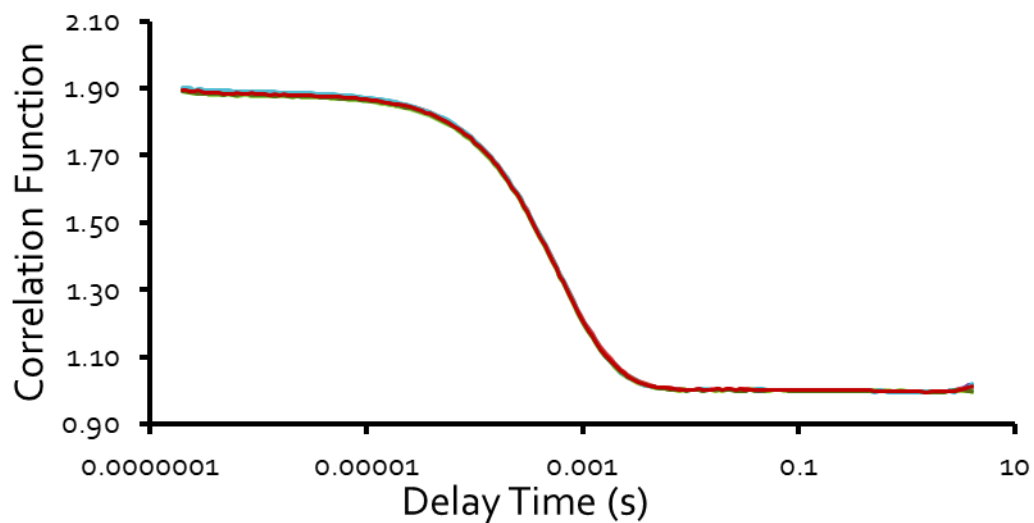


Figure S47 – Correlation function data for 10 DLS runs of compound **21** (0.56 mM) in an EtOH:H<sub>2</sub>O (1:19) solution at 298 K

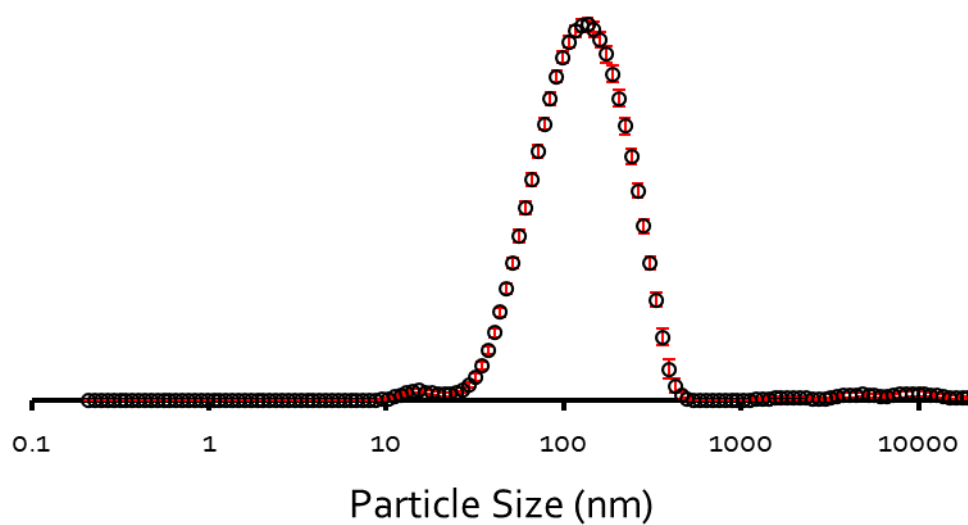


Figure S48 – The average intensity particle size distribution calculated (127 nm) using 10 DLS runs for compound **21** (0.56 mM) in an EtOH:H<sub>2</sub>O (1:19) solution at 298 K.

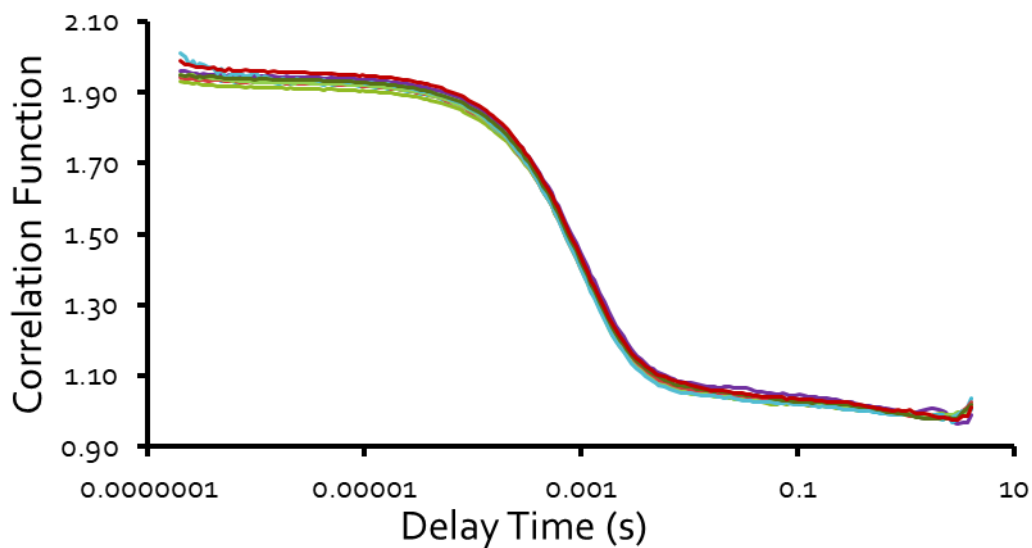


Figure S49 - Correlation function data for 10 DLS runs of compound **22** (0.56 mM) in an EtOH:H<sub>2</sub>O (1:19) solution at 298 K.

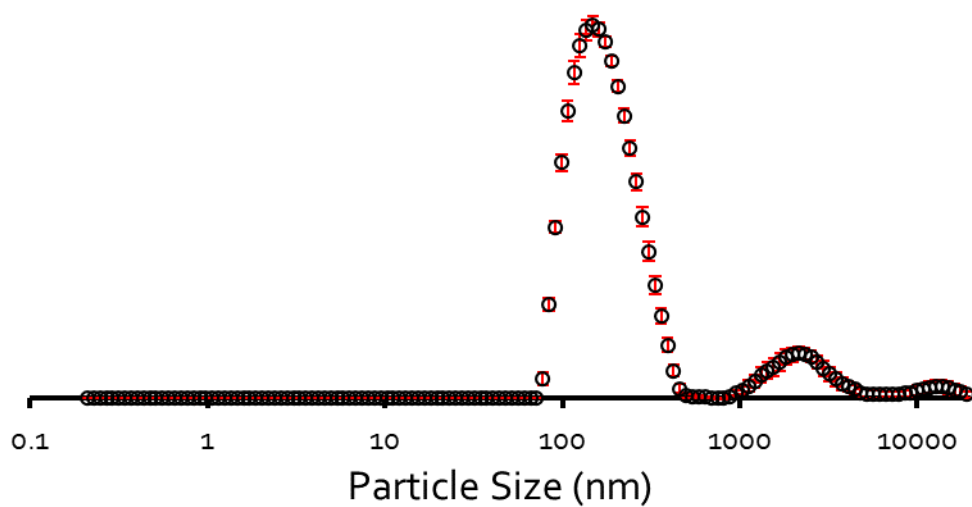


Figure S50 - The average intensity particle size distribution calculated (127 nm) using 10 DLS runs for compound **22** (0.56 mM) in an EtOH:H<sub>2</sub>O (1:19) solution at 298 K.

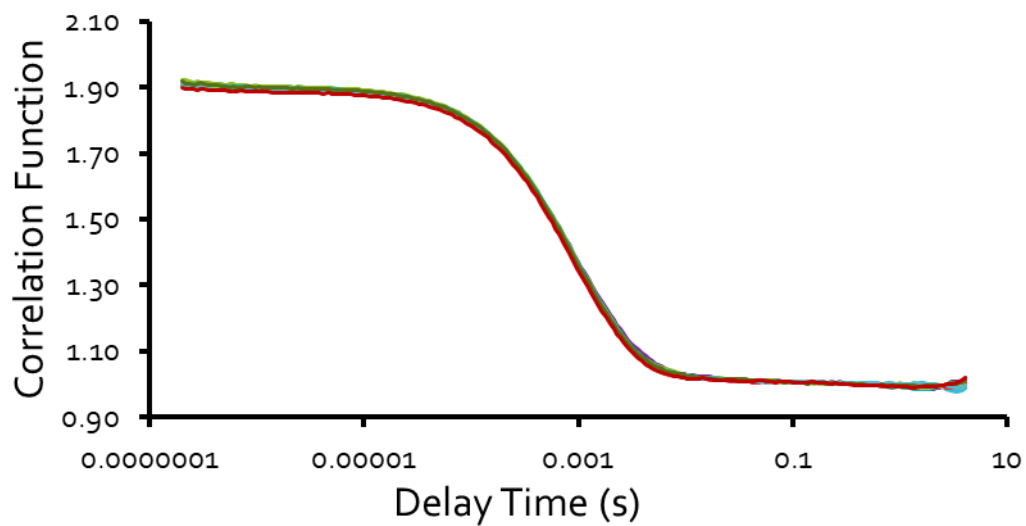


Figure S51 – Correlation function data for 10 DLS runs of compound **23** (5.56 mM) in an EtOH: H<sub>2</sub>O (1:19) solution at 298K.

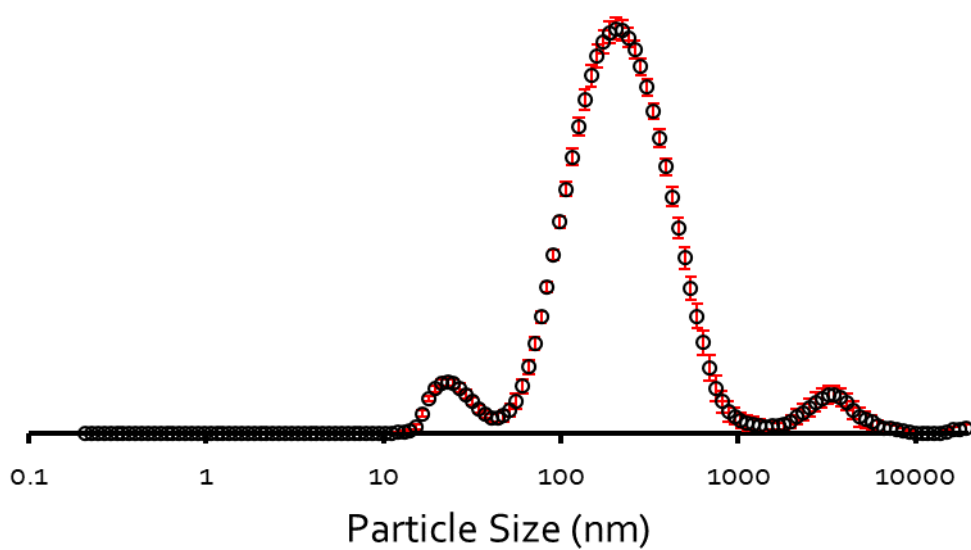


Figure S52 – The average intensity particle size distribution calculated (215 nm) using 10 DLS runs for compound **23** (5.56 mM) in an EtOH:H<sub>2</sub>O (1:19) solution at 298 K.

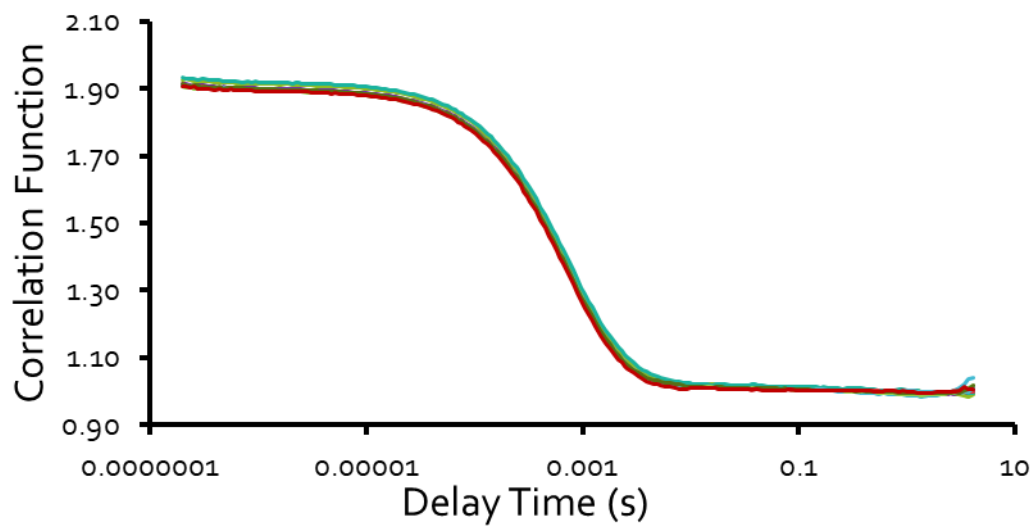


Figure S53 – Correlation function data for 10 DLS runs of compound **23** (0.56 mM) in an EtOH:H<sub>2</sub>O (1:19) solution at 298 K.

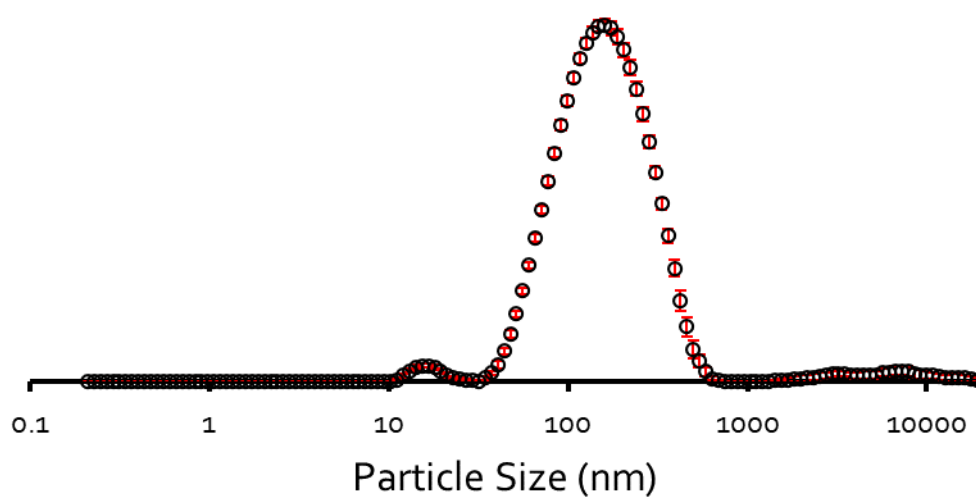


Figure S54 – The average intensity particle size distribution calculated (153 nm) using 10 DLS runs for compound **23** (0.56 mM) in an EtOH:H<sub>2</sub>O (1:19) solution at 298 K.

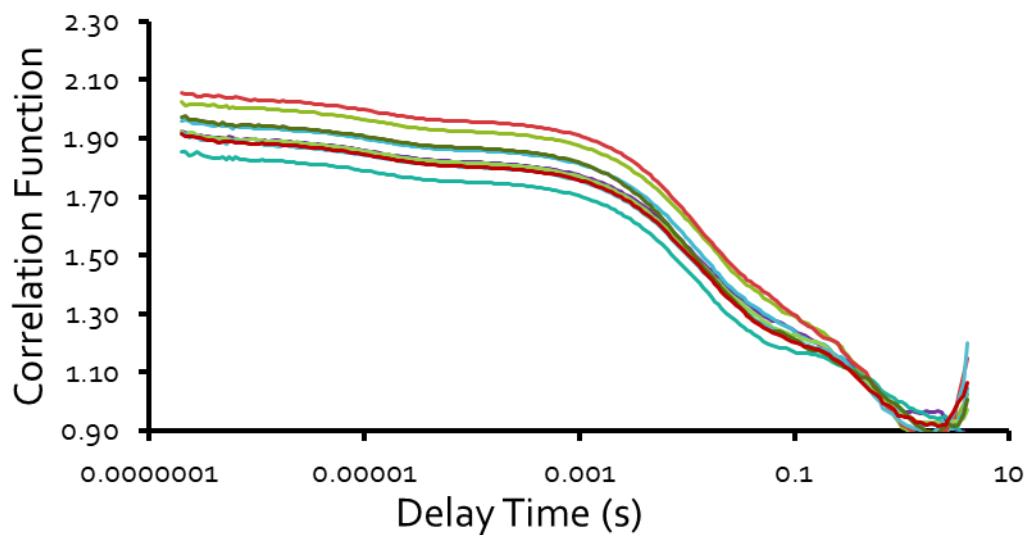


Figure S55 - Correlation function data for 10 DLS runs of compound **23** (111.2 mM) in a DMSO solution at 298 K.

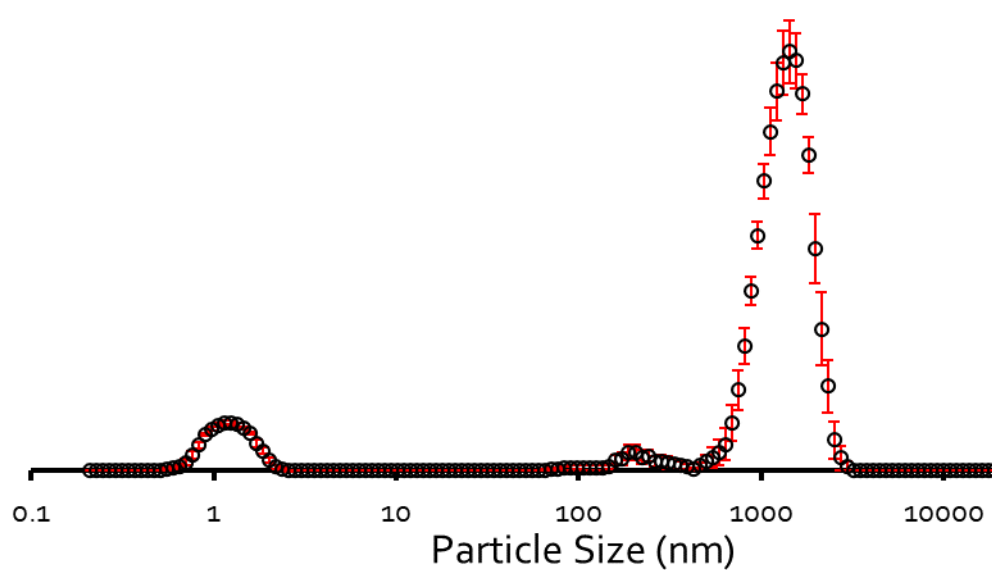


Figure S56 - The average intensity particle size distribution calculated (4074 nm) using 10 DLS runs for compound **23** (111.2 mM) in a DMSO solution at 298 K.

### 9.4.1. Overview

Table 5 – Summary of average intensity particle size distribution data in EtOH:H<sub>2</sub>O 1:19 solution. Error = standard error of the mean given to 1 dp.

Compound	Concentration (mM)	Peak maxima (nm)	Polydispersity (%)
<b>20</b>	5.56	199.94 (± 3.1 %)	26.05 (± 0.3 %)
	0.56	156.33 (± 1.8 %)	24.74 (± 0.5 %)
<b>21</b>	5.56	153.86 (± 1.1 %)	24.67 (± 0.1 %)
	0.56	142.49 (± 1.8 %)	24.81 (± 0.2 %)
<b>22</b>	0.56	180.95 (± 2.5 %)	25.93 (± 0.2 %)
<b>23</b>	5.56	255.42 (± 7.1 %)	27.37 (± 0.2 %)
	0.56	155.46 (± 2.4 %)	15.96 (± 0.3 %)

Table S6– Summary of average intensity particle size distribution data in DMSO. Error = standard error of the mean given to 1 dp.

Compound	Concentration (mM)	Peak maxima (nm)	Polydispersity (%)
<b>20</b>	<i>a</i>	<i>a</i>	<i>a</i>
<b>21</b>	<i>a</i>	<i>a</i>	<i>a</i>
<b>22</b>	<i>a</i>	<i>a</i>	<i>a</i>
<b>23</b>	111.12	1380.55 (± 23.17)	35.74 (± 1.4 %)

*a* – Larger structures not present.

### 9.5. Zeta potential data

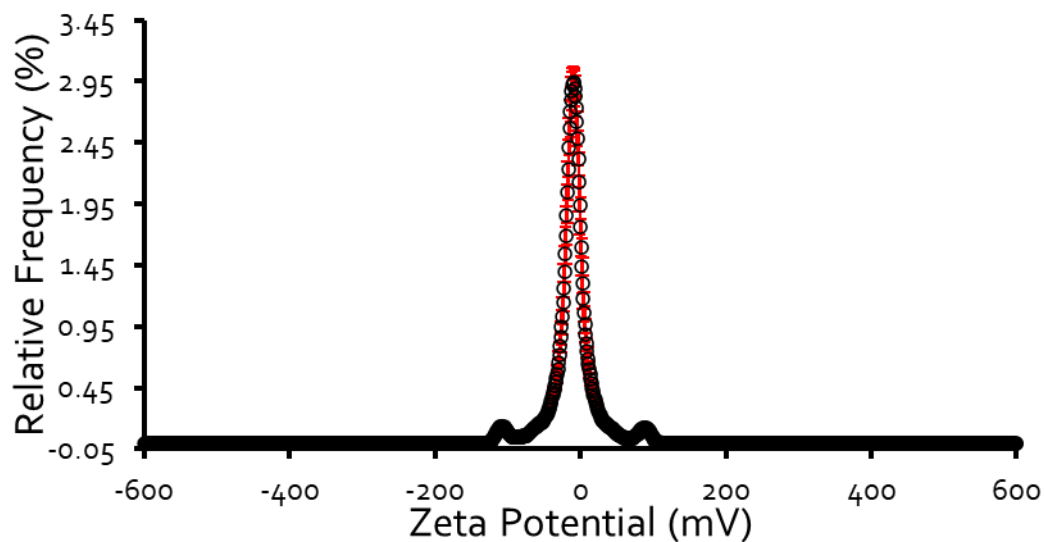


Figure S57 – The average zeta potential distribution calculated using 10 runs for compound **20** (5.56 mM) in EtOH:H<sub>2</sub>O (1:19) solution at 298 K. Average measurement value -13.77 mV.

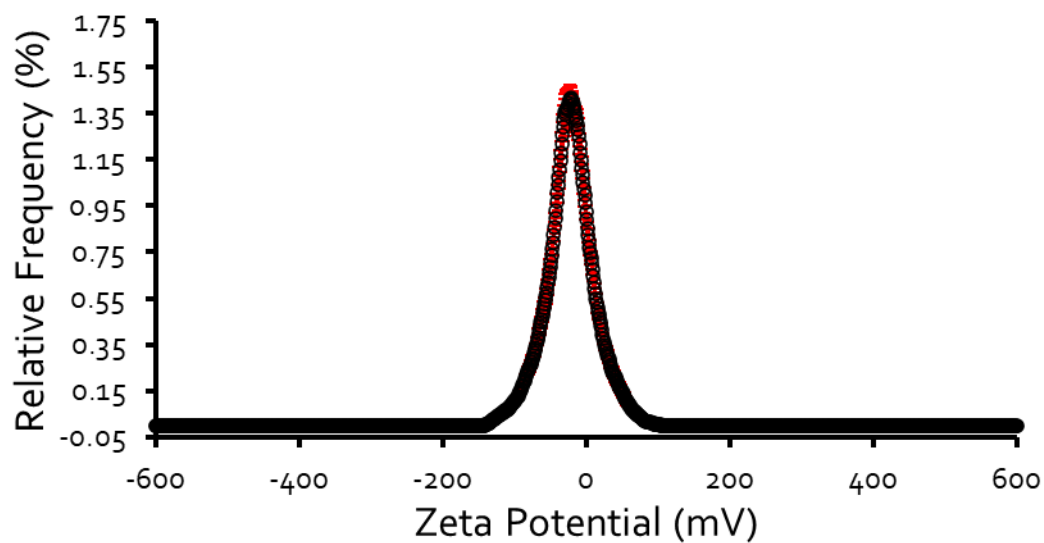


Figure S58 – The average zeta potential distribution calculated using 10 runs for compound **21** (5.56 mM) in EtOH:H<sub>2</sub>O (1:19) solution at 298 K. Average measurement value -24.03 mV.

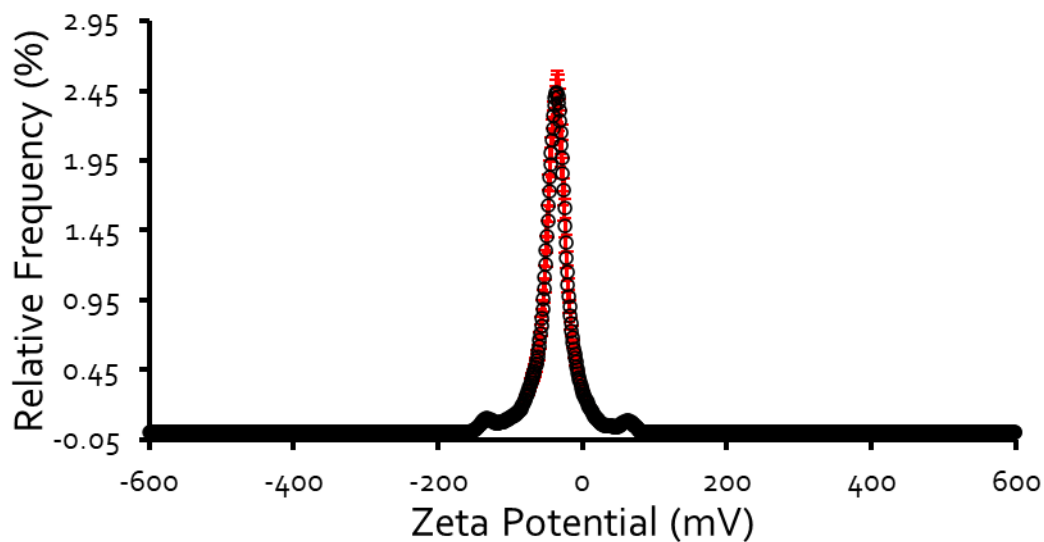


Figure S59 - The average zeta potential distribution calculated using 10 runs for compound **22** (0.56 mM) in EtOH:H<sub>2</sub>O (1:19) solution at 298 K. Average measurement value -42.71 mV.

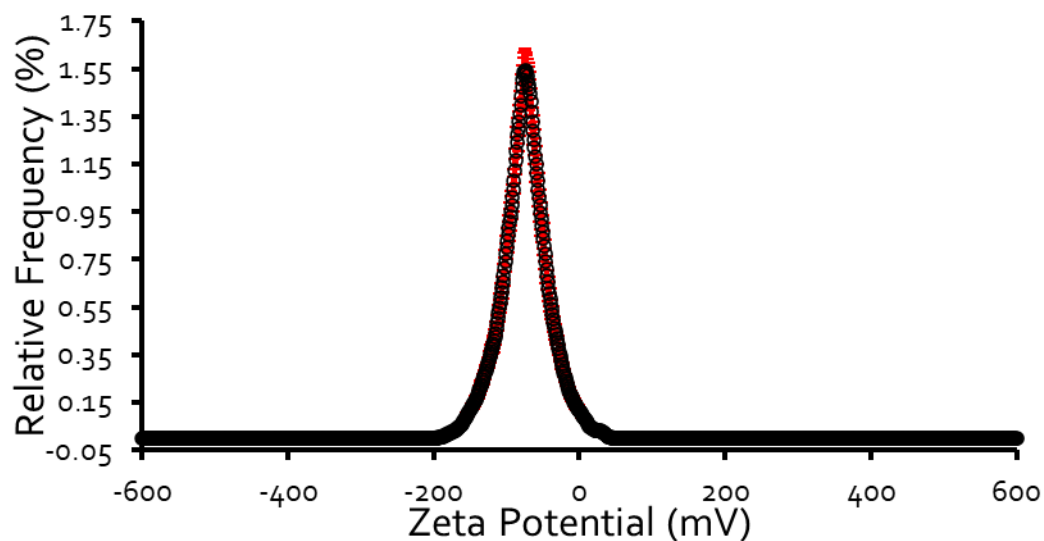


Figure S60 - The average zeta potential distribution calculated using 10 runs for compound **23** (5.56 mM) in EtOH:H<sub>2</sub>O (1:19) solution at 298 K. Average measurement value -67.13 mV.

### 9.5.1. Overview

Table 7 – Summary of zeta potential at 5.56 mM for **20**, **21** and **23**, and 0.56 mM for **22**. Data obtained in an EtOH:H<sub>2</sub>O (1:19) solution.

<b>Compound</b>	<b>Zeta potential (mV)</b>
<b>20</b>	-13.77
<b>21</b>	-24.03
<b>22</b>	-42.71
<b>23</b>	-67.13

## 9.6. Single Crystal X-ray Structures

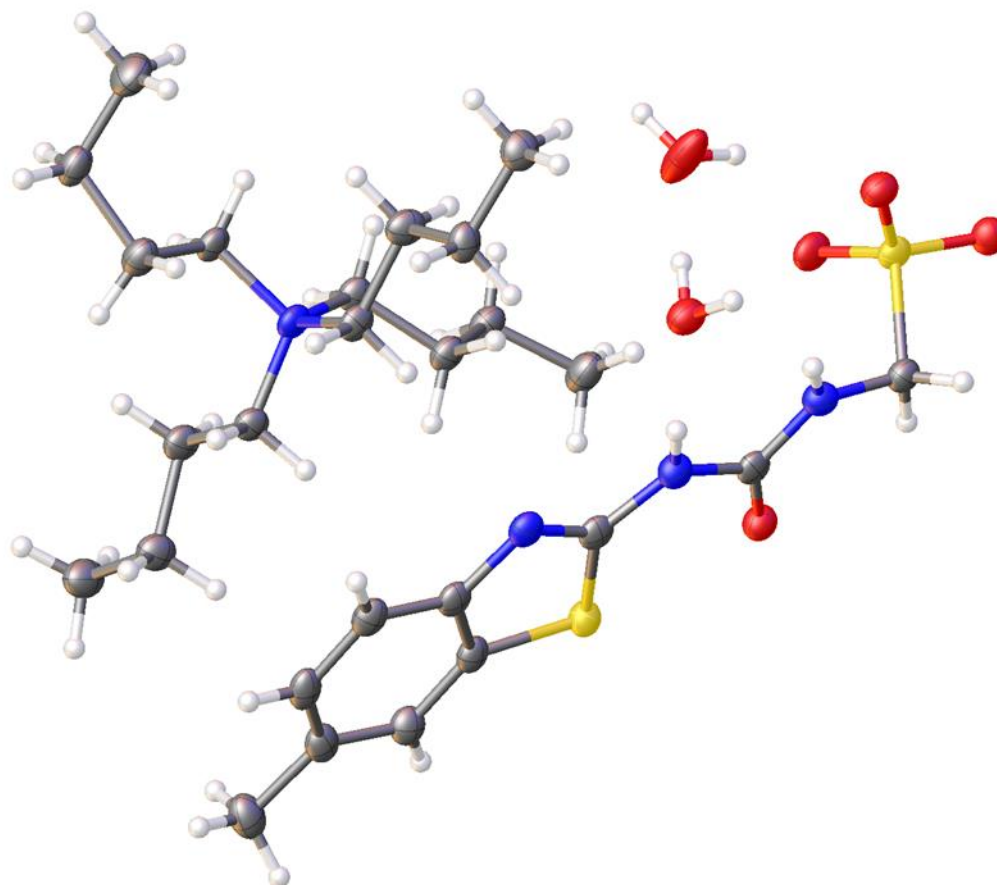


Figure S61 - Single crystal X-ray structure of **22**: red = oxygen; yellow = sulfur; blue = nitrogen; white = hydrogen; grey = carbon. CCDC 2022536,  $C_{26}H_{50}N_4O_6S_2$  ( $M = 578.82$ ): monoclinic, space group  $P 21/n$ ,  $a = 8.4322(1) \text{ \AA}$ ,  $b = 16.2622(2) \text{ \AA}$ ,  $c = 23.0023(3) \text{ \AA}$ ,  $\alpha = 90^\circ$ ,  $\beta = 100.426(1)^\circ$ ,  $\gamma = 90^\circ$ ,  $V = 3102.14(7) \text{ \AA}^3$ ,  $Z = 4$ ,  $T = 100(1) \text{ K}$ ,  $CuK\alpha = 1.5418 \text{ \AA}$ ,  $D_{\text{calc}} = 1.239 \text{ g/cm}^3$ , 21823 reflections measured ( $7.816 \leq 2\theta \leq 144.206$ ), 6021 unique ( $R_{\text{int}} = 0.0513$ ,  $R_{\text{sigma}} = 0.0427$ ) which were used in all calculations. The final  $R_1$  was 0.0392 ( $I > 2\sigma(I)$ ) and  $wR_2$  was 0.1069 (all data).

Table S8 - Hydrogen bond distances and angles observed for **22**, calculated from the single crystal X-ray structure shown in Figure S61.

Hydrogen bond donor	Hydrogen bond acceptor	Hydrogen bond length (D•••A) (Å)	Hydrogen bond angle (D-H•••A) (°)
N1	O1	3.0716(10)	3.0716(18)
N1	O5	3.125(2)	140.8 (1)
N2	O5	2.7277(18)	163.64 (10)
O5	O2	2.7833(17)	173.60 (8)
O5	O6	2.7021(19)	169.88 (10)
O6	O1	2.8691(19)	152.52 (10)
O6	O3	2.8365 (18)	172.02 (12)

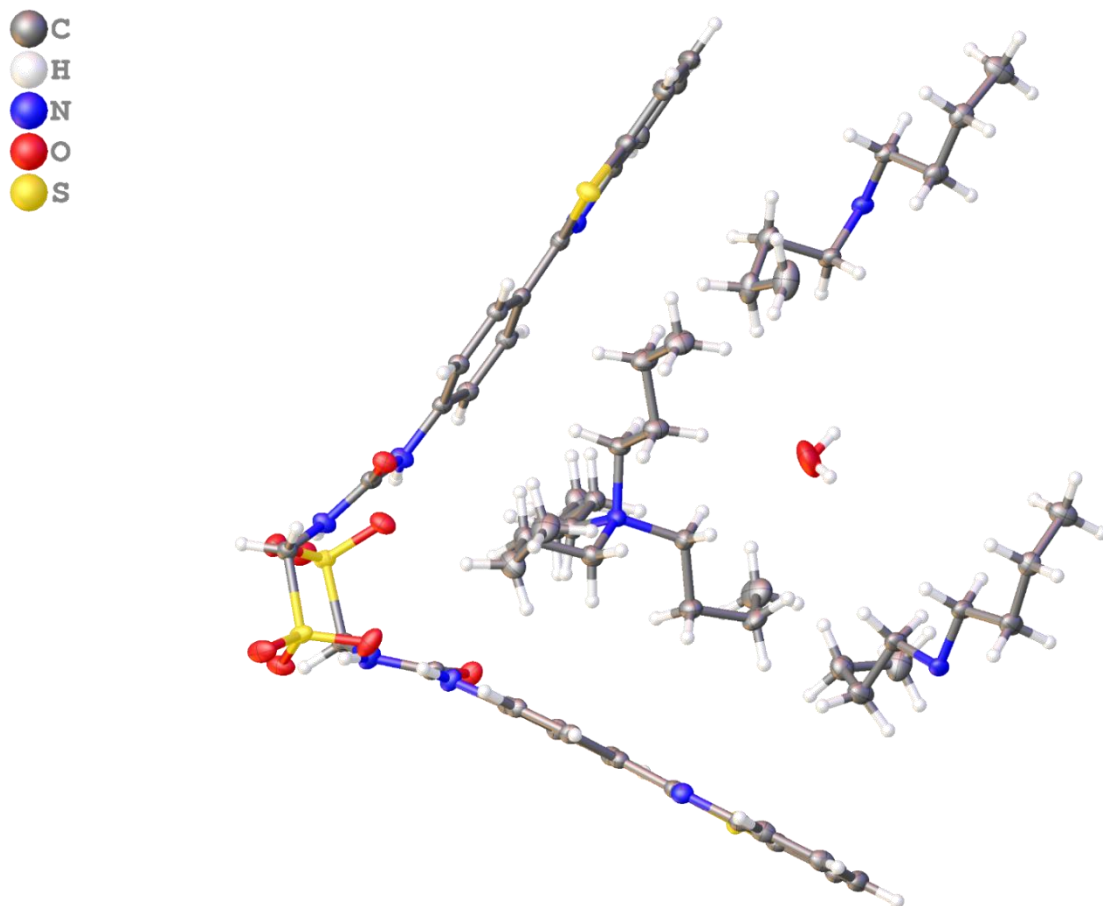


Figure S62 - Single crystal X-ray structure of **23**: red = oxygen; yellow = sulfur; blue = nitrogen; white = hydrogen; grey = carbon. CCDC 1997675,  $C_{62}H_{98}N_8O_9S_4$  ( $M = 1227.72$ ): monoclinic, space group  $P 2/n$ ,  $a = 19.22676(16)$  Å,  $b = 13.73691(14)$  Å,  $c = 25.4779(2)$  Å,  $\alpha = 90^\circ$ ,  $\beta = 107.0098(10)^\circ$ ,  $\gamma = 90^\circ$ ,  $V = 6434.76(11)$  Å<sup>3</sup>,  $Z = 4$ ,  $T = 148(1)$  K,  $CuK\alpha = 1.5418$  Å,  $D_{calc} = 1.267$  g/cm<sup>3</sup>, 42981 reflections measured ( $7.256 \leq 2\theta \leq 133.202$ ), 11367 unique ( $R_{int} = 0.0440$ ,  $R_{sigma} = 0.0365$ ) which were used in all calculations. The final  $R_1$  was 0.0379 ( $I > 2\sigma(I)$ ) and  $wR_2$  was 0.1033 (all data). Internal angle of dimerization =  $53.65(8)^\circ$ .

Table S9 - Hydrogen bond distances and angles observed for **23**, calculated from the single crystal X-ray structure shown in Figure S62.

Hydrogen bond donor	Hydrogen bond acceptor	Hydrogen bond length (D•••A) (Å)	Hydrogen bond angle (D-H•••A) (°)
N1	O5	2.9066(19)	163.53(11)
N2	O7	2.9093(19)	175.23(10)
N4	O3	2.2953(19)	178.69(12)
N5	O1	2.9089(19)	171.00(11)
O9	O5	2.827(2)	165.38(14)
O9	O3	2.852(2)	154.13(12)

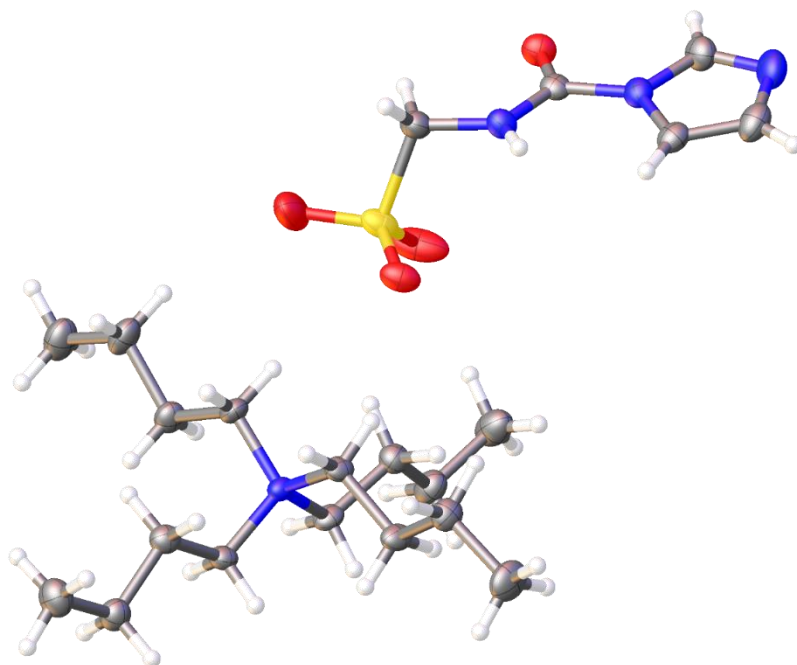


Figure S63 - Single crystal X-ray structure of **24**: red = oxygen; yellow = sulfur; blue = nitrogen; white = hydrogen; grey = carbon. CCDC 1997676,  $C_{21}H_{42}N_4O_4S$  ( $M = 446.65$ ): monoclinic, space group P 21/c,  $a = 9.8358(6)$  Å,  $b = 15.9107(8)$  Å,  $c = 16.2624(10)$  Å,  $\alpha = 90^\circ$ ,  $\beta = 89.958(6)^\circ$ ,  $\gamma = 90^\circ$ ,  $V = 2545.0(3)$  Å<sup>3</sup>,  $Z = 4$ ,  $T = 148(1)$  K,  $CuK\alpha = 1.5418$  Å,  $D_{calc} = 1.166$  g/cm<sup>3</sup>, 17127 reflections measured ( $7.774 \leq 2\theta \leq 133.194$ ), 4505 unique ( $R_{int} = 0.0768$ ,  $R_{sigma} = 0.0713$ ) which were used in all calculations. The final  $R_1$  was 0.0577 ( $I > 2\sigma(I)$ ) and  $wR_2$  was 0.1497 (all data).

Table S10 - Hydrogen bond distances and angles observed for **24**, calculated from the single crystal X-ray structure shown in Figure S63.

Hydrogen bond donor	Hydrogen bond acceptor	Hydrogen bond length (D•••A) (Å)	Hydrogen bond angle (D-H•••A) (°)
N1	O1	2.751(3)	143.52(17)

### 9.7. Low Level *in silico* Modelling

Computational calculations to identify primary hydrogen bond donating and accepting sites were conducted in line with studies reported by Hunter using Spartan 16<sup>''</sup>.<sup>45</sup> Calculations were performed using semi-empirical PM6 methods, after energy minimisation calculations, to identify  $E_{\max}$ ,  $E_{\min}$  and LogP values. PM6 was used over AM1 in line with research conducted by Stewart.<sup>175</sup>

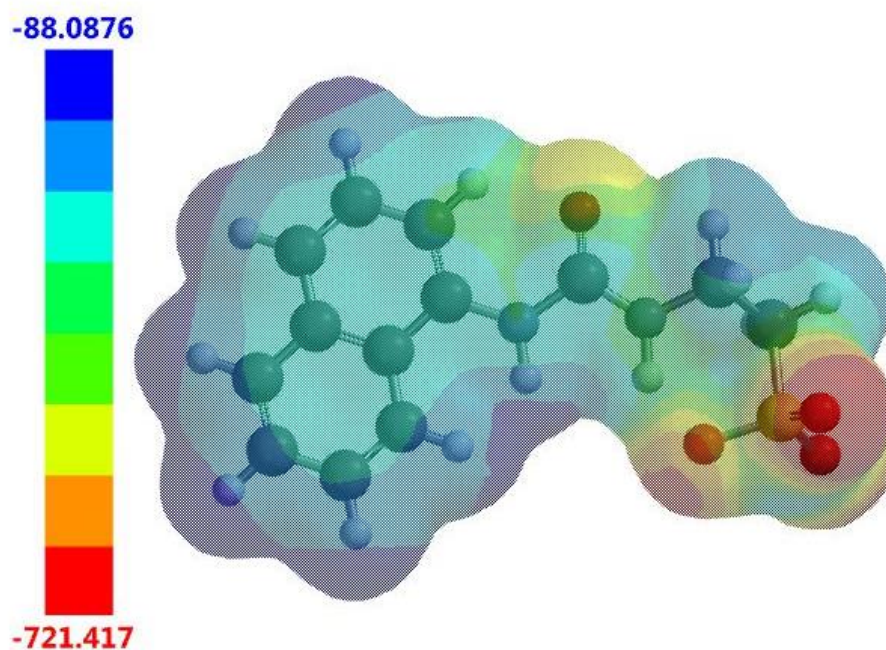


Figure S64 - Electrostatic potential map calculated for compound **20**.  $E_{\max}$  and  $E_{\min}$  values depicted in the Figure legends are given in kJ mol<sup>-1</sup>.

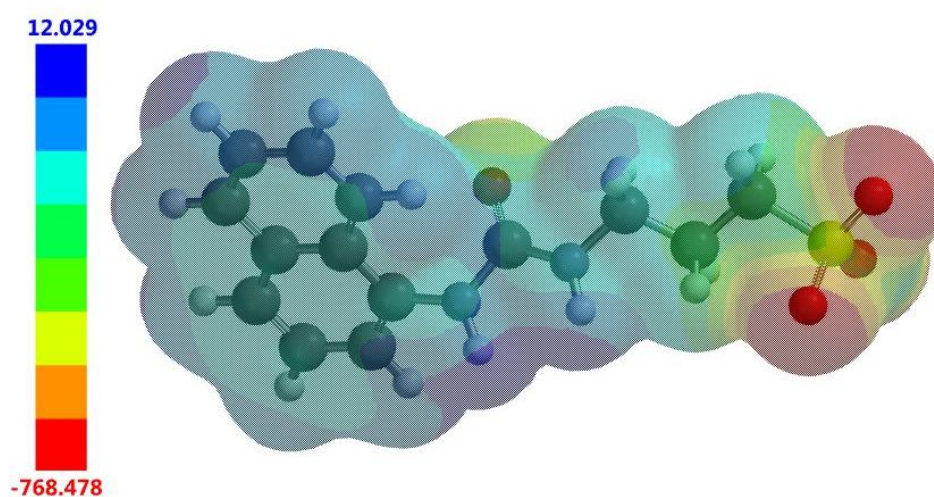


Figure S65 - Electrostatic potential map calculated for compound **21**.  $E_{\max}$  and  $E_{\min}$  values depicted in the Figure legends are given in kJ mol<sup>-1</sup>.

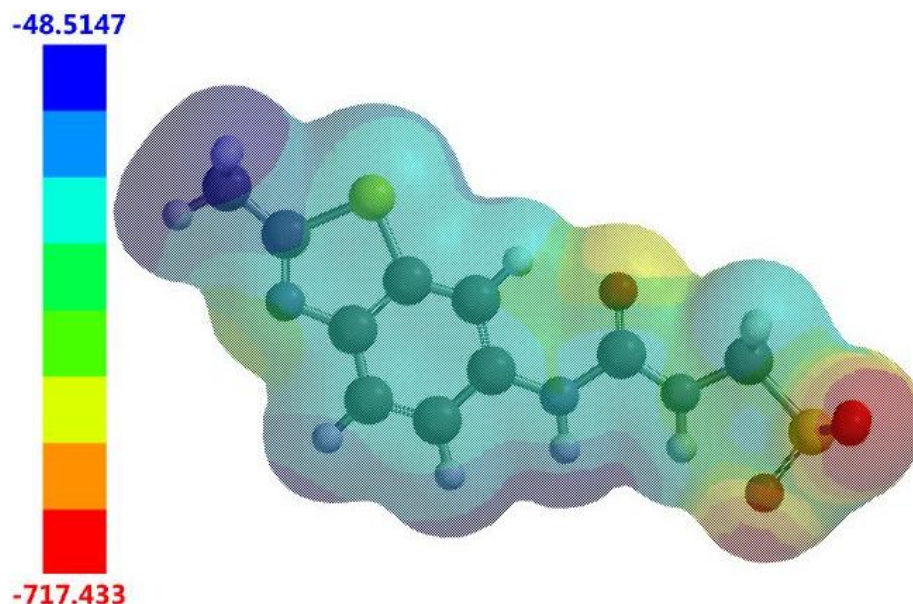


Figure S66 - Electrostatic potential map calculated for compound **22**.  $E_{\max}$  and  $E_{\min}$  values depicted in the Figure legends are given in  $\text{kJ mol}^{-1}$ .

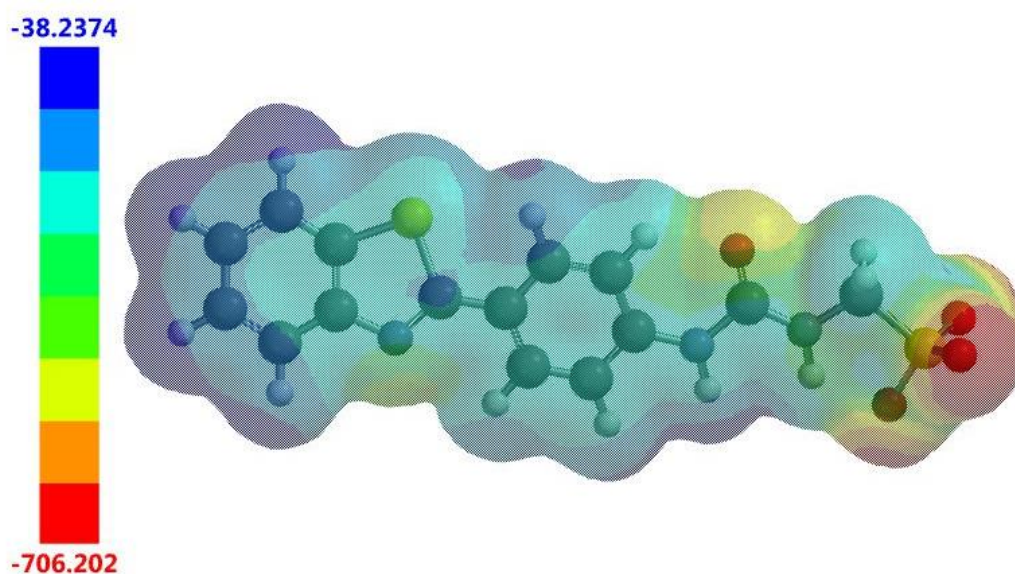


Figure S67 - Electrostatic potential map calculated for compound **23**.  $E_{\max}$  and  $E_{\min}$  values depicted in the Figure legends are given in  $\text{kJ mol}^{-1}$ .

### 9.7.1. Overview

Table S11 – Summary of  $E_{\max}$ ,  $E_{\min}$ , and  $\text{Log}P$  values for **20** – **23**.

Compound	$E_{\max}$ ( $\text{kJ mol}^{-1}$ )	$E_{\min}$ ( $\text{kJ mol}^{-1}$ )	$\text{Log}P$
<b>20</b>	-721.417	-88.0876	1.05
<b>21</b>	-768.478	12.0290	1.51
<b>22</b>	-717.433	-48.5147	0.86
<b>23</b>	-706.202	-38.2374	1.86

## 9.8. Mass Spectrum Data

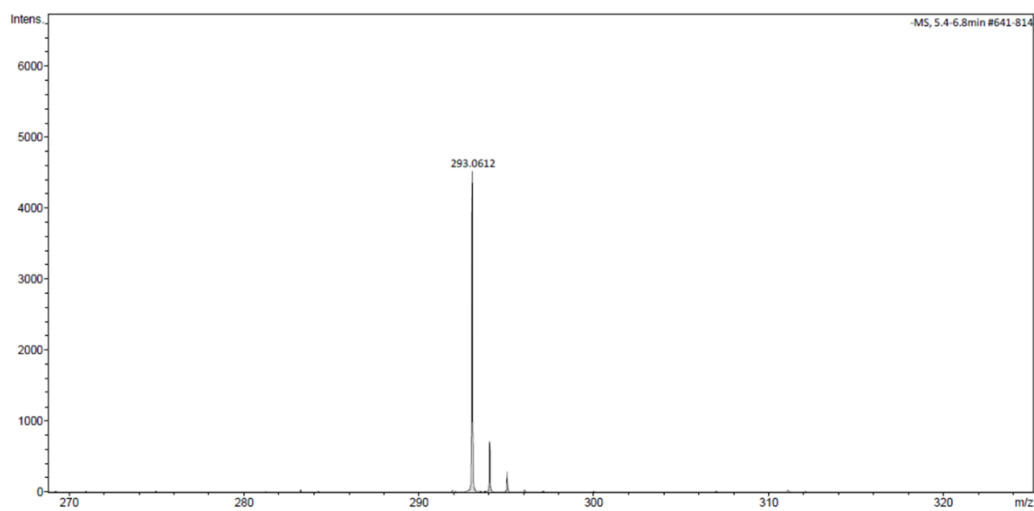


Figure S68 - A high-resolution mass spectrum (ESI<sup>-</sup>) obtained for compound **20** in methanol,  $m/z$  [M].

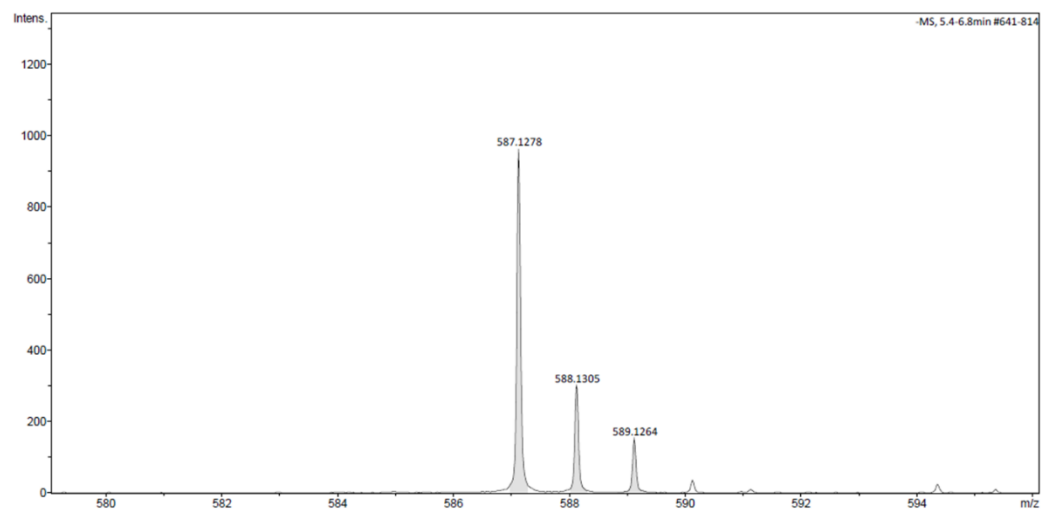


Figure S69 - A high-resolution mass spectrum (ESI<sup>-</sup>) obtained for dimeric species of compound **20** in methanol,  $m/z$  [M + M + H<sup>+</sup>].

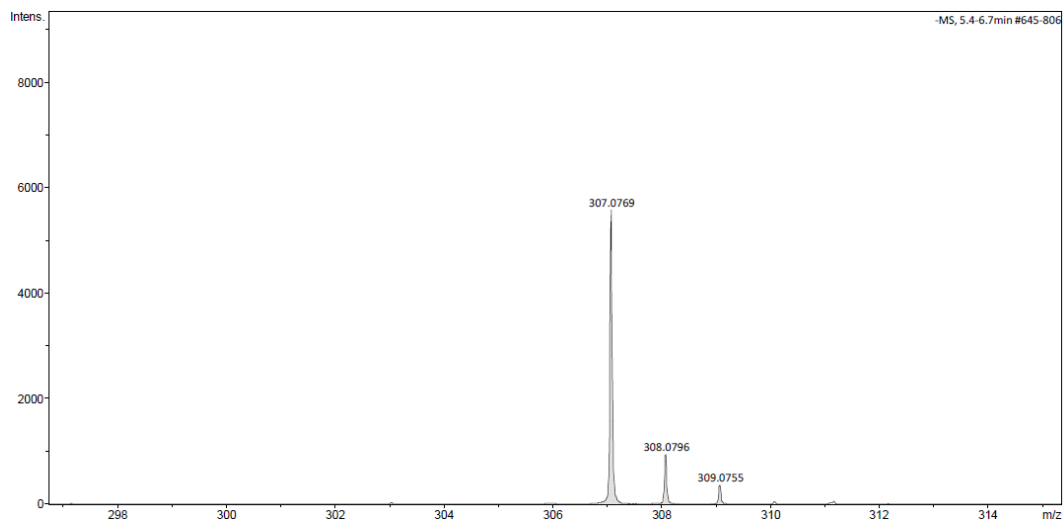


Figure S70 - A high-resolution mass spectrum (ESI<sup>-</sup>) obtained for compound **21** in methanol,  $m/z$  [M].

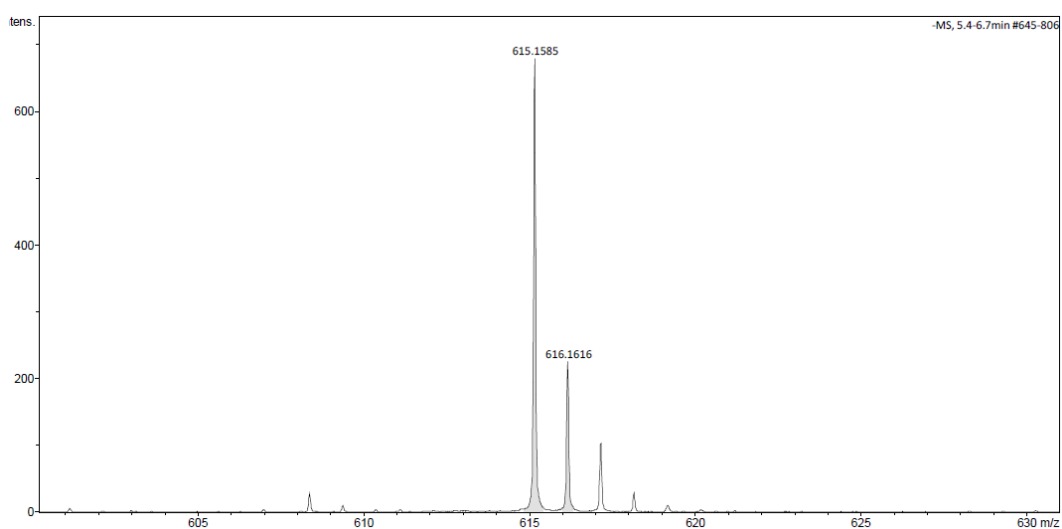


Figure S71 - A high-resolution mass spectrum (ESI<sup>-</sup>) obtained for dimeric species of compound **21** in methanol,  $m/z$  [M + M + H<sup>+</sup>].

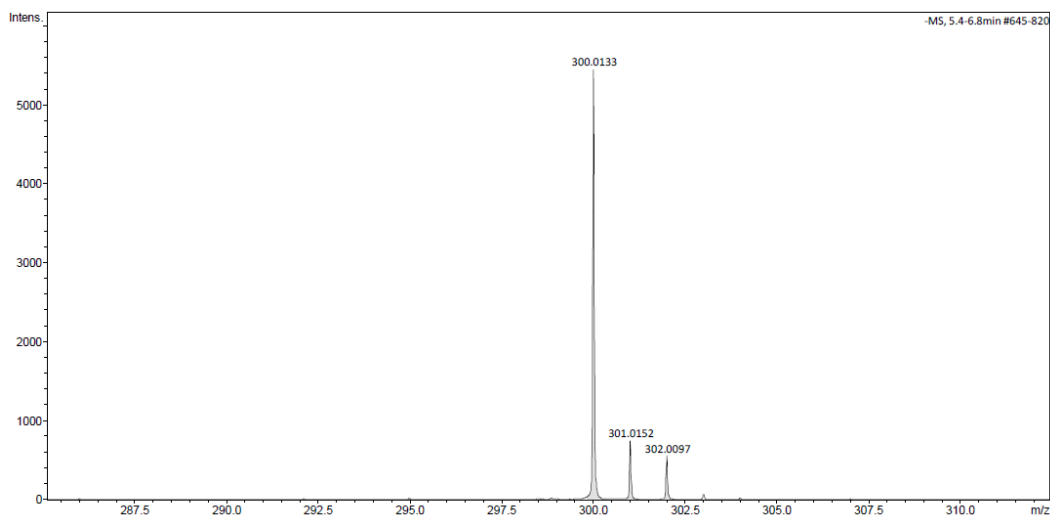


Figure S72 - A high-resolution mass spectrum (ESI<sup>-</sup>) obtained for compound **22** in methanol,  $m/z$  [M].

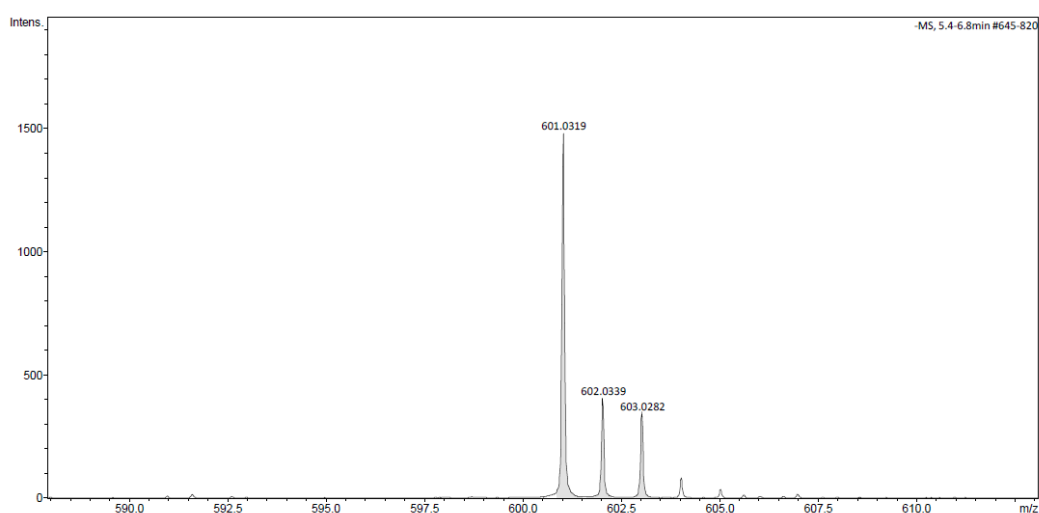


Figure S73 - A high-resolution mass spectrum (ESI<sup>-</sup>) obtained for dimeric species of compound **22** in methanol,  $m/z$  [M + M + H<sup>+</sup>].

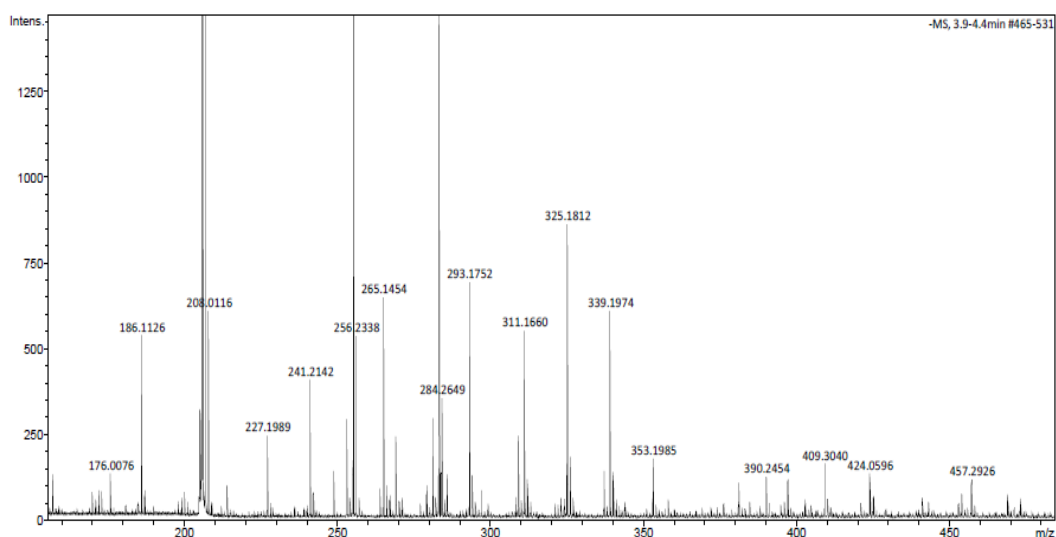


Figure S74 - A high-resolution mass spectrum (ESI<sup>-</sup>) obtained for compound **23** in methanol,  $m/z$  [M + C<sub>2</sub>H<sub>4</sub>].

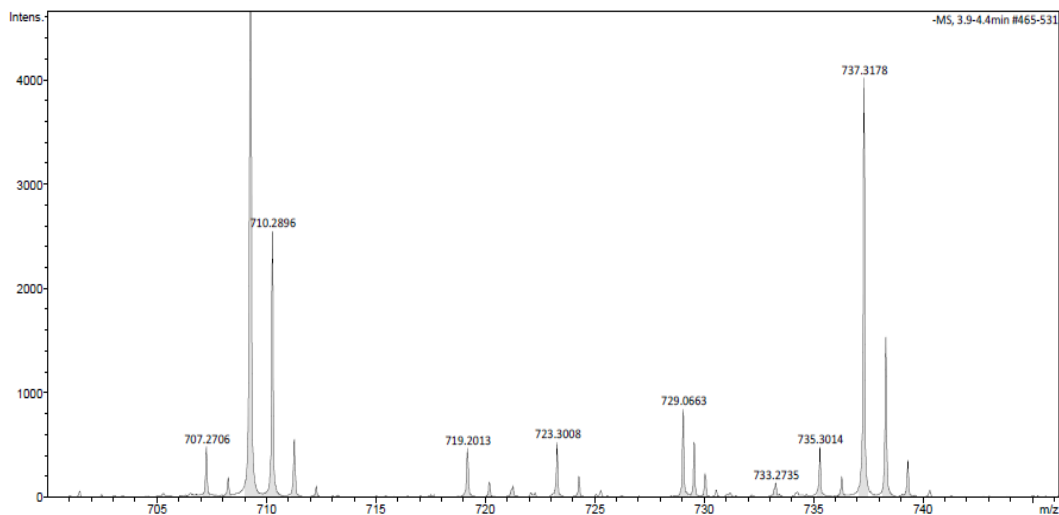


Figure S75 – A high-resolution mass spectrum (ESI<sup>-</sup>) obtained for dimeric species of compound **23** in methanol,  $m/z$  [ $M^- + M + H^+$ ].

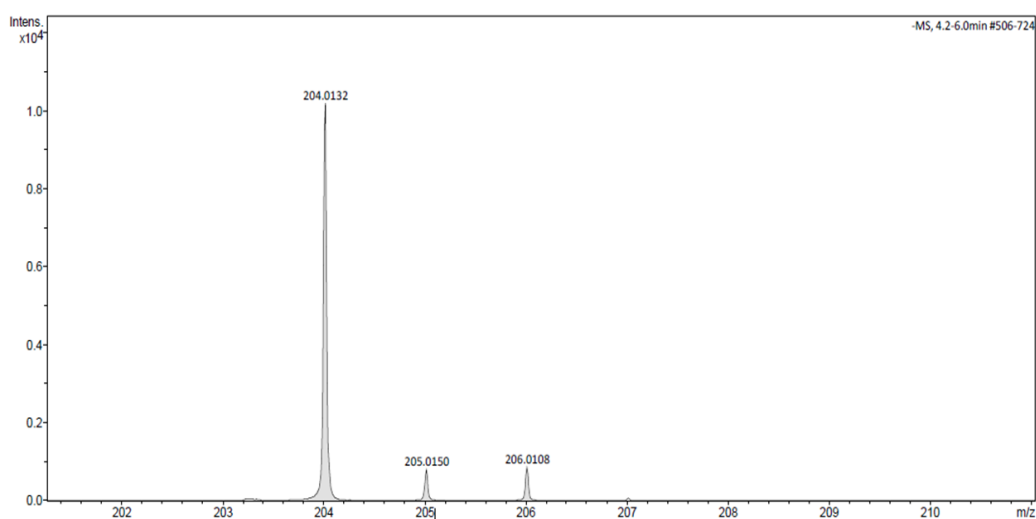


Figure S76 - A high-resolution mass spectrum (ESI<sup>-</sup>) obtained for dimeric species of compound **24** in methanol,  $m/z$  [ $M$ ].

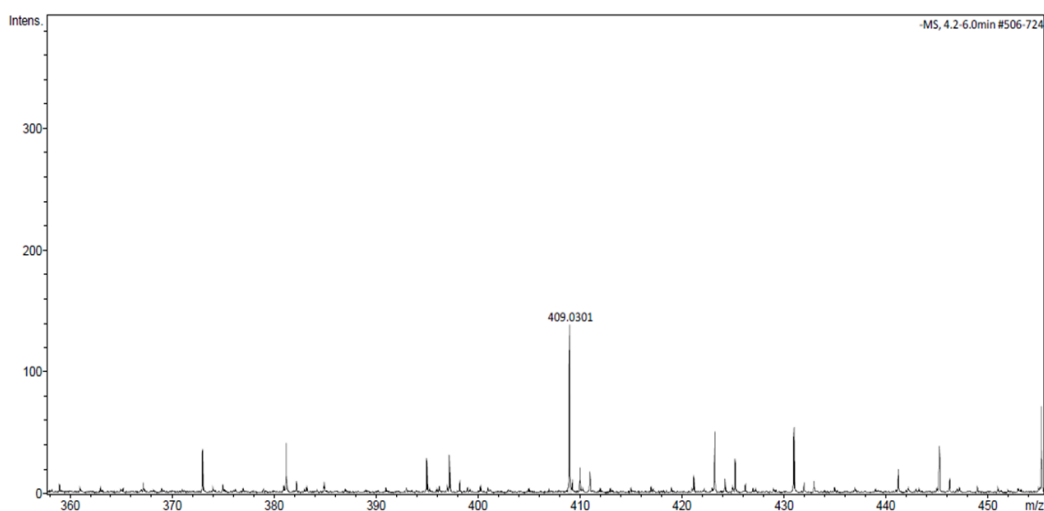


Figure S77 - A high-resolution mass spectrum (ESI<sup>-</sup>) obtained for dimeric species of compound **24** in methanol,  $m/z$  [ $M + M + H^+$ ].

### 9.8.1. Overview

Table S12 – High resolution ESI<sup>-</sup> mass spectrometry theoretical and experimentally derived values of **20 – 24**.

Compound	m/z [M]		m/z [M + M + H]	
	Theoretical	Actual	Theoretical	Actual
<b>20</b>	293.0602	293.0612	587.1204	587.1278
<b>21</b>	307.0758	307.0769	615.1516	615.1585
<b>22</b>	300.0118	300.0133	300.0236	601.0319
<b>23</b>	362.0275	390.2425	723.0550	723.3008
<b>24</b>	200.0084	204.0132	409.0168	409.0301

## 9.9. Rheology

### 9.9.1. Amplitude sweep

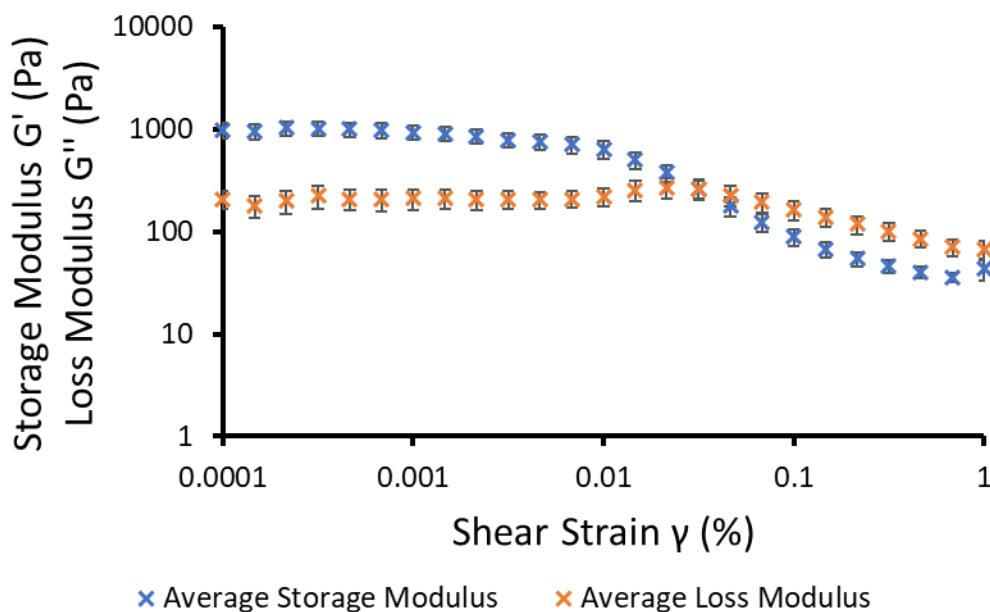


Figure S78 - Graph showing average results (n=3) from amplitude sweep experiments used to define the linear viscoelastic region of the sample at 298 K. Compound **23** (5 mg) in 1 mL of aqueous NaCl solution (0.505 M) (1 = 100 %).

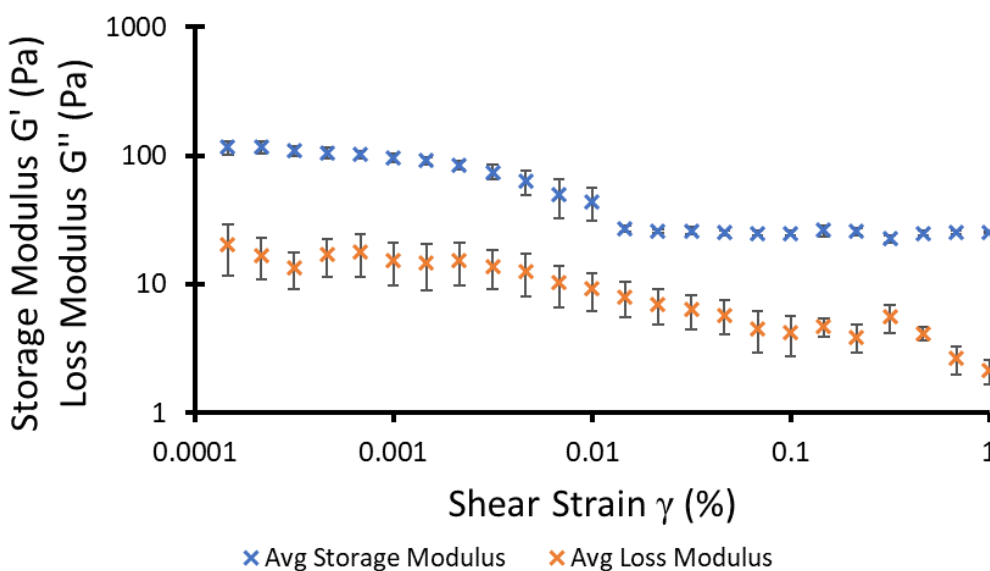


Figure S79 - Graph showing average results (n=3) from amplitude sweep experiments used to define the linear viscoelastic region of the sample at 298 K. Compound **23** (5 mg) in 1 mL of aqueous NaNO<sub>3</sub> solution (0.505 M) (1 = 100 %).

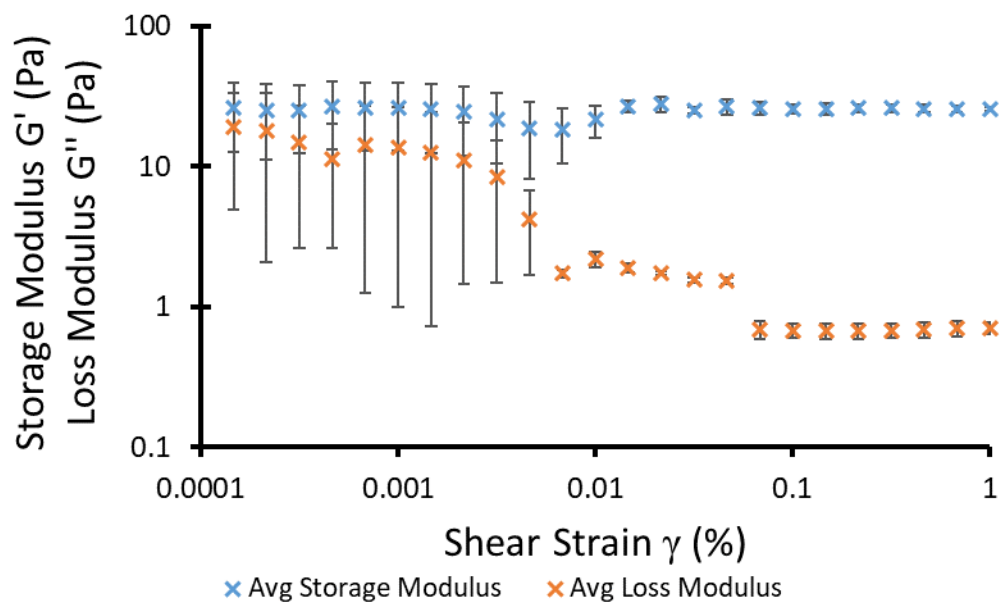


Figure S80 - Graph showing average results (n=3) from amplitude sweep experiments used to define the linear viscoelastic region of the sample at 298 K. Compound **23** (5 mg) in 1 mL of aqueous NaOBz solution (0.505 M) (1 = 100 %).

### 9.9.2. The best way to conduct experiments

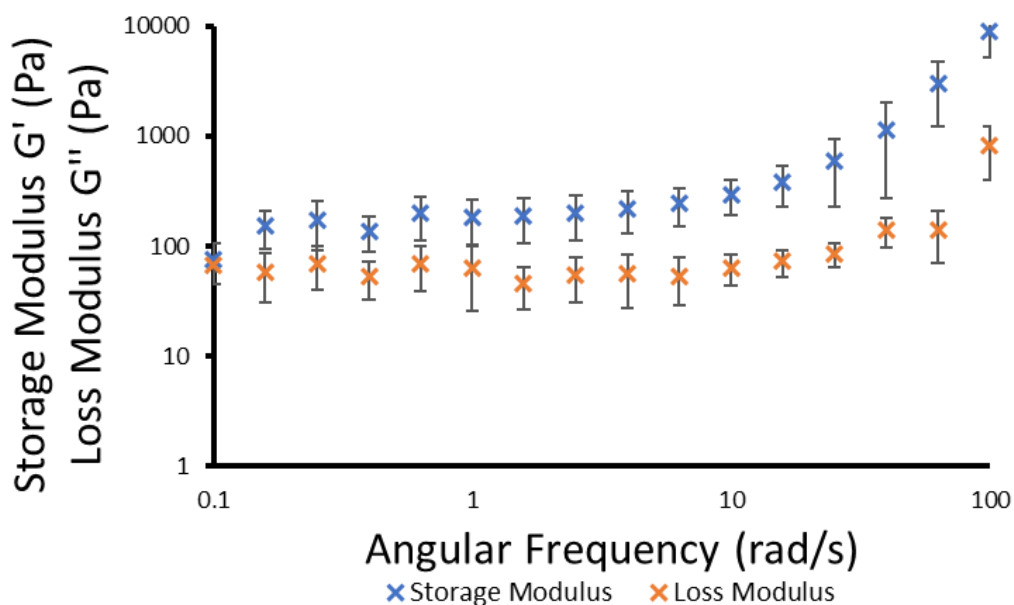


Figure S81 - Graph showing average results (n=3) from frequency sweep experiments obtained from the linear viscoelastic region under a constant shear strain ( $\gamma$ ) of 0.0277 % (298 K). Solution heated and gel formed around geometry. Compound **23** (5 mg) in 1 mL of aqueous NaCl solution (0.505 M) (1 = 100 %).

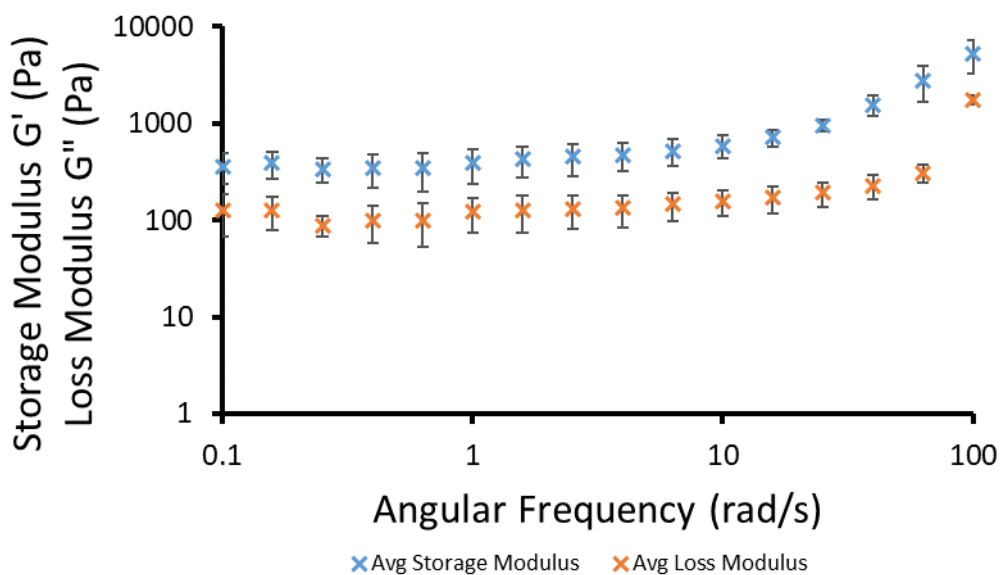


Figure S82 - Graph showing average results (n=3) from frequency sweep experiments obtained from the linear viscoelastic region under a constant shear strain ( $\gamma$ ) of 0.0277 % (298 K). Solution heated and gel formed before inserting geometry. Compound **23** (5 mg) in 1 mL of aqueous NaCl solution (0.505 M) (1 = 100 %).

### 9.9.3. Frequency sweep

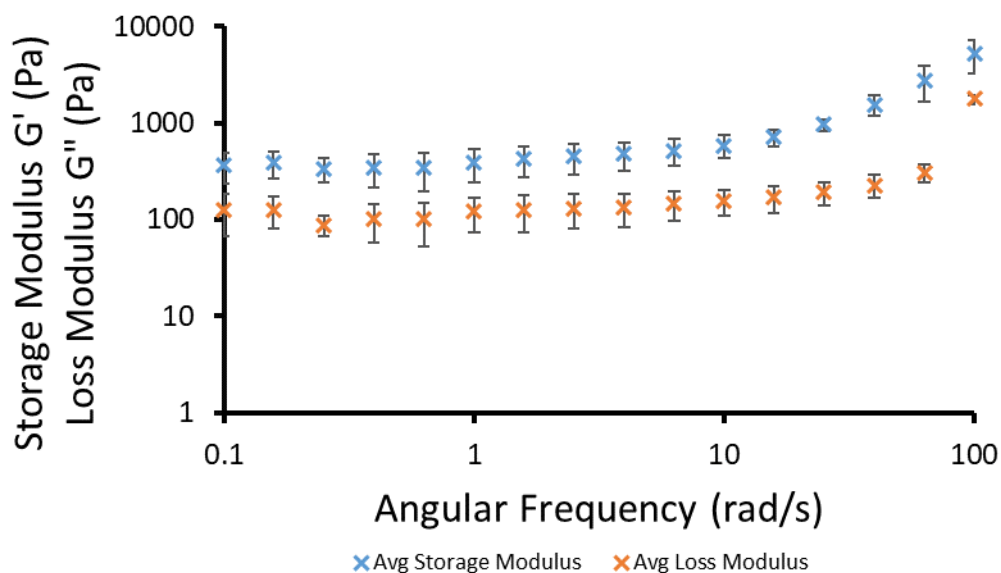


Figure S83 - Graph showing average results ( $n=3$ ) from frequency sweep experiments obtained from the linear viscoelastic region under a constant shear strain ( $\gamma$ ) of 0.0277 % (298 K). Compound **23** (5 mg) in 1 mL of aqueous NaCl solution (0.505 M).

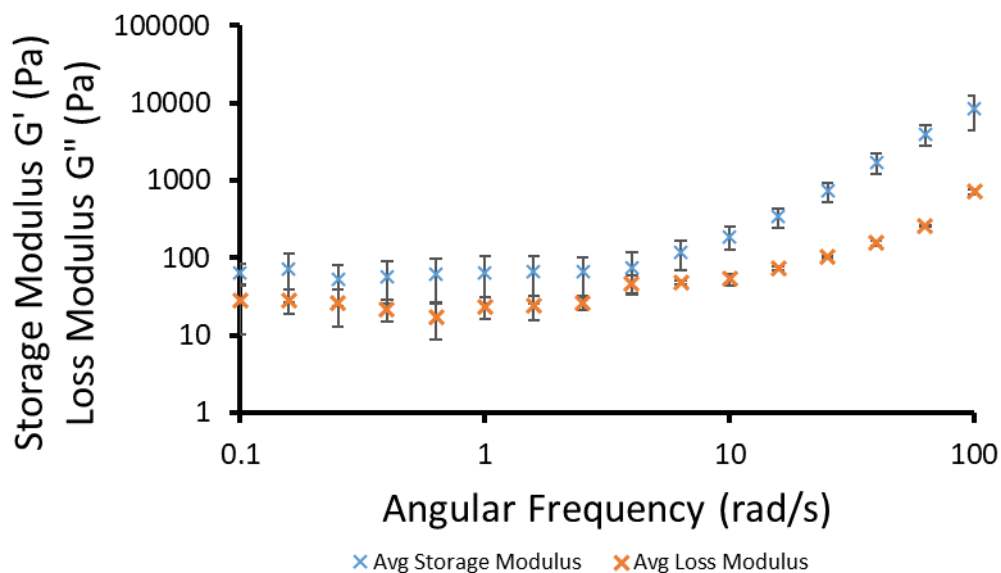


Figure S84 - Graph showing average results ( $n=3$ ) from frequency sweep experiments obtained from the linear viscoelastic region under a constant shear strain ( $\gamma$ ) of 0.0195 % (298 K). Compound **23** (5 mg) in 1 mL of aqueous NaNO<sub>3</sub> solution (0.505 M).

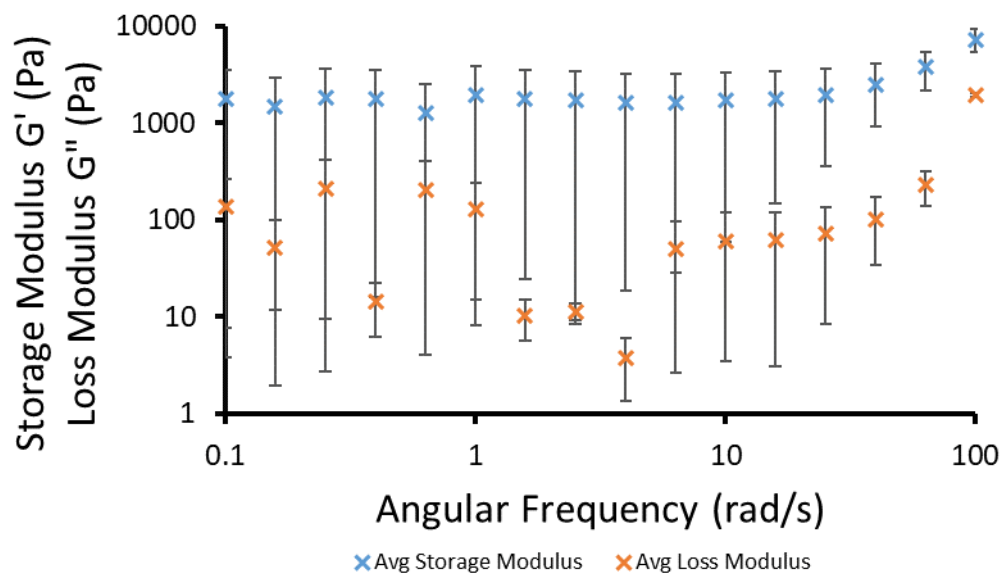


Figure S85 - Graph showing average results (n=3) from frequency sweep experiments obtained from the linear viscoelastic region under a constant shear strain ( $\gamma$ ) of 0.0720 % (298 K). Compound **23** (5 mg) in 1 mL of aqueous NaOBz solution (0.505 M).

#### 9.9.4. Test of oscillatory stress

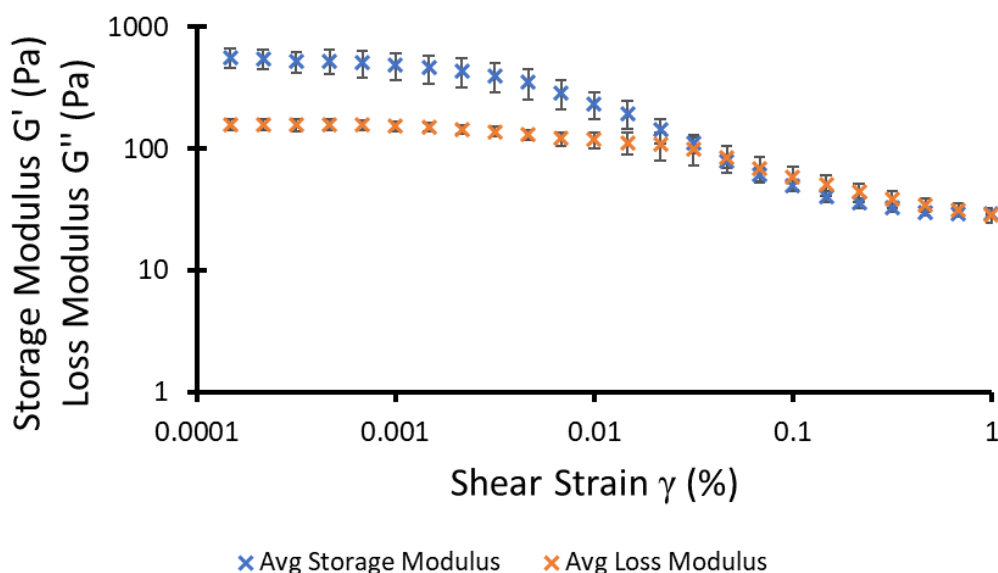


Figure S86 - Graph showing average results (n=3) from amplitude sweep experiments used to define the linear viscoelastic region of the sample at 298 K. Compound **23** (5 mg) in 1 mL of aqueous NaNO<sub>3</sub> solution (0.505 M) (1 = 100 %).

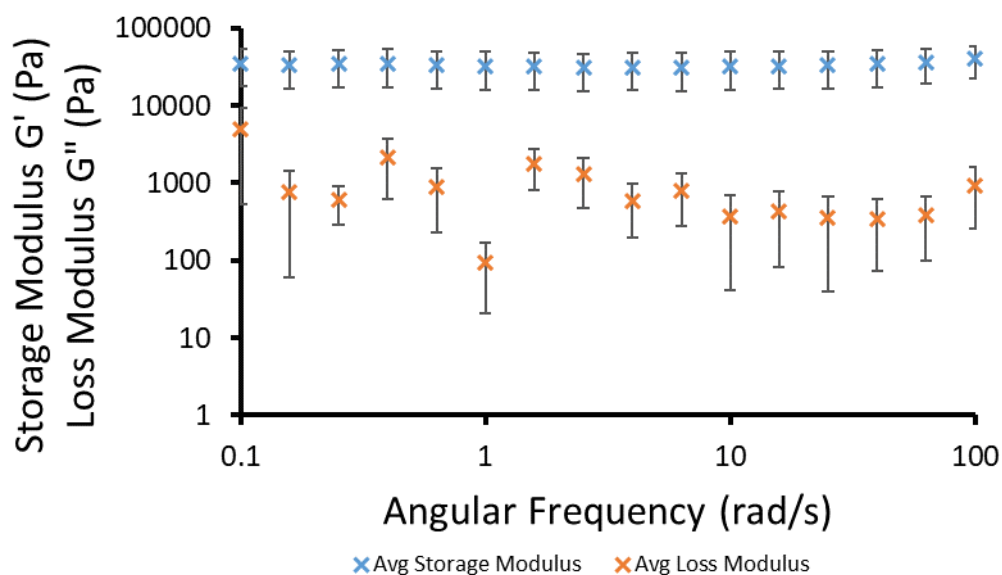


Figure S87 - Graph showing average results (n=3) from frequency sweep experiments obtained from the linear viscoelastic region under a constant shear strain ( $\gamma$ ) of 0.0209 % (298 K), after running an amplitude sweep on the same sample (Figure S86). Compound **23** (5 mg) in 1 mL of aqueous NaNO<sub>3</sub> solution (0.505 M).

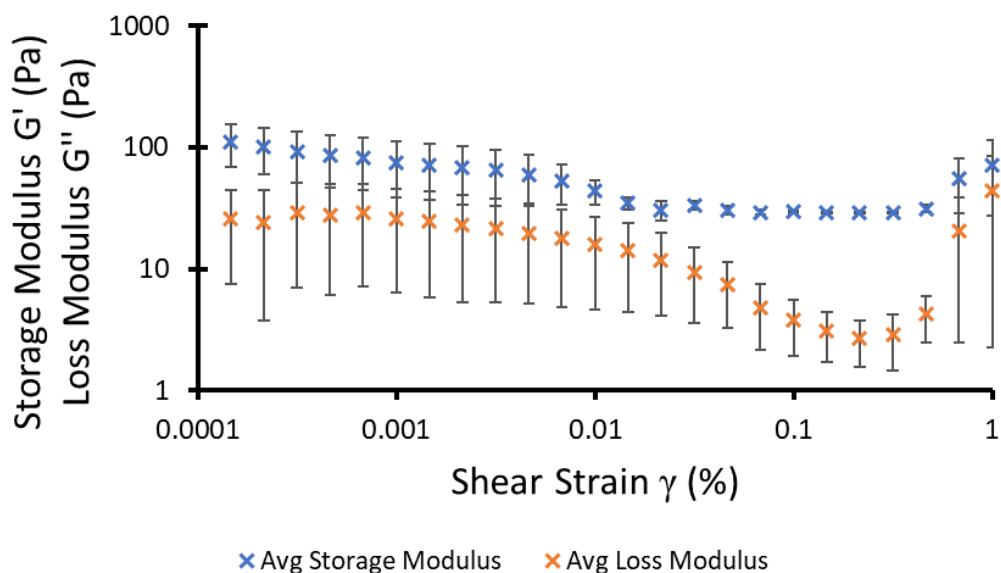


Figure S88 - Graph showing average results (n=3) from amplitude sweep experiments used to define the linear viscoelastic region of the sample at 298 K. Compound **23** (5 mg) in 1 mL of aqueous NaOBz solution (0.505 M) (1 = 100 %).

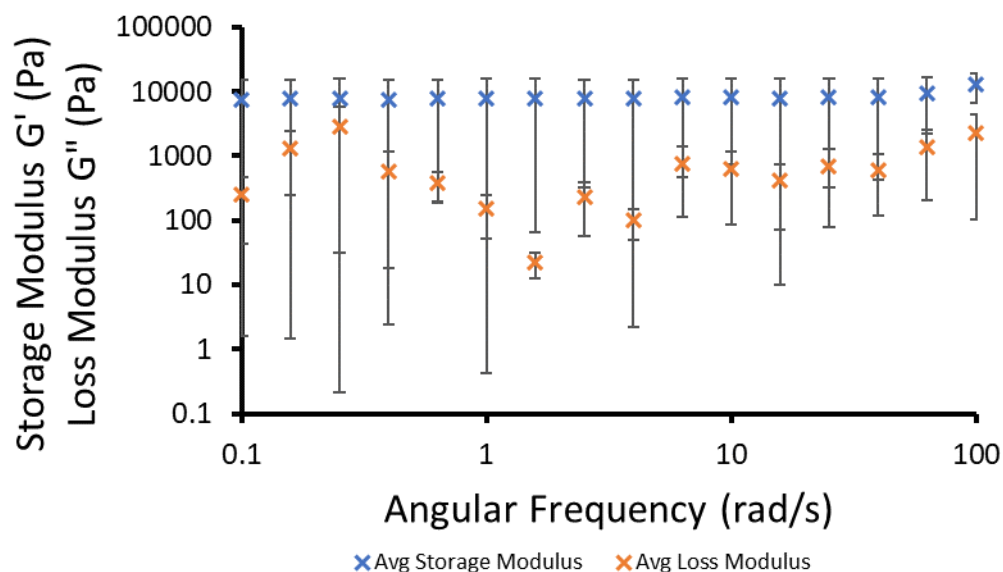


Figure S89 - Graph showing average results (n=3) from frequency sweep experiments obtained from the linear viscoelastic region under a constant shear strain ( $\gamma$ ) of 0.0174 % (298 K), after running an amplitude sweep on the same sample (Figure S88). Compound **23** (5 mg) in 1 mL of aqueous NaOBz solution (0.505 M).

#### 9.9.5. Sonication test

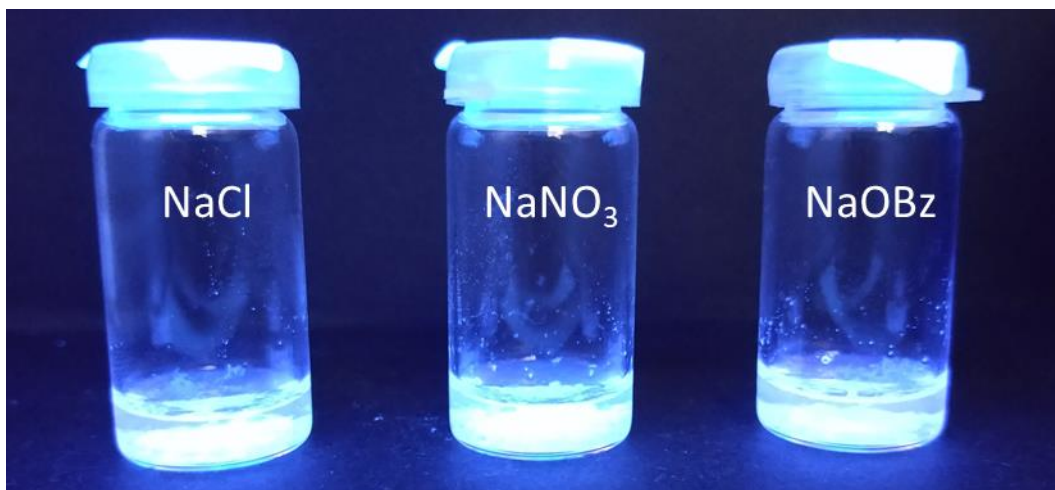


Figure S90 – Sonication test at 0 minutes. Compound **23** (5 mg, 1 mL) in NaCl, NaNO<sub>3</sub> and NaOBz imaged under UV irradiation (test no. 1).

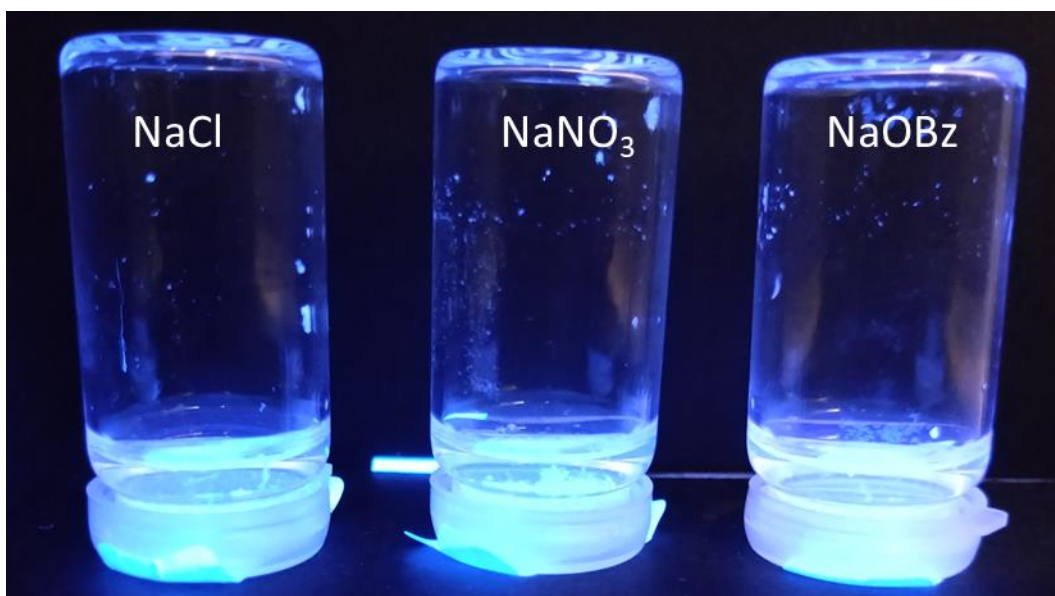


Figure S91 - Sonication test at 0 minutes. Compound **23** (5 mg, 1 mL) in NaCl, NaNO<sub>3</sub> and NaOBz inverted imaged under UV irradiation (test no. 1).

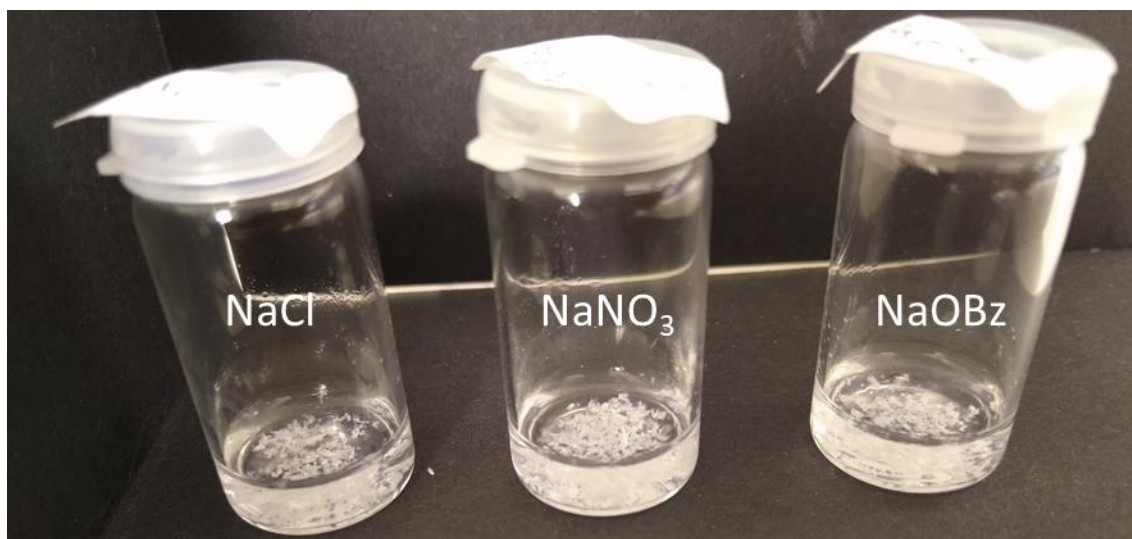


Figure S92 - Sonication test at 0 minutes. Compound **23** (5 mg, 1 mL) in NaCl, NaNO<sub>3</sub> and NaOBz (test no. 1).

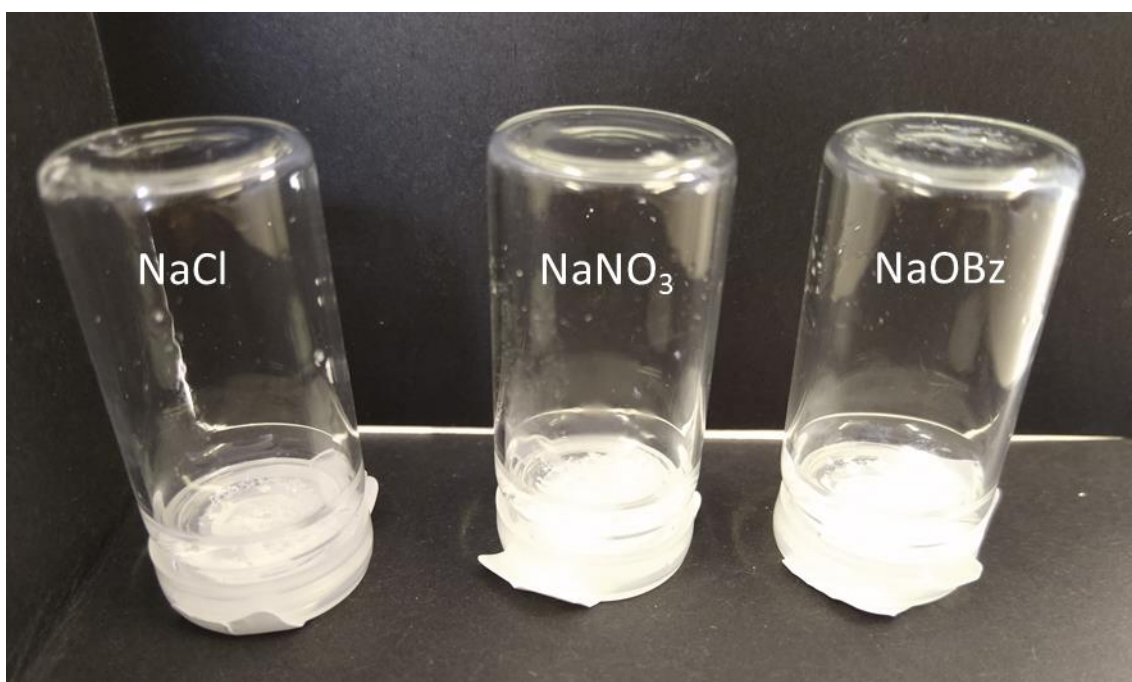


Figure S93 - Sonication test at 0 minutes. Compound **23** (5 mg, 1 mL) in NaCl, NaNO<sub>3</sub> and NaOBz inverted (test no. 1).

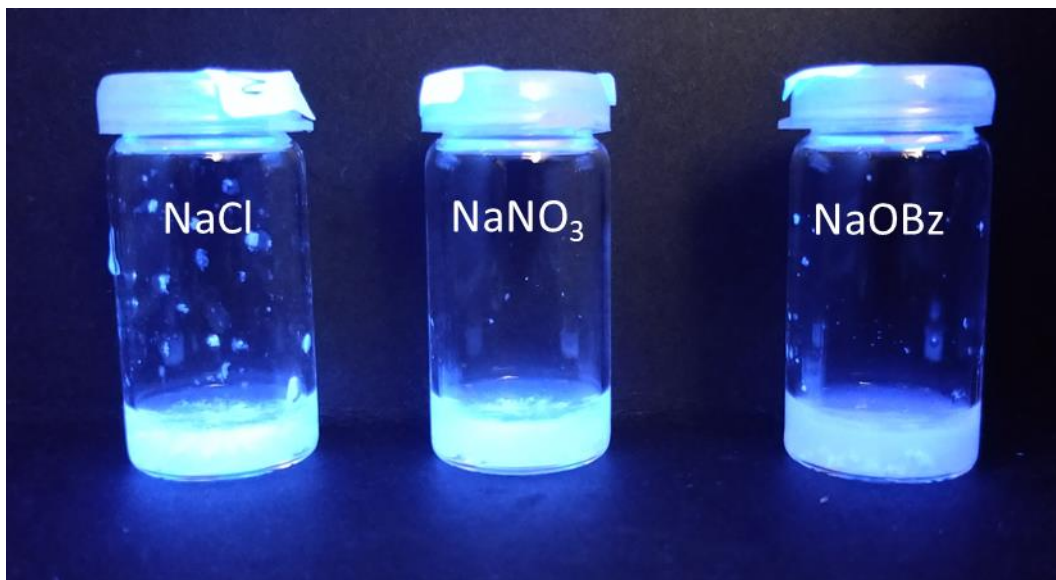


Figure S94 - Sonication test at 5 minutes. Compound **23** (5 mg, 1 mL) in NaCl, NaNO<sub>3</sub> and NaOBz imaged under UV irradiation (test no. 1).

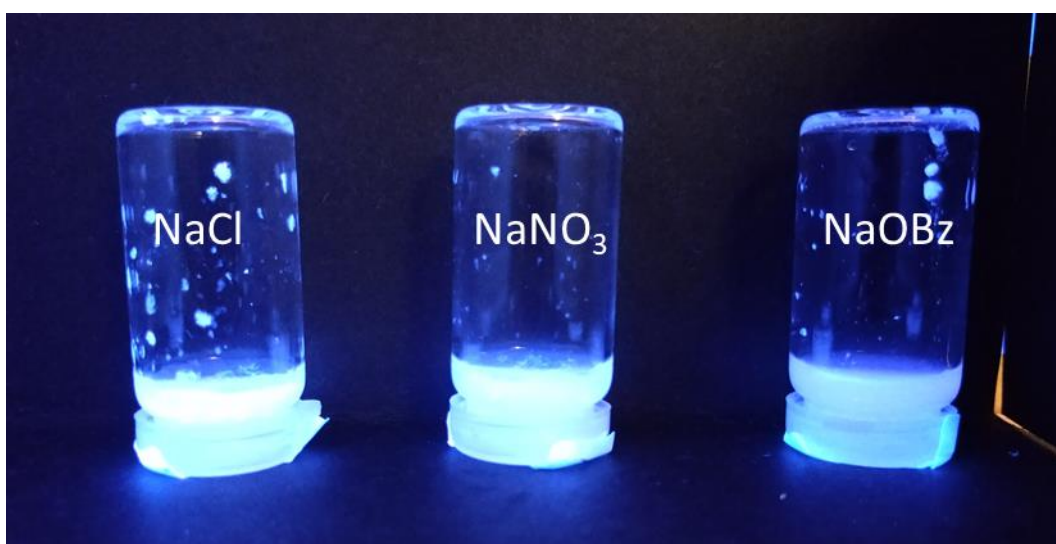


Figure S95 - Sonication test at 5 minutes. Compound **23** (5 mg, 1 mL) in NaCl, NaNO<sub>3</sub> and NaOBz inverted imaged under UV irradiation (test no. 1).

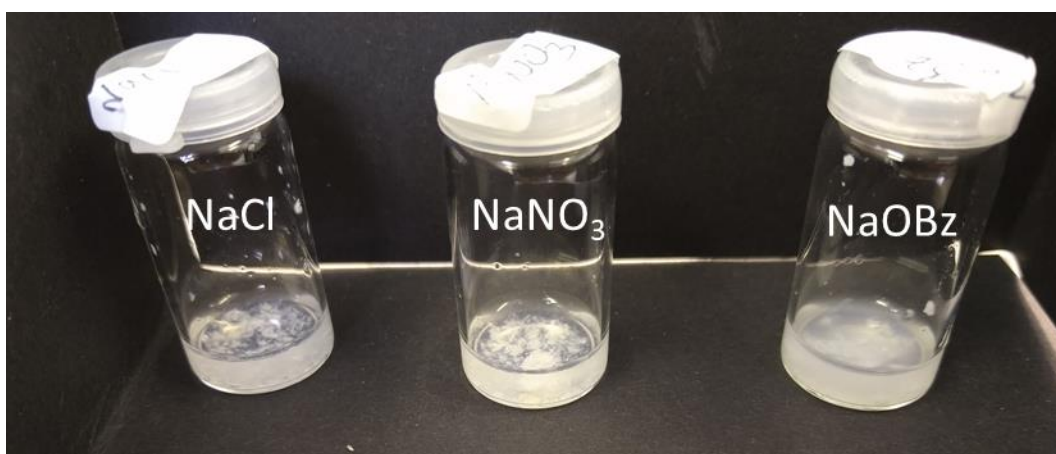


Figure S96 - Sonication test at 5 minutes. Compound **23** (5 mg, 1 mL) in NaCl, NaNO<sub>3</sub> and NaOBz (test no. 1).

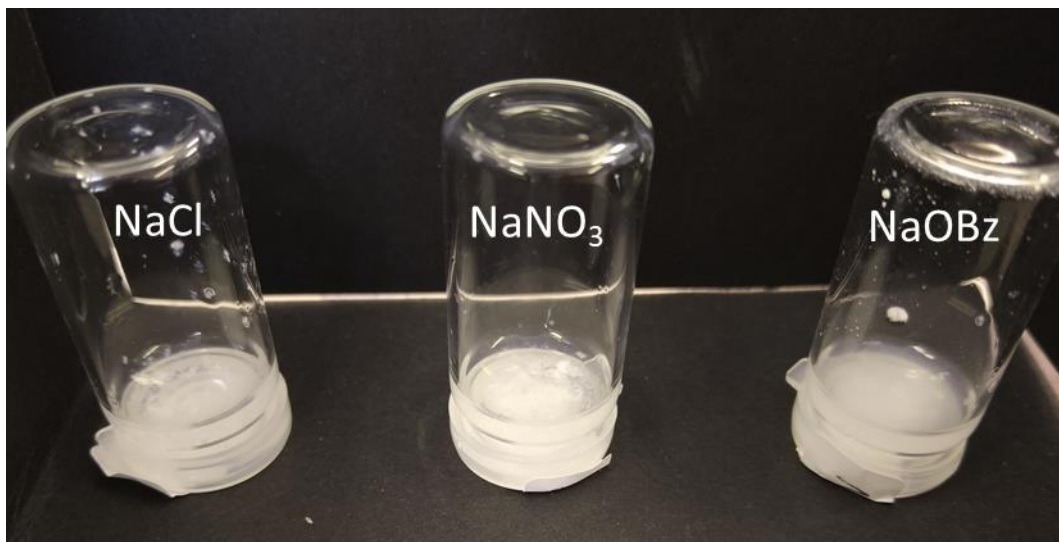


Figure S97 - Sonication test at 5 minutes. Compound **23** (5 mg, 1 mL) in NaCl, NaNO<sub>3</sub> and NaOBz inverted (test no. 1).

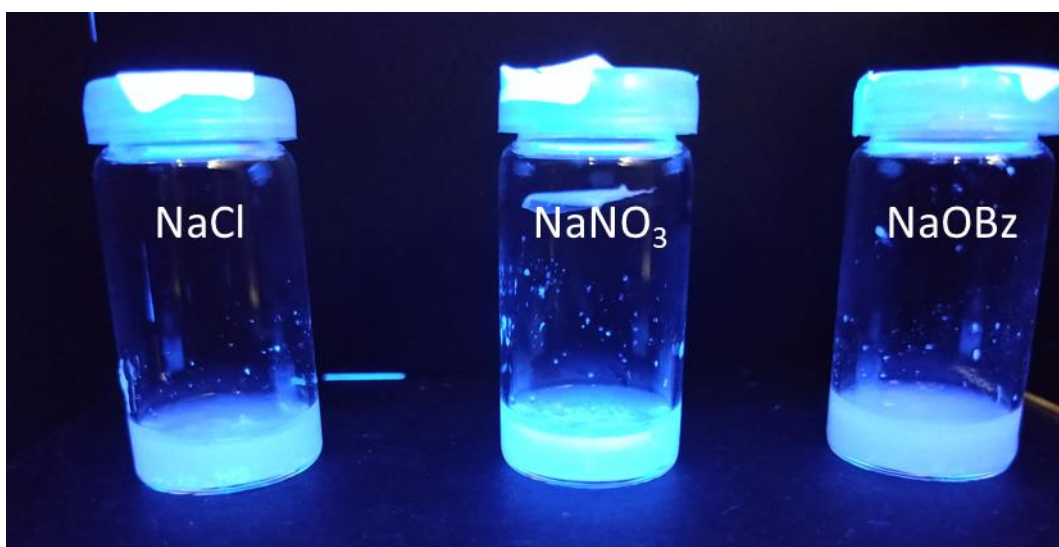


Figure S98 - Sonication test at 10 minutes. Compound **23** (5 mg, 1 mL) in NaCl, NaNO<sub>3</sub> and NaOBz imaged under UV irradiation (test no. 1).

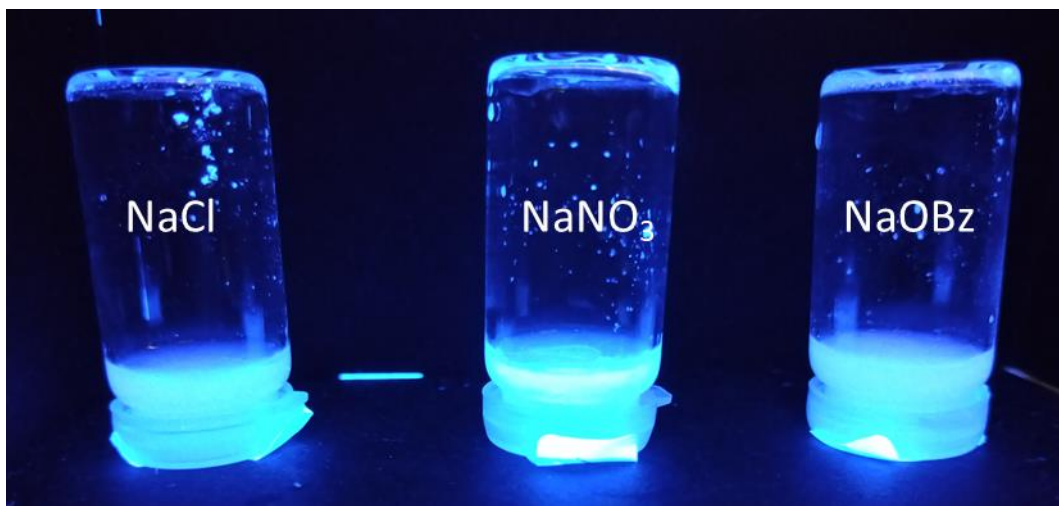


Figure S99 - Sonication test at 10 minutes. Compound **23** (5 mg, 1 mL) in NaCl, NaNO<sub>3</sub> and NaOBz inverted imaged under UV irradiation (test no. 1).

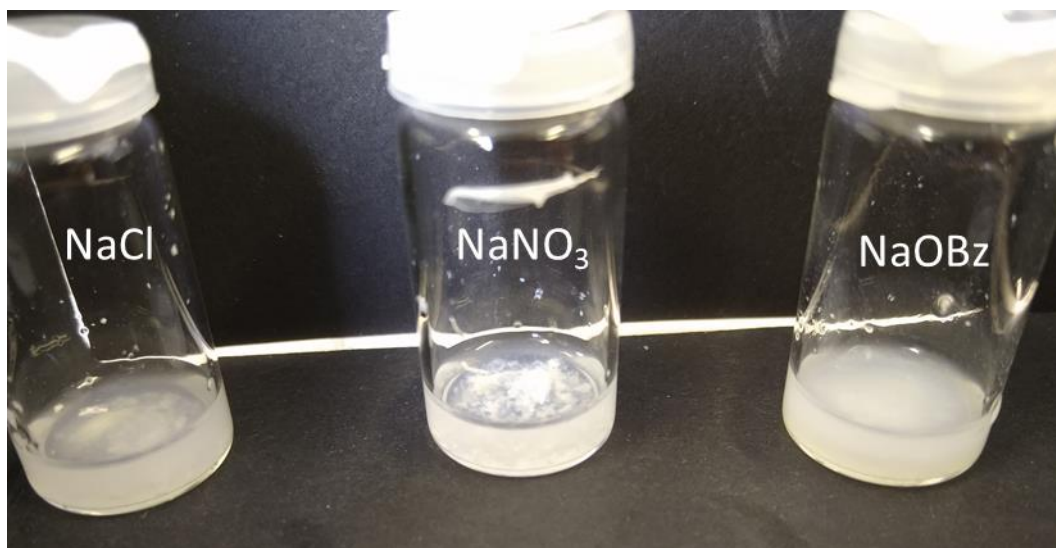


Figure S100 - Sonication test at 10 minutes. Compound **23** (5 mg, 1 mL) in NaCl, NaNO<sub>3</sub> and NaOBz (test no. 1).

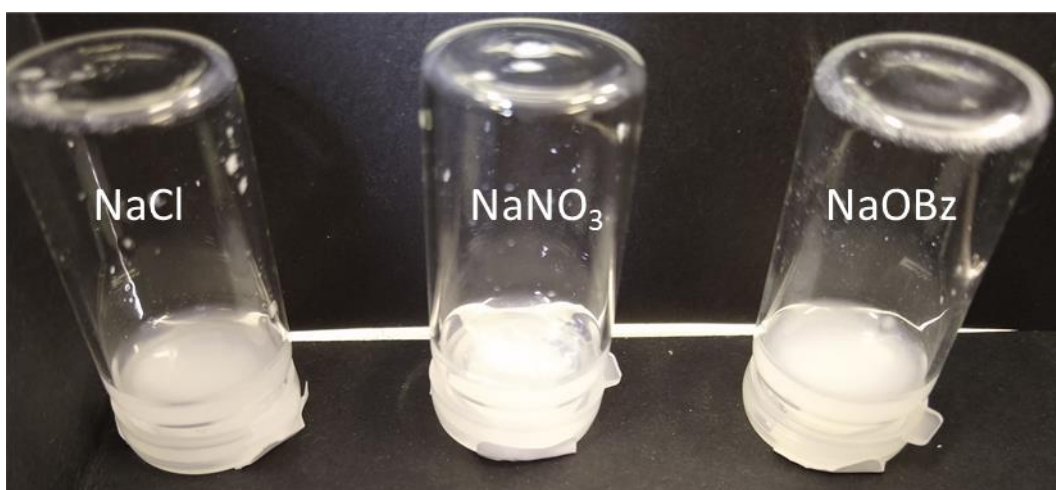


Figure S101 - Sonication test at 10 minutes. Compound **23** (5 mg, 1 mL) in NaCl, NaNO<sub>3</sub> and NaOBz inverted (test no. 1).

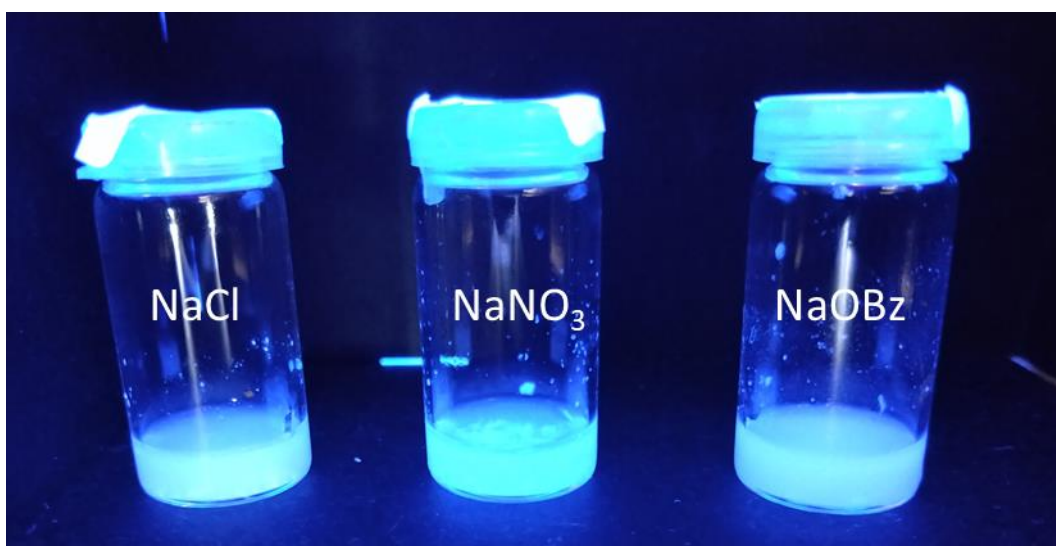


Figure S102 - Sonication test at 15 minutes. Compound **23** (5 mg, 1 mL) in NaCl, NaNO<sub>3</sub> and NaOBz imaged under UV irradiation (test no. 1).

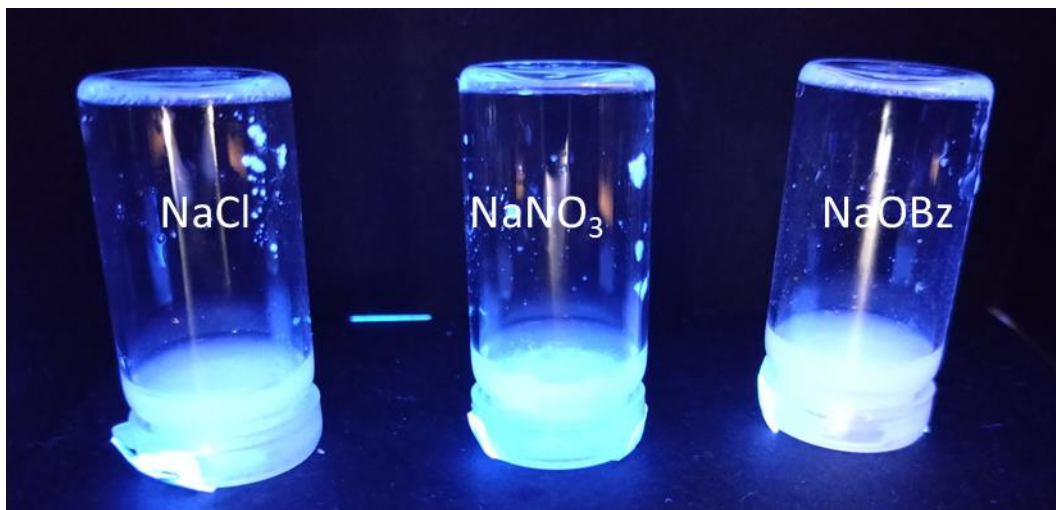


Figure S103 - Sonication test at 15 minutes. Compound **23** (5 mg, 1 mL) in NaCl, NaNO<sub>3</sub> and NaOBz inverted imaged under UV irradiation (test no. 1).

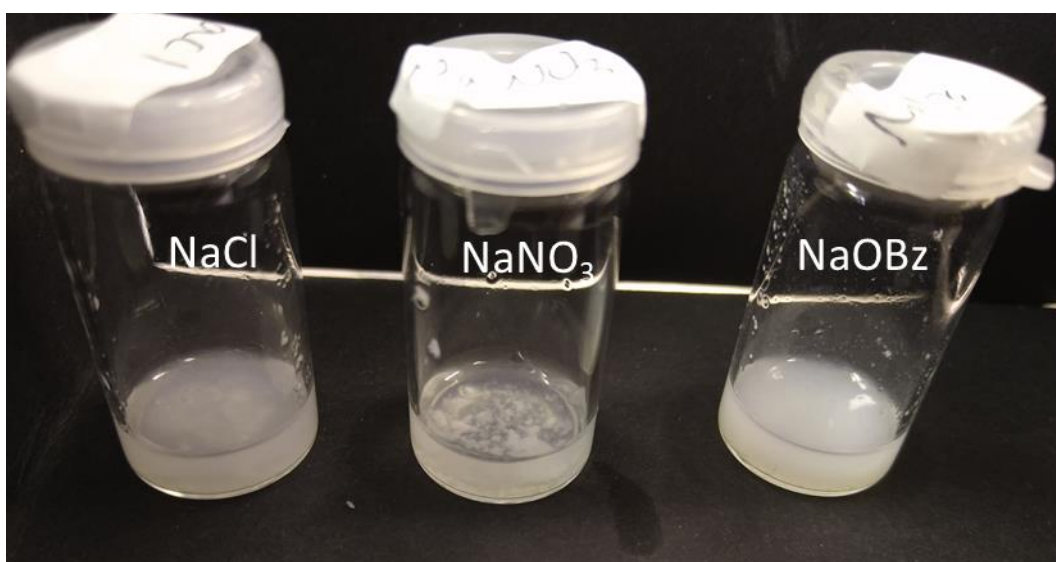


Figure S104 - Sonication test at 15 minutes. Compound **23** (5 mg, 1 mL) in NaCl, NaNO<sub>3</sub> and NaOBz (test no. 1).

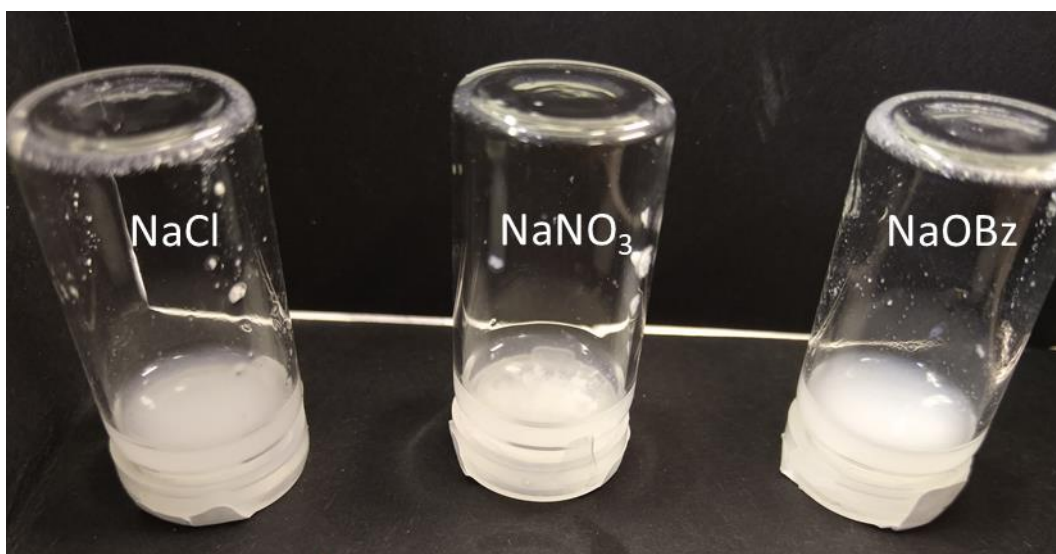


Figure S105 - Sonication test at 15 minutes. Compound **23** (5 mg, 1 mL) in NaCl, NaNO<sub>3</sub> and NaOBz inverted (test no. 1).

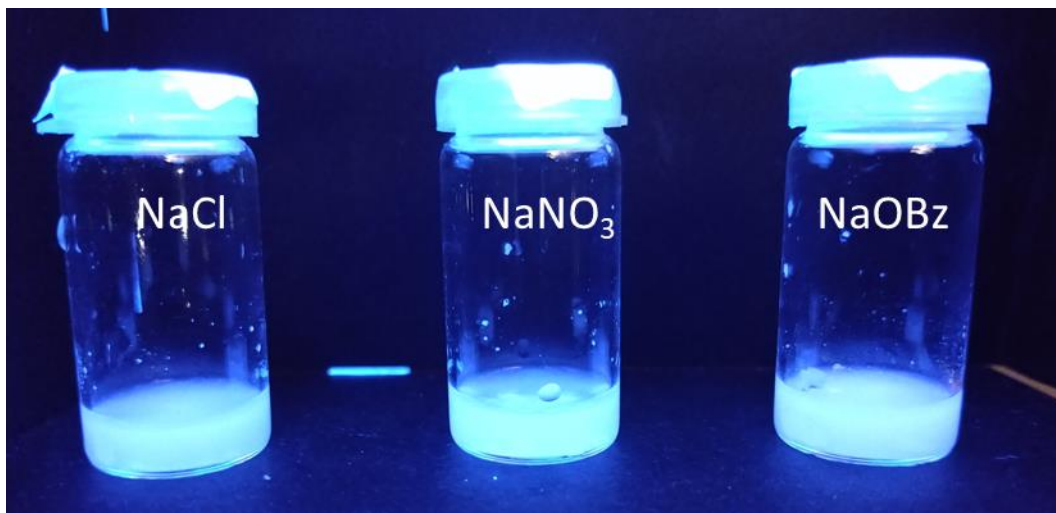


Figure S106 - Sonication test at 20 minutes. Compound **23** (5 mg, 1 mL) in NaCl, NaNO<sub>3</sub> and NaOBz imaged under UV irradiation (test no. 1).

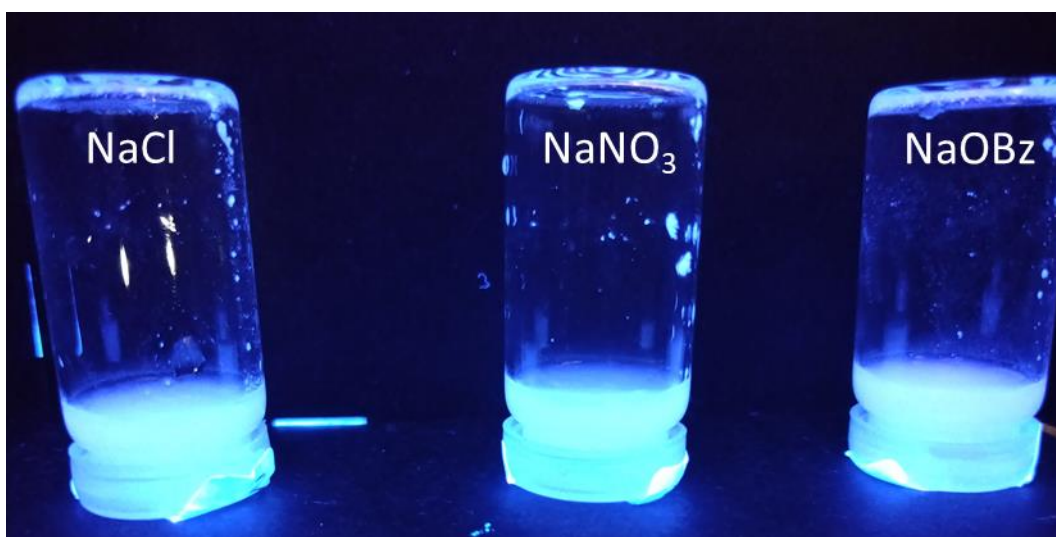


Figure S107 - Sonication test at 20 minutes. Compound **23** (5 mg, 1 mL) in NaCl, NaNO<sub>3</sub> and NaOBz inverted imaged under UV irradiation (test no. 1).

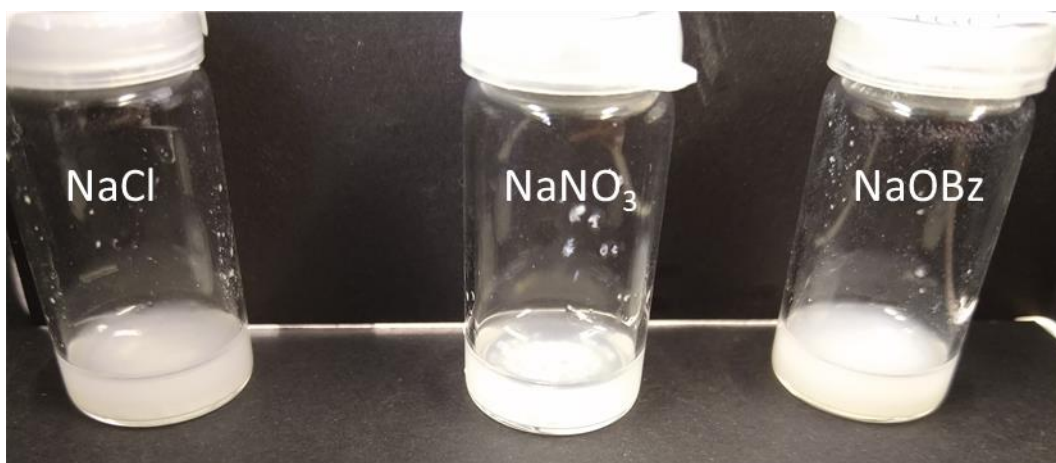


Figure S108 - Sonication test at 20 minutes. Compound **23** (5 mg, 1 mL) in NaCl, NaNO<sub>3</sub> and NaOBz (test no. 1).

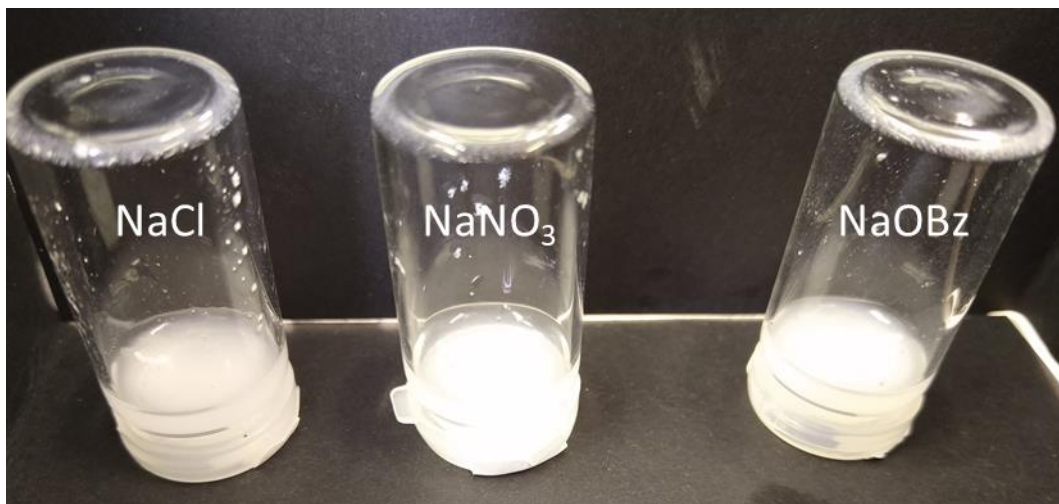


Figure S109 - Sonication test at 20 minutes. Compound **23** (5 mg, 1 mL) in NaCl, NaNO<sub>3</sub> and NaOBz inverted (test no. 1).

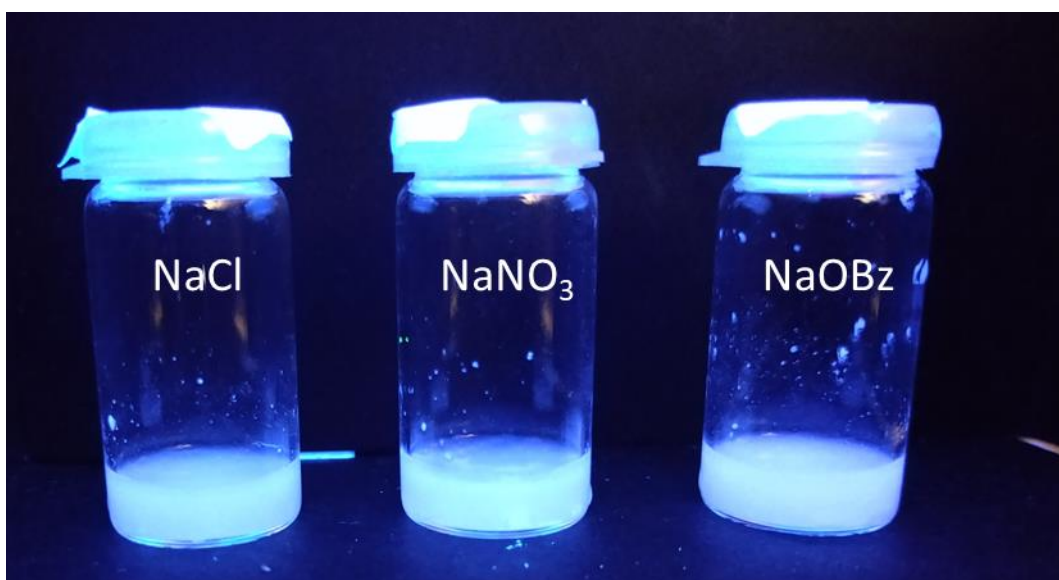


Figure S110 - Sonication test at 25 minutes. Compound **23** (5 mg, 1 mL) in NaCl, NaNO<sub>3</sub> and NaOBz imaged under UV irradiation (test no. 1).

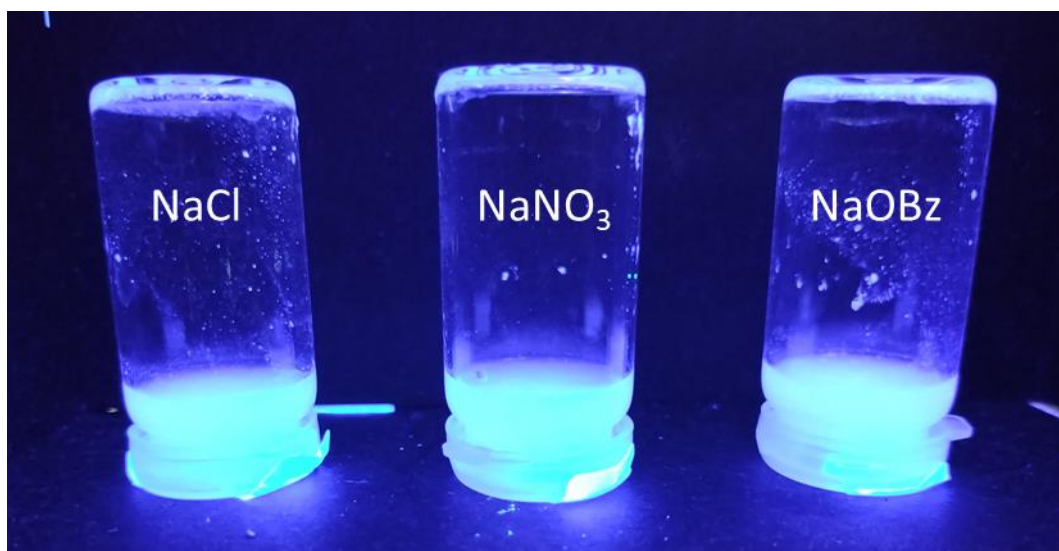


Figure S111 - Sonication test at 25 minutes. Compound **23** (5 mg, 1 mL) in NaCl, NaNO<sub>3</sub> and NaOBz inverted imaged under UV irradiation (test no. 1).

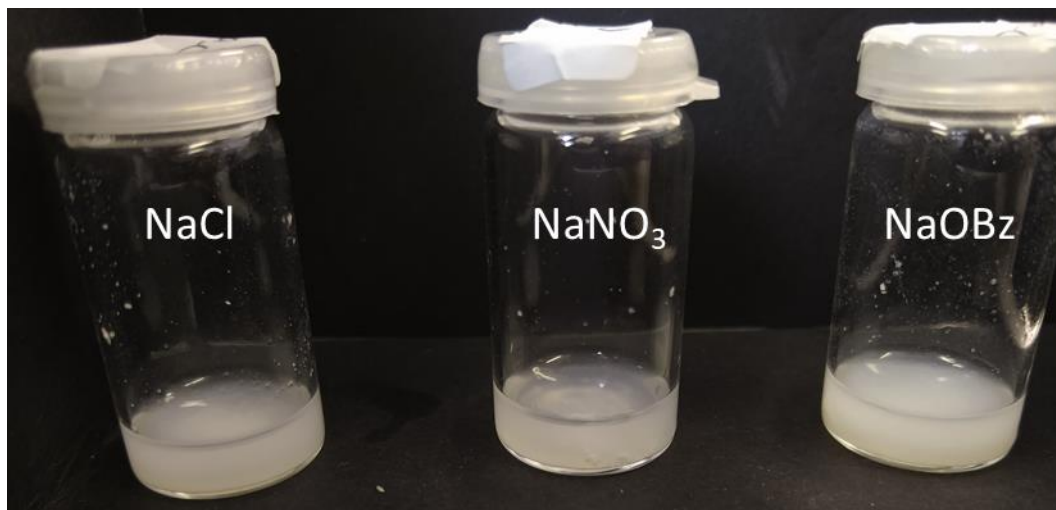


Figure S112 - Sonication test at 25 minutes. Compound **23** (5 mg, 1 mL) in NaCl, NaNO<sub>3</sub> and NaOBz (test no. 1).

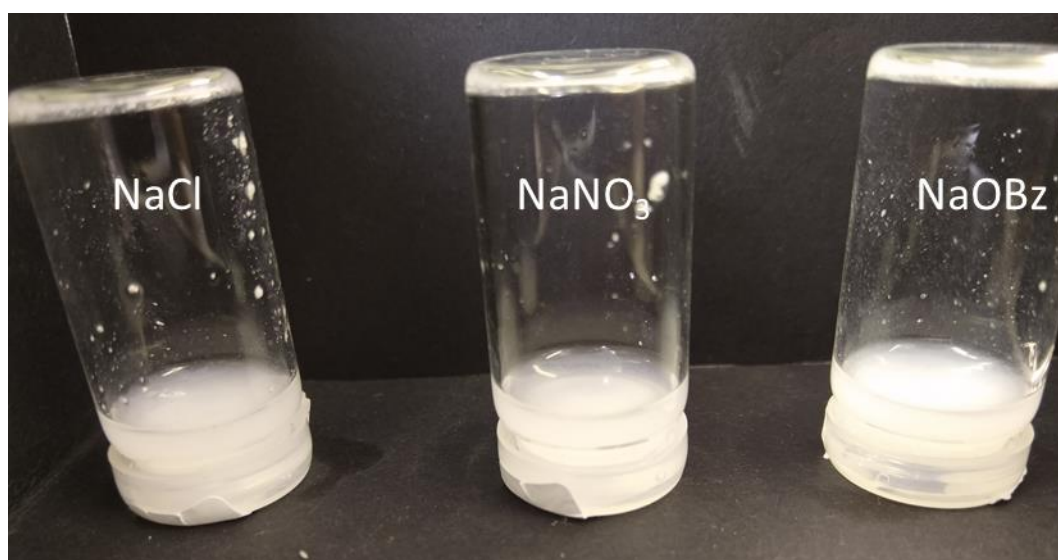


Figure S113 - Sonication test at 25 minutes. Compound **23** (5 mg, 1 mL) in NaCl, NaNO<sub>3</sub> and NaOBz inverted (test no. 1).

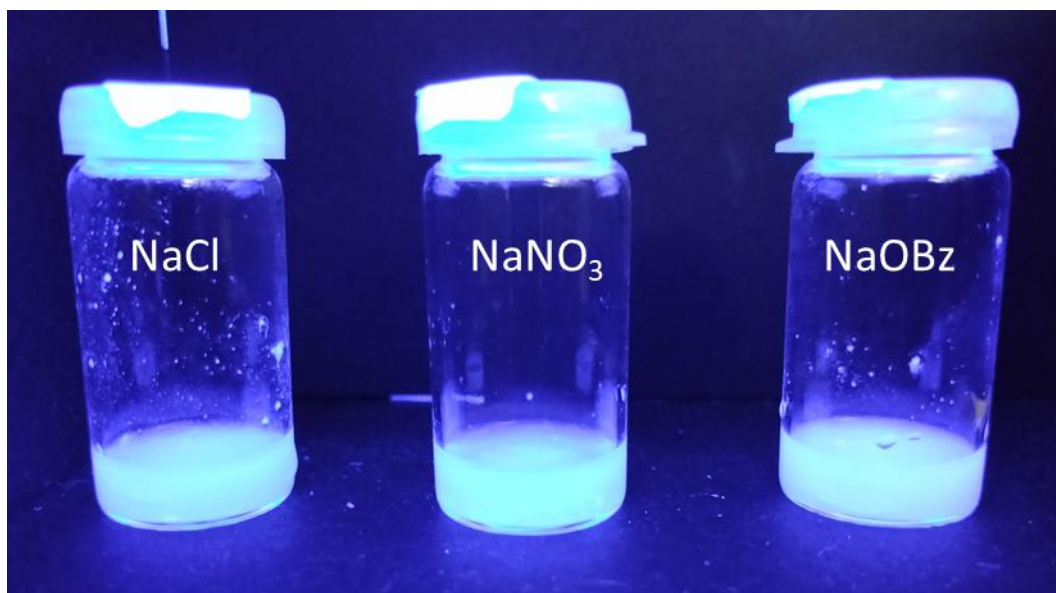


Figure S114 - Sonication test at 30 minutes. Compound **23** (5 mg, 1 mL) in NaCl, NaNO<sub>3</sub> and NaOBz imaged under UV irradiation (test no. 1).

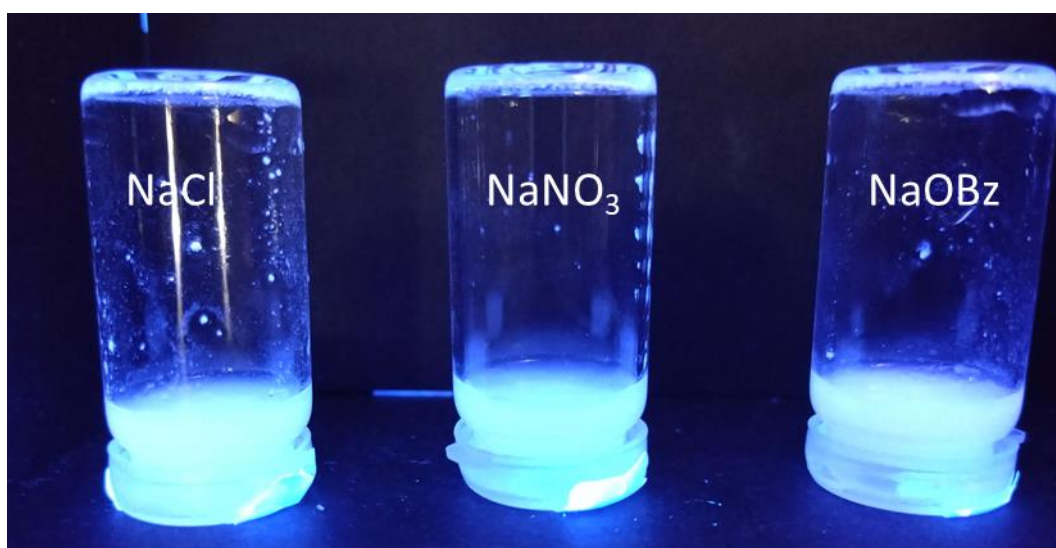


Figure S115 - Sonication test at 30 minutes. Compound **23** (5 mg, 1 mL) in NaCl, NaNO<sub>3</sub> and NaOBz inverted imaged under UV irradiation (test no. 1).

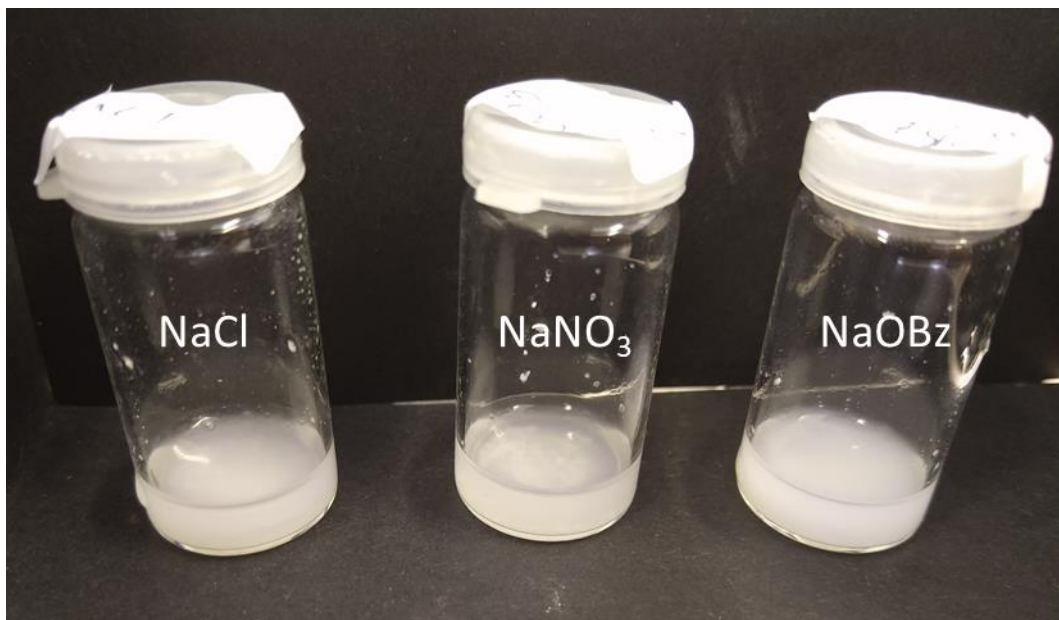


Figure S116 - Sonication test at 30 minutes. Compound **23** (5 mg, 1 mL) in NaCl, NaNO<sub>3</sub> and NaOBz (test no. 1).

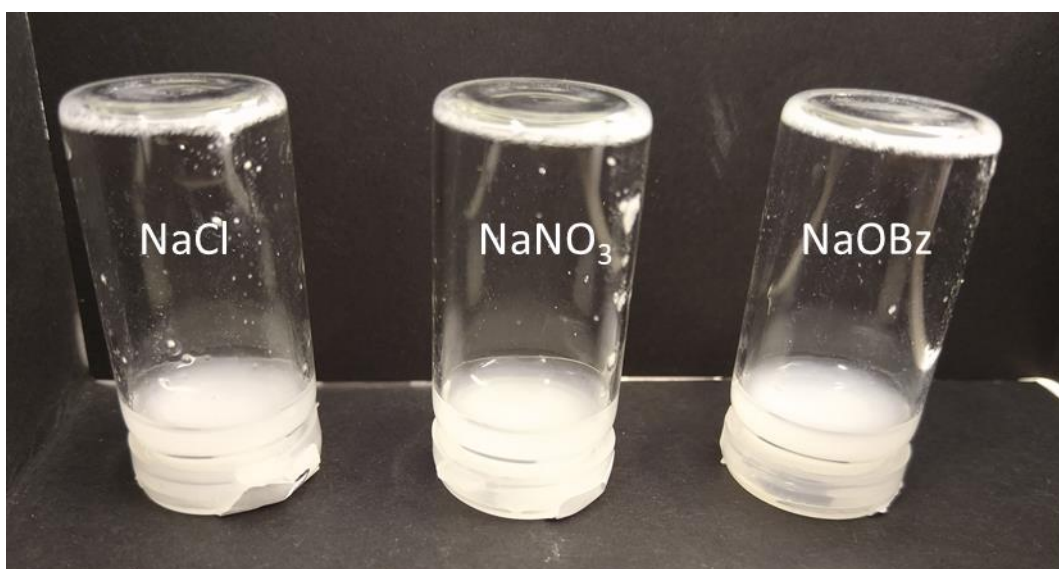


Figure S117 - Sonication test at 30 minutes. Compound **23** (5 mg, 1 mL) in NaCl, NaNO<sub>3</sub> and NaOBz inverted (test no. 1).

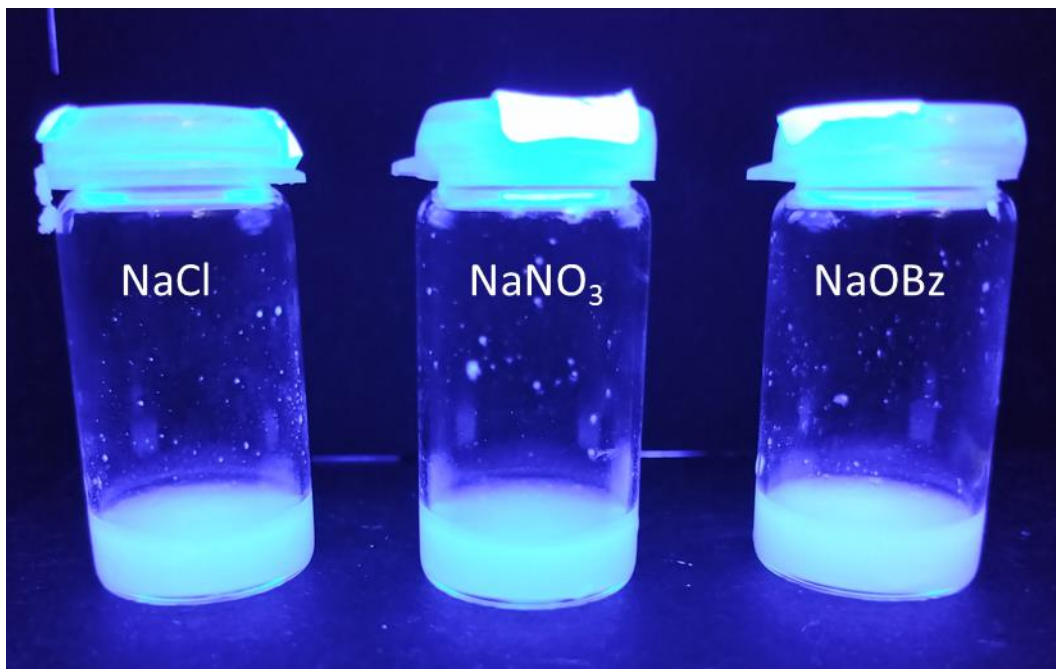


Figure S118 - Sonication test at 40 minutes. Compound **23** (5 mg, 1 mL) in NaCl, NaNO<sub>3</sub> and NaOBz imaged under UV irradiation (test no. 1).

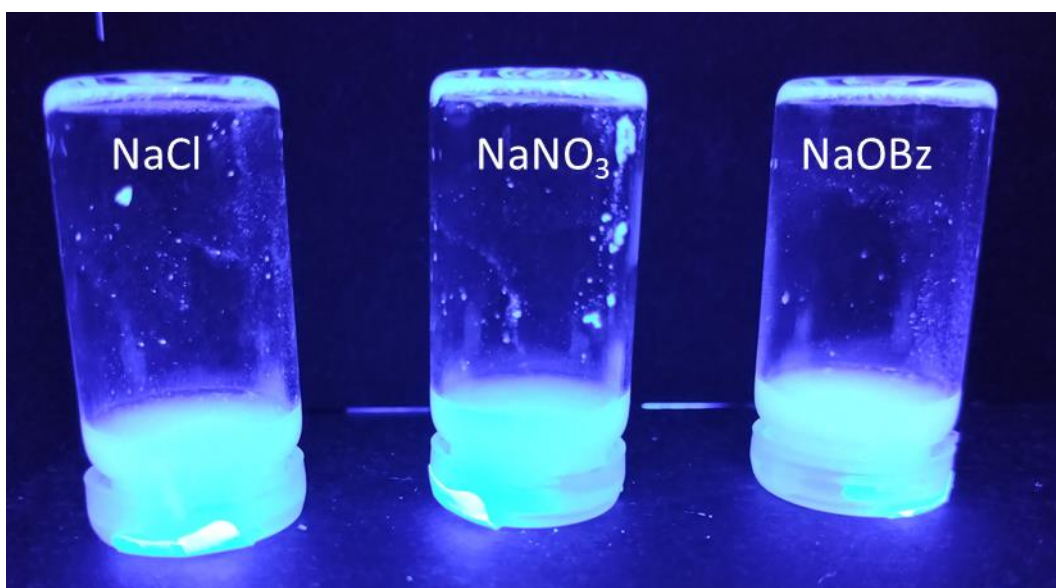


Figure S119 - Sonication test at 40 minutes. Compound **23** (5 mg, 1 mL) in NaCl, NaNO<sub>3</sub> and NaOBz inverted imaged under UV irradiation (test no. 1).

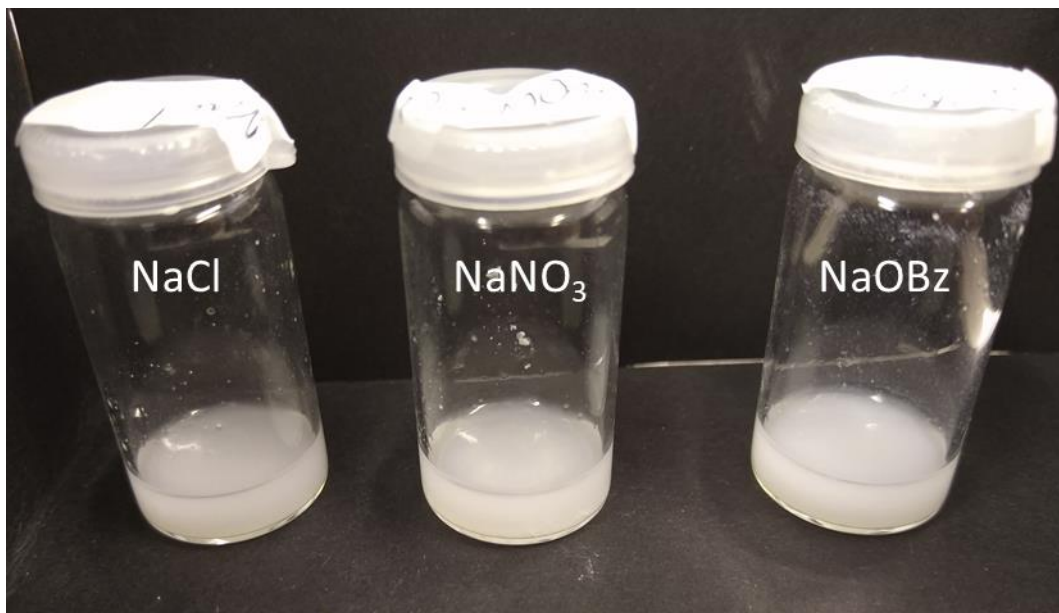


Figure S120 - Sonication test at 40 minutes. Compound **23** (5 mg, 1 mL) in NaCl, NaNO<sub>3</sub> and NaOBz (test no. 1).

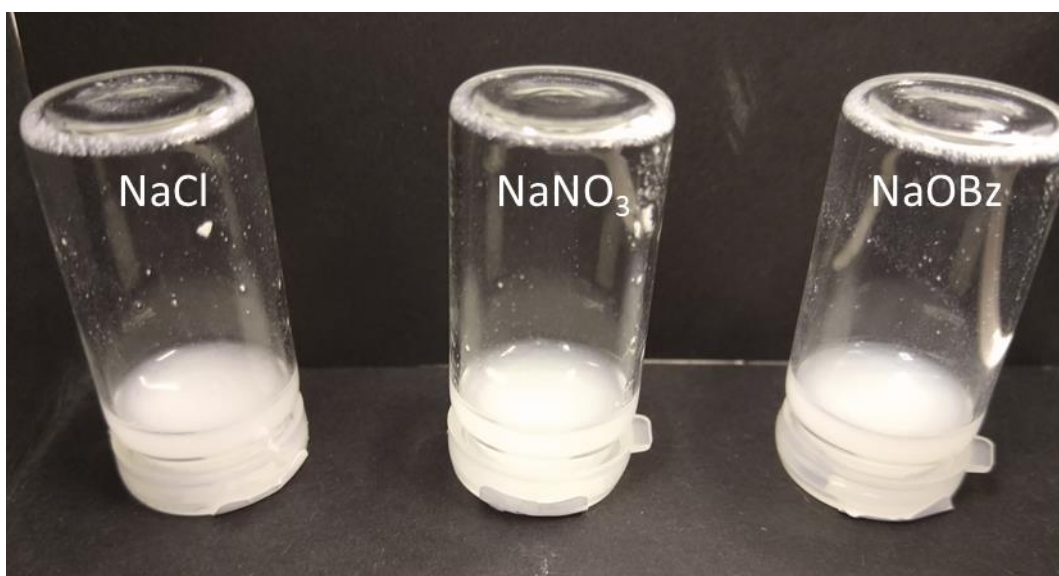


Figure S121 - Sonication test at 40 minutes. Compound **23** (5 mg, 1 mL) in NaCl, NaNO<sub>3</sub> and NaOBz inverted (test no. 1).

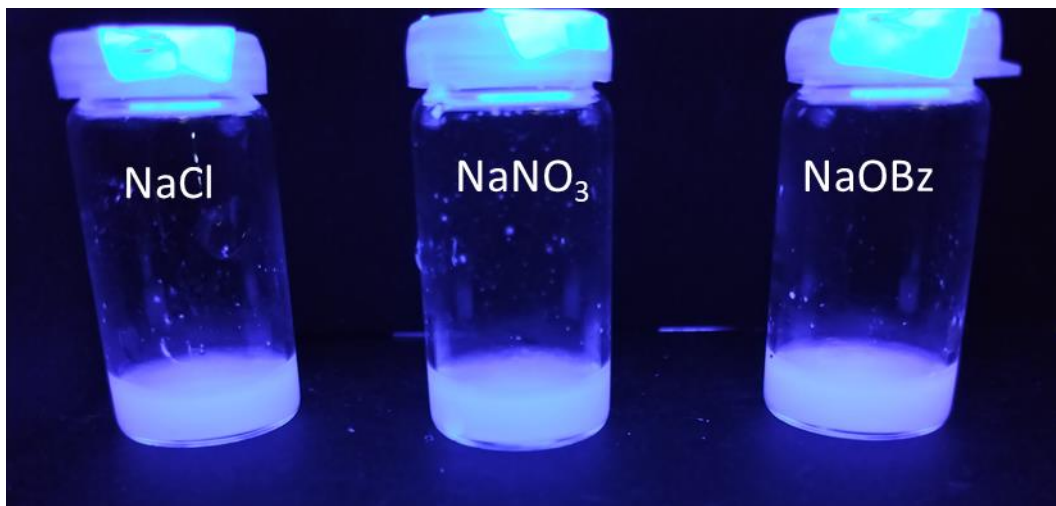


Figure S122 - Sonication test at 50 minutes. Compound **23** (5 mg, 1 mL) in NaCl, NaNO<sub>3</sub> and NaOBz imaged under UV irradiation (test no. 1).

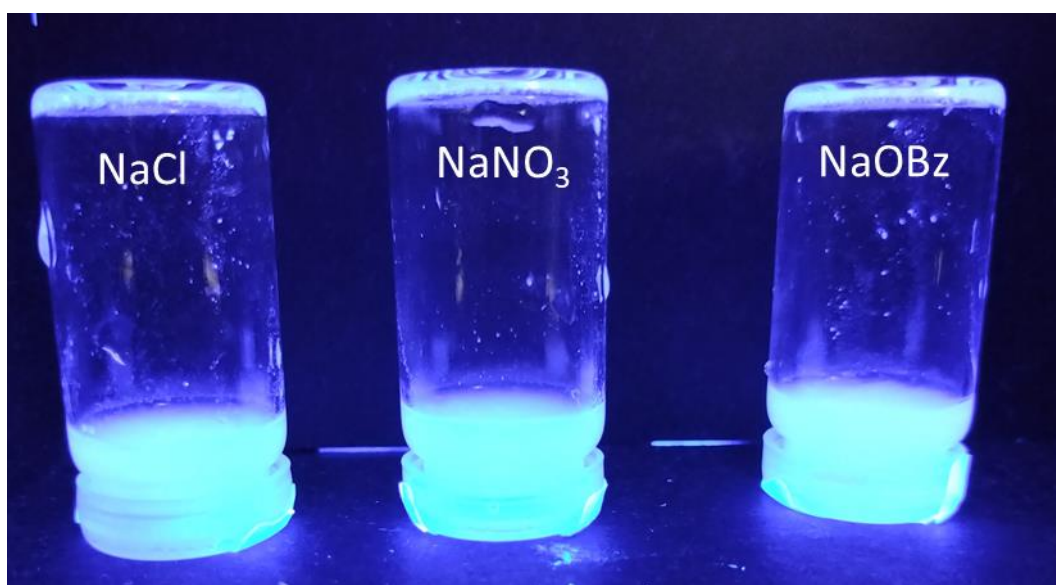


Figure S123 - Sonication test at 50 minutes. Compound **23** (5 mg, 1 mL) in NaCl, NaNO<sub>3</sub> and NaOBz inverted imaged under UV irradiation (test no. 1).

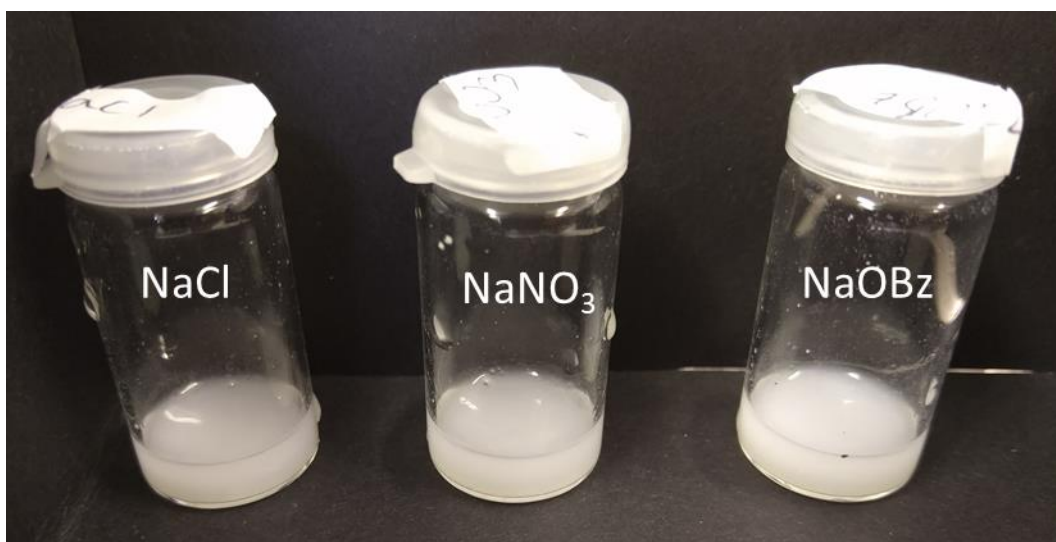


Figure S124 - Sonication test at 50 minutes. Compound **23** (5 mg, 1 mL) in NaCl, NaNO<sub>3</sub> and NaOBz (test no. 1).

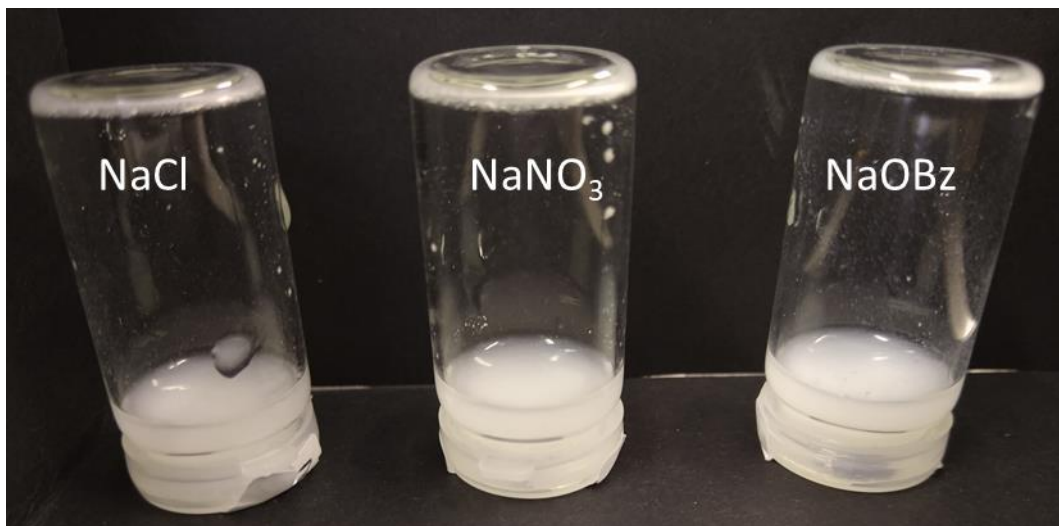


Figure S125 - Sonication test at 50 minutes. Compound **23** (5 mg, 1 mL) in NaCl, NaNO<sub>3</sub> and NaOBz inverted (test no. 1).

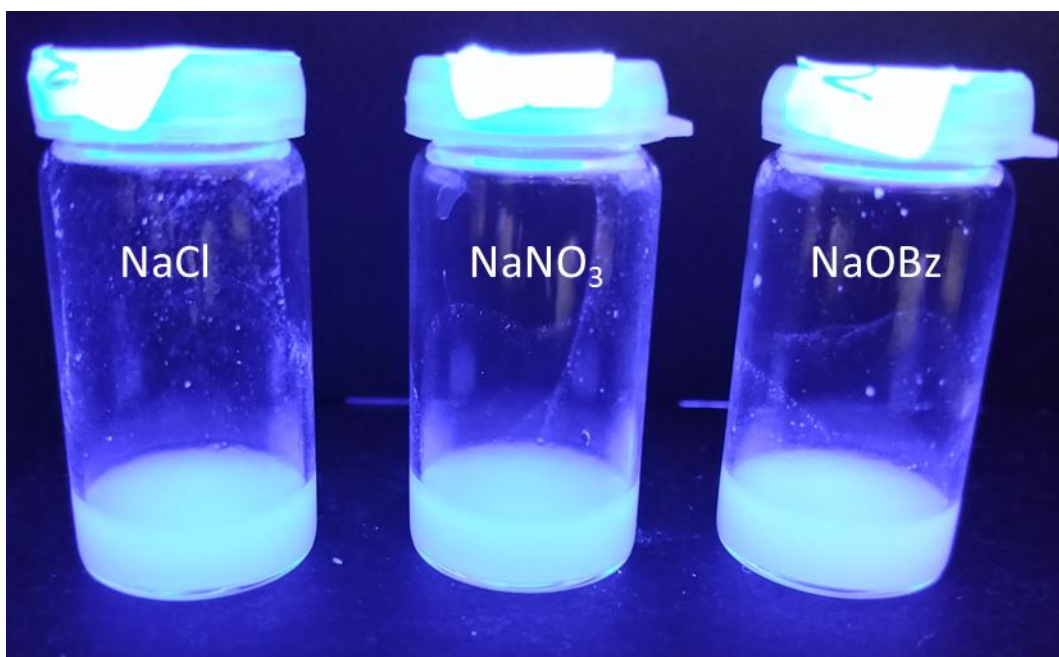


Figure S126 - Sonication test at 60 minutes. Compound **23** (5 mg, 1 mL) in NaCl, NaNO<sub>3</sub> and NaOBz imaged under UV irradiation (test no. 1).

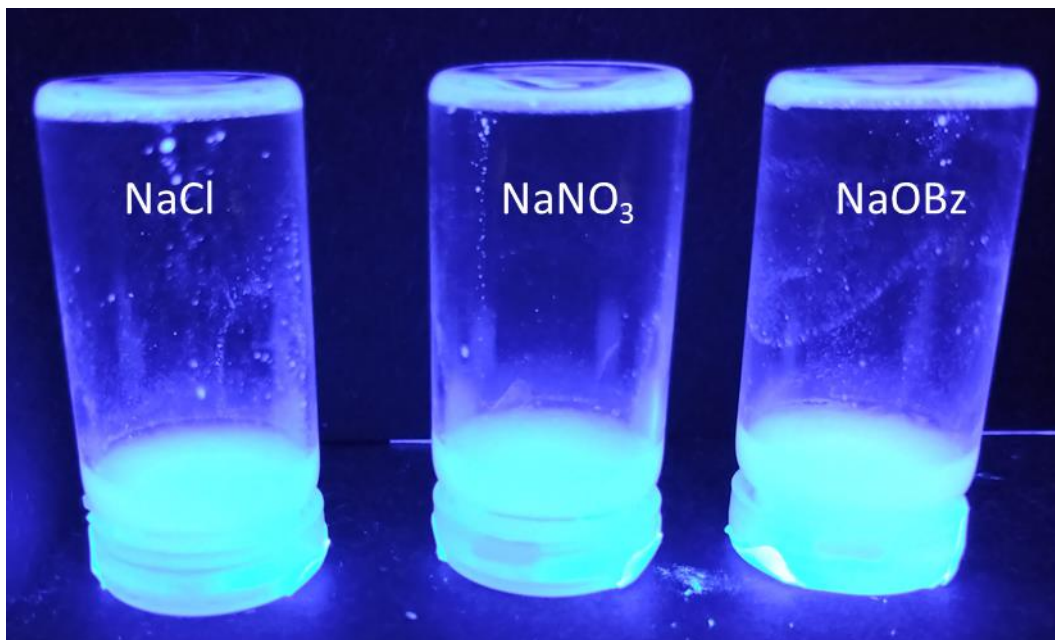


Figure S127 - Sonication test at 60 minutes. Compound **23** (5 mg, 1 mL) in NaCl, NaNO<sub>3</sub> and NaOBz inverted imaged under UV irradiation (test no. 1).

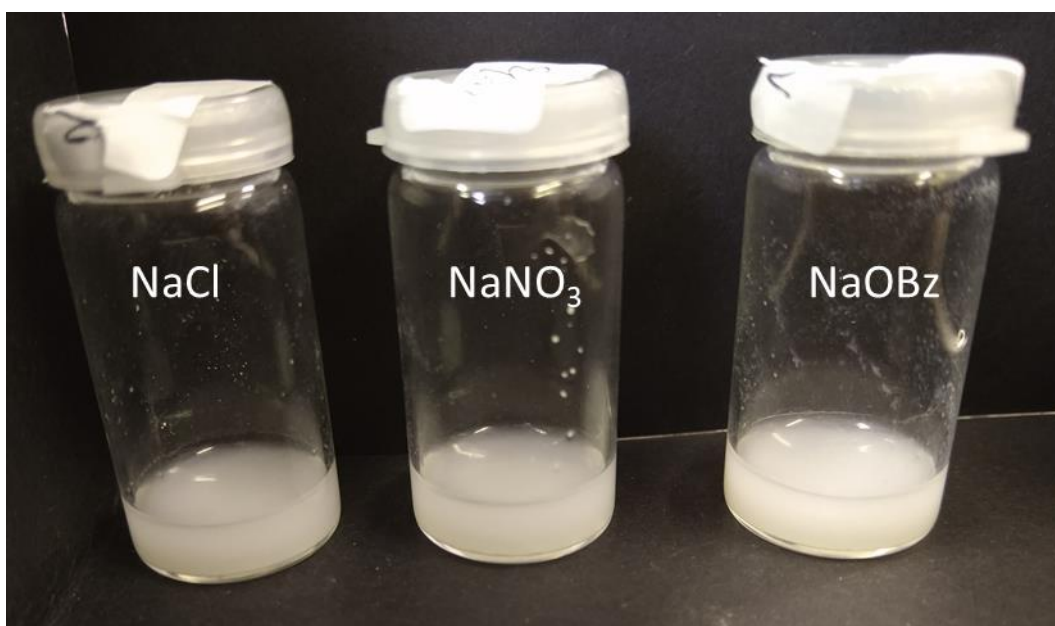


Figure S128 - Sonication test at 60 minutes. Compound **23** (5 mg, 1 mL) in NaCl, NaNO<sub>3</sub> and NaOBz (test no. 1).

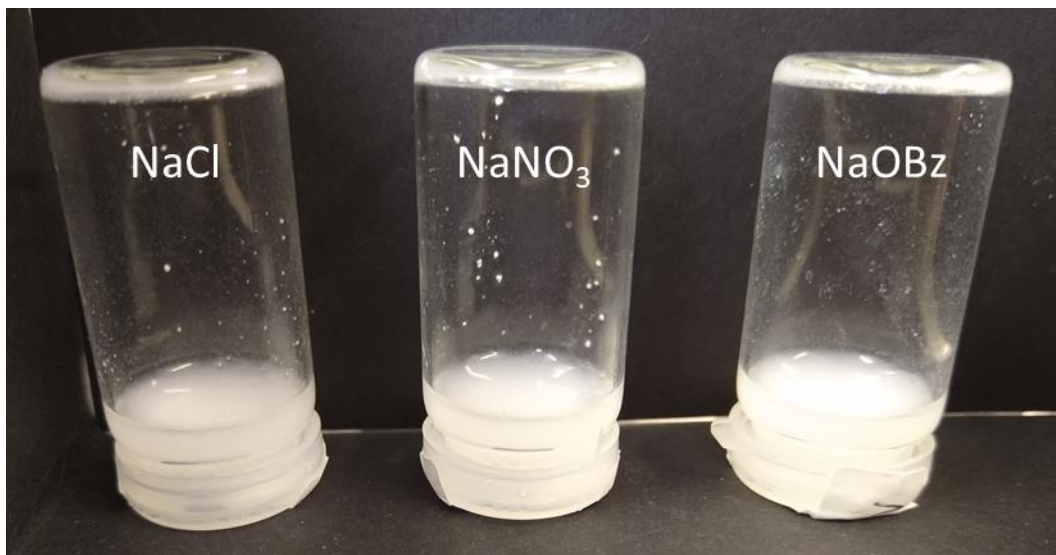


Figure S129 - Sonication test at 60 minutes. Compound **23** (5 mg, 1 mL) in NaCl, NaNO<sub>3</sub> and NaOBz inverted (test no. 1).

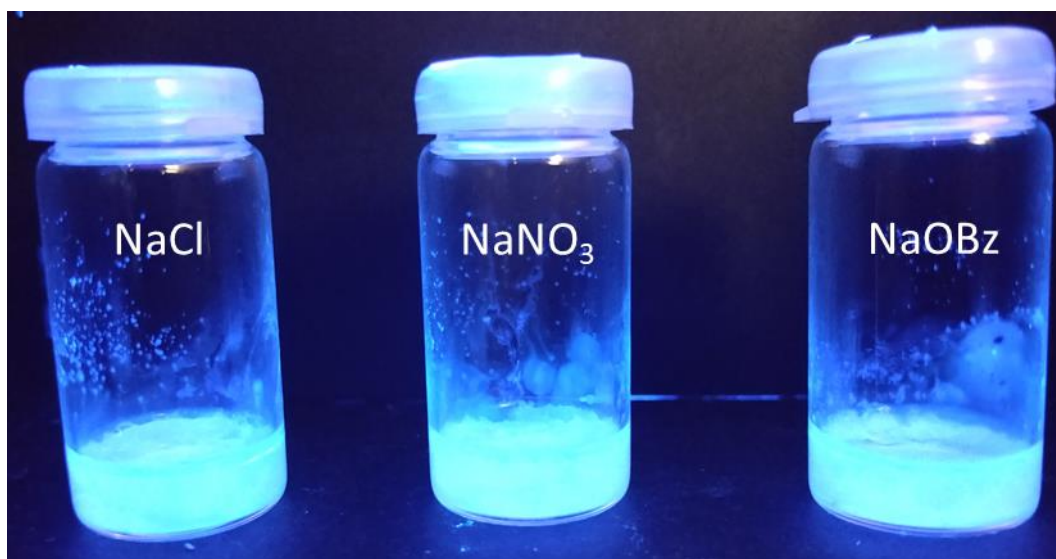


Figure S130 - Sonication test at 0 minutes. Compound **23** (5 mg, 1 mL) in NaCl, NaNO<sub>3</sub> and NaOBz imaged under UV irradiation (test no. 2).

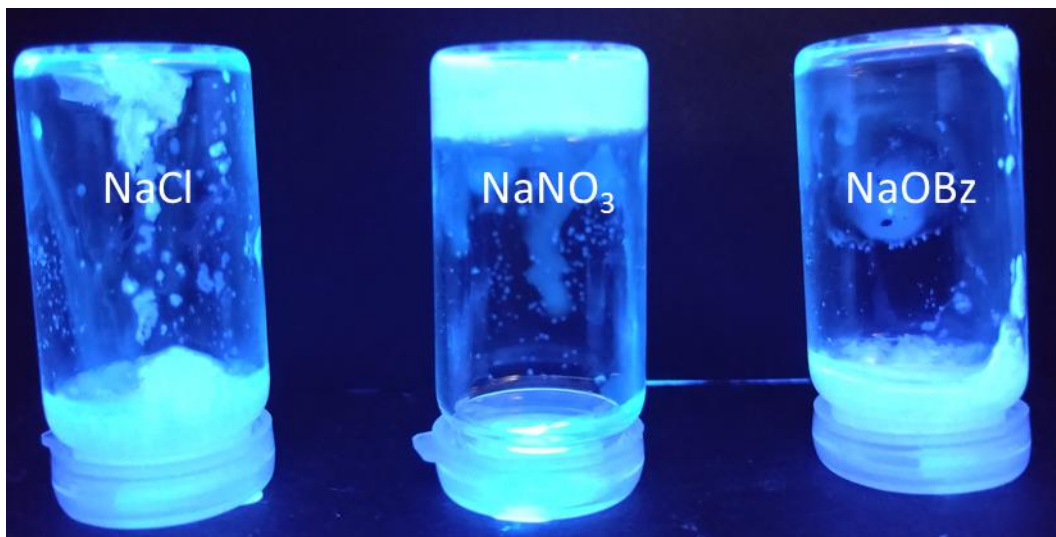


Figure S131 - Sonication test at 0 minutes. Compound **23** (5 mg, 1 mL) in NaCl, NaNO<sub>3</sub> and NaOBz inverted imaged under UV irradiation (test no. 2).

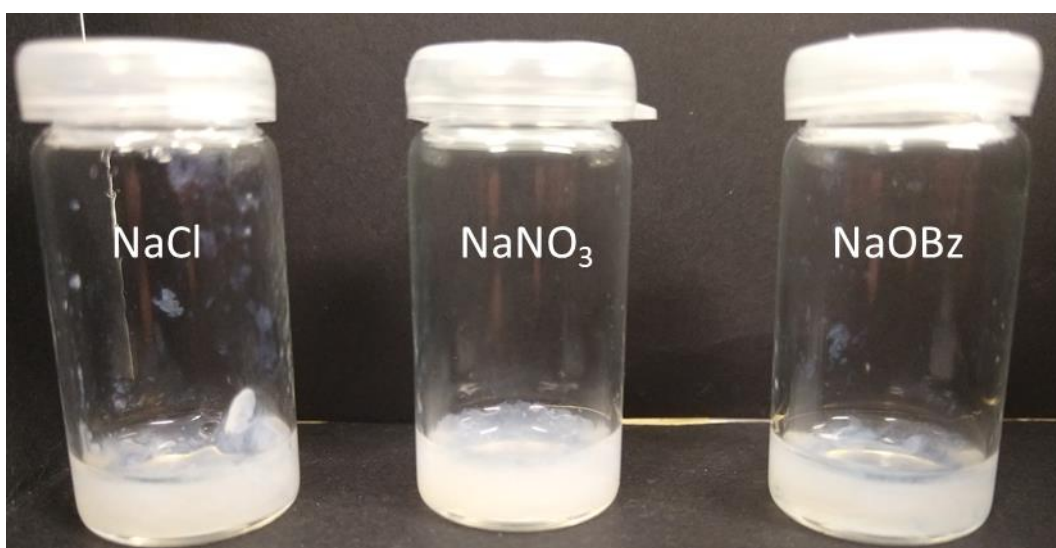


Figure S132 - Sonication test at 0 minutes. Compound **23** (5 mg, 1 mL) in NaCl, NaNO<sub>3</sub> and NaOBz (test no. 2).

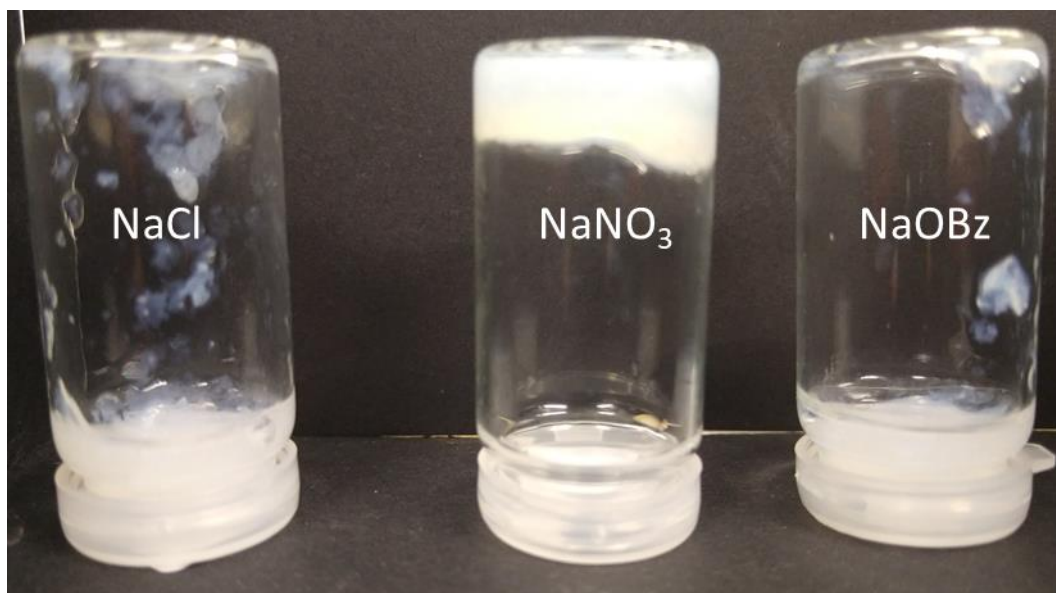


Figure S133 - Sonication test at 0 minutes. Compound **23** (5 mg, 1 mL) in NaCl, NaNO<sub>3</sub> and NaOBz inverted (test no. 2).

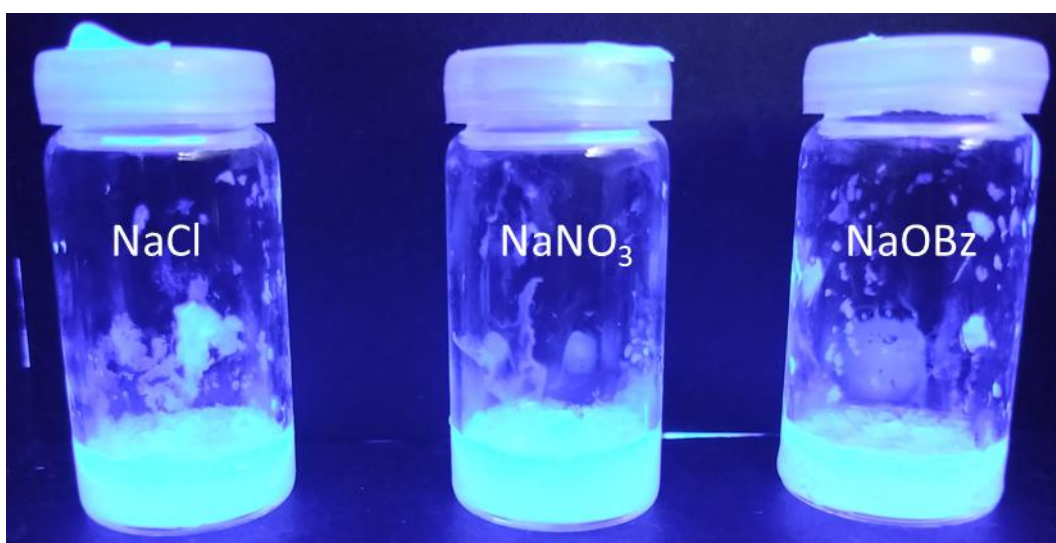


Figure S134 - Sonication test at 5 minutes. Compound **23** (5 mg, 1 mL) in NaCl, NaNO<sub>3</sub> and NaOBz imaged under UV irradiation (test no. 2).

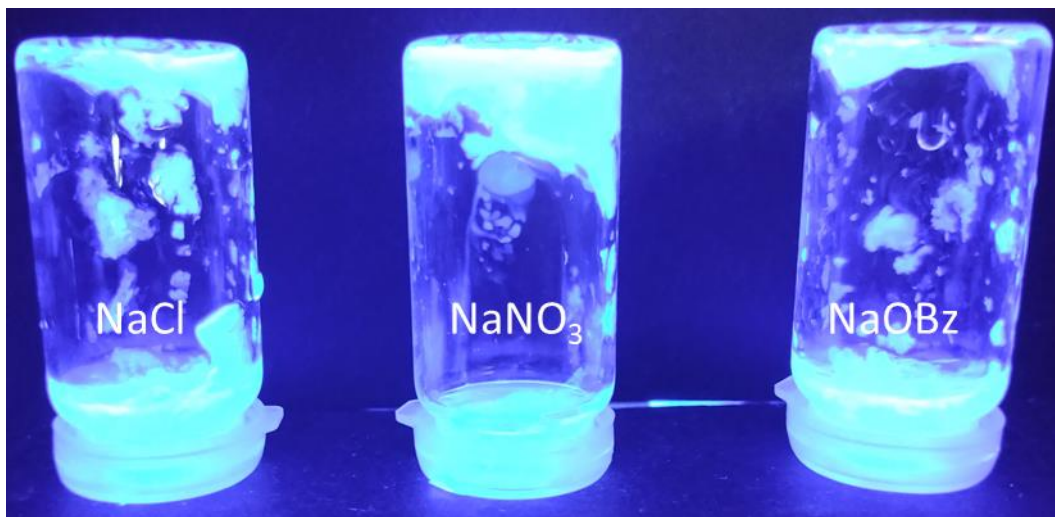


Figure S135 - Sonication test at 5 minutes. Compound **23** (5 mg, 1 mL) in NaCl, NaNO<sub>3</sub> and NaOBz inverted imaged under UV irradiation (test no. 2).

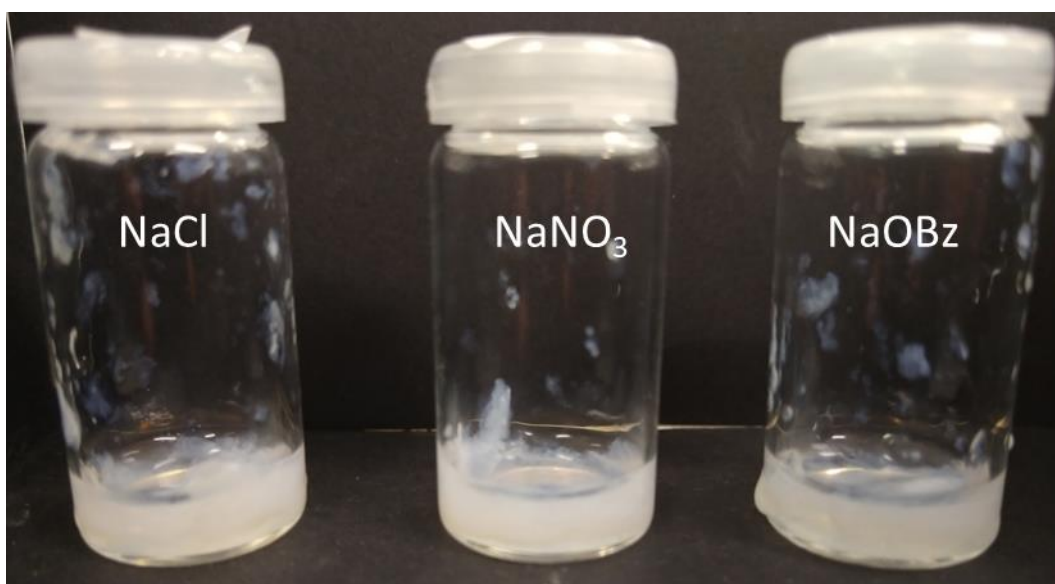


Figure S136 - Sonication test at 5 minutes. Compound **23** (5 mg, 1 mL) in NaCl, NaNO<sub>3</sub> and NaOBz (test no. 2).

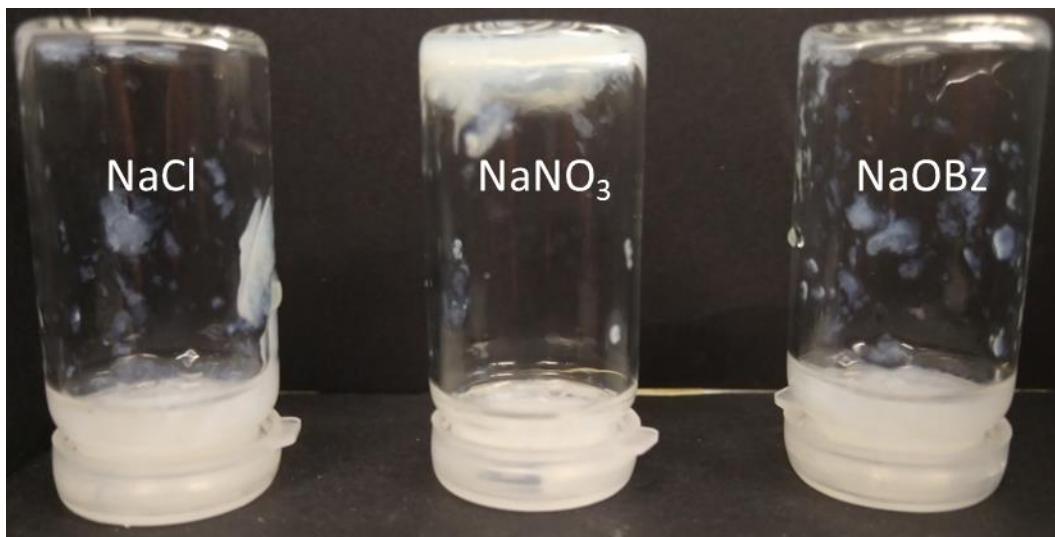


Figure S137- Sonication test at 5 minutes. Compound **23** (5 mg, 1 mL) in NaCl, NaNO<sub>3</sub> and NaOBz inverted (test no. 2).

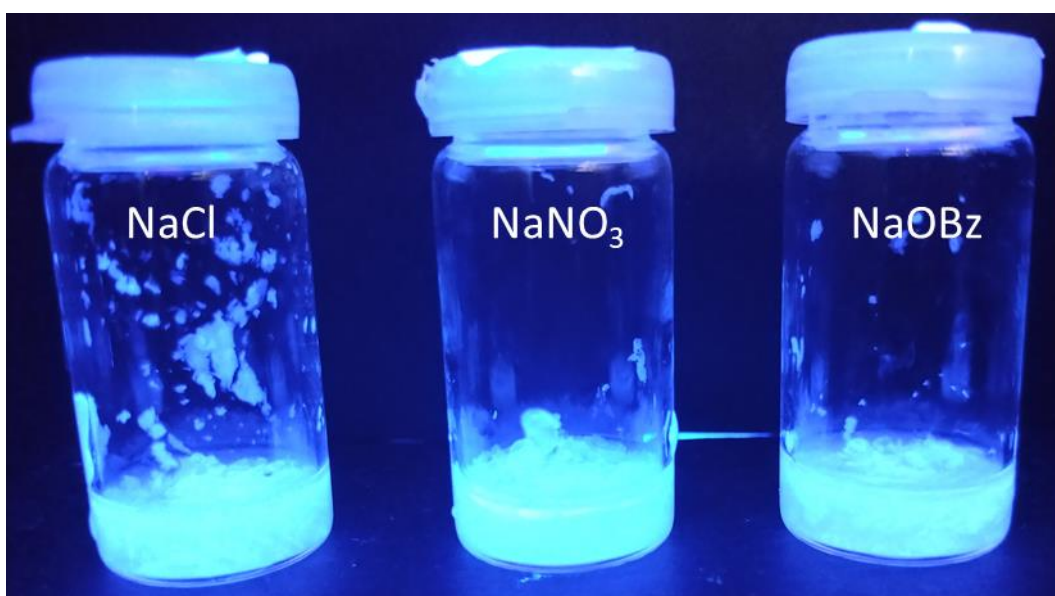


Figure S138 - Sonication test at 10 minutes. Compound **23** (5 mg, 1 mL) in NaCl, NaNO<sub>3</sub> and NaOBz imaged under UV irradiation (test no. 2).

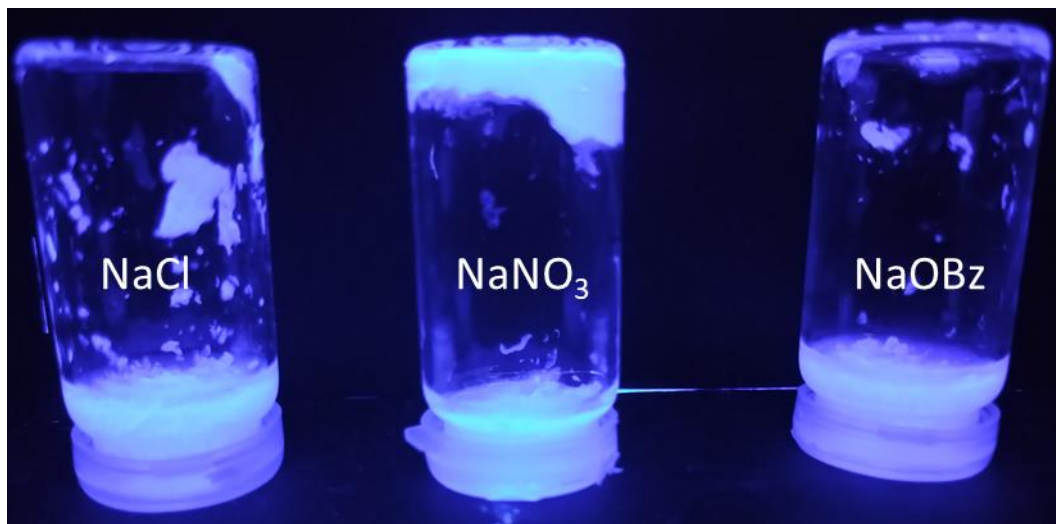


Figure S139 - Sonication test at 10 minutes. Compound **23** (5 mg, 1 mL) in NaCl, NaNO<sub>3</sub> and NaOBz inverted imaged under UV irradiation (test no. 2).

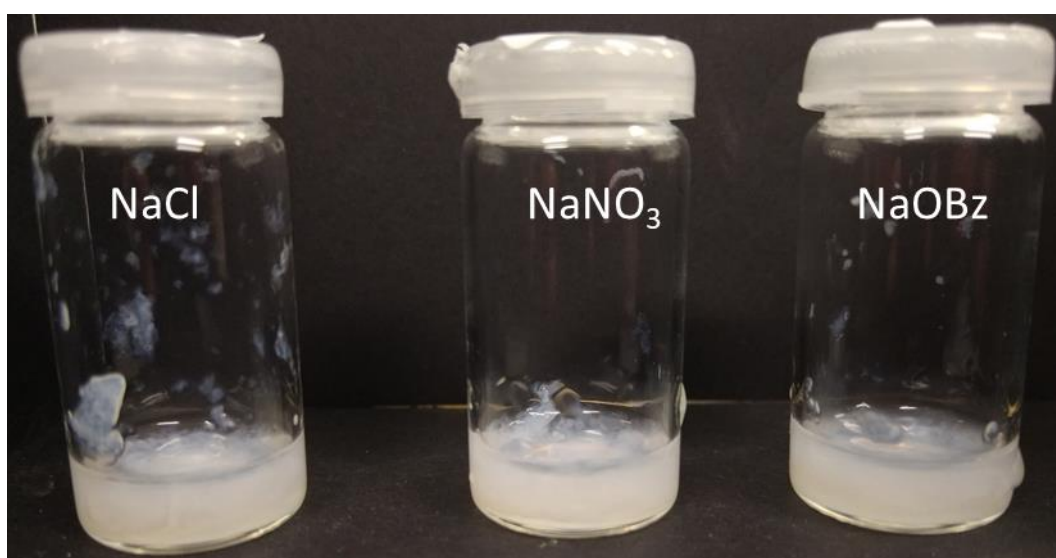


Figure S140 - Sonication test at 10 minutes. Compound **23** (5 mg, 1 mL) in NaCl, NaNO<sub>3</sub> and NaOBz (test no. 2).

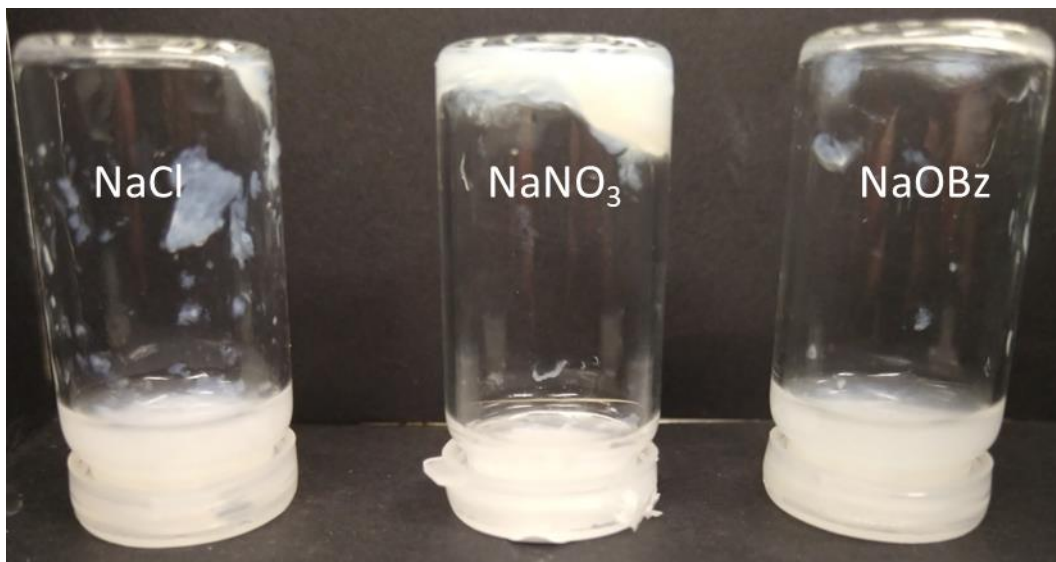


Figure S141 - Sonication test at 10 minutes. Compound **23** (5 mg, 1 mL) in NaCl, NaNO<sub>3</sub> and NaOBz (test no. 2).

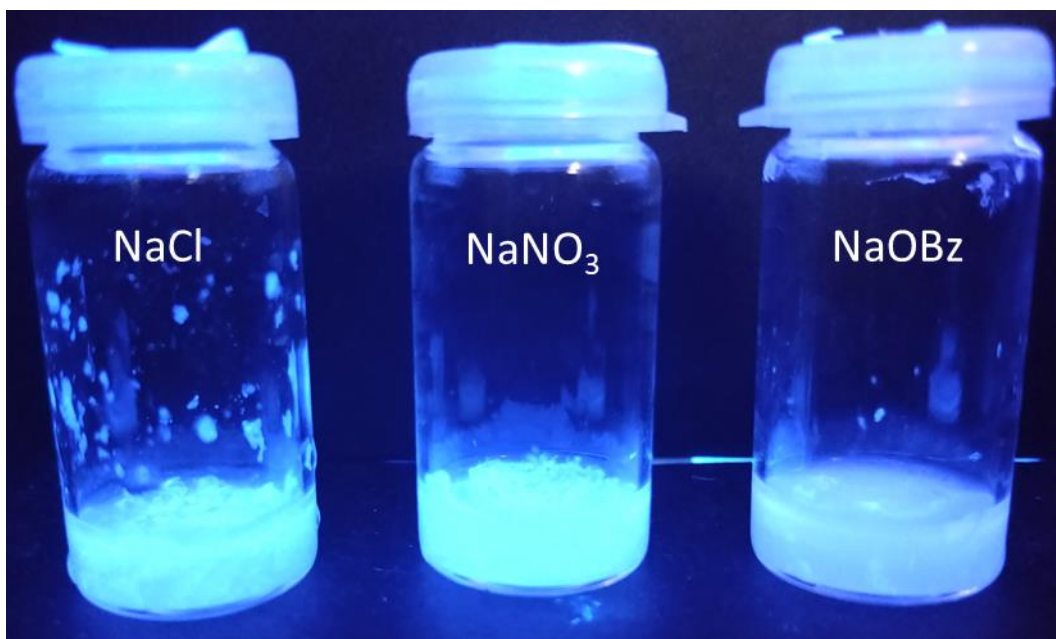


Figure S142 - Sonication test at 15 minutes. Compound **23** (5 mg, 1 mL) in NaCl, NaNO<sub>3</sub> and NaOBz imaged under UV irradiation (test no. 2).

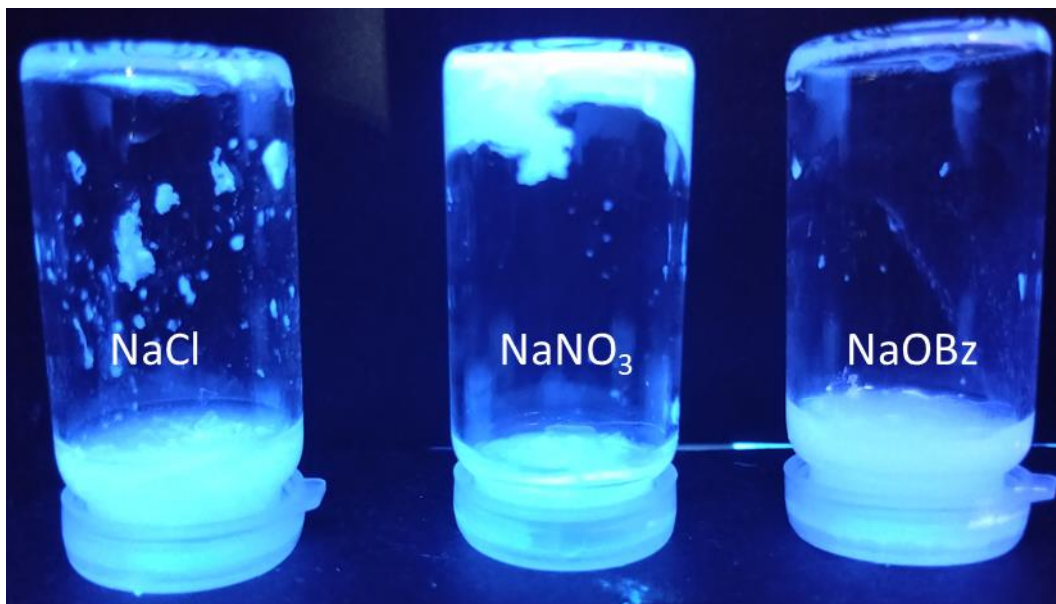


Figure S143 - Sonication test at 15 minutes. Compound **23** (5 mg, 1 mL) in NaCl, NaNO<sub>3</sub> and NaOBz inverted imaged under UV irradiation (test no. 2).

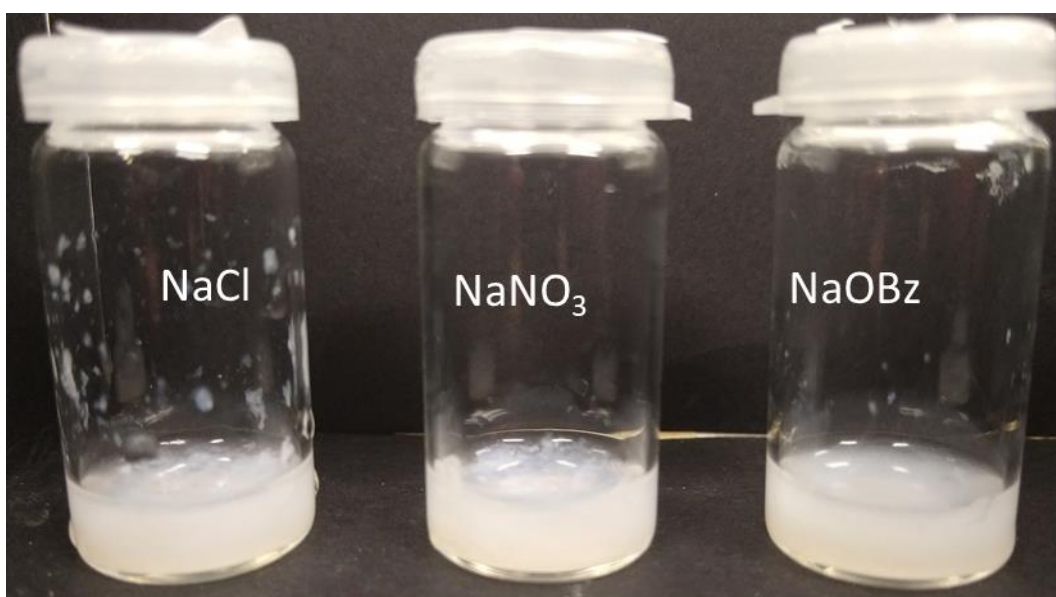


Figure S144 - Sonication test at 15 minutes. Compound **23** (5 mg, 1 mL) in NaCl, NaNO<sub>3</sub> and NaOBz (test no. 2).

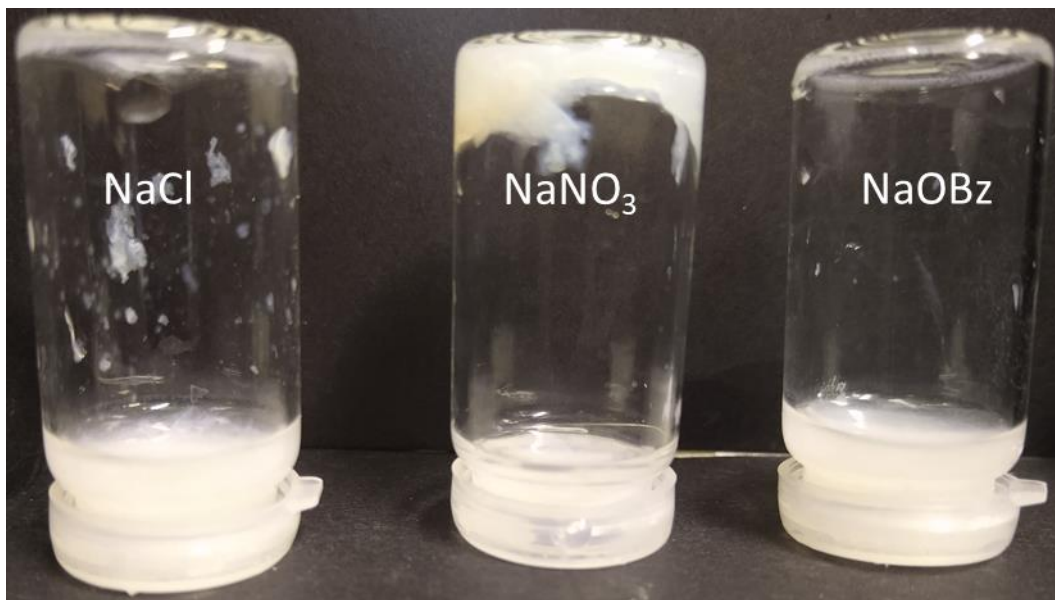


Figure S145 - Sonication test at 15 minutes. Compound **23** (5 mg, 1 mL) in NaCl, NaNO<sub>3</sub> and NaOBz inverted (test no. 2).

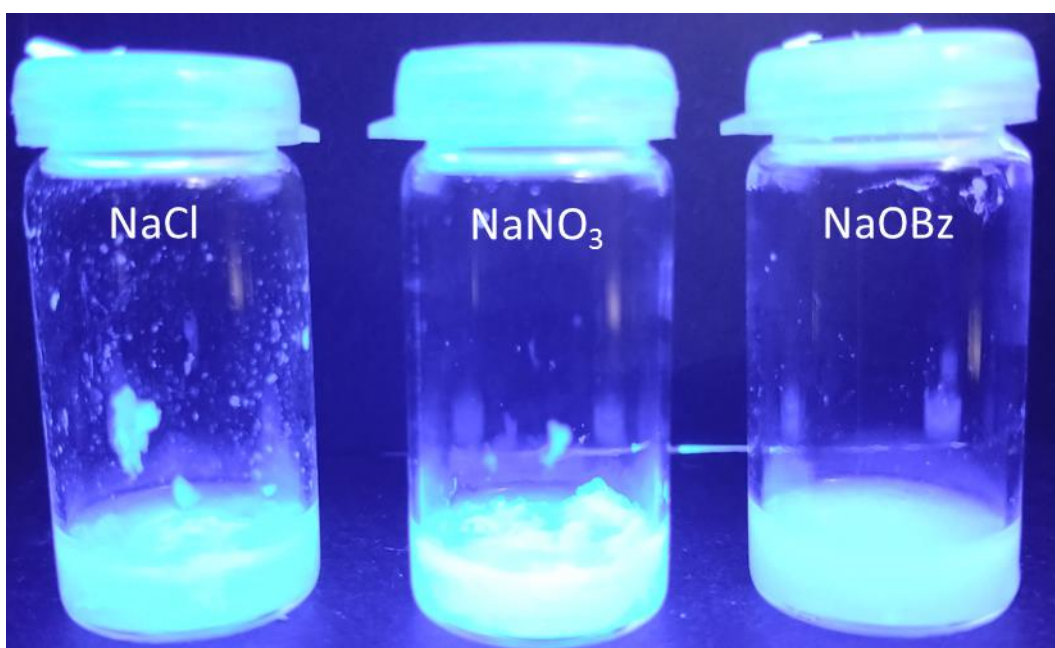


Figure S146 - Sonication test at 20 minutes. Compound **23** (5 mg, 1 mL) in NaCl, NaNO<sub>3</sub> and NaOBz imaged under UV irradiation (test no. 2).

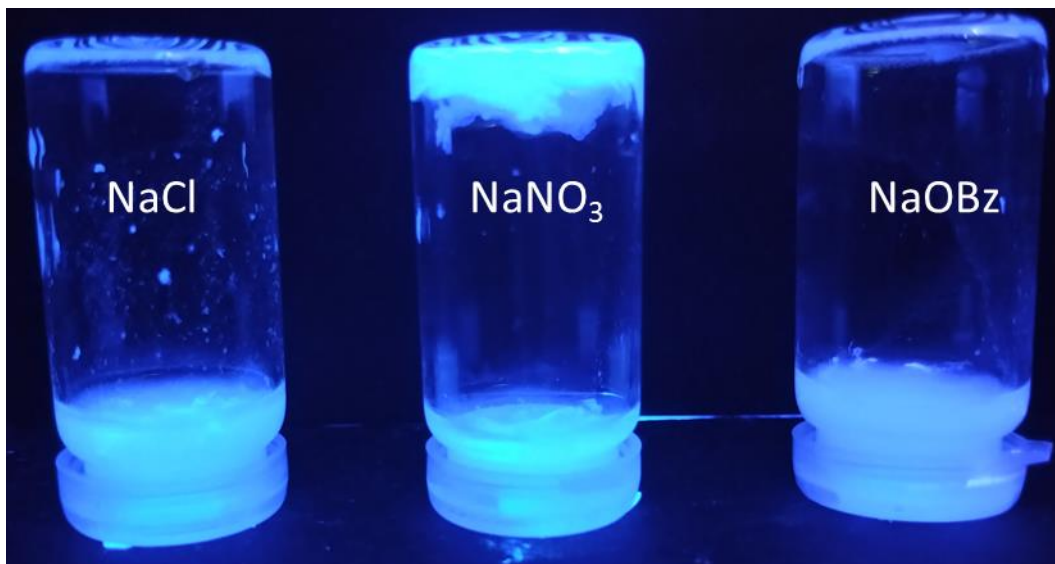


Figure S147 - Sonication test at 20 minutes. Compound **23** (5 mg, 1 mL) in NaCl, NaNO<sub>3</sub> and NaOBz inverted imaged under UV irradiation (test no. 2).

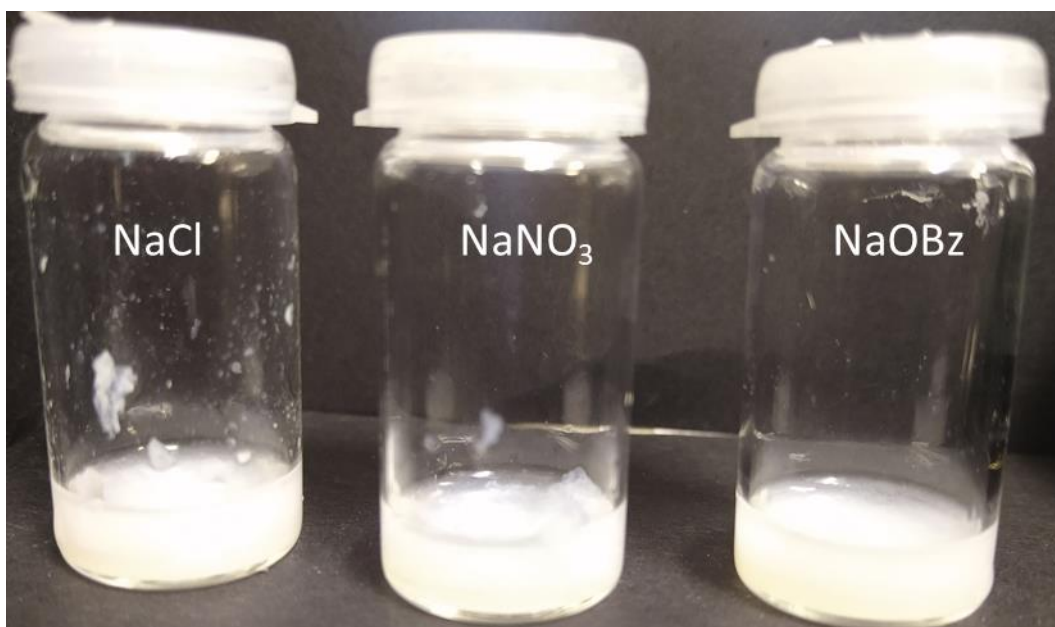


Figure S148 - Sonication test at 20 minutes. Compound **23** (5 mg, 1 mL) in NaCl, NaNO<sub>3</sub> and NaOBz (test no. 2).

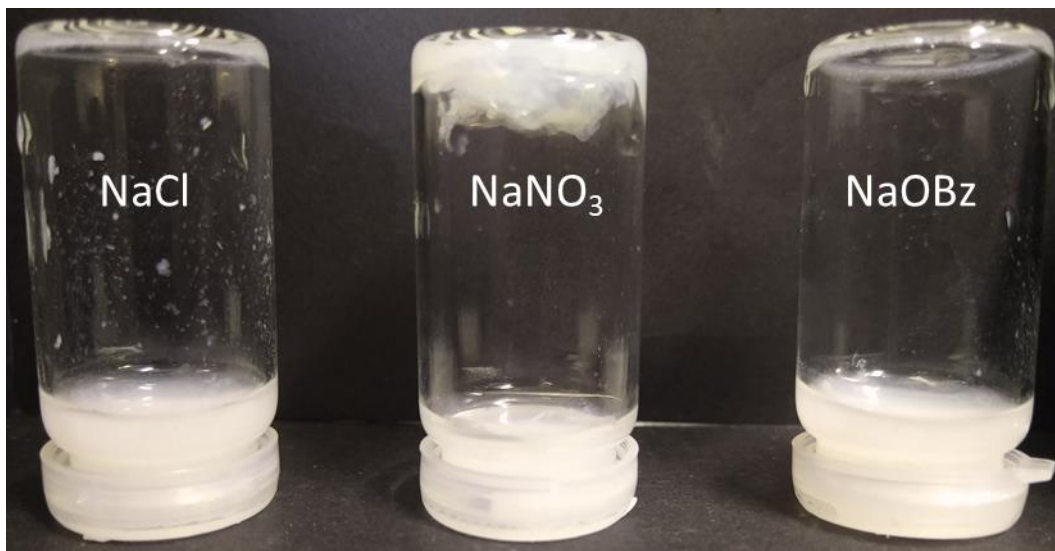


Figure S149 - Sonication test at 20 minutes. Compound **23** (5 mg, 1 mL) in NaCl, NaNO<sub>3</sub> and NaOBz inverted (test no. 2).

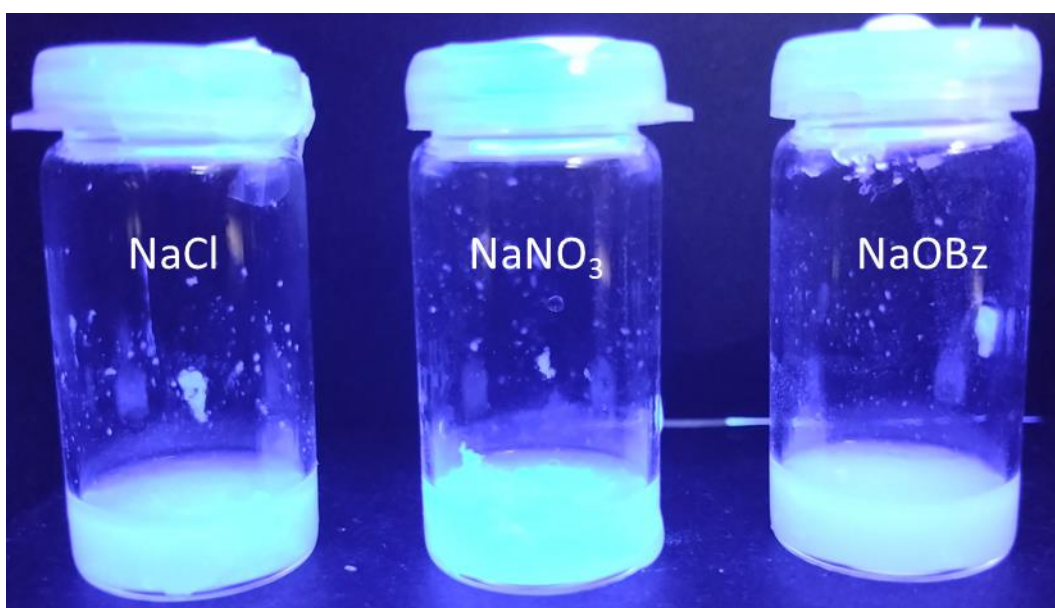


Figure S150 - Sonication test at 25 minutes. Compound **23** (5 mg, 1 mL) in NaCl, NaNO<sub>3</sub> and NaOBz imaged under UV irradiation (test no. 2).

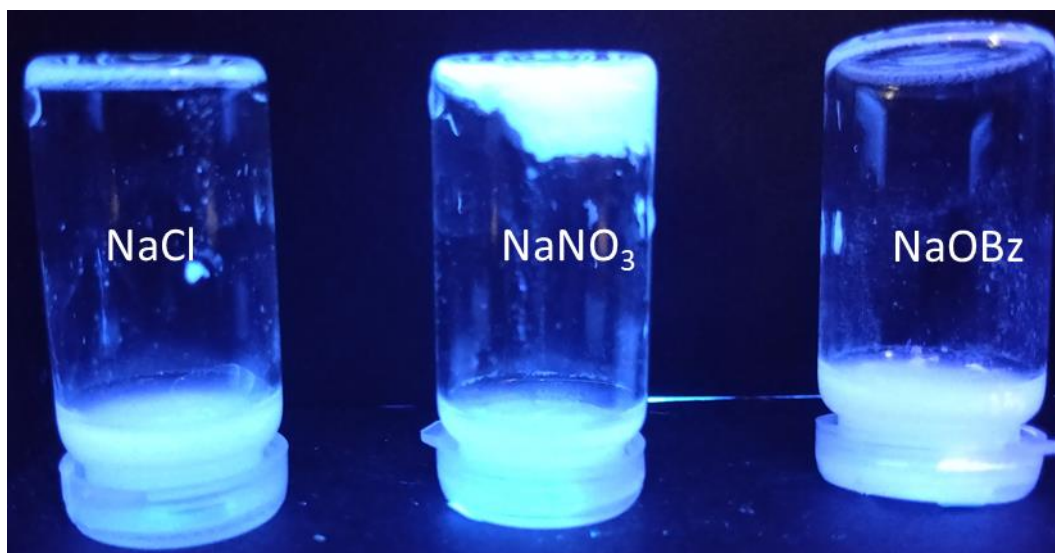


Figure S151 - Sonication test at 25 minutes. Compound **23** (5 mg, 1 mL) in NaCl, NaNO<sub>3</sub> and NaOBz inverted imaged under UV irradiation (test no. 2).

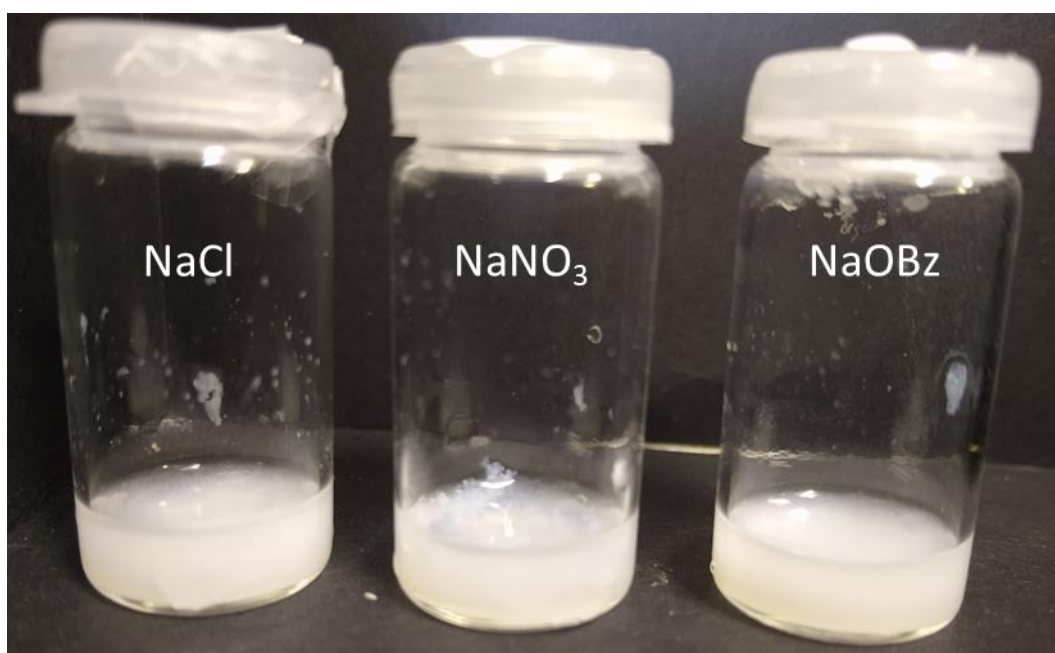


Figure S152 - Sonication test at 25 minutes. Compound **23** (5 mg, 1 mL) in NaCl, NaNO<sub>3</sub> and NaOBz (test no. 2).

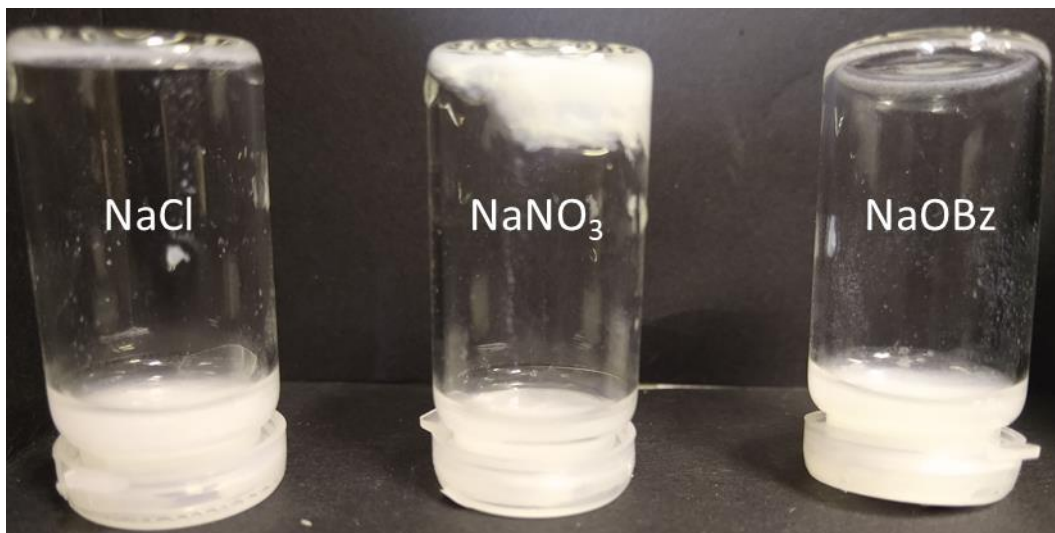


Figure S153 - Sonication test at 25 minutes. Compound **23** (5 mg, 1 mL) in NaCl, NaNO<sub>3</sub> and NaOBz inverted (test no. 2).

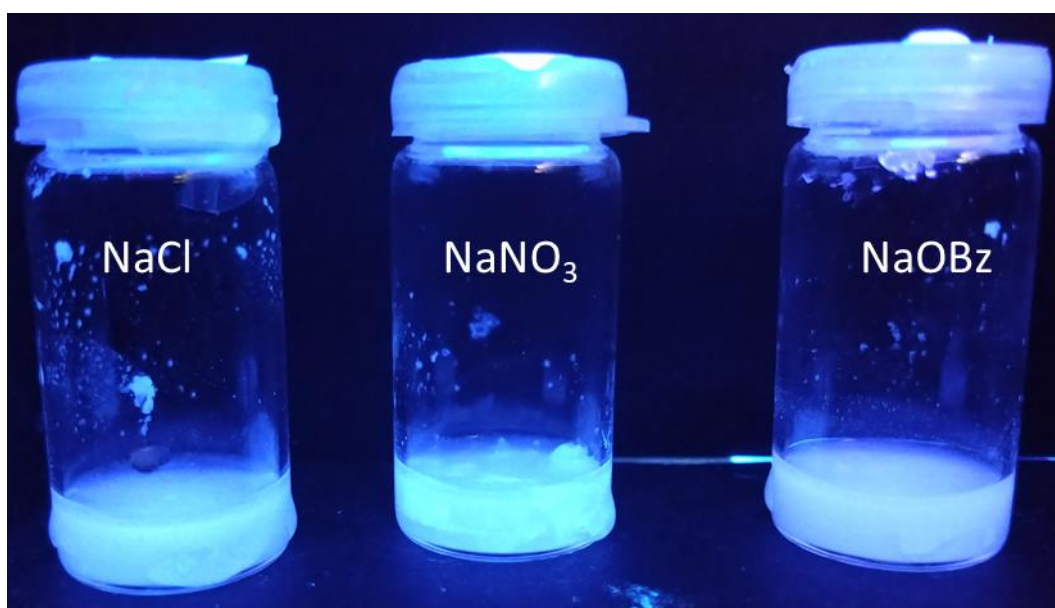


Figure S154 - Sonication test at 30 minutes. Compound **23** (5 mg, 1 mL) in NaCl, NaNO<sub>3</sub> and NaOBz imaged under UV irradiation (test no. 2).

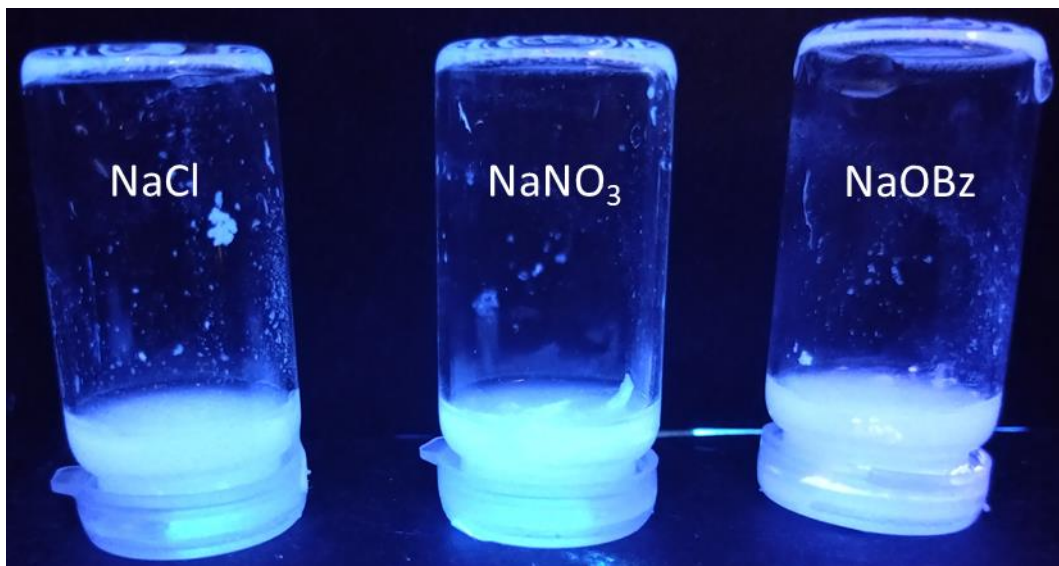


Figure S155 - Sonication test at 30 minutes. Compound **23** (5 mg, 1 mL) in NaCl, NaNO<sub>3</sub> and NaOBz inverted imaged under UV irradiation (test no. 2).

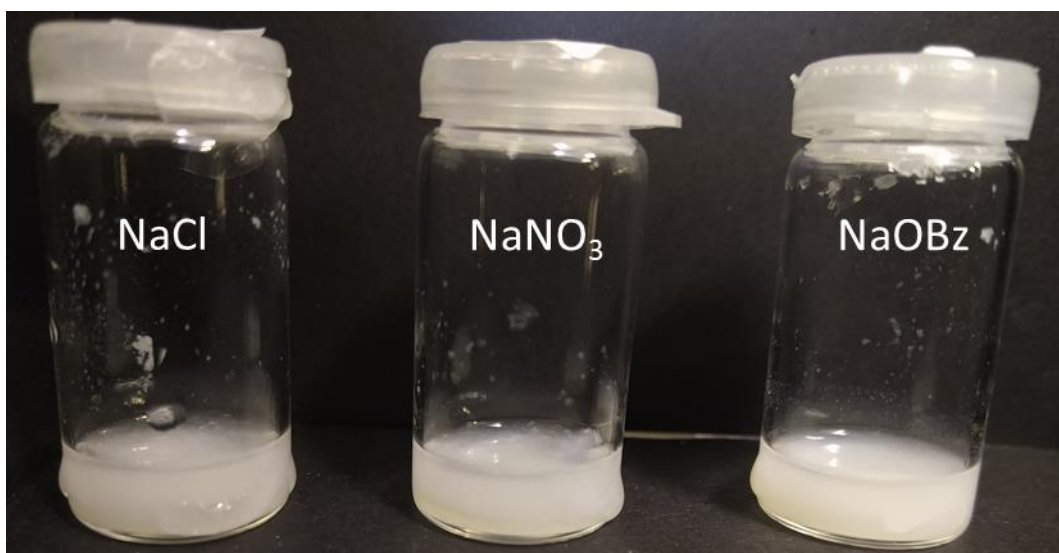


Figure S156 - Sonication test at 30 minutes. Compound **23** (5 mg, 1 mL) in NaCl, NaNO<sub>3</sub> and NaOBz (test no. 2).

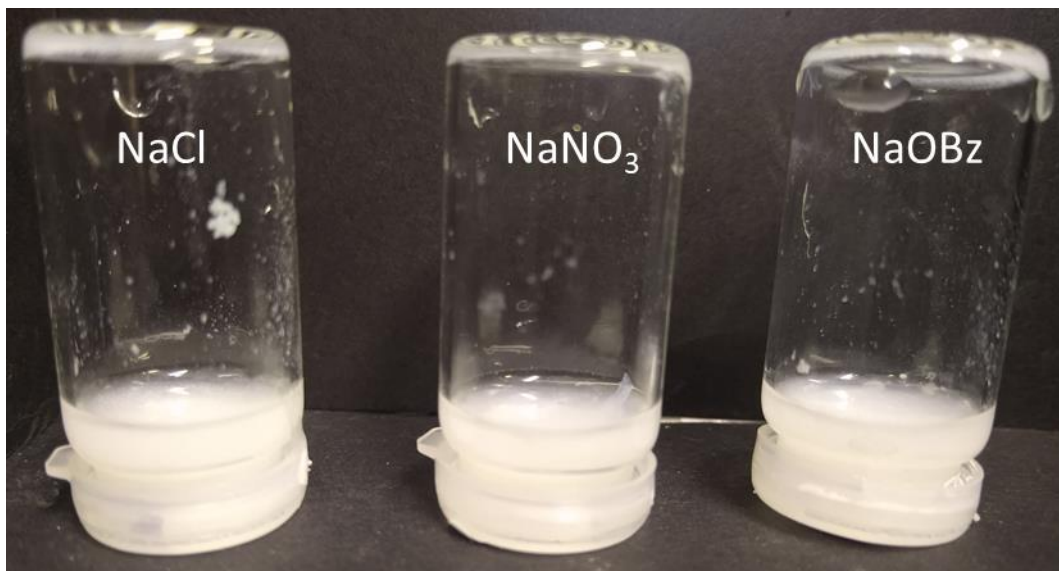


Figure S157 - Sonication test at 30 minutes. Compound **23** (5 mg, 1 mL) in NaCl, NaNO<sub>3</sub> and NaOBz inverted (test no. 2).

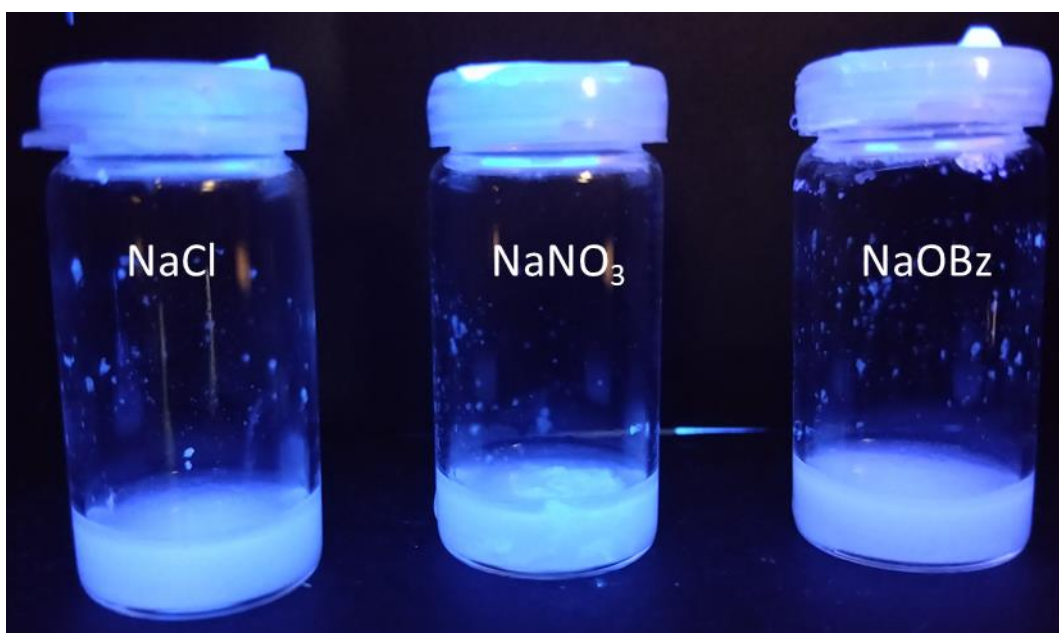


Figure S158 - Sonication test at 40 minutes. Compound **23** (5 mg, 1 mL) in NaCl, NaNO<sub>3</sub> and NaOBz imaged under UV irradiation (test no. 2).

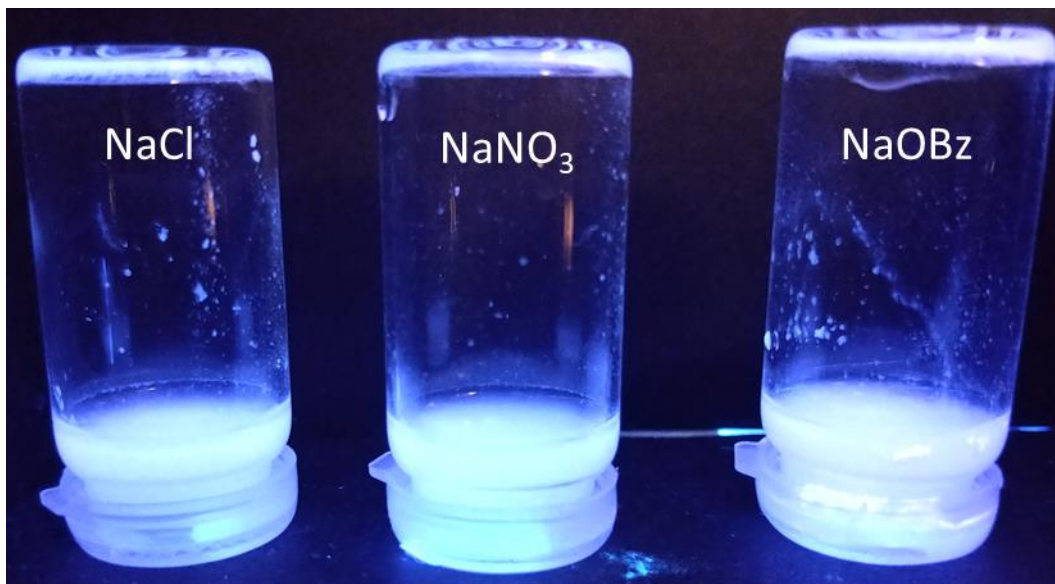


Figure S159 - Sonication test at 40 minutes. Compound **23** (5 mg, 1 mL) in NaCl, NaNO<sub>3</sub> and NaOBz inverted imaged under UV irradiation (test no. 2).

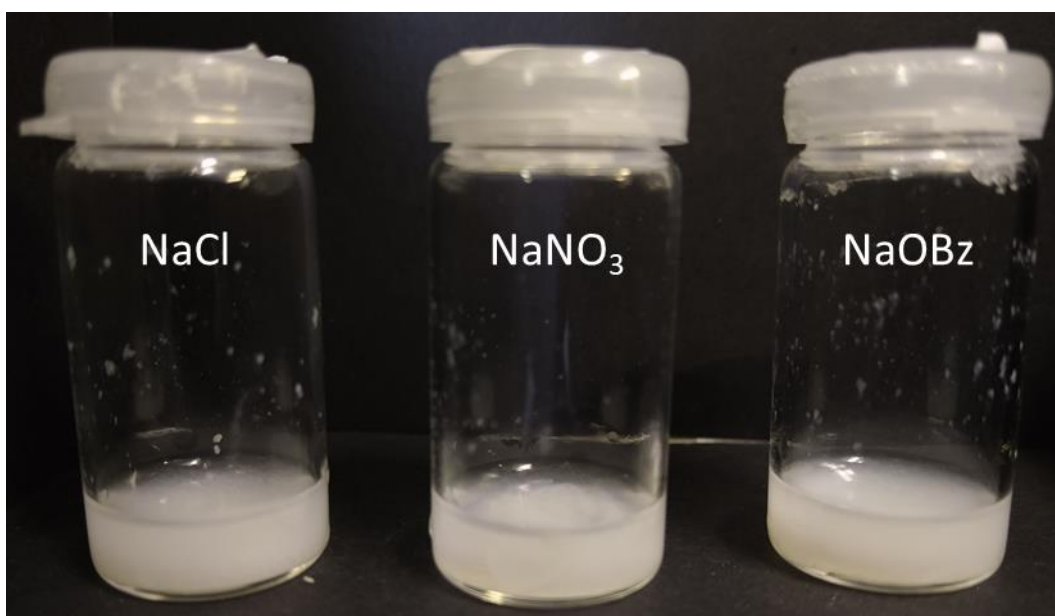


Figure S160 - Sonication test at 40 minutes. Compound **23** (5 mg, 1 mL) in NaCl, NaNO<sub>3</sub> and NaOBz (test no. 2).

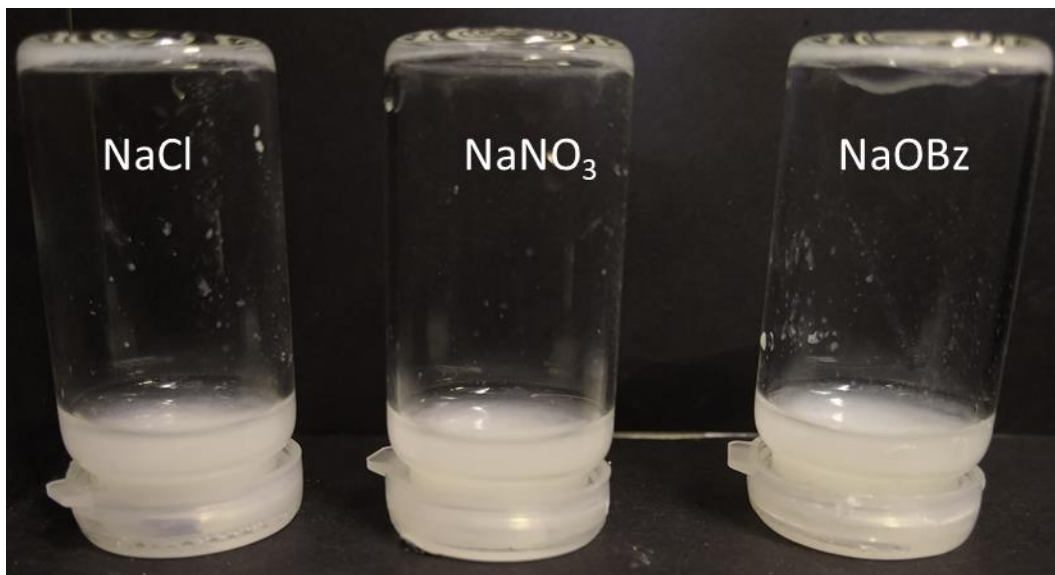


Figure S161 - Sonication test at 40 minutes. Compound **23** (5 mg, 1 mL) in NaCl, NaNO<sub>3</sub> and NaOBz inverted (test no. 2).

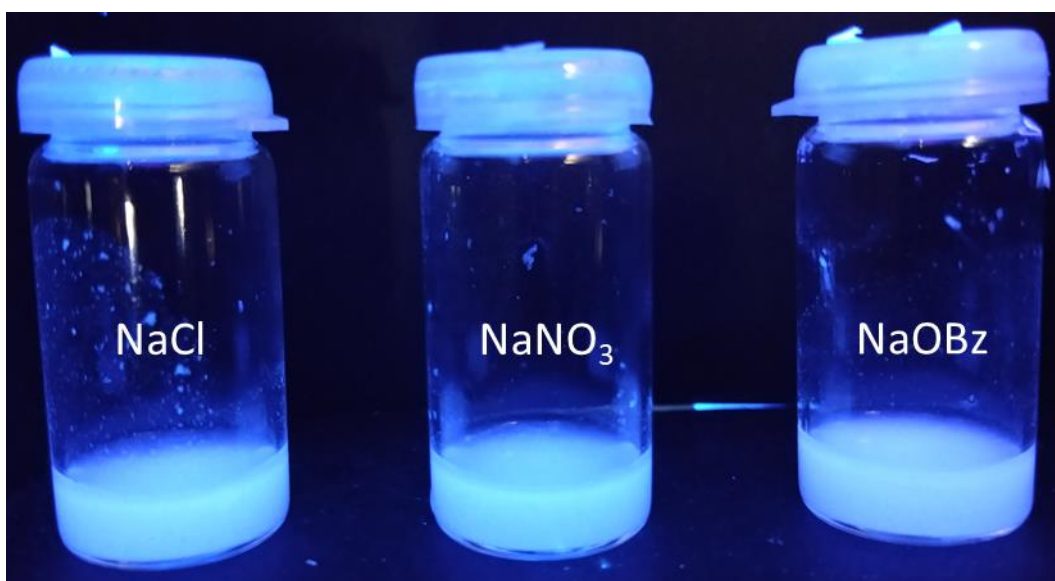


Figure S162 - Sonication test at 50 minutes. Compound **23** (5 mg, 1 mL) in NaCl, NaNO<sub>3</sub> and NaOBz imaged under UV irradiation (test no. 2).

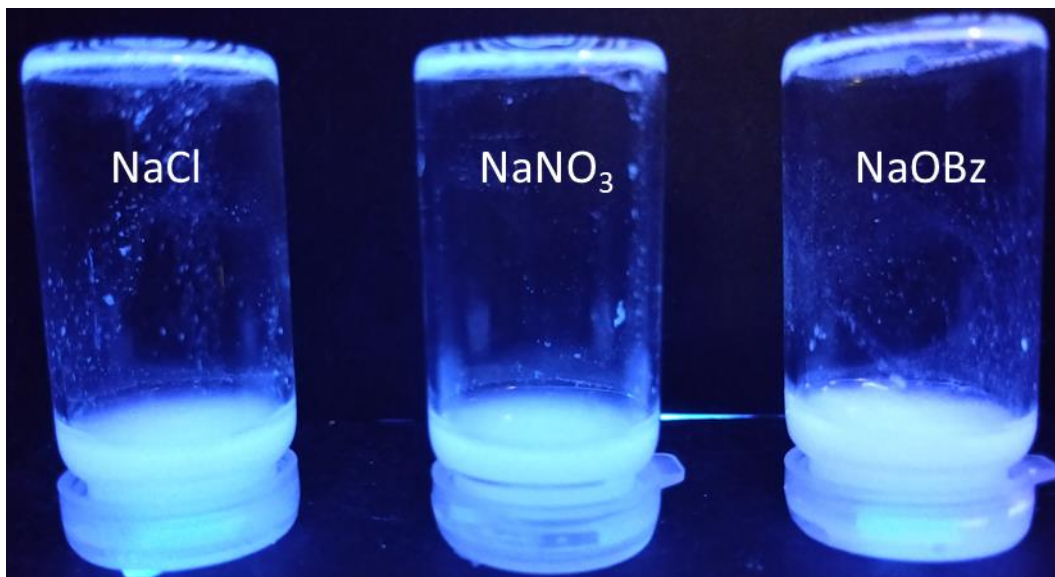


Figure S163 - Sonication test at 50 minutes. Compound **23** (5 mg, 1 mL) in NaCl, NaNO<sub>3</sub> and NaOBz inverted imaged under UV irradiation (test no. 2).

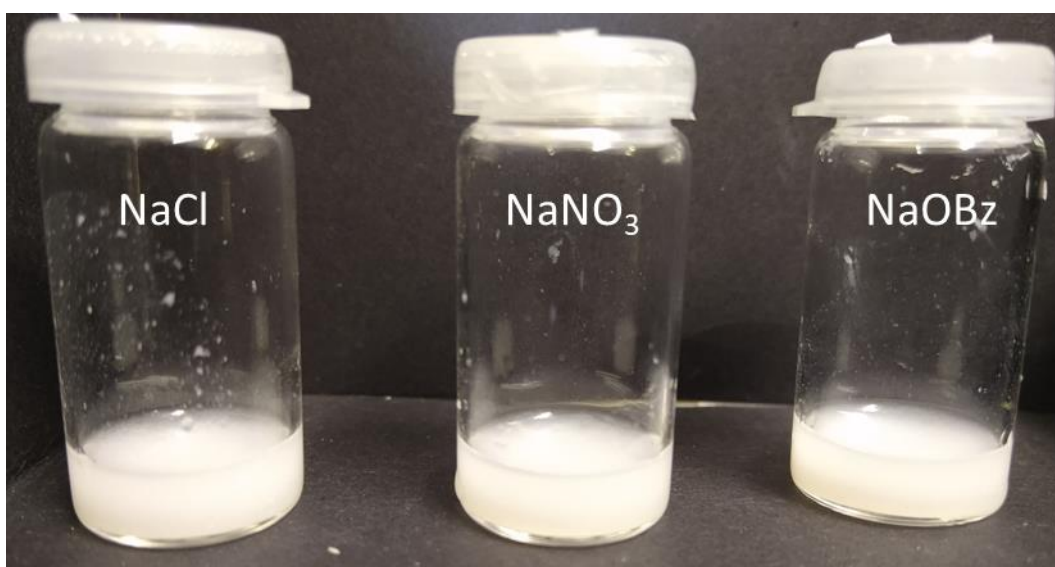


Figure S164 - Sonication test at 50 minutes. Compound **23** (5 mg, 1 mL) in NaCl, NaNO<sub>3</sub> and NaOBz (test no. 2).

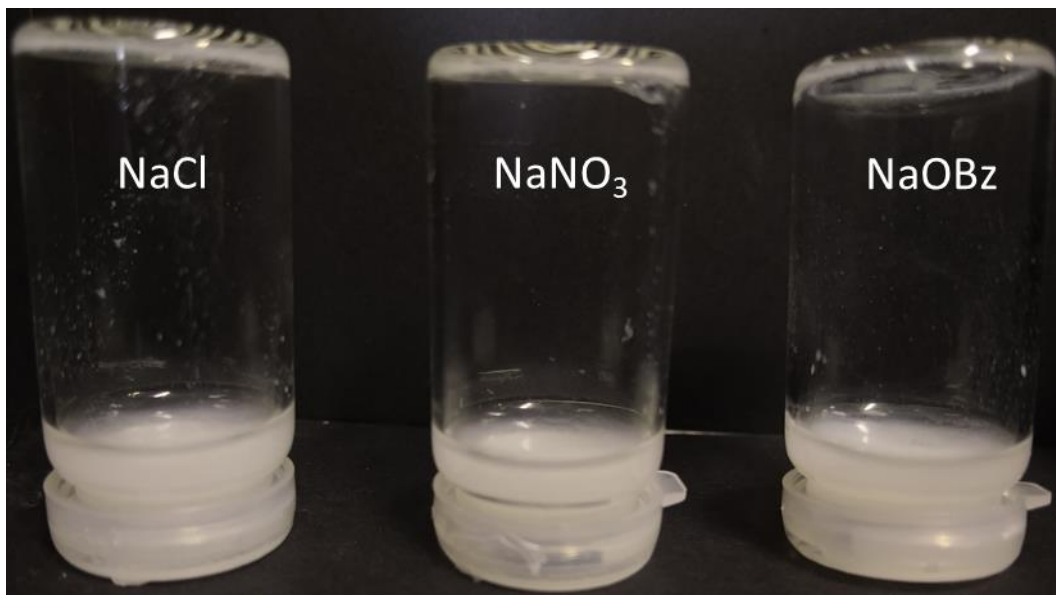


Figure S165 - Sonication test at 50 minutes. Compound **23** (5 mg, 1 mL) in NaCl, NaNO<sub>3</sub> and NaOBz inverted (test no. 2).

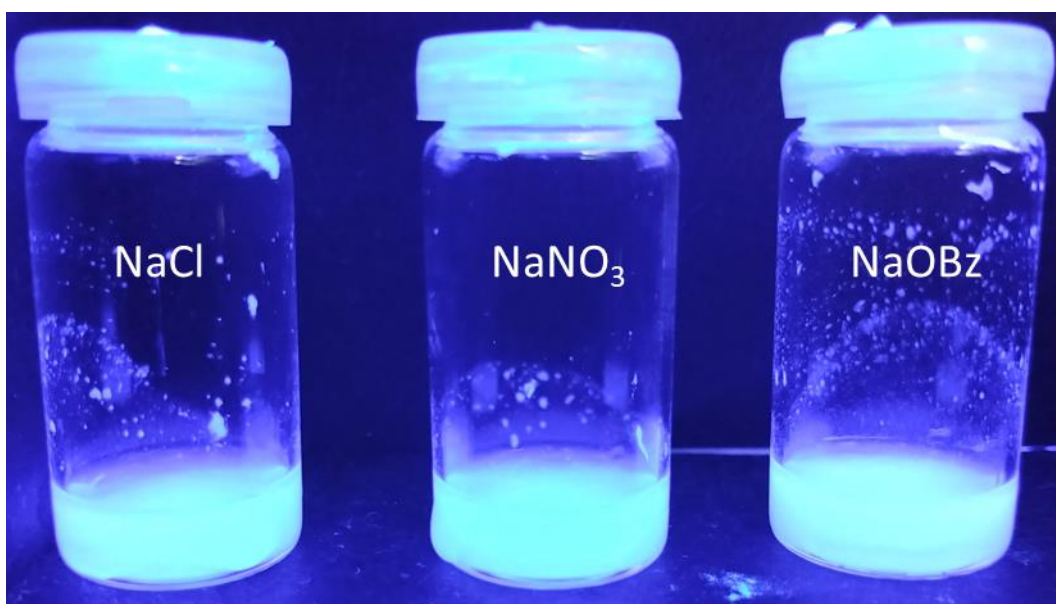


Figure S166 - Sonication test at 60 minutes. Compound **23** (5 mg, 1 mL) in NaCl, NaNO<sub>3</sub> and NaOBz imaged under UV irradiation (test no. 2).

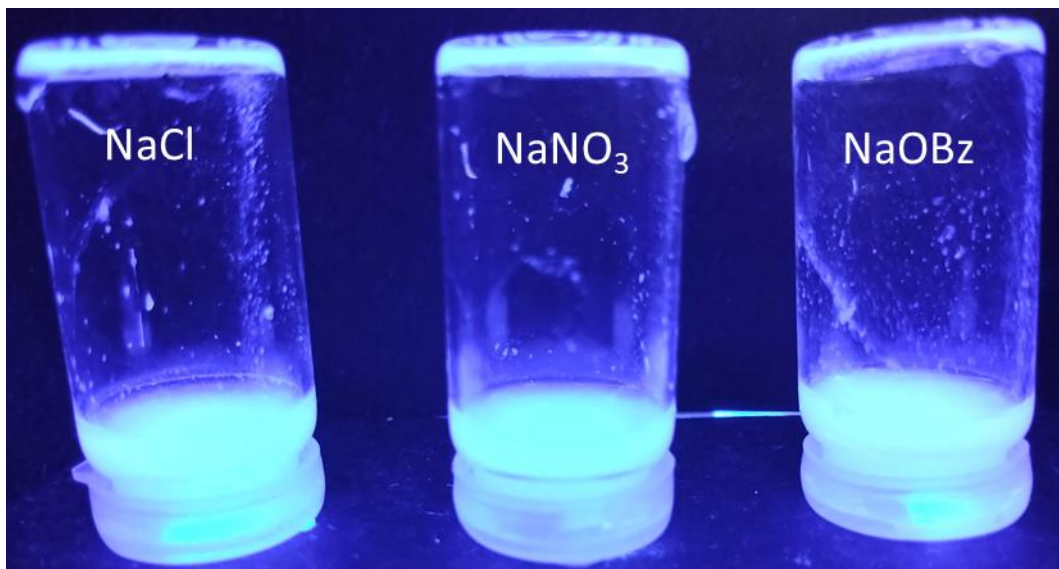


Figure S167 - Sonication test at 60 minutes. Compound **23** (5 mg, 1 mL) in NaCl, NaNO<sub>3</sub> and NaOBz inverted imaged under UV irradiation (test no. 2).

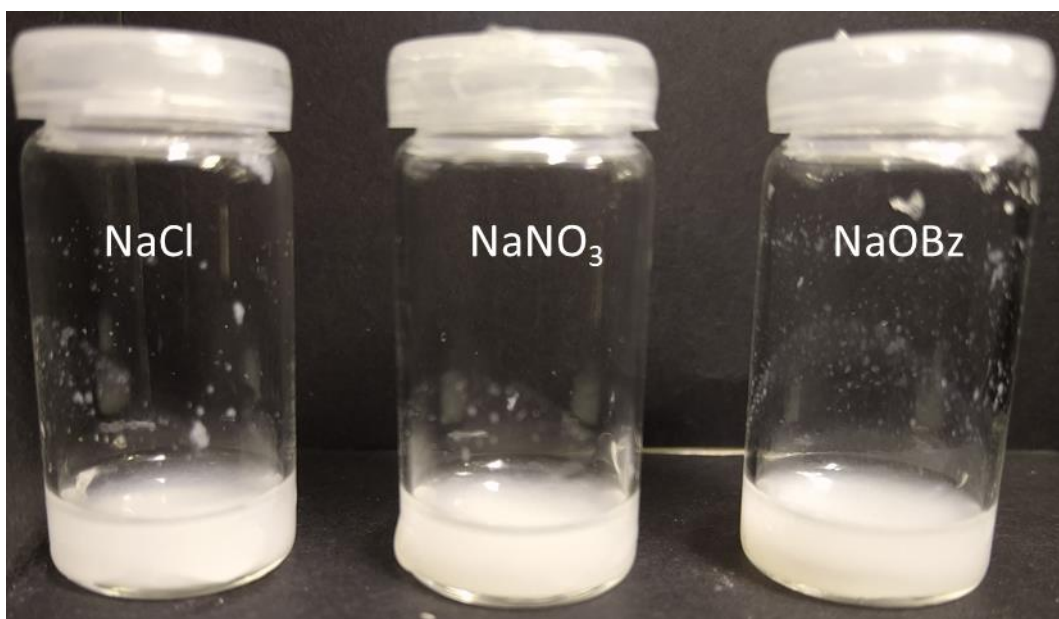


Figure S168 - Sonication test at 60 minutes. Compound **23** (5 mg, 1 mL) in NaCl, NaNO<sub>3</sub> and NaOBz (test no. 2).

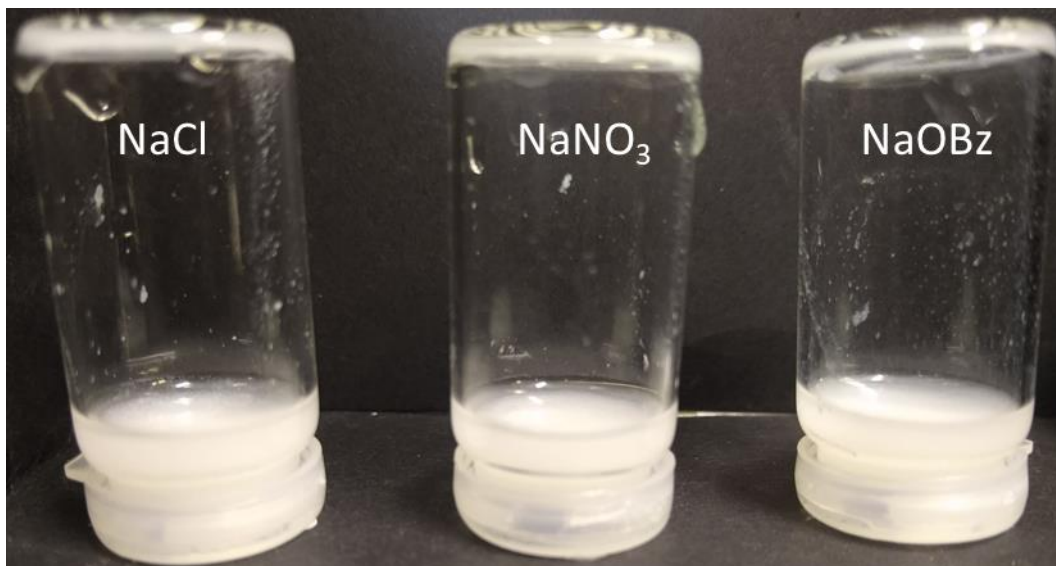


Figure S169 - Sonication test at 60 minutes. Compound **23** (5 mg, 1 mL) in NaCl, NaNO<sub>3</sub> and NaOBz inverted (test no. 2).

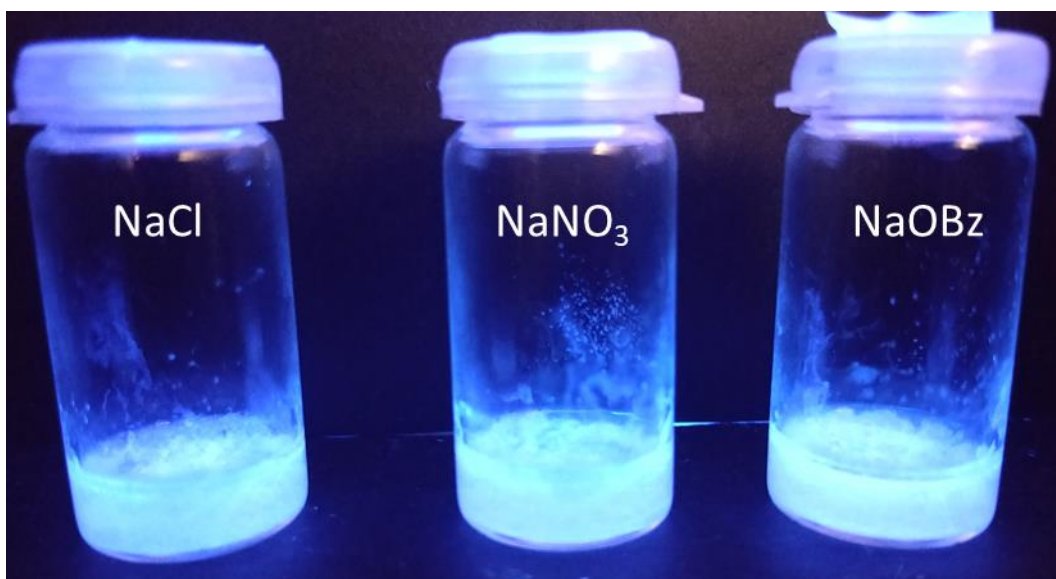


Figure S170 - Sonication test at 0 minutes. Compound **23** (5 mg, 1 mL) in NaCl, NaNO<sub>3</sub> and NaOBz imaged under UV irradiation (test no. 3).

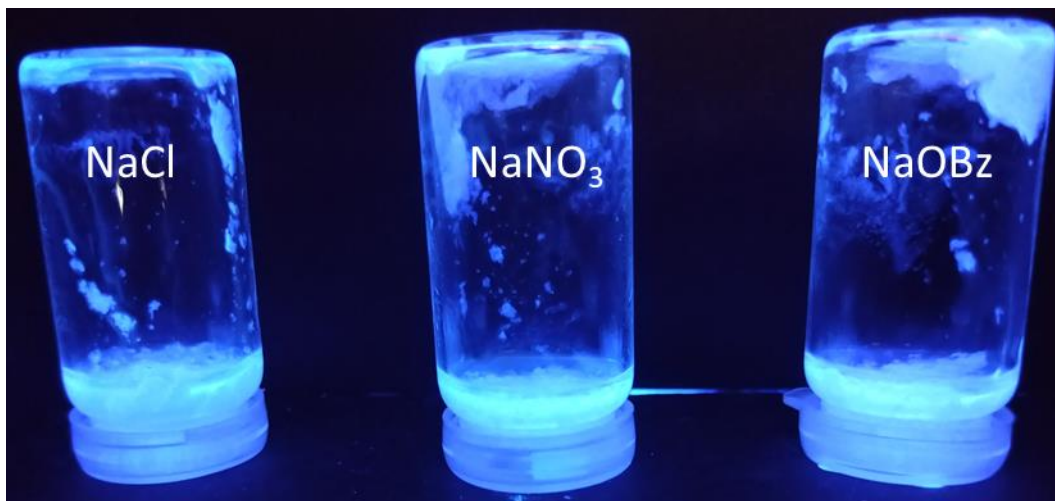


Figure S171 - Sonication test at 0 minutes. Compound **23** (5 mg, 1 mL) in NaCl, NaNO<sub>3</sub> and NaOBz inverted imaged under UV irradiation (test no. 3).

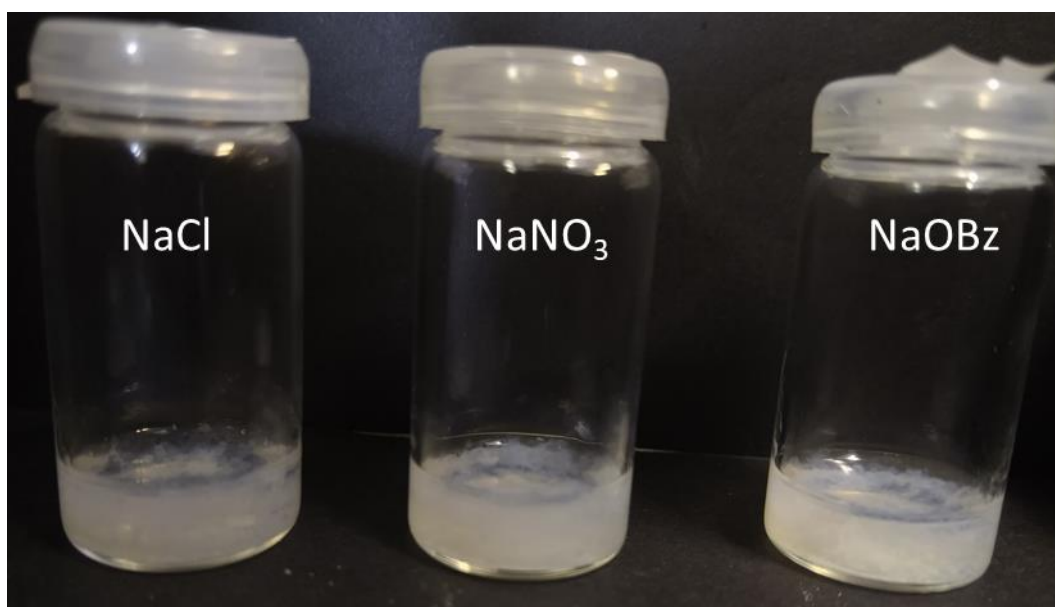


Figure S172 - Sonication test at 0 minutes. Compound **23** (5 mg, 1 mL) in NaCl, NaNO<sub>3</sub> and NaOBz (test no. 3).

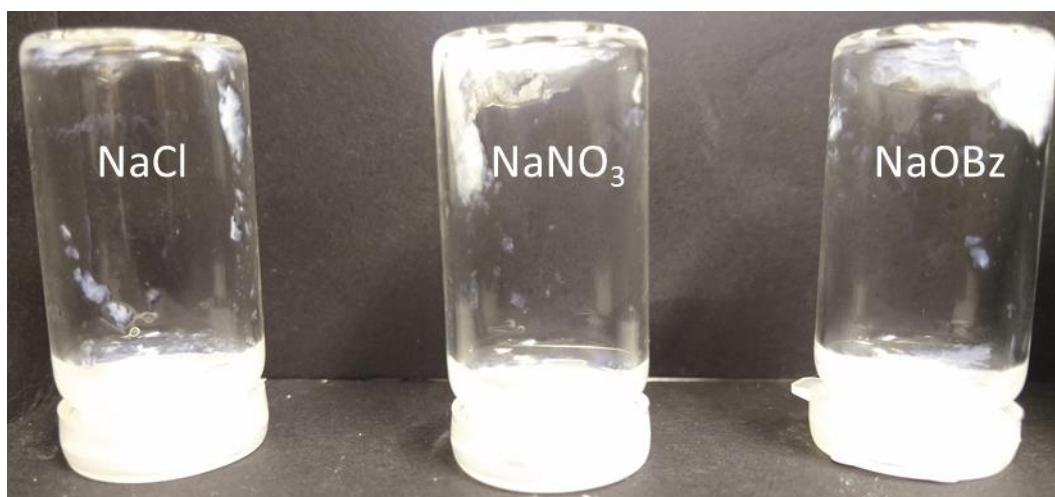


Figure S173 - Sonication test at 0 minutes. Compound **23** (5 mg, 1 mL) in NaCl, NaNO<sub>3</sub> and NaOBz inverted (test no. 3).

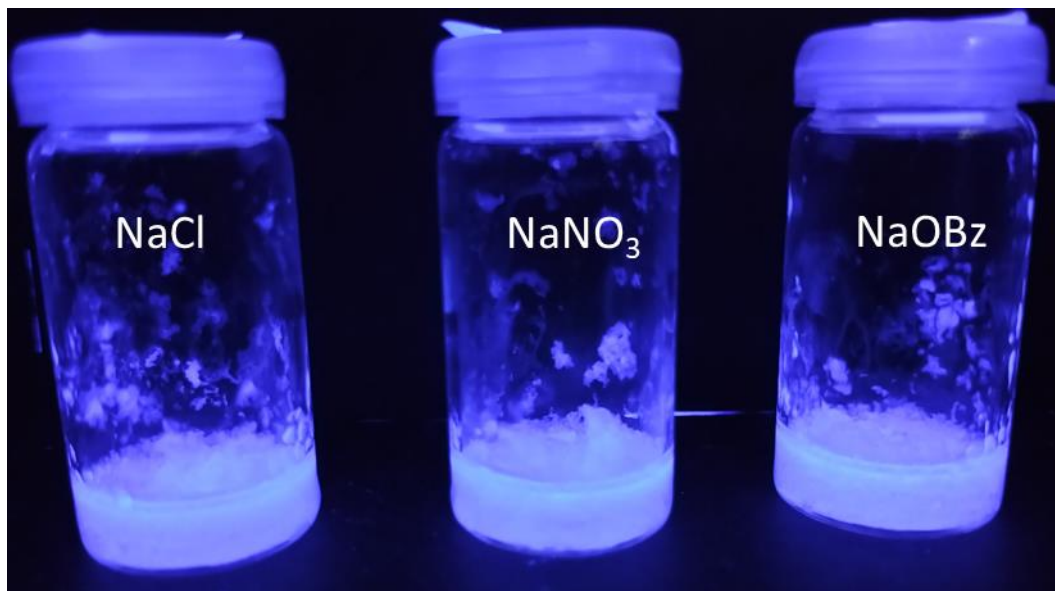


Figure S174 - Sonication test at 5 minutes. Compound **23** (5 mg, 1 mL) in NaCl, NaNO<sub>3</sub> and NaOBz imaged under UV irradiation (test no. 3).

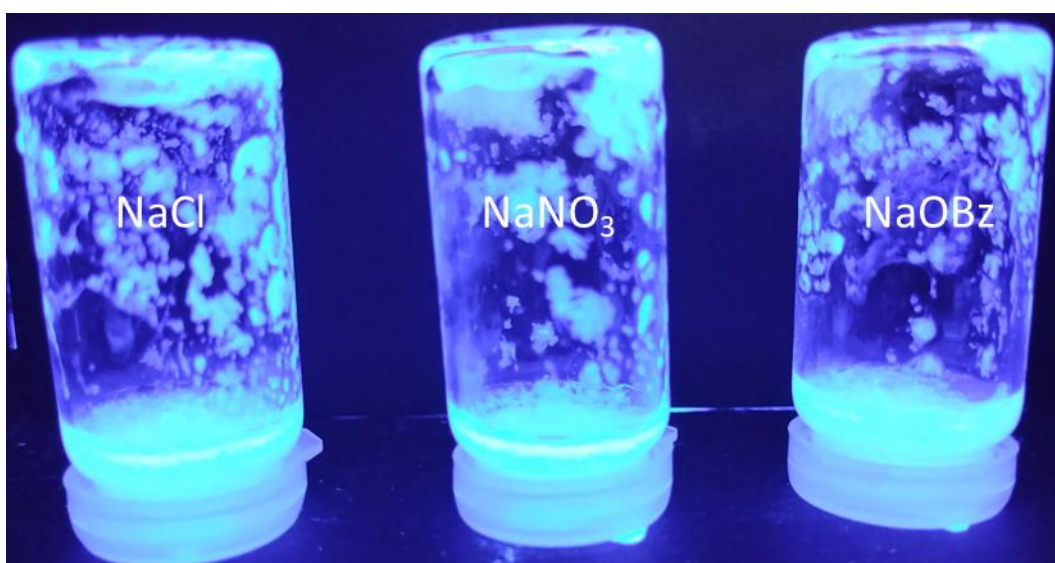


Figure S175 - Sonication test at 5 minutes. Compound **23** (5 mg, 1 mL) in NaCl, NaNO<sub>3</sub> and NaOBz inverted imaged under UV irradiation (test no. 3).

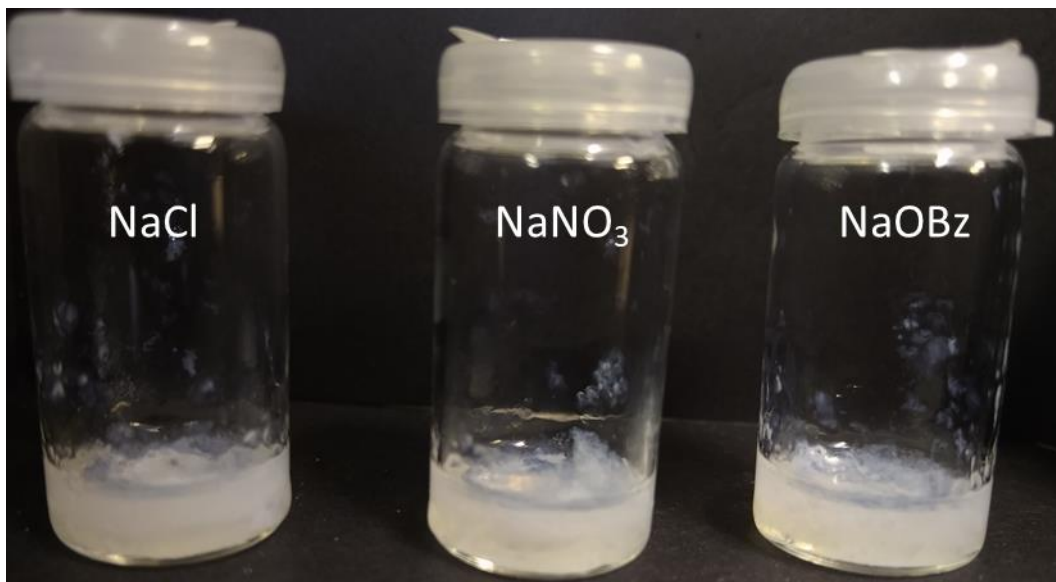


Figure S176 - Sonication test at 5 minutes. Compound **23** (5 mg, 1 mL) in NaCl, NaNO<sub>3</sub> and NaOBz (test no. 3).

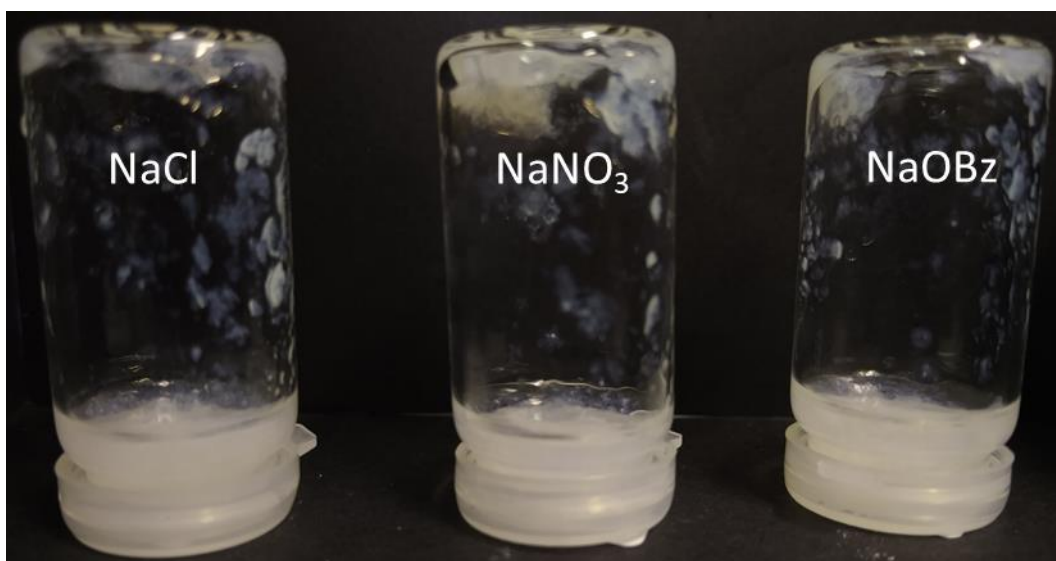


Figure S177 - Sonication test at 5 minutes. Compound **23** (5 mg, 1 mL) in NaCl, NaNO<sub>3</sub> and NaOBz inverted (test no. 3).

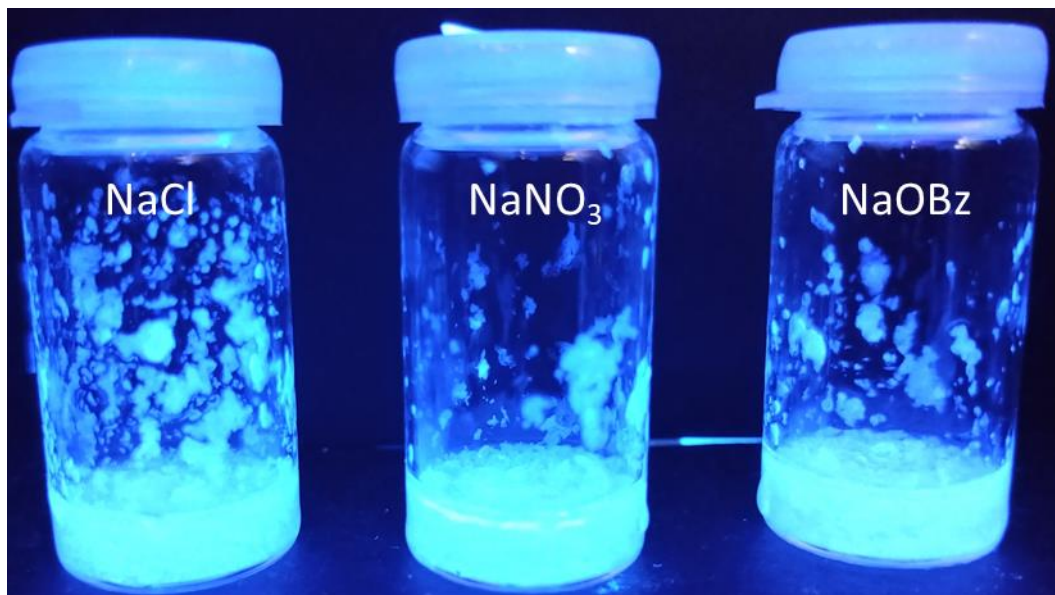


Figure S178 - Sonication test at 10 minutes. Compound **23** (5 mg, 1 mL) in NaCl, NaNO<sub>3</sub> and NaOBz imaged under UV irradiation (test no. 3).

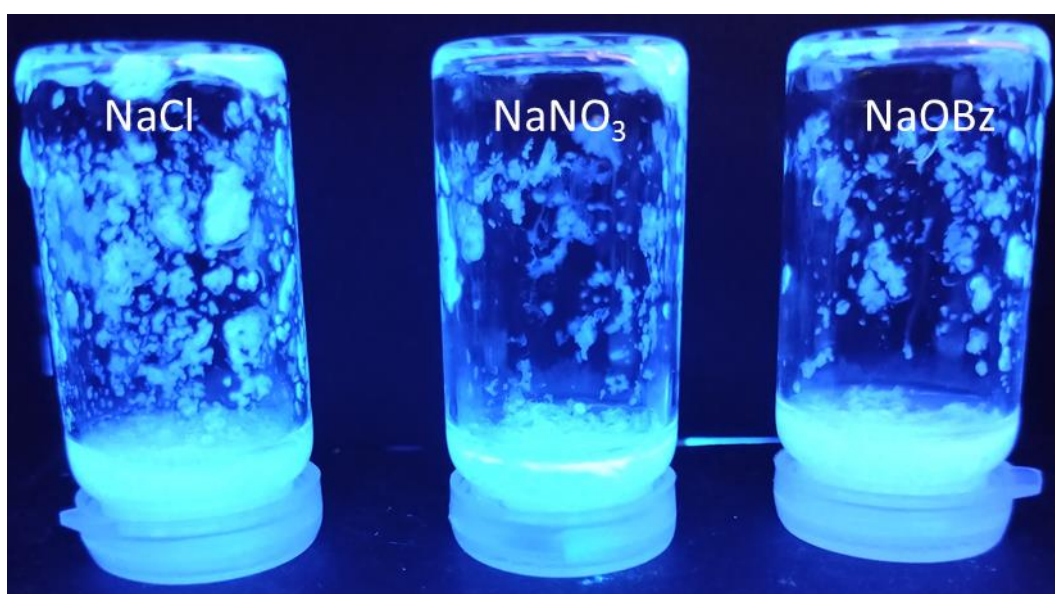


Figure S179 - Sonication test at 10 minutes. Compound **23** (5 mg, 1 mL) in NaCl, NaNO<sub>3</sub> and NaOBz inverted imaged under UV irradiation (test no. 3).

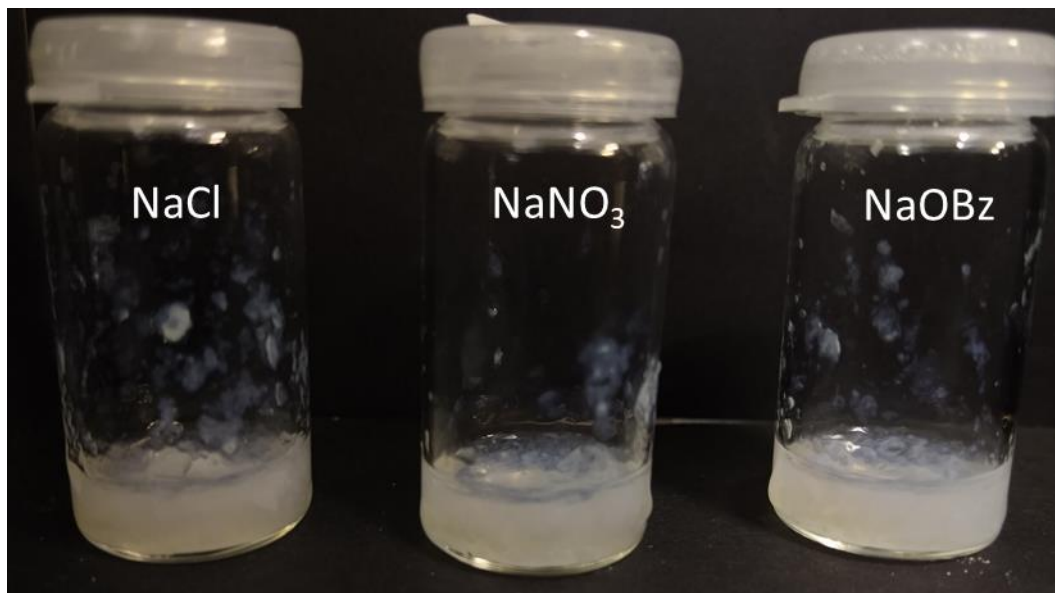


Figure S180 - Sonication test at 10 minutes. Compound **23** (5 mg, 1 mL) in NaCl, NaNO<sub>3</sub> and NaOBz (test no. 3).

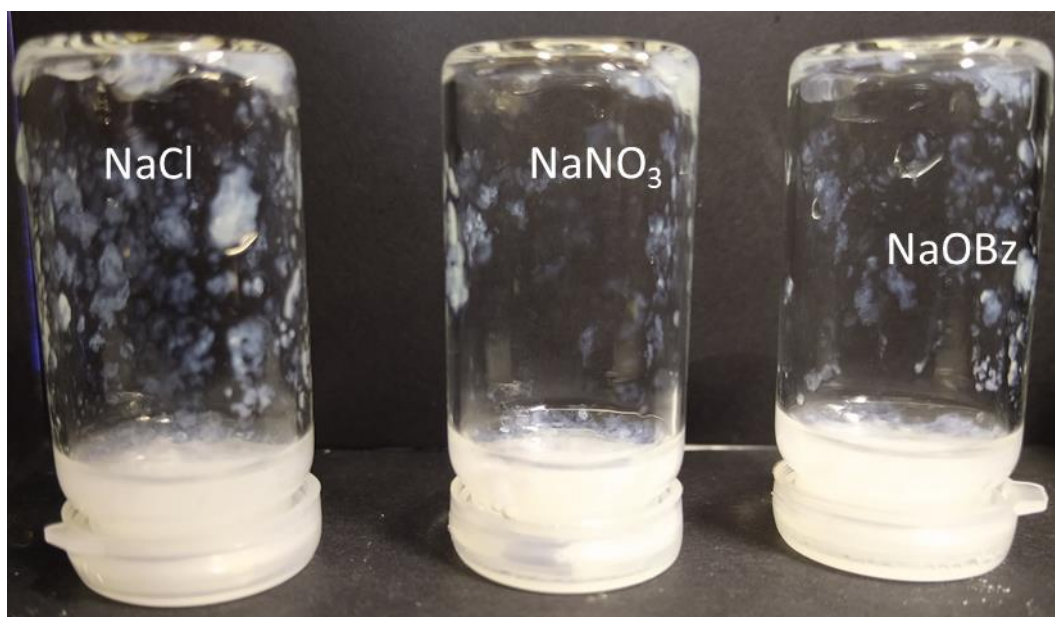


Figure S181 - Sonication test at 10 minutes. Compound **23** (5 mg, 1 mL) in NaCl, NaNO<sub>3</sub> and NaOBz inverted (test no. 3).

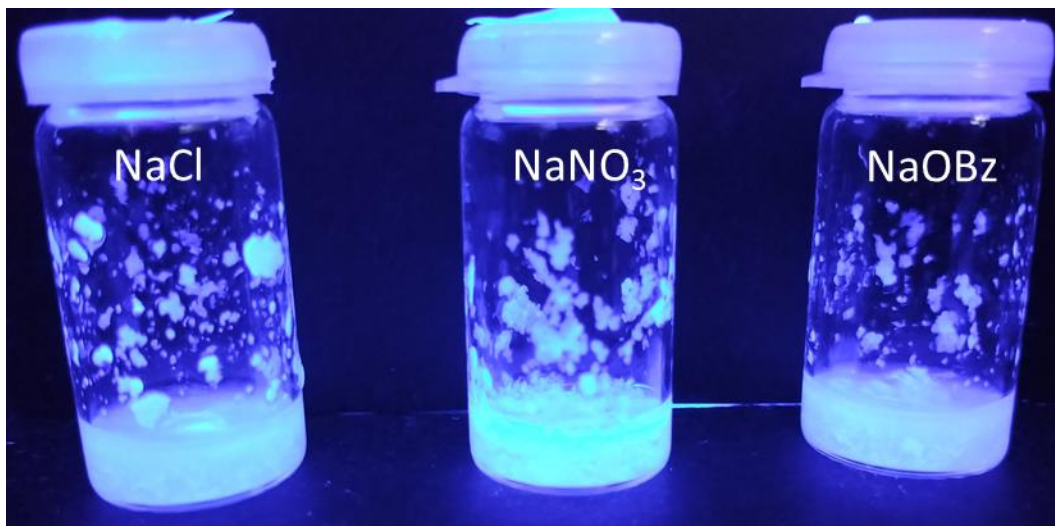


Figure S182 - Sonication test at 15 minutes. Compound **23** (5 mg, 1 mL) in NaCl, NaNO<sub>3</sub> and NaOBz imaged under UV irradiation (test no. 3).

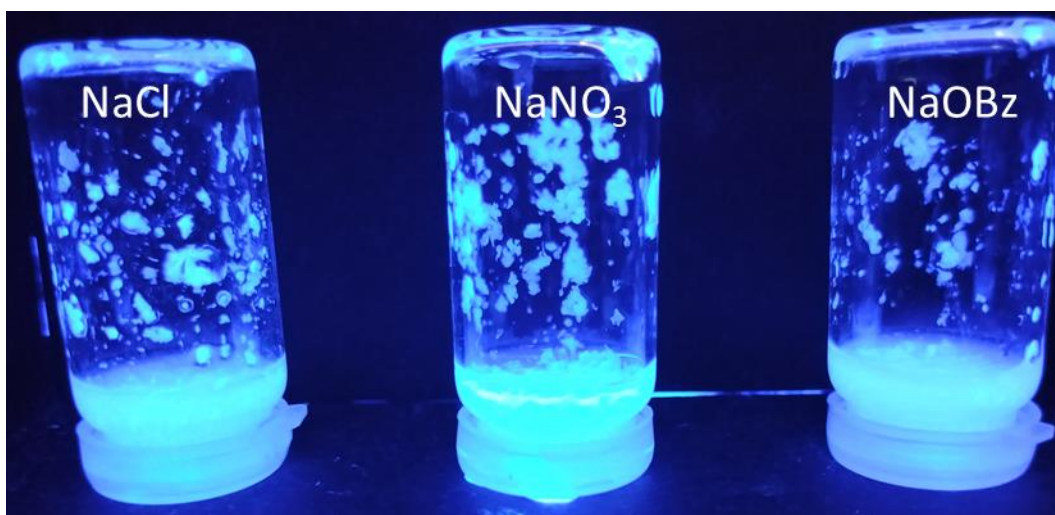


Figure S183 - Sonication test at 15 minutes. Compound **23** (5 mg, 1 mL) in NaCl, NaNO<sub>3</sub> and NaOBz inverted imaged under UV irradiation (test no. 3).

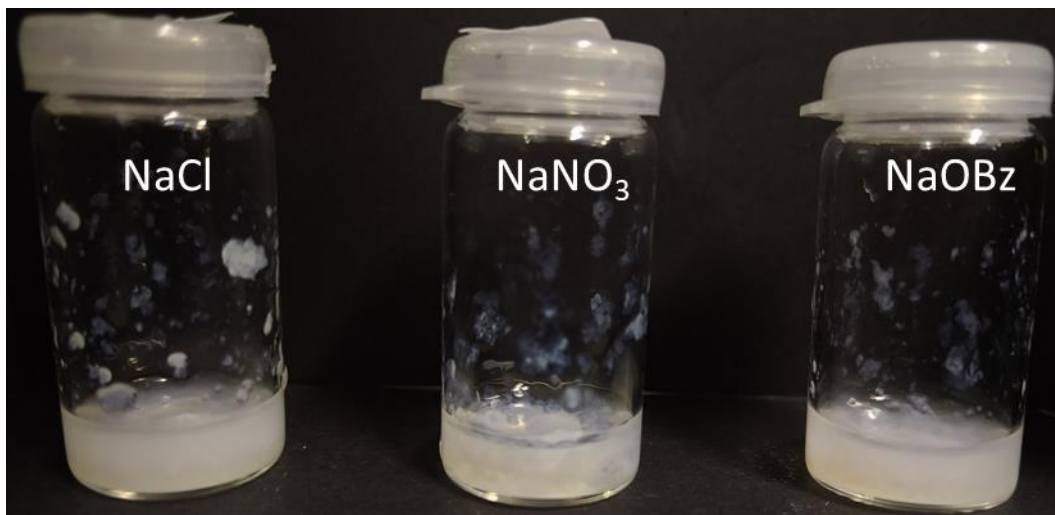


Figure S184 - Sonication test at 15 minutes. Compound **23** (5 mg, 1 mL) in NaCl, NaNO<sub>3</sub> and NaOBz (test no. 3).

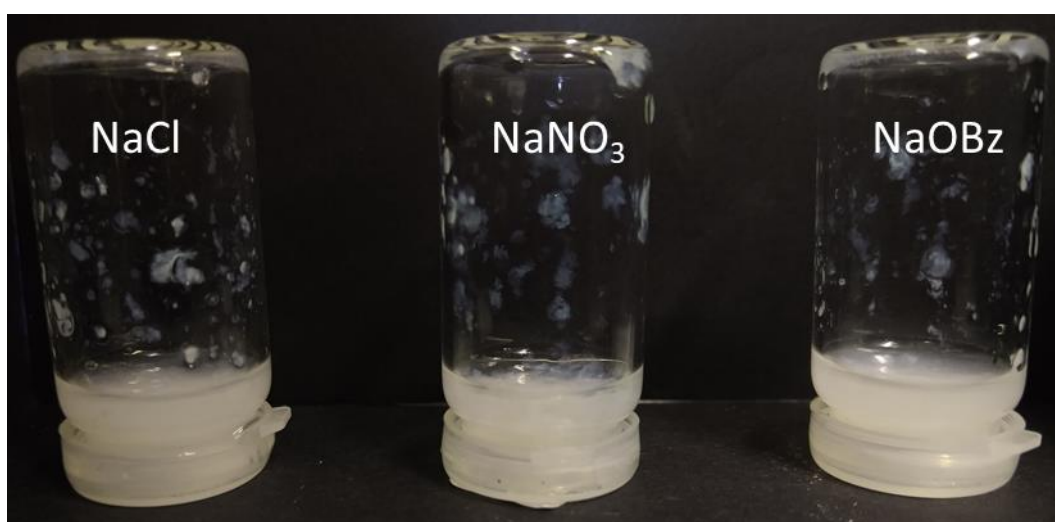


Figure S185 - Sonication test at 15 minutes. Compound **23** (5 mg, 1 mL) in NaCl, NaNO<sub>3</sub> and NaOBz inverted (test no. 3).

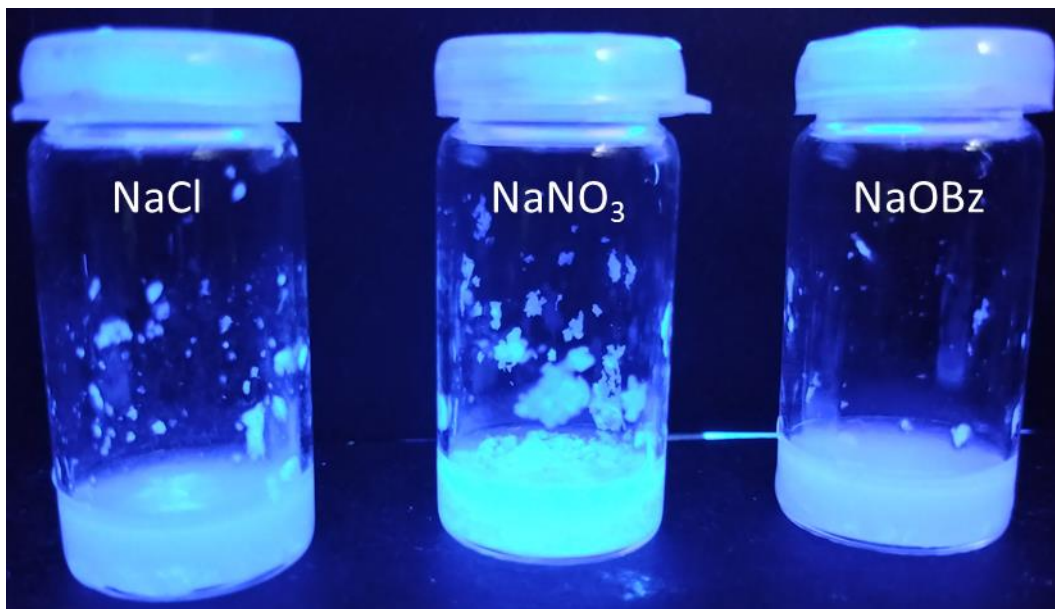


Figure S186 - Sonication test at 20 minutes. Compound **23** (5 mg, 1 mL) in NaCl, NaNO<sub>3</sub> and NaOBz imaged under UV irradiation (test no. 3).

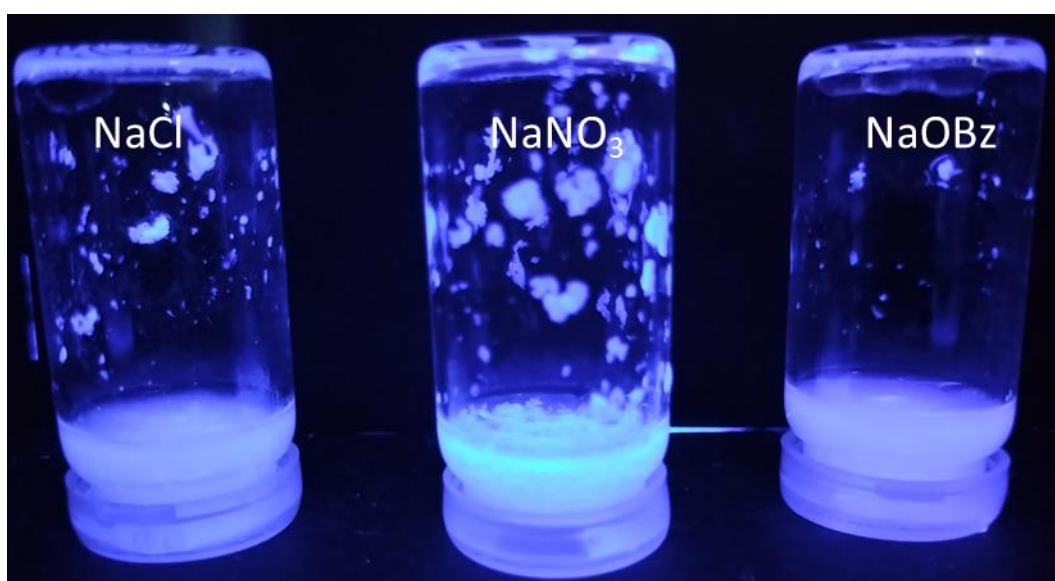


Figure S187 - Sonication test at 20 minutes. Compound **23** (5 mg, 1 mL) in NaCl, NaNO<sub>3</sub> and NaOBz inverted imaged under UV irradiation (test no. 3).

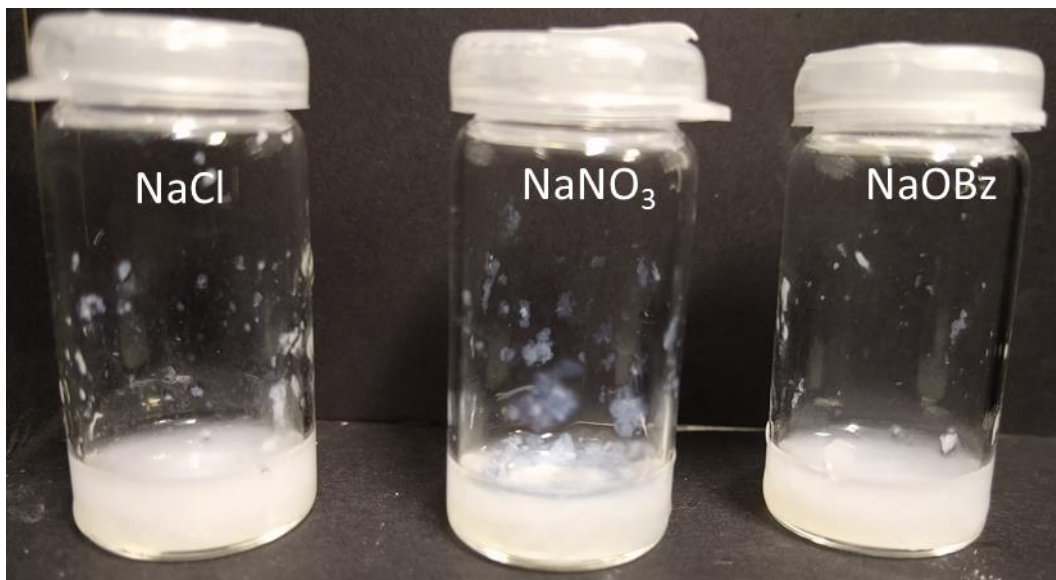


Figure S188 - Sonication test at 20 minutes. Compound **23** (5 mg, 1 mL) in NaCl, NaNO<sub>3</sub> and NaOBz (test no. 3).

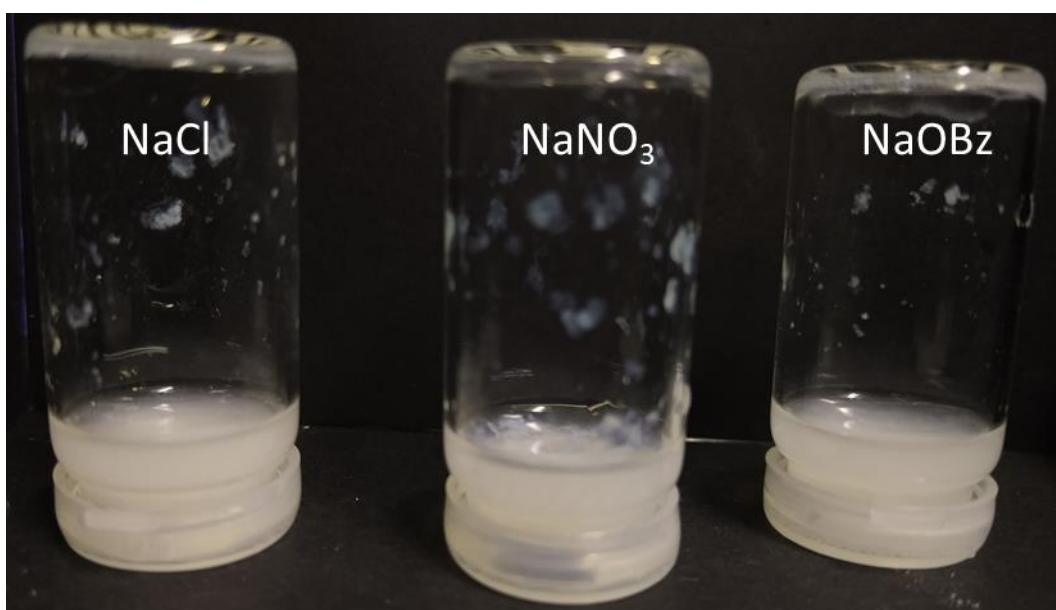


Figure S189 - Sonication test at 20 minutes. Compound **23** (5 mg, 1 mL) in NaCl, NaNO<sub>3</sub> and NaOBz inverted (test no. 3).

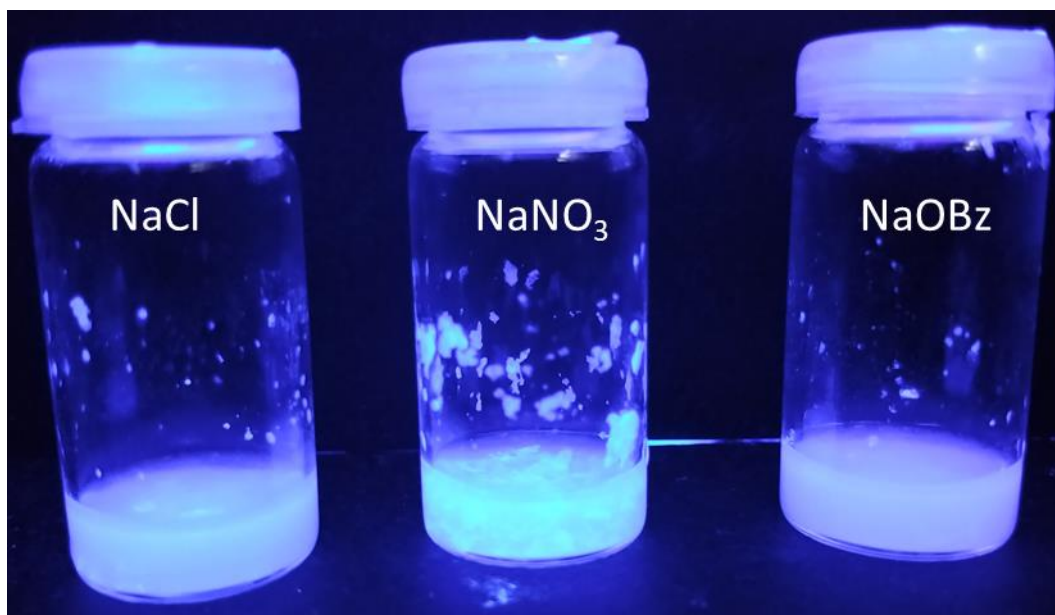


Figure S190 - Sonication test at 25 minutes. Compound **23** (5 mg, 1 mL) in NaCl, NaNO<sub>3</sub> and NaOBz imaged under UV irradiation (test no. 3).

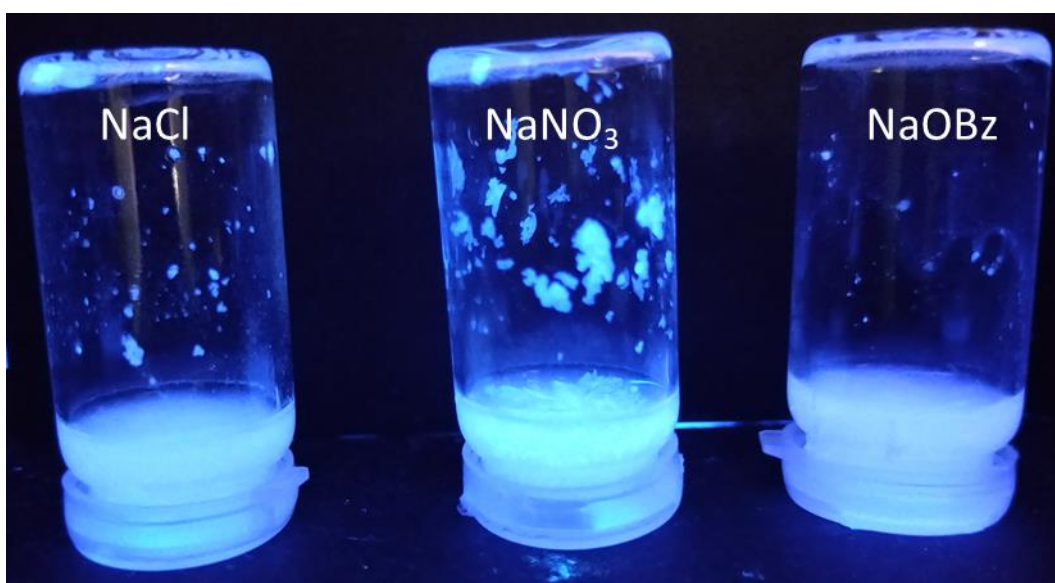


Figure S191 - Sonication test at 25 minutes. Compound **23** (5 mg, 1 mL) in NaCl, NaNO<sub>3</sub> and NaOBz inverted imaged under UV irradiation (test no. 3).

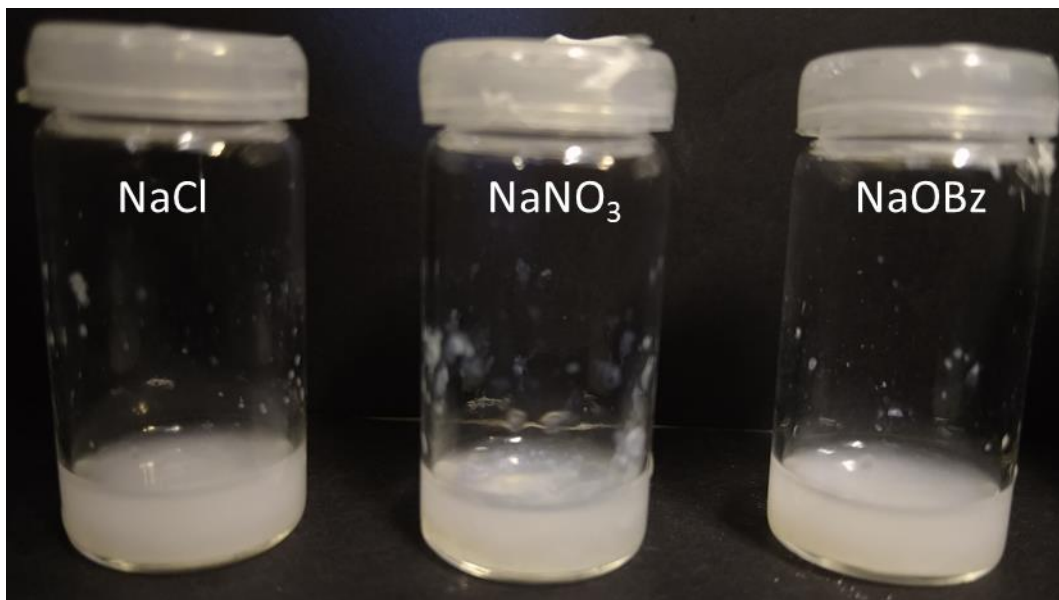


Figure S192 - Sonication test at 25 minutes. Compound **23** (5 mg, 1 mL) in NaCl, NaNO<sub>3</sub> and NaOBz (test no. 3).

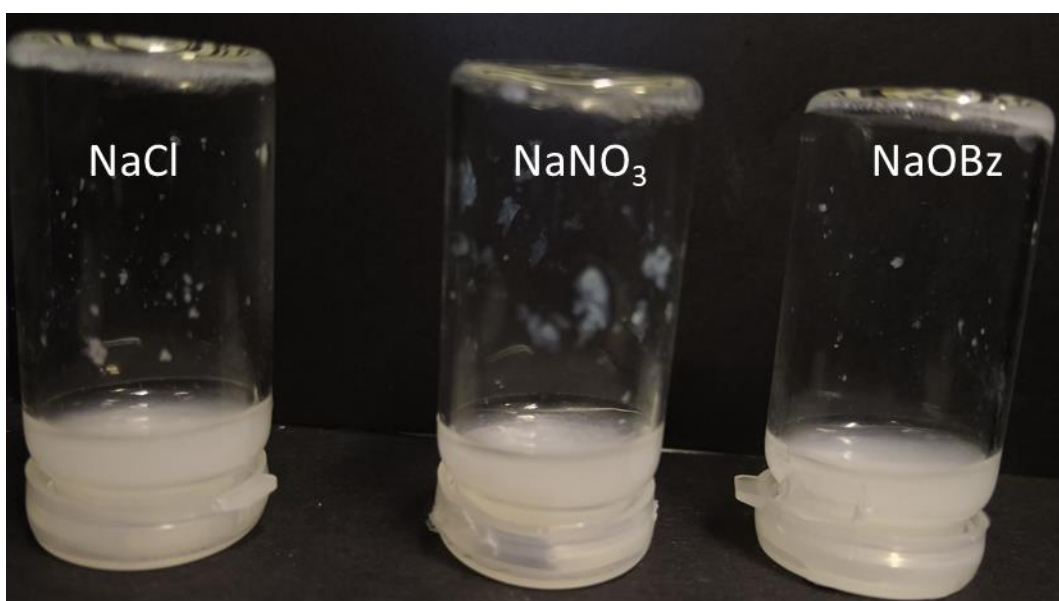
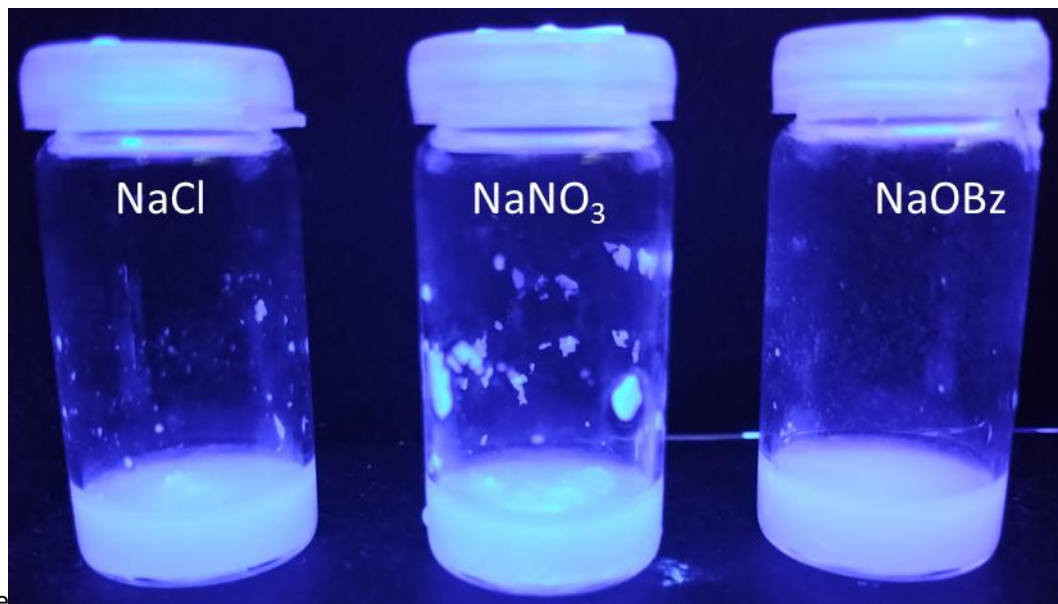


Figure S193 - Sonication test at 25 minutes. Compound **23** (5 mg, 1 mL) in NaCl, NaNO<sub>3</sub> and NaOBz inverted (test no. 3).



e  
Figure S194 - Sonication test at 30 minutes. Compound **23** (5 mg, 1 mL) in NaCl, NaNO<sub>3</sub> and NaOBz imaged under UV irradiation (test no. 3).

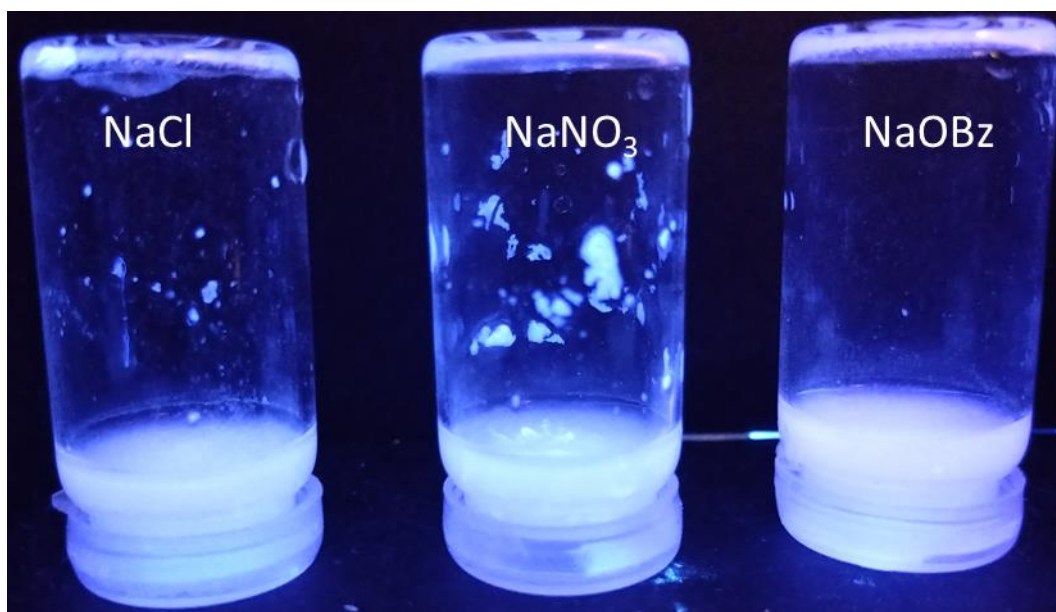


Figure S195 - Sonication test at 30 minutes. Compound **23** (5 mg, 1 mL) in NaCl, NaNO<sub>3</sub> and NaOBz inverted imaged under UV irradiation (test no. 3).

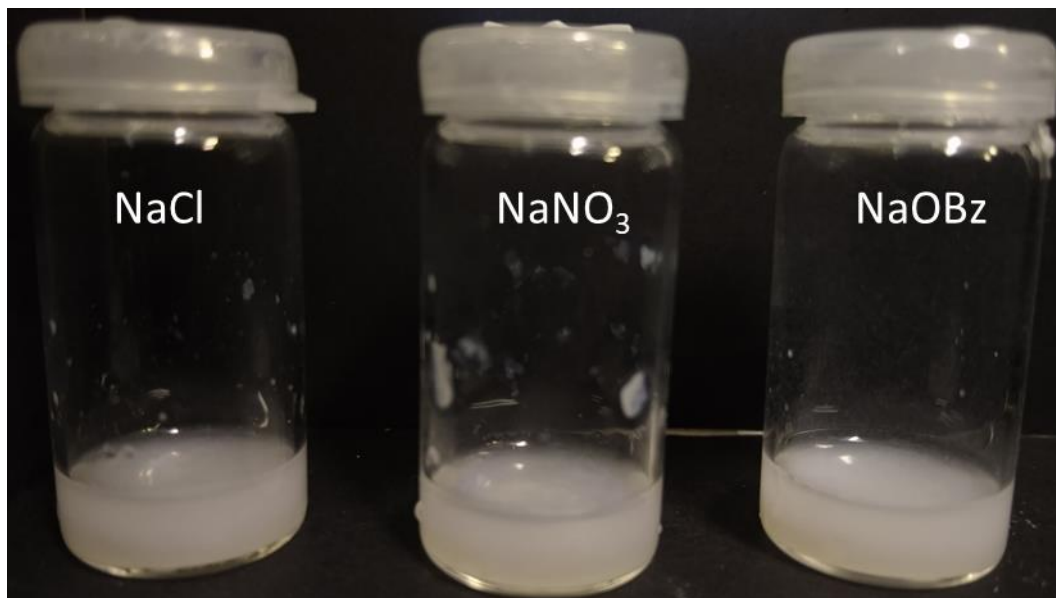


Figure S196 - Sonication test at 30 minutes. Compound **23** (5 mg, 1 mL) in NaCl, NaNO<sub>3</sub> and NaOBz (test no. 3).

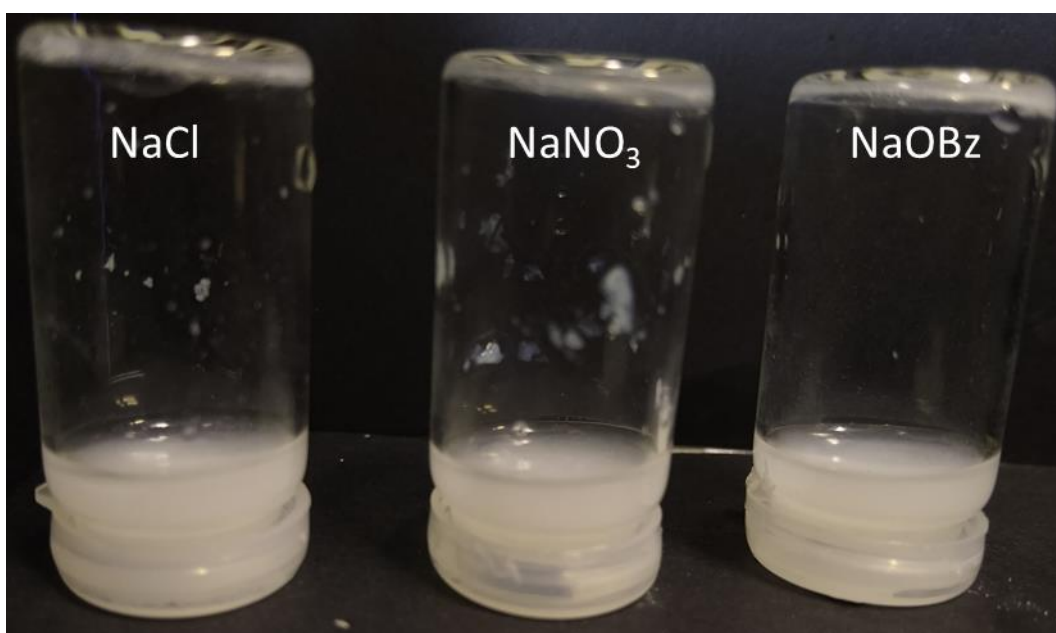


Figure S197 - Sonication test at 30 minutes. Compound **23** (5 mg, 1 mL) in NaCl, NaNO<sub>3</sub> and NaOBz inverted (test no. 3).

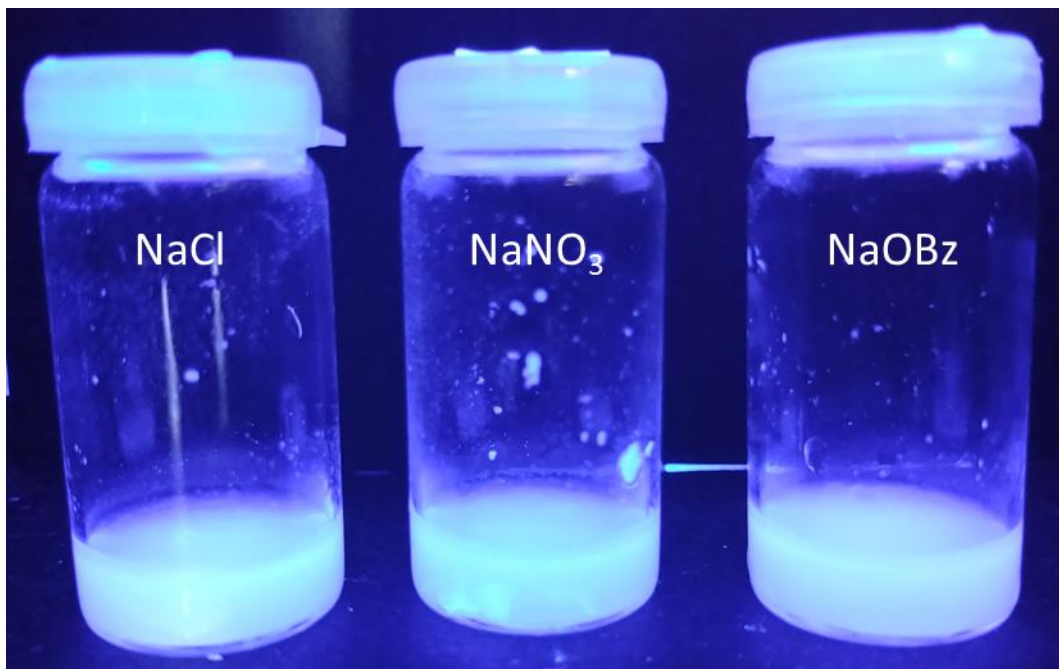


Figure S198 - Sonication test at 40 minutes. Compound **23** (5 mg, 1 mL) in NaCl, NaNO<sub>3</sub> and NaOBz imaged under UV irradiation (test no. 3).

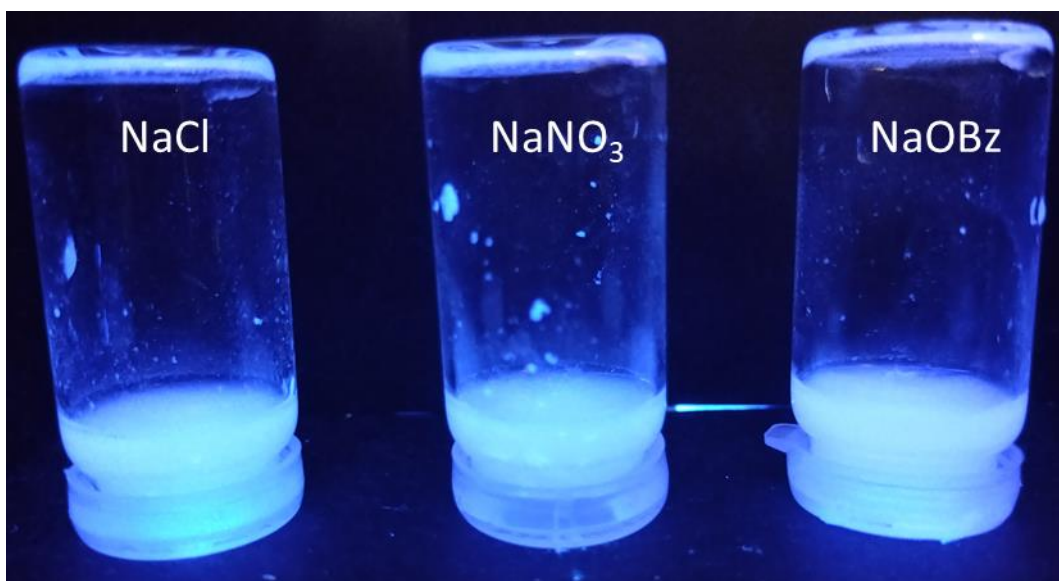


Figure S199 - Sonication test at 40 minutes. Compound **23** (5 mg, 1 mL) in NaCl, NaNO<sub>3</sub> and NaOBz inverted imaged under UV irradiation (test no. 3).

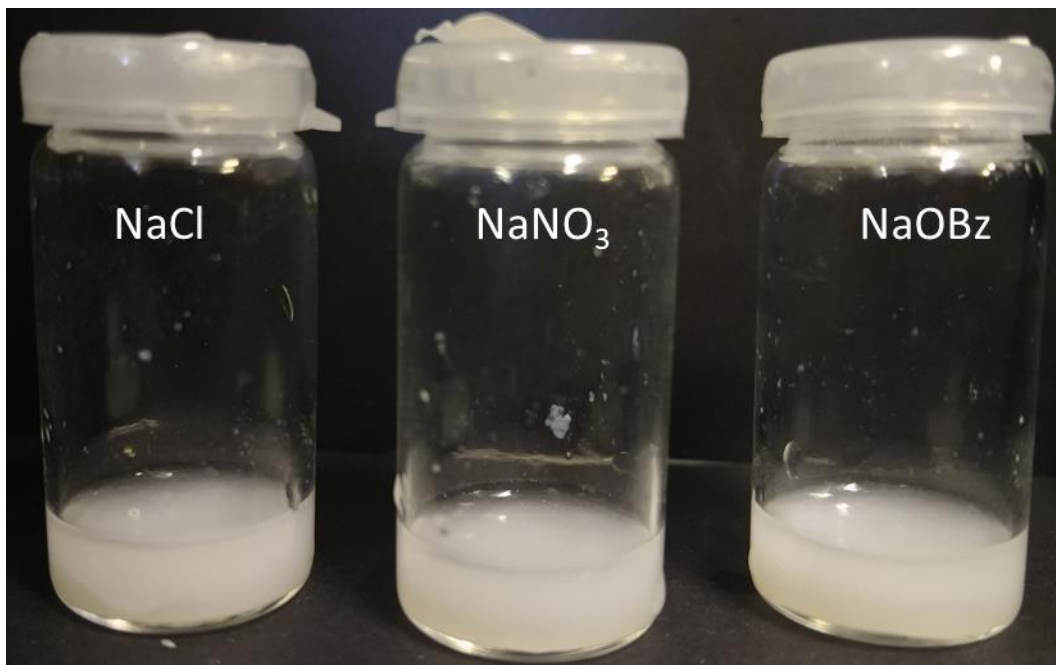


Figure S200 - Sonication test at 40 minutes. Compound **23** (5 mg, 1 mL) in NaCl, NaNO<sub>3</sub> and NaOBz (test no. 3).

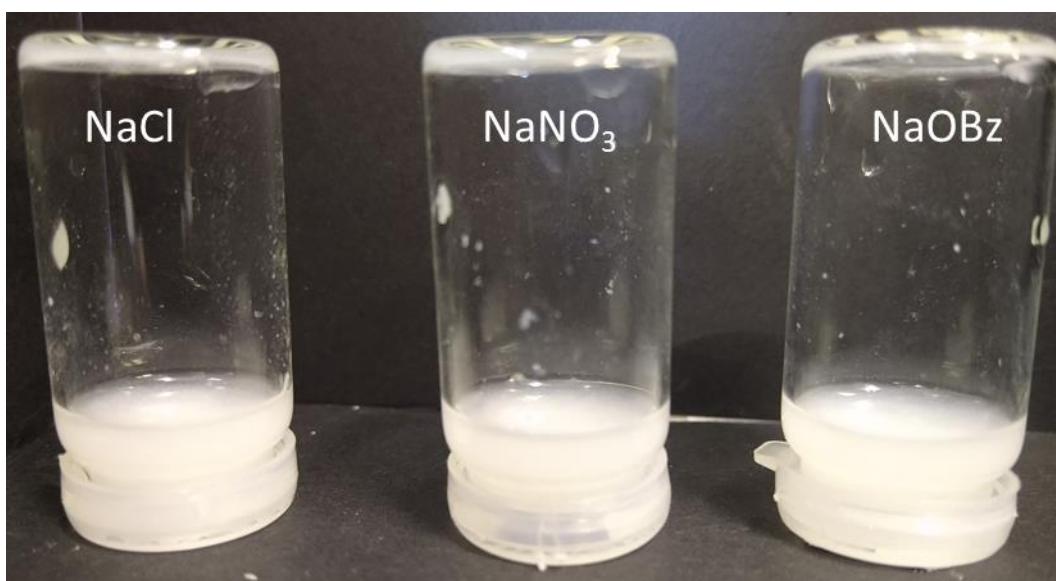


Figure S201 - Sonication test at 40 minutes. Compound **23** (5 mg, 1 mL) in NaCl, NaNO<sub>3</sub> and NaOBz inverted (test no. 3).

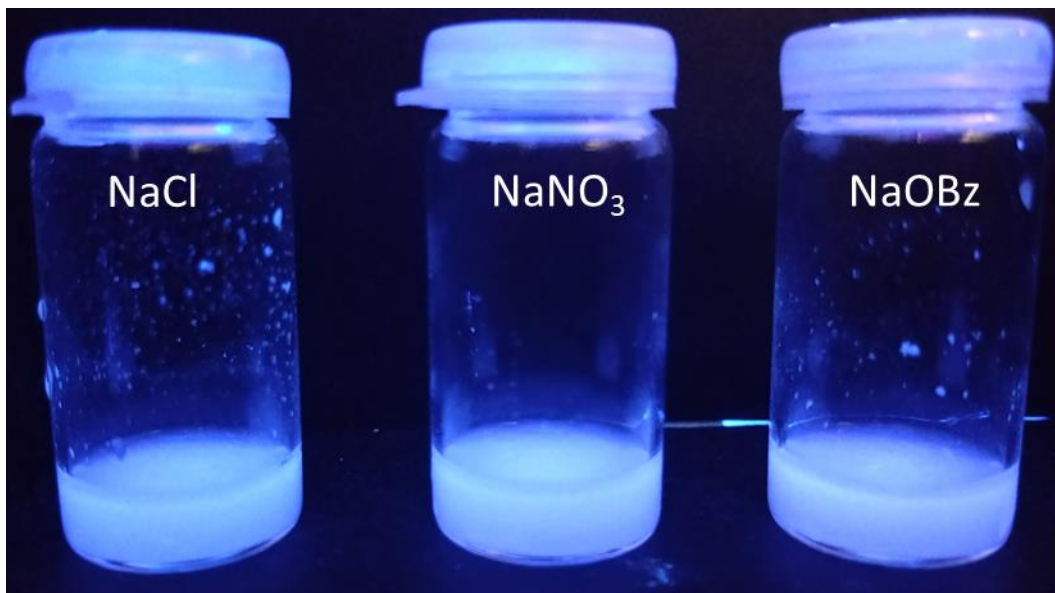


Figure S202 - Sonication test at 50 minutes. Compound **23** (5 mg, 1 mL) in NaCl, NaNO<sub>3</sub> and NaOBz imaged under UV irradiation (test no. 3).

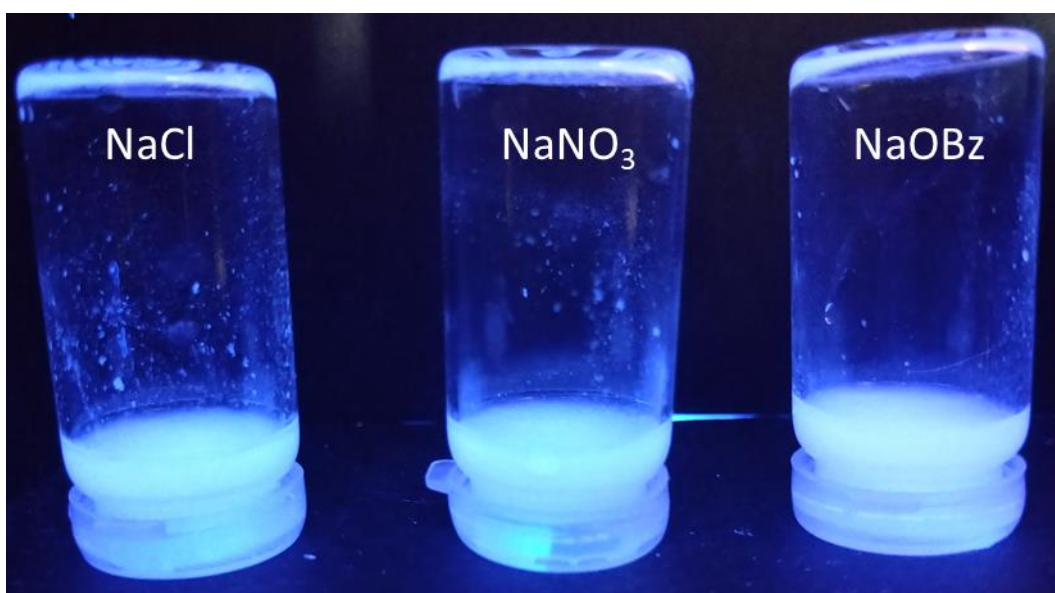


Figure S203 - Sonication test at 50 minutes. Compound **23** (5 mg, 1 mL) in NaCl, NaNO<sub>3</sub> and NaOBz inverted imaged under UV irradiation (test no. 3).

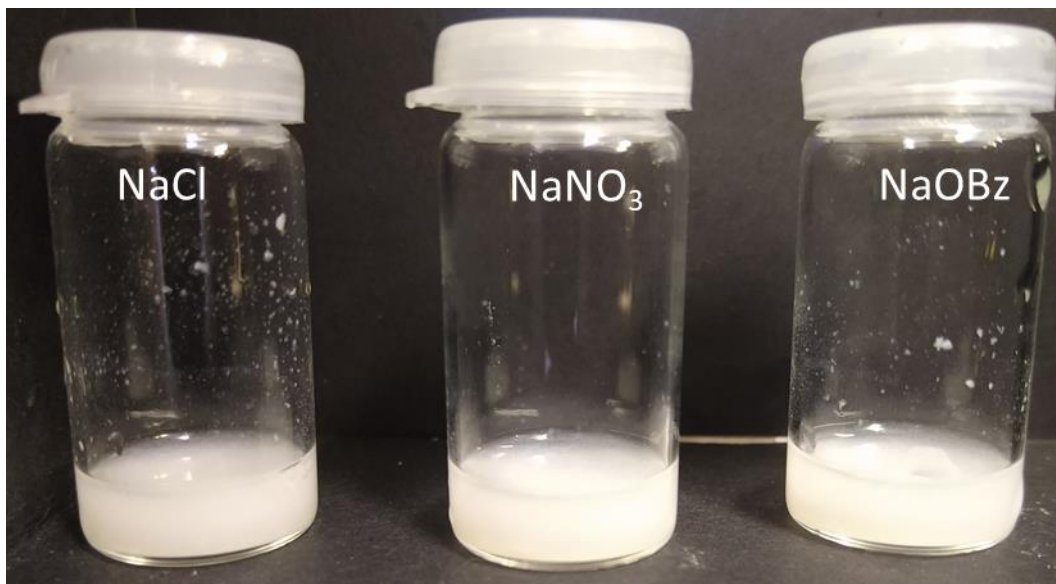


Figure S204 - Sonication test at 50 minutes. Compound **23** (5 mg, 1 mL) in NaCl, NaNO<sub>3</sub> and NaOBz (test no. 3).

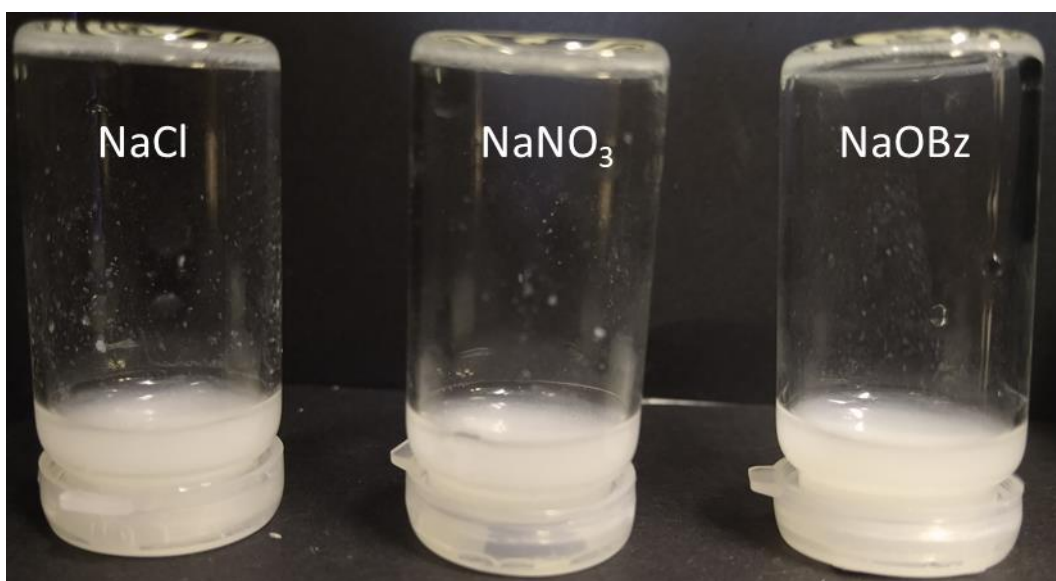


Figure S205 - Sonication test at 50 minutes. Compound **23** (5 mg, 1 mL) in NaCl, NaNO<sub>3</sub> and NaOBz inverted (test no. 3).

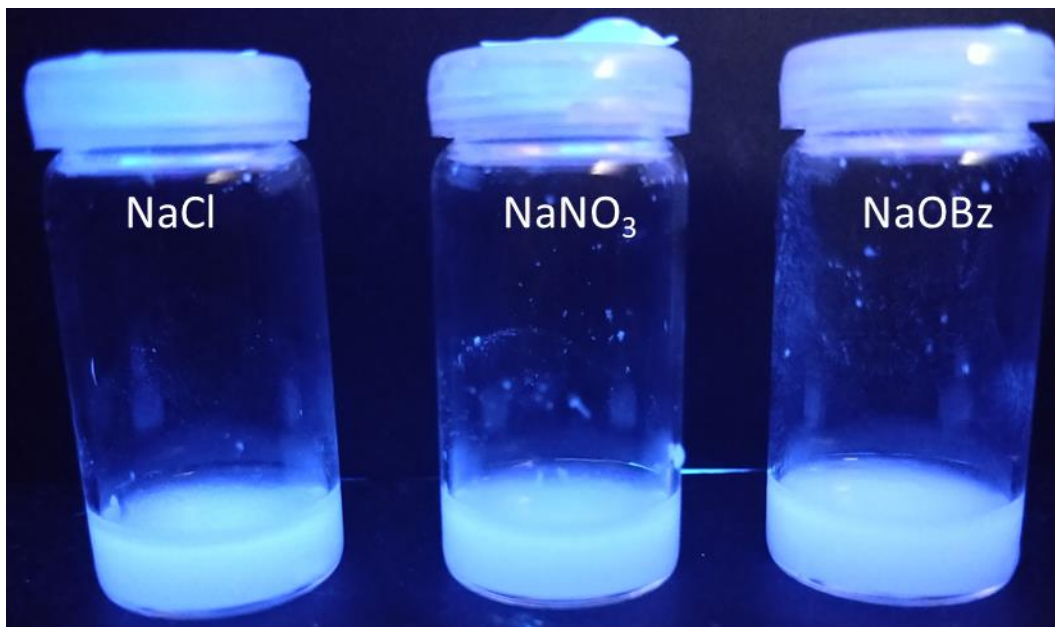


Figure S206 - Sonication test at 60 minutes. Compound **23** (5 mg, 1 mL) in NaCl, NaNO<sub>3</sub> and NaOBz imaged under UV irradiation (test no. 3).

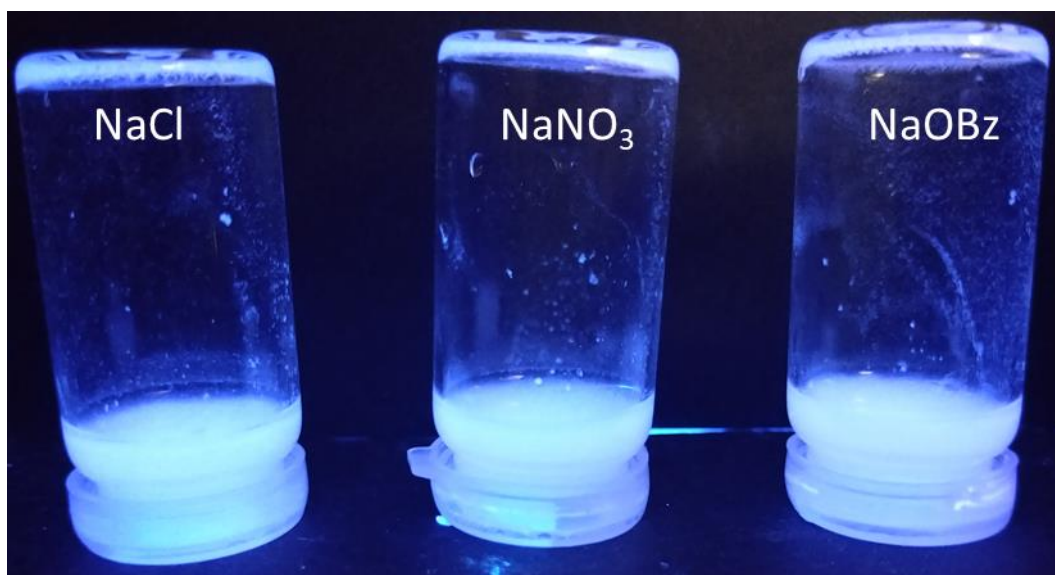


Figure S207 - Sonication test at 60 minutes. Compound **23** (5 mg, 1 mL) in NaCl, NaNO<sub>3</sub> and NaOBz inverted imaged under UV irradiation (test no. 3).

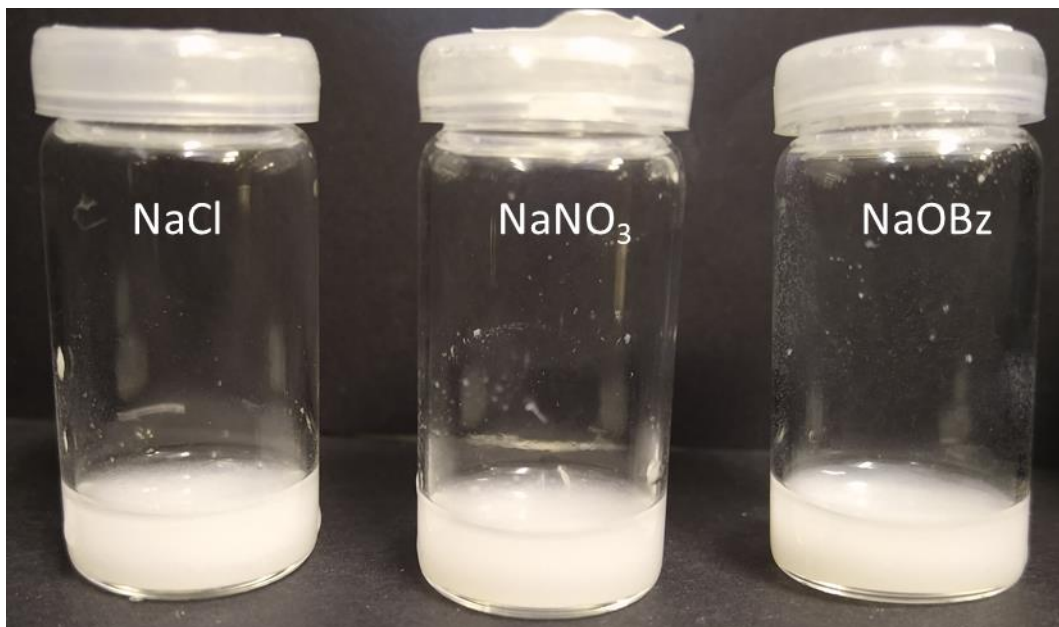


Figure S208 - Sonication test at 60 minutes. Compound **23** (5 mg, 1 mL) in NaCl, NaNO<sub>3</sub> and NaOBz (test no. 3).

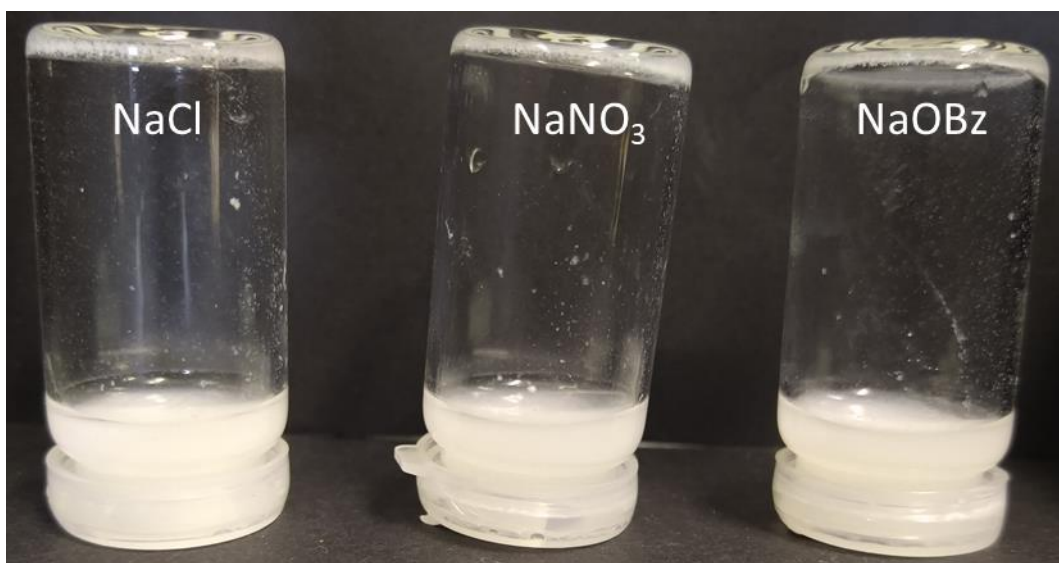


Figure S209 - Sonication test at 60 minutes. Compound **23** (5 mg, 1 mL) in NaCl, NaNO<sub>3</sub> and NaOBz inverted (test no. 3).

## 9.10. Microscopy

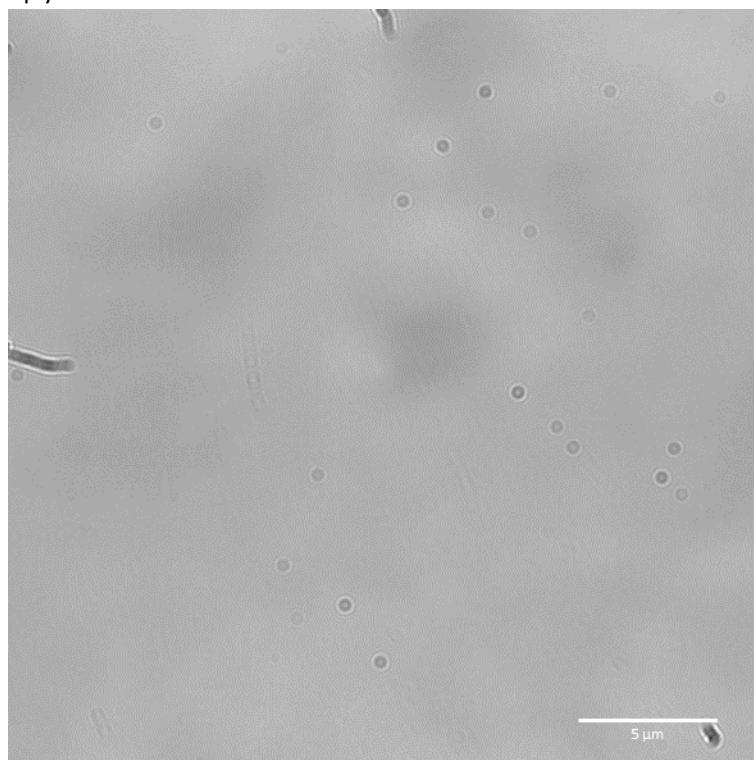


Figure S210 – Transmitted LED microscopy image of compound **22** (5 mg/mL) in NaCl (0.505 M).

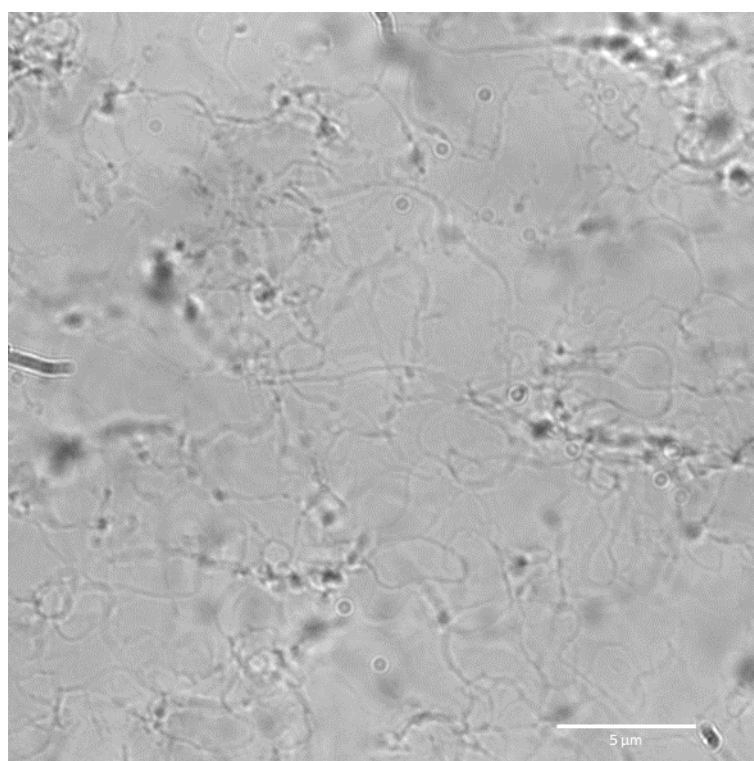


Figure S211 - Transmitted LED microscopy image of a hydrogel containing compound **23** (5 mg/mL) in NaCl (0.505 M).

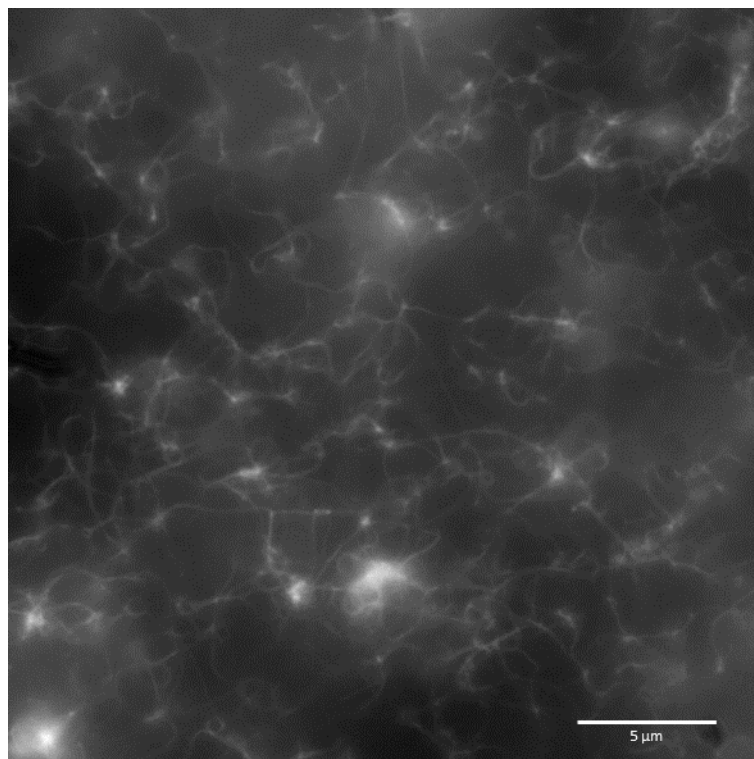


Figure S212 - DAPI LED microscopy image of a hydrogel containing compound **23** (5 mg/mL) in NaCl (0.505 M).

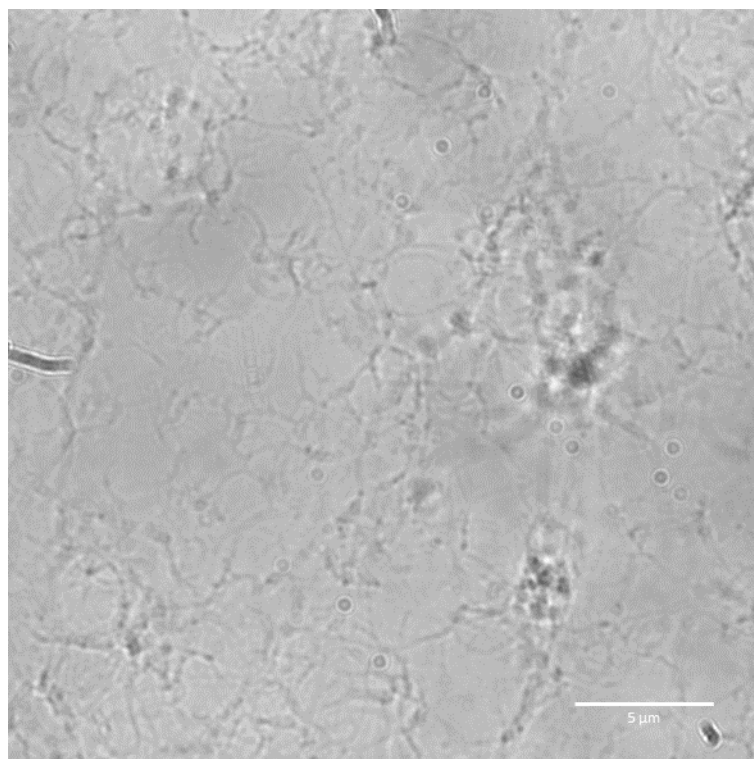


Figure S213 - Transmitted LED microscopy image of a hydrogel containing compound **23** (5 mg/mL) in KCl (0.505 M).

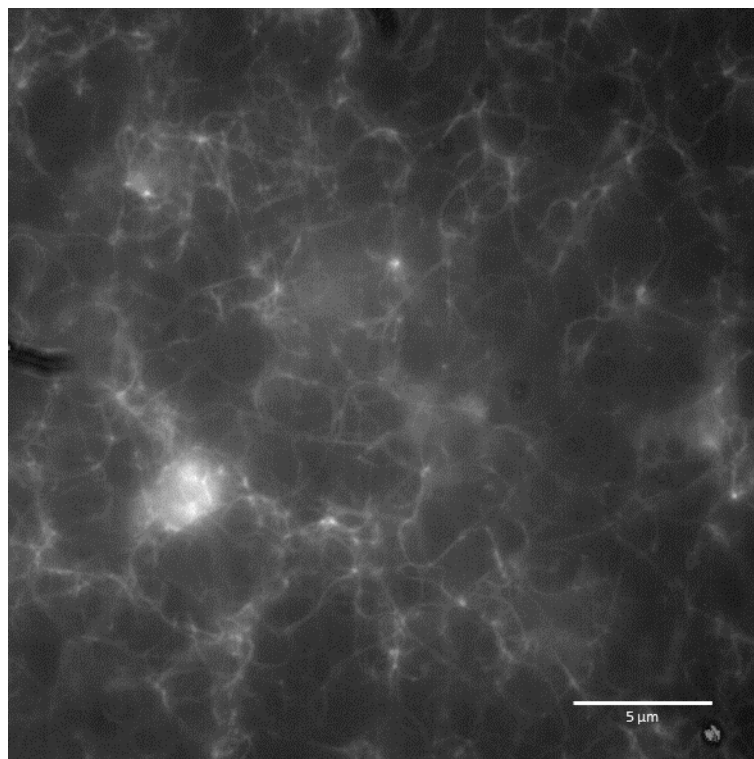


Figure S214 - DAPI LED microscopy image of a hydrogel containing compound **23** (5 mg/mL) in KCl (0.505 M).

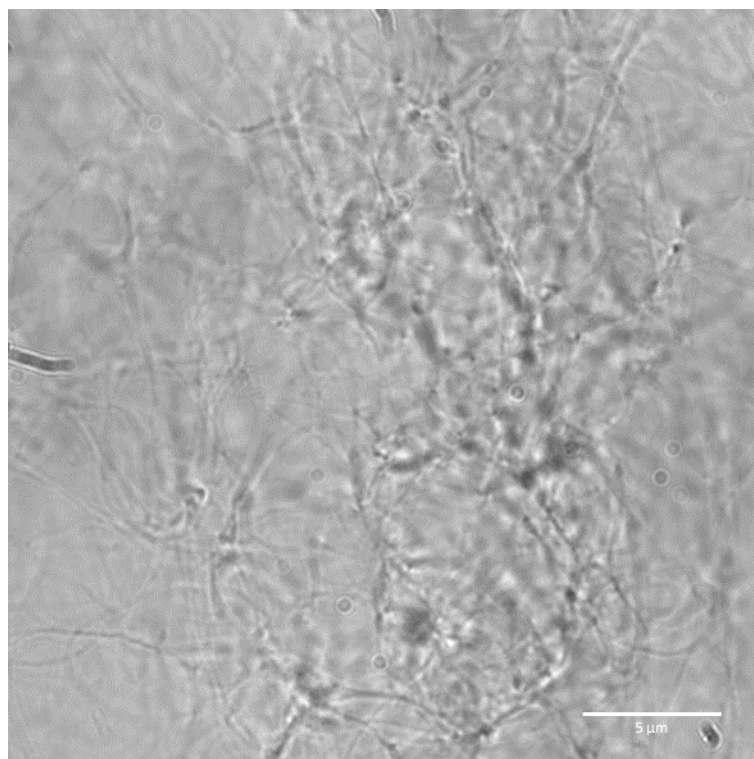


Figure S215 - Transmitted LED microscopy image of a hydrogel containing compound **23** (5 mg/mL) in NaNO<sub>3</sub> (0.505 M).

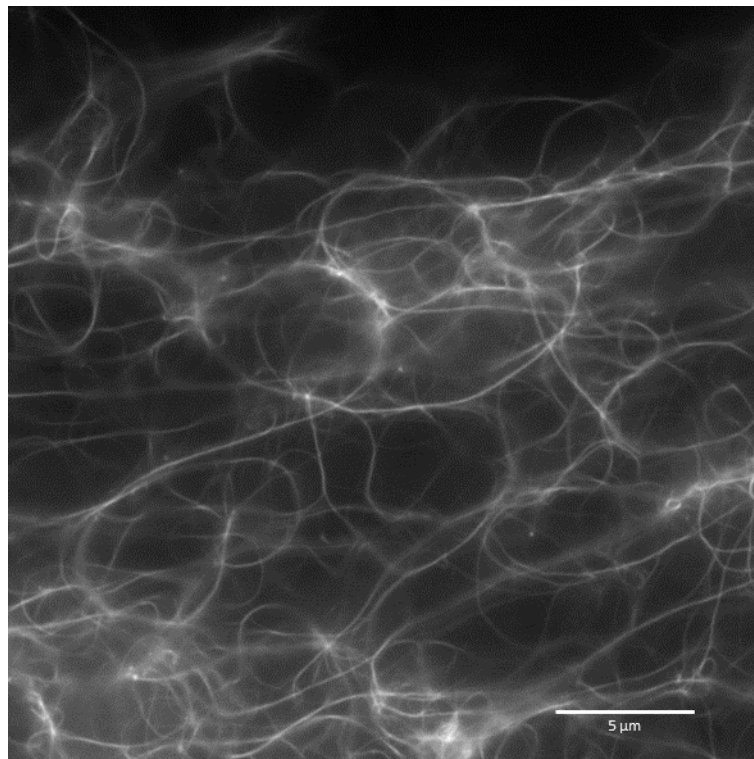


Figure S216 - DAPI LED microscopy image of a hydrogel containing compound **23** (5 mg/mL) in  $\text{NaNO}_3$  (0.505 M).

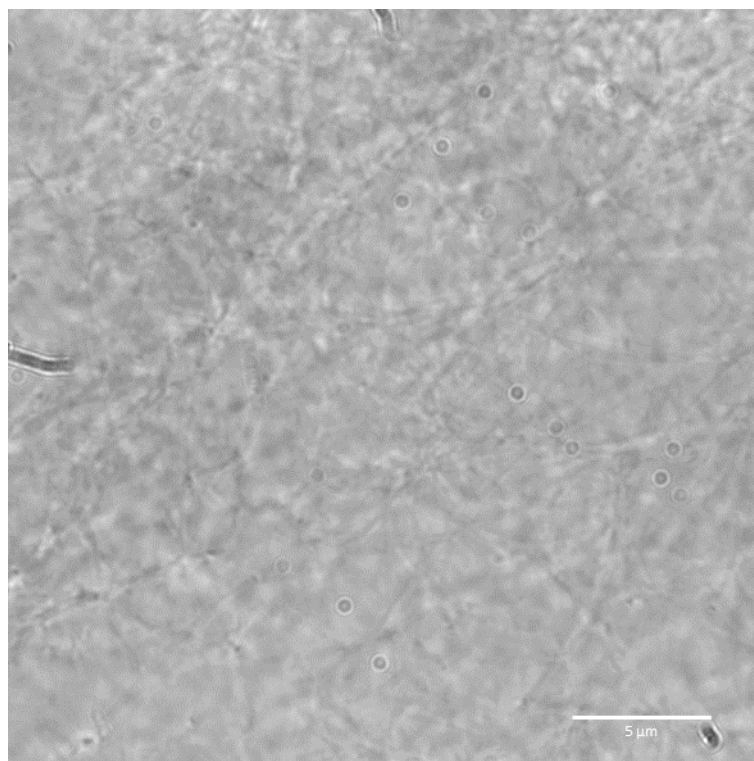


Figure S217 - Transmitted LED microscopy image of a hydrogel containing compound **23** (5 mg/mL) in  $\text{NaH}_2\text{PO}_4$  (0.505 M).

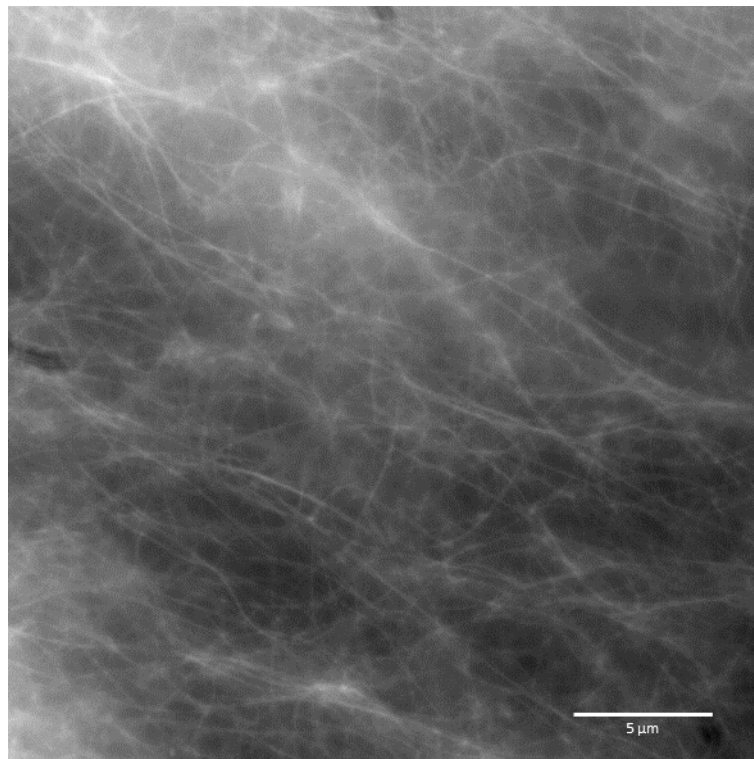


Figure S218 - DAPI LED microscopy image of a hydrogel containing compound **23** (5 mg/mL) in  $\text{NaH}_2\text{PO}_4$  (0.505 M).

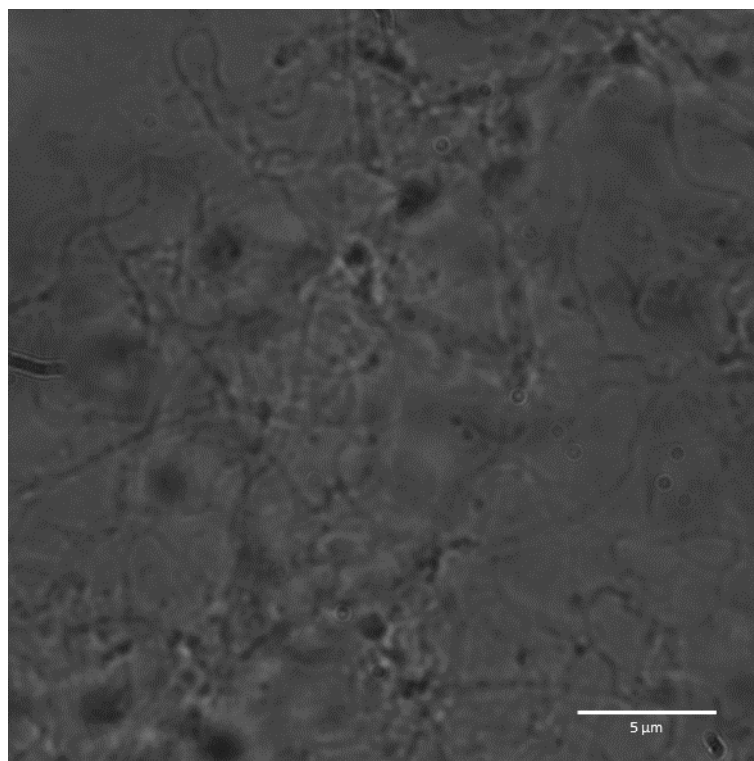


Figure S219 - Transmitted LED microscopy image of a hydrogel containing compound **23** (5 mg/mL) in  $\text{NaOBz}$  (0.505 M).

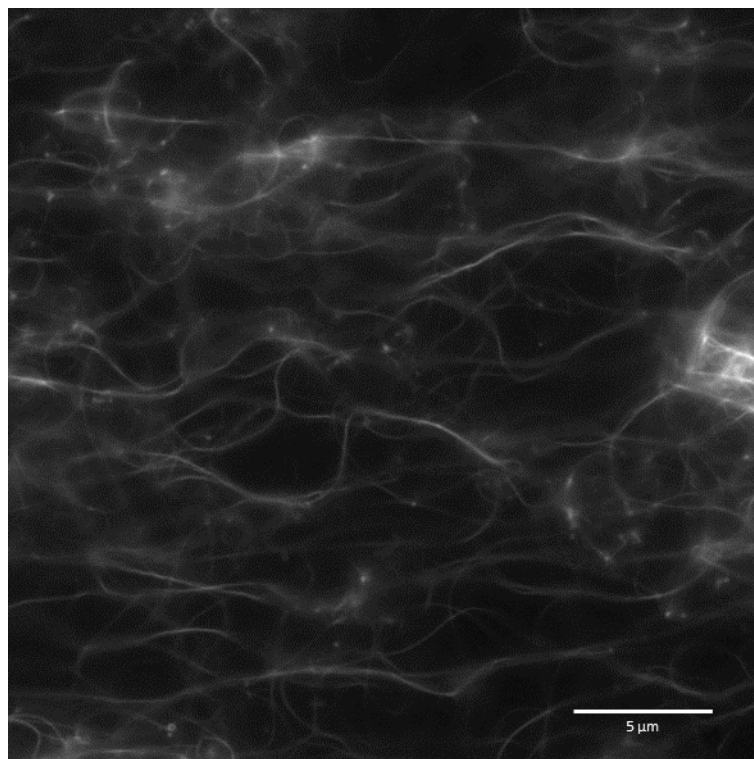


Figure S220 - DAPI LED microscopy image of a hydrogel containing compound **23** (5 mg/mL) in NaOBz (0.505 M).

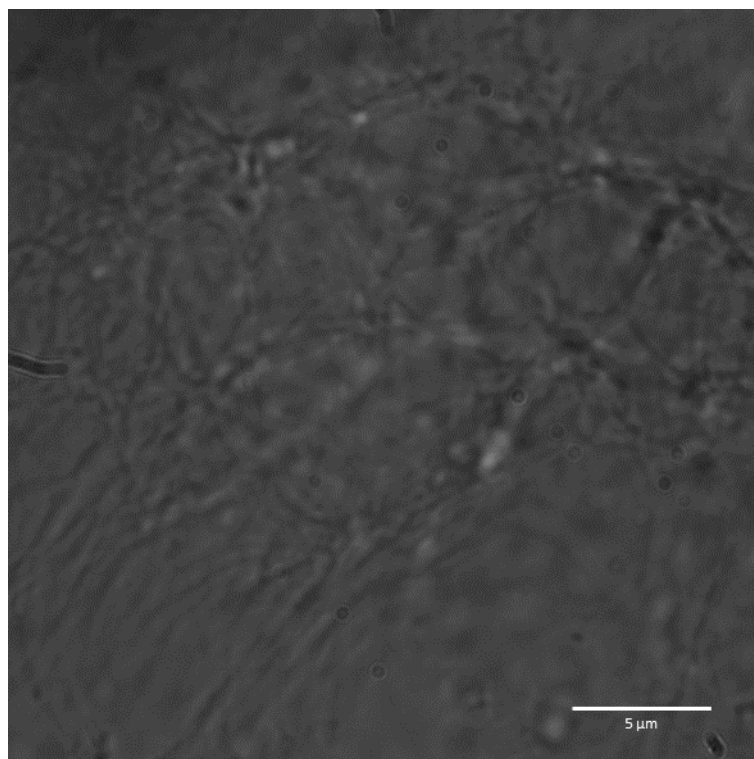


Figure S221 - Transmitted LED microscopy image of a hydrogel containing compound **23** (5 mg/mL) in Na<sub>2</sub>SO<sub>4</sub> (0.505 M).

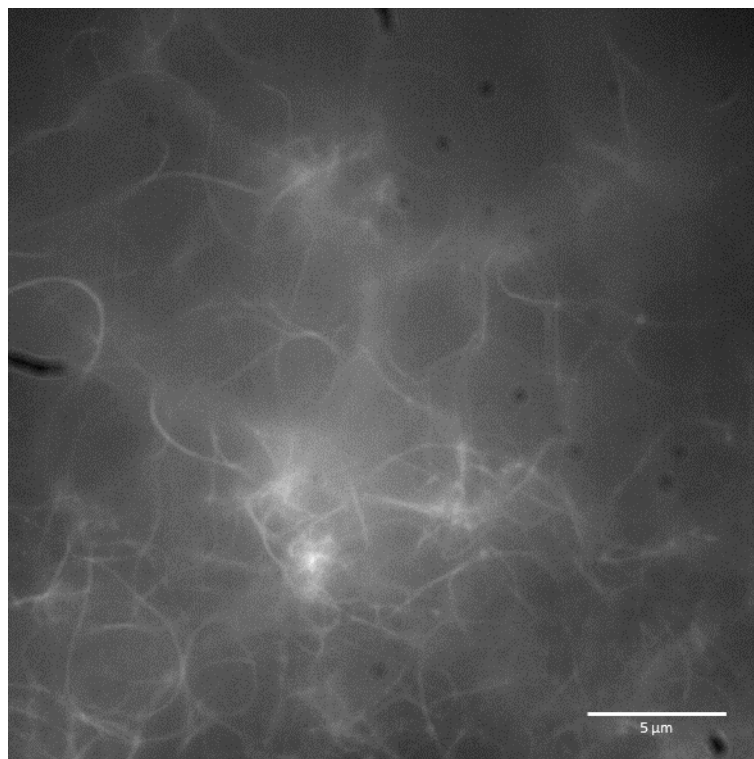


Figure S222 - DAPI LED microscopy image of a hydrogel containing compound **23** (5 mg/mL) in  $\text{Na}_2\text{SO}_4$  (0.505 M).

## 9.11. Biological experiments

### 9.11.1 Screening

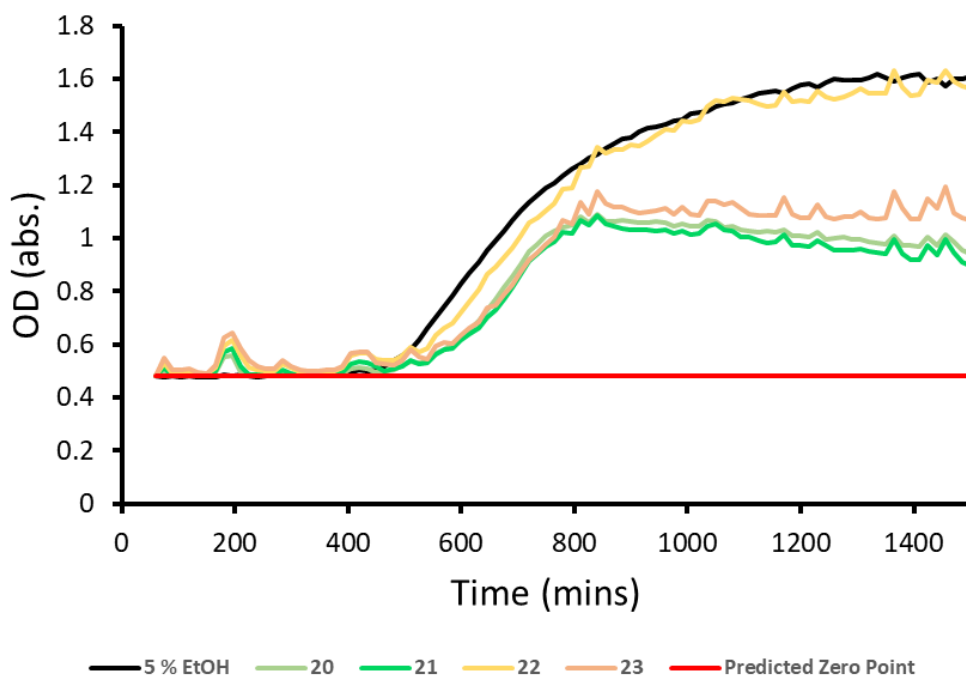


Figure S223 - Averaged growth curves created from absorbance readings of *E. coli* in the presence of different compounds at 3.33 mM. The 5 % EtOH acts as the control.

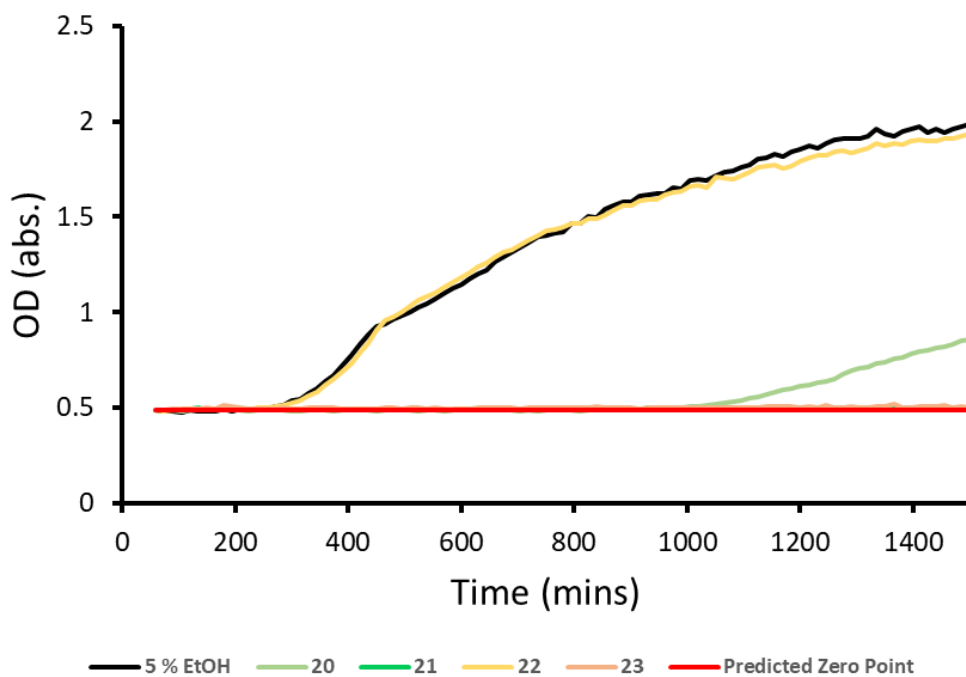


Figure S224 - Averaged growth curves created from absorbance readings of *S. aureus* in the presence of different compounds at 3.33 mM. The 5 % EtOH acts as the control.

9.11.2. MIC<sub>50</sub> data for *E. coli*

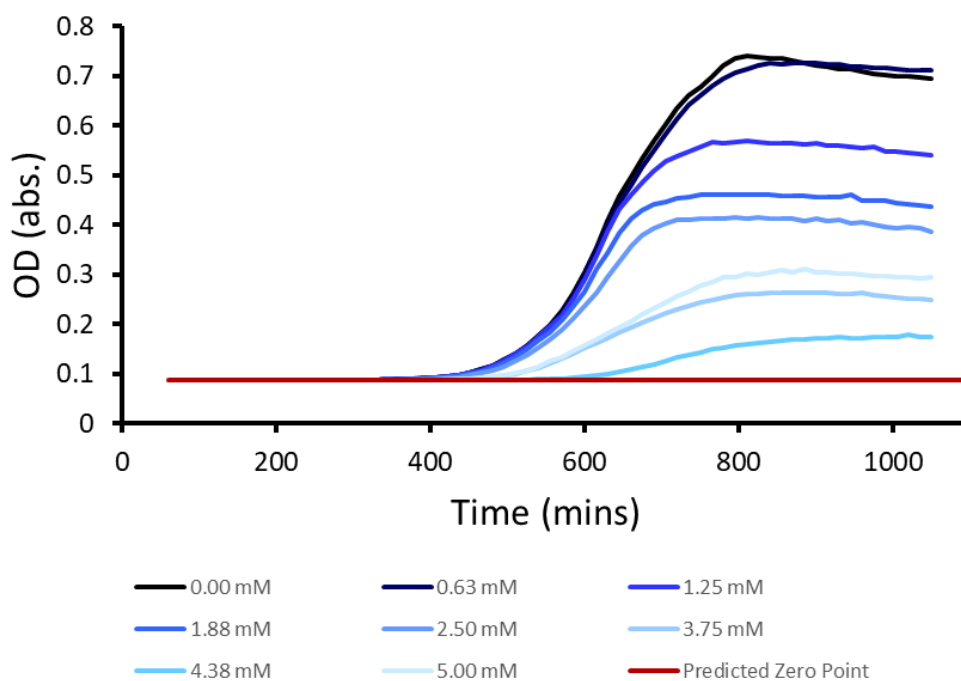


Figure S225 – First MIC<sub>50</sub> biological repeat of **20**. The 5 % EtOH acts as the control.

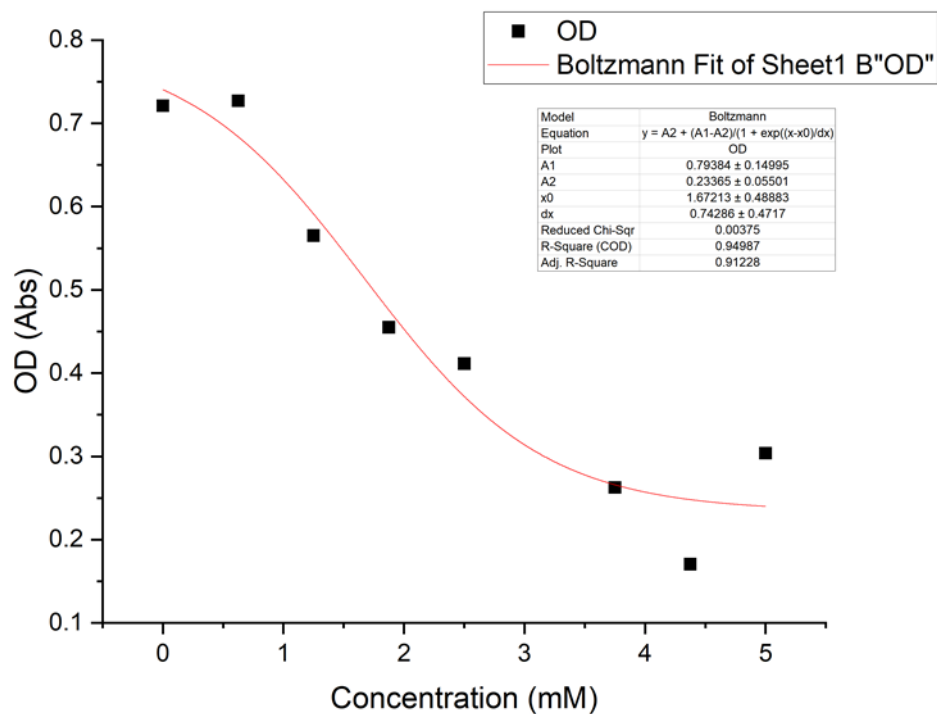


Figure S226 - Origin graph created using absorbance values at 900 minutes for **20** at varying concentrations.

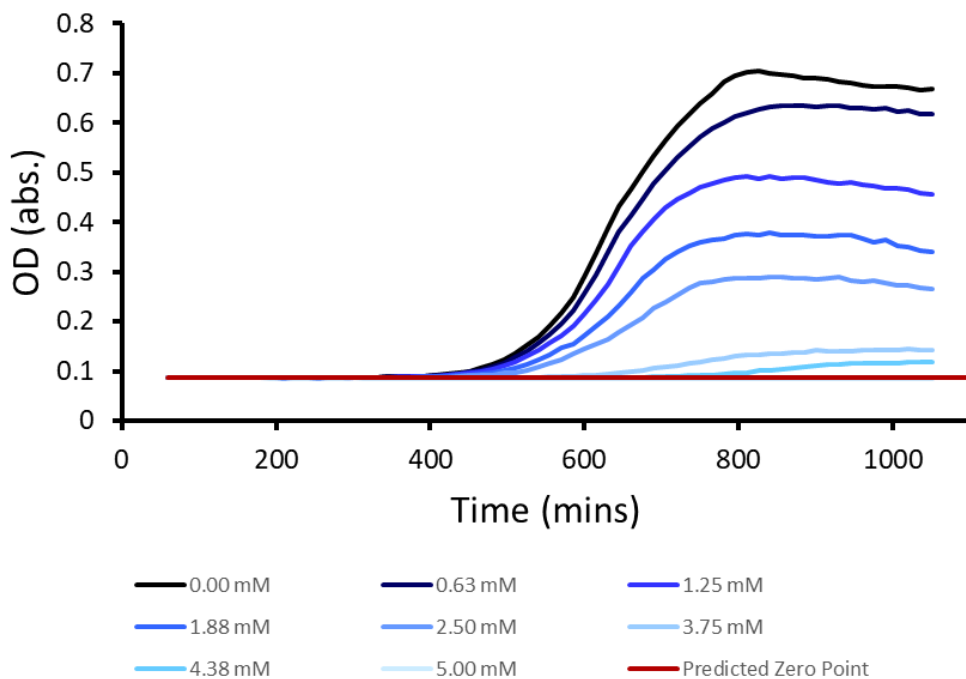


Figure S227 - First MIC<sub>50</sub> biological repeat of **21**. The 5 % EtOH acts as the control.

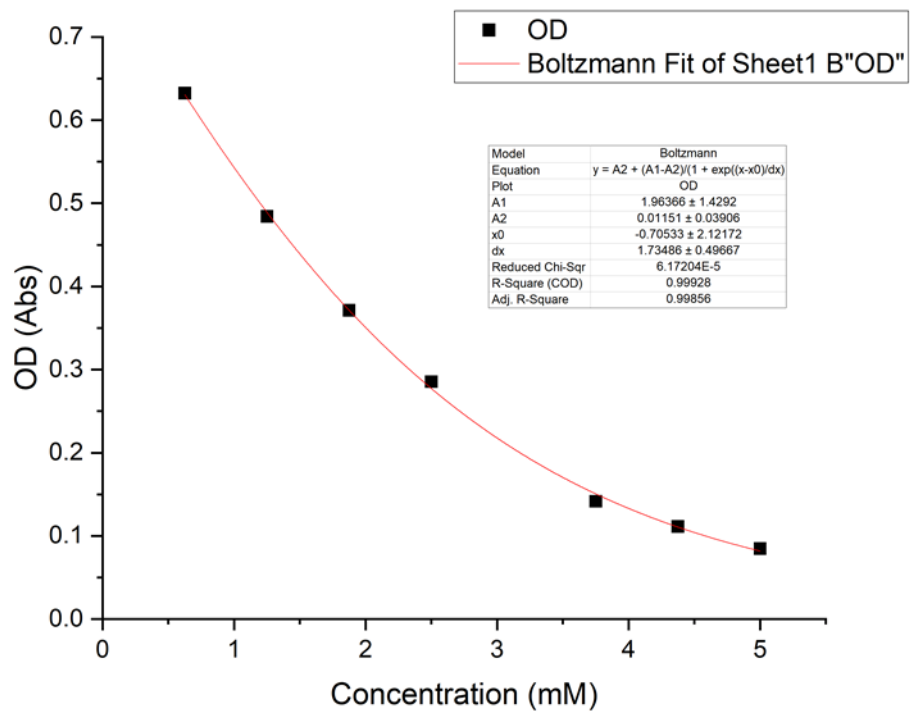


Figure S228 - Origin graph created using absorbance values at 900 minutes for **21** at varying concentrations.

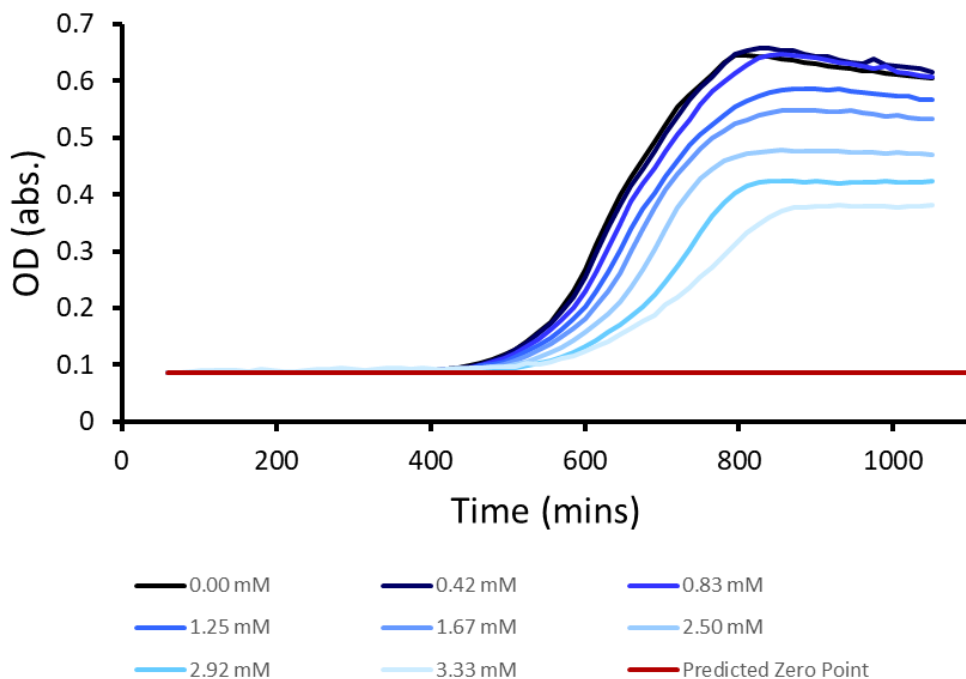


Figure S229 - First MIC<sub>50</sub> biological repeat of **23**. The 5 % EtOH acts as the control.

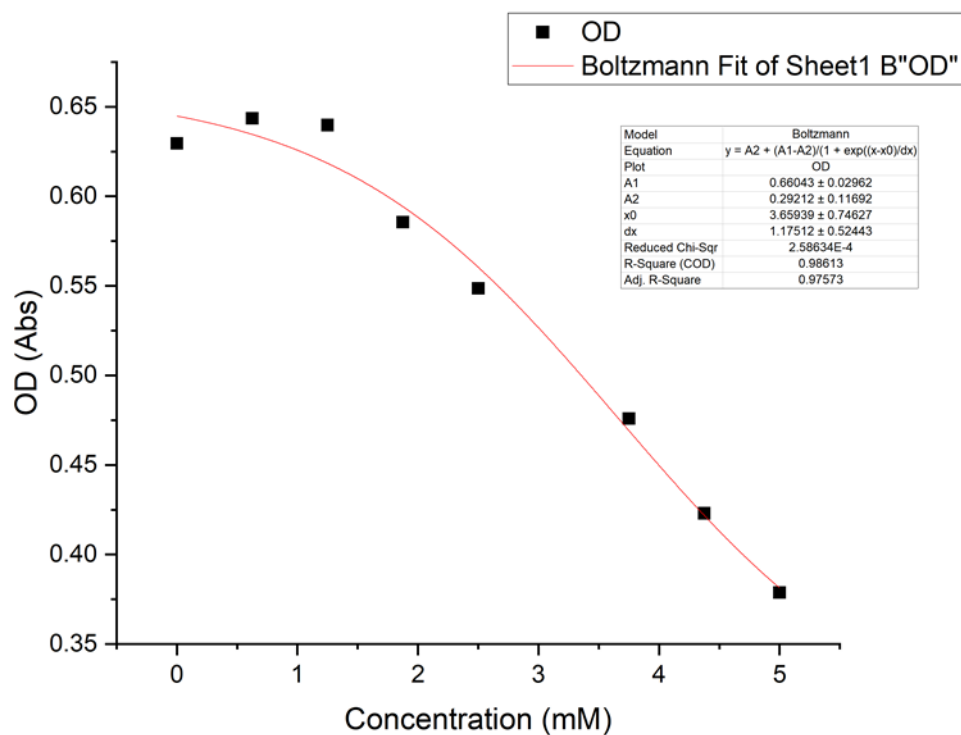


Figure S230 - Origin graph created using absorbance values at 900 minutes for **23** at varying concentrations.

### 9.11.3. MIC<sub>50</sub> data for MRSA

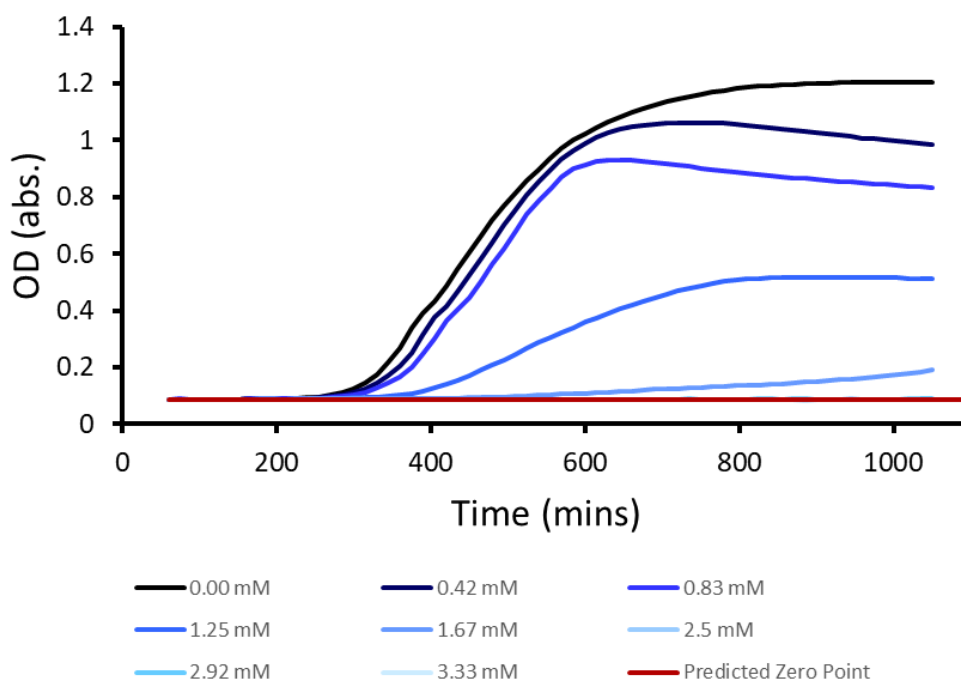


Figure S231 - First MIC<sub>50</sub> biological repeat of **20**. The 5% EtOH acts as the control.

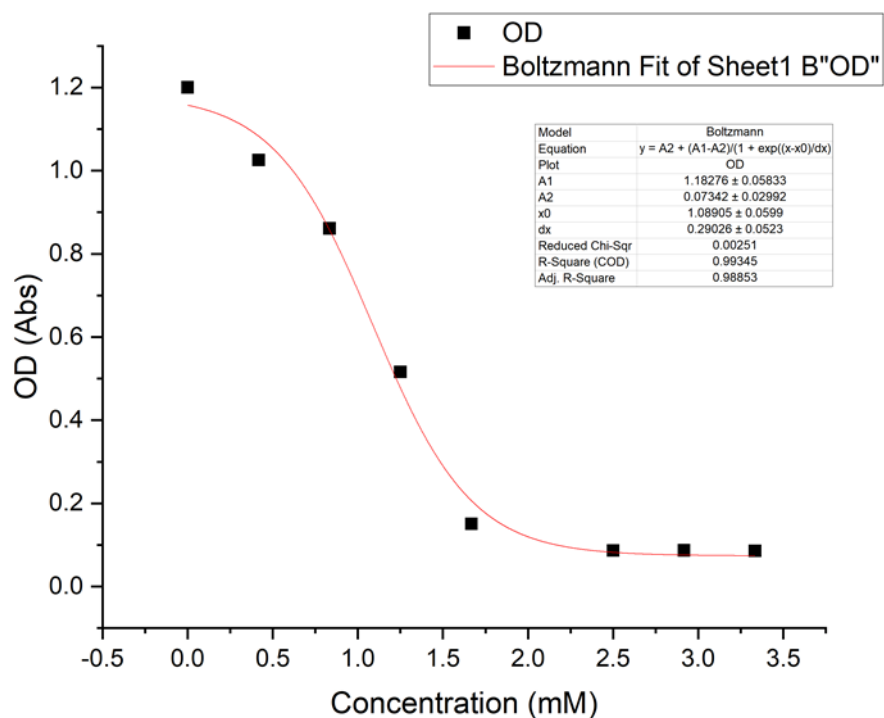


Figure S232 - Origin graph created using absorbance values at 900 minutes for **20** at varying concentrations.

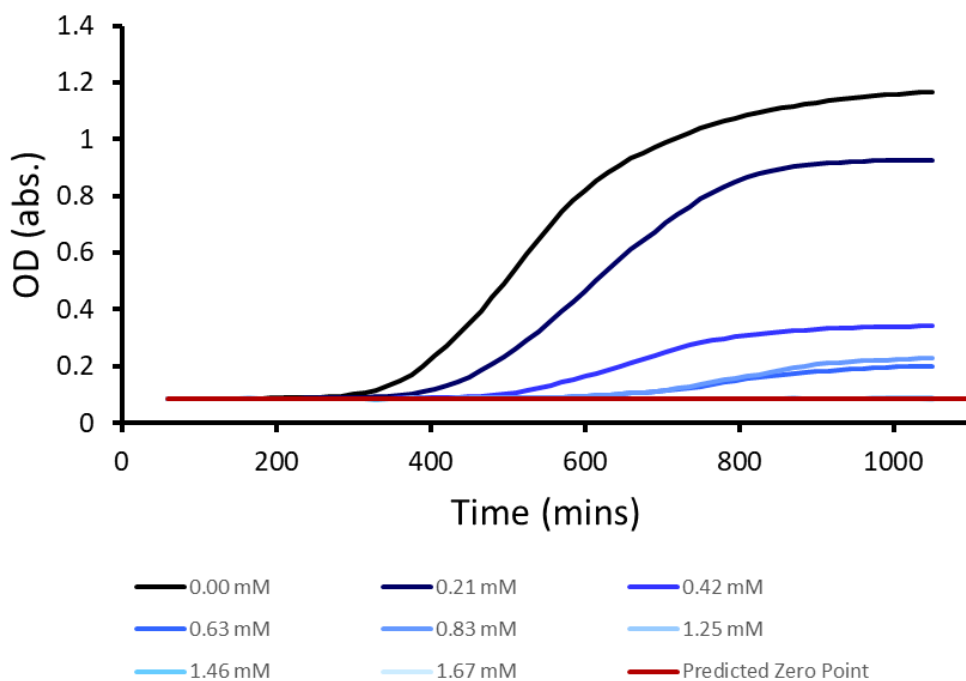


Figure S233 - First MIC<sub>50</sub> biological repeat of **21**. The 5 % EtOH acts as the control.

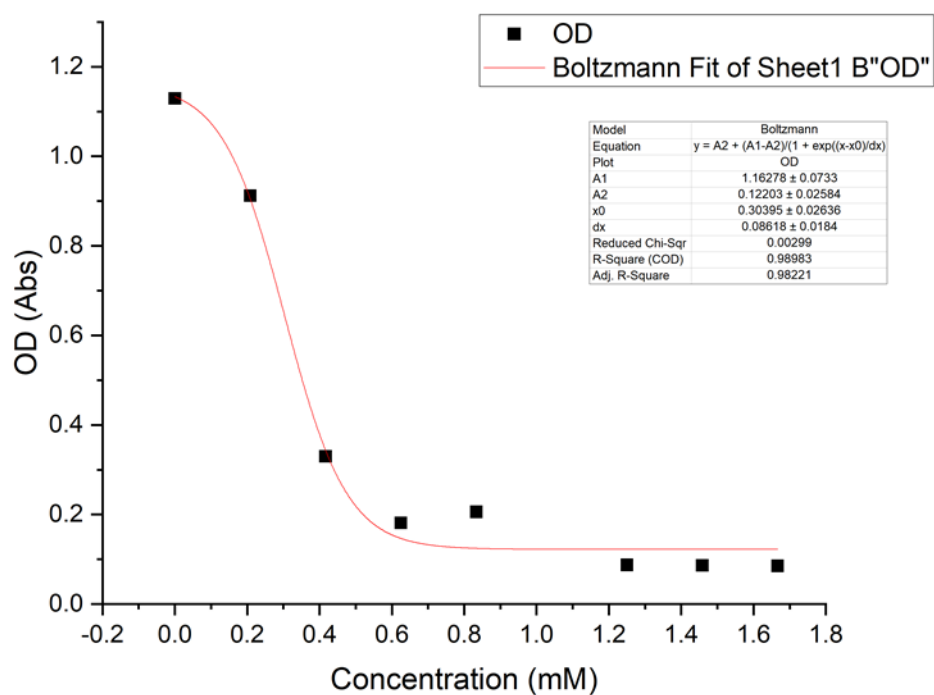


Figure S234 - Origin graph created using absorbance values at 900 minutes for **21** at varying concentrations.

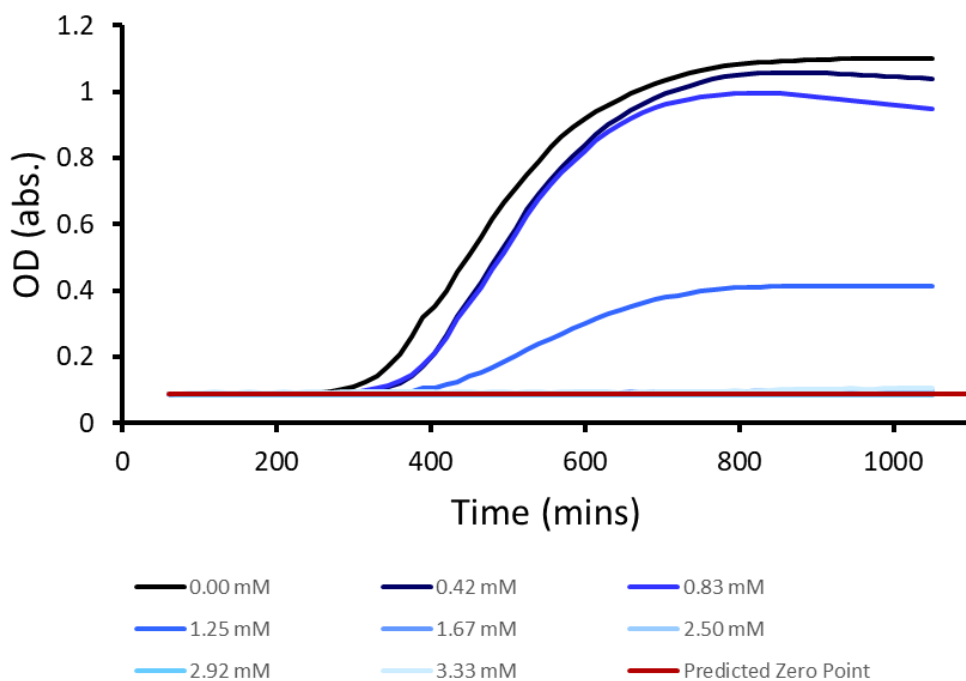


Figure S235 - First MIC<sub>50</sub> biological repeat of **23**. The 5 % EtOH acts as the control.

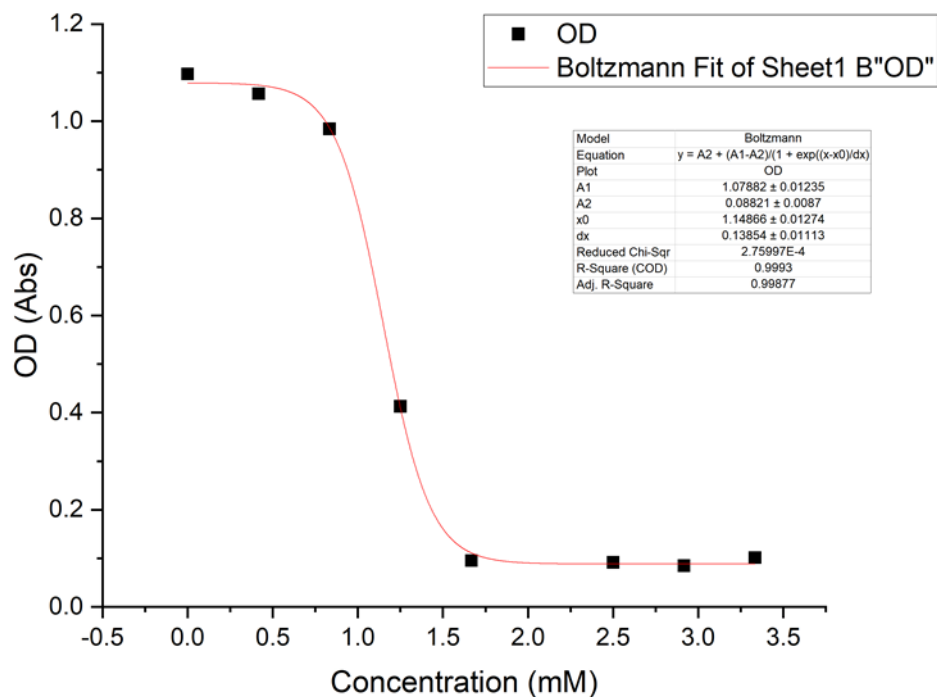


Figure S236 - Origin graph created using absorbance values at 900 minutes for **23** at varying concentrations.

#### 9.11.4. Hydrogel antimicrobial efficacy experiments



Figure S237 - Disc diffusion assays control on *E. coli* DH5B.



Figure S238 - Disc diffusion assays showing the zone of inhibition of growth of *E. coli* DH5B due to the presence of  $\approx 50$  mg SSA hydrogel gel of **1-15** formed in NaCl solution (0.505 M) on the surface of the plate.

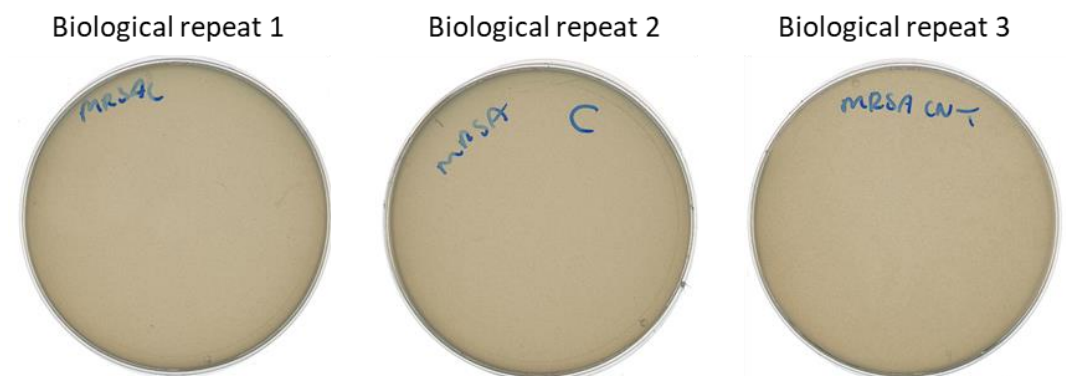


Figure S239 - Disc diffusion assays control on MRSA USA300.

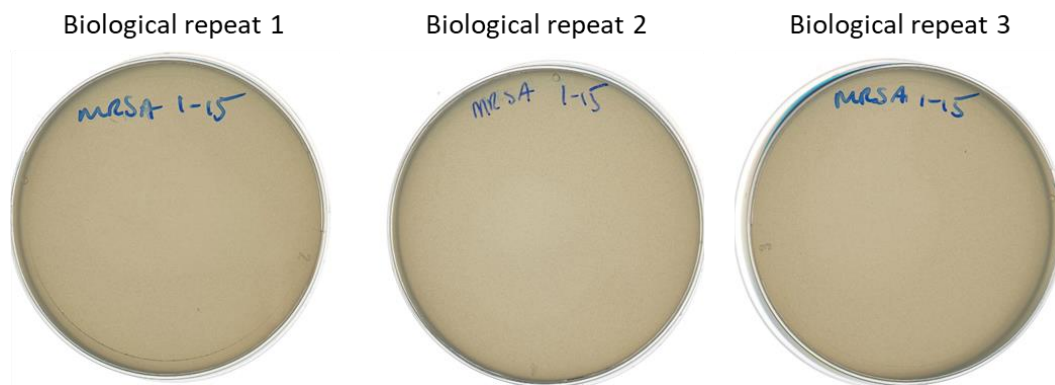


Figure S240 - Disc diffusion assays showing the zone of inhibition of growth of MRSA USA300 due to the presence of  $\approx 50$  mg SSA hydrogel gel of **1-15** formed in NaCl solution (0.505 M) on the surface of the plate.